



DESIGN FOR MANUFACTURE OF BRUSHLESS PERMANENT MAGNET SYNCHRONOUS SERVOMOTORS

A thesis submitted to the University of East London in partial fulfillment of the requirements for the degree of Doctor of Philosophy in Engineering

by

Helder Sá Alves da Silva

School of Architecture, Computing and Engineering (ACE)

University of East London (UEL)

September 2014

ABSTRACT

This thesis presents research into the design of brushless permanent magnet (BPM) interior rotor synchronous servomotor for both performance and manufacturability. The investigation has been supported by experimental evidence gathered with the aid of two prototype servomotors, having the same frame sizes and stator stack lengths, designed by the author and manufactured by the sponsoring company, Control Techniques Dynamics (CTD) Ltd. One servomotor, upon which the research is focussed, has the relatively new segmented stator structure containing concentrated windings. The other servomotor has a conventional structure with a solid stator containing distributed windings and this has provided the means of assessing the degree of improvement attainable with the new structure. It has been established that the new structure enables more cost-effective manufacture than attainable with the conventional structure.

A significant contribution of the research programme is the special notch for retention of the surface mounted permanent magnets in the rotor. This innovation enables a more uniform and smaller air gap, which greatly improves the dynamic and thermal performance for a given frame size and stator stack length, thereby advancing the state of the art. This, together with the greatly reduced stator winding overhang in the new structure, enables a physically smaller motor for a given application, thereby reducing active material usage. Also the design methodology has focused on reducing energy and eliminating waste in the manufacturing process.

Regarding the thermal aspects, only natural cooling has been considered. Conduction, convection and radiation heat transfer in the servomotor has been investigated theoretically, by simulation and by experiments to identify where design improvements can be made. The most critical area identified is the paper wall insulation and comprehensive experiments have been carried out to identify the commercially available material with the highest thermal conductivity to maximise the removal of heat from the stator windings. An array of strategically located thermocouples was used to obtain temperature distributions.

The performance indicators for comparison of the new and conventional servomotors are cogging torque, iron loss and dynamic torque. The cogging torque proved to

increase with the permanent magnet retaining feature for the new servomotor and becomes unpredictable but this disadvantage was offset by material saving and its maximum torque being approximately 40% greater than that of the conventional servomotor. The iron losses have been measured at speeds ranging from 500 r/m to 6000 r/m and at surface housing reference temperatures approximately 81°C. At maximum reference winding temperature ranging from 100°C and 125°C, the dynamic torque rating performances of the new and conventional servomotor prototypes have been compared, the torque/speed characteristics being generated from a near stall speed of 50 r/m to the rated 3000 r/m.

The contributions of this research programme may be summarised as follows:

1. Above all this thesis provides valuable design steps for permanent magnet synchronous servomotors using three world leading software packages (OPERA_2D, SPEED and Motor-CAD) for machine design and will therefore be a useful reference for electrical machine designers, especially beginners.
2. Material saving and simplified BPM synchronous servomotor manufacturing process for segmented stator, concentrated winding configuration.
3. Novel permanent magnet retaining method permitting more uniform and smaller air gap giving performance enhancement.
4. Systematic finite element analysis (FEA) based optimisation is applied to implement a new design principle for BPM synchronous servomotors regarding the stator parameters.
5. A simplified frequency dependent equation for open-circuit iron loss calculation.
6. Experimental and theoretical investigation of thermal impact of stator wall paper insulation entailing comparison of several different materials.
7. Direct benefit to industry through adoption of the new servomotor design by the company who supported the research.

CONTENTS

	Page
ABSTRACT	ii
CONTENTS	iv
LIST OF TABLES	ix
LIST OF FIGURES	x
NOMENCLATURES	xviii
ACKNOWLEDGEMENTS	xxvii
DEDICATION	xxviii

Chapter

1. INTRODUCTION	1
1.1. Overview	1
1.2. Outline of the Thesis	3
1.3. Background	5
1.4. Classification of Brushless Motors	9
1.5. Research Aim and Objectives	12
1.6. Literature Review	15
1.7. Research Contributions	23
2. BRUSHLESS SERVOMOTOR DESIGN AND MANUFACTURE	26
2.1. Introduction	26
2.2. Radial-Flux BPM Synchronous Servomotor	27
2.3. Basic Design Parameters	30
2.3.1. Overview	30
2.3.2. Dimensional Parameters	31
2.3.3. Magnetic Parameters	37
2.3.4. Electric Parameters	52

2.3.4.1. Overview	52
2.3.4.2. The AC Line Voltage	52
2.3.4.3. Current Loading	53
2.3.4.4. Stator Winding Resistance	57
2.3.4.5. Inductances	58
2.3.4.6. Back E.M.F.	59
2.4. Slot-Pole Combination	60
2.5. Torque Performance Analysis	63
2.5.1. Overview	63
2.5.2. Cogging Torque	64
2.5.2.1. Sensitivity Analysis of 12-10 Slot-Pole Design	69
2.5.2.2. Sensitivity Analysis of 12-14 Slot-Pole Design	72
2.5.2.3. Sensitivity Analysis of 18-16 Slot-Pole Design	76
2.5.3. Torque Constant	78
2.5.4. Current Angle	80
2.5.5. Torque Ripple	85
2.5.6. Torque Rating	88
2.6. Iron Loss	90
2.7. Design Selection	91
2.8. Permanent Magnet Material usage	92
2.9. Manufacturing Process of Brushless Motors	95
2.9.1. Stator Core Assembly	95
2.9.1.1. Overview	95
2.9.1.2. Stack and Electric Wall Insulation Process	96
2.9.1.3. Coil Winding and Insertion Process	98
2.9.1.4. Skewing Process	100
2.9.1.5. Impregnation Process	102
2.9.2. Rotor Side.....	104
2.9.2.1. Rotor Lamination Assembly	106
2.9.2.2. Magnet Assembly	106
2.9.2.3. Rotor Taping	107
2.9.2.4. Turning Down	108
2.10. Design for PM Retention of New Servomotor	109

3. THERMAL ANALYSIS OF BRUSHLESS SERVOMOTOR	115
3.1. Introduction	115
3.2. Importance of Thermal Analysis	116
3.3. Thermal Aspect of Prototype Brushless Servomotors	118
3.4. Traditional Design Methods	119
3.4.1. Traditional Sizing Methods	119
3.4.2. Typical Rules of Thumb	120
3.5. Modern Design Methods	121
3.5.1. Thermal Lumped Circuit Model	122
3.5.2. Numerical Thermal Analysis	123
3.6. Heat Sources in Brushless Servomotor	126
3.6.1. Copper Loss Calculation	126
3.6.1.1. Copper Loss and Winding Temperature	127
3.6.1.2. Copper Loss and Magnet Temperature	127
3.6.2. Iron Loss Calculation	128
3.6.2.1. Iron Loss Calculation (Analytical)	128
3.6.2.2. Iron Loss Calculation (Numerical)	131
3.6.3. Magnet Loss Calculation	131
3.6.4. Windage Loss Calculation	131
3.7. Lumped Parameter Thermal Model of a Brushless Servomotor	133
3.7.1. General Concepts	135
3.7.2. Conduction Heat Transfer	137
3.7.2.1. Winding Modelling	139
3.7.2.2. Stator Teeth Modelling	141
3.7.2.3. Stator Back Iron Modelling	143
3.7.2.4. Air-Gap Modelling	144
3.7.2.5. Permanent Magnets Modelling	148
3.7.2.6. Rotor Modelling	149
3.7.2.7. Shaft Modelling	150
3.7.3. Calculation for Prediction of Convection and Radiation Heat Transfer from Housing Surface	150
3.7.3.1. Convection from Housing Surface	151
3.7.3.2. Convection from Heat Sink Plate	153
3.7.3.3. Radiation from Housing and Heat Sink Plate	153

3.8.	Matrix Thermal Model Solver	154
3.9.	Summary	160
4.	EXPERIMENTAL RIG AND TEST PROCEDURES	161
4.1.	Introduction	161
4.2.	Experimental Setup	161
4.2.1.	Cogging Torque Test Setup	162
4.2.2.	Open Circuit Iron Loss Test Setup	163
4.2.3.	Dynamic Torque Rating Test Setup	164
4.3.	Experimental Procedures	168
4.3.1.	Cogging Torque Test Procedure	169
4.3.2.	Open Circuit Iron Loss Test Procedure	170
4.3.3.	Dynamic Torque Rating Test Procedure	170
4.4.	Temperature Measurements	171
4.5.	Summary	173
5.	RESULTS AND COMPARISON OF WINDING CONFIGURATIONS	174
5.1.	Introduction	174
5.2.	Cogging Torque Test Results	175
5.3.	Open Circuit Iron Loss Test Results	179
5.4.	Dynamic Torque Rating Test Results	190
5.5.	Summary	196
6.	INFLUENCE OF WALL INSULATION MATERIAL	197
6.1.	Introduction	197
6.2.	Why Paper Electric Wall Insulation Material	197
6.3.	Thermal Properties of Paper Electric Wall Insulation Material	198
6.4.	Two-Plate Experimental Rig	200
6.4.1.	Thermal Conductivity Test	201
6.4.2.	High-Voltage Insulation Material Testing for Safety	204
6.5.	Experiments Investigating Variation of Thermal Conductivity	207
6.5.1.	Prototype Construction	209
6.5.2.	BPM Synchronous Servomotor	214
6.6.	Simulation Predicting Variations of Thermal Conductivity	216

6.6.1. Motor-CAD Thermal Modelling	217
6.6.2. Motor-CAD Sensitivity Analysis	236
6.7. Summary and Concluding Remarks	240
7. CONCLUSIONS AND RECOMMENDATIONS	242
7.1. Conclusions	242
7.1.1. Overview	242
7.1.2. Manufacturing Aspects	243
7.1.3. Thermal Modelling and Performance Prediction	244
7.1.4. Electromagnetic Modelling and Performance Prediction	244
7.1.5. Test Results	245
7.1.6. Thermal Impact of Paper Wall Insulation Material	245
7.2. Recommendations	246
REFERENCES	248
APPENDICES	257

LIST OF TABLES

TABLE 2.1. Dimensions and parameters of current distributed winding	36
TABLE 2.2. Winding factors for different slot-pole pair combinations	61
TABLE 2.3. Winding layout for the selected slot-pole per combinations	62
TABLE 2.4. The least common multiplier N_c (of Q_s and N_p) values for concentrated wound fractional slot machines	66
TABLE 3.1. Typical current densities (continuous operation)	121
TABLE 3.2. Typical heat transfer coefficients (continuous operation)	121
TABLE 3.3. Numerical thermal analysis (NTA) and the respective strengths and weaknesses	125
TABLE 3.4. Evaluation of Nu according to the range of Ta	145
TABLE 3.5. Evaluation of Nu according to the range of Ta with 10% increase due to radiation	145
TABLE 5.1. Brushless servomotor iron losses for different lengths	189
TABLE 6.1. Important material properties and delta temperature	199
TABLE 6.2. Brushless servomotor details for the same application	210
TABLE 6.3. Temperature difference between winding and housing	216
TABLE 6.4. Colour of layers in Fig. 6.33 representing different brushless servomotor materials in the slot	225
TABLE 6.5. Colour coding for thermal resistors of Motor-CAD software	235
TABLE 6.6. Results for naturally cooled servomotor	236

LIST OF FIGURES

Fig. 1.1.	Inner-rotor (a) and outer-rotor (b) motor construction possibilities	9
Fig. 1.2.	Different rotor constructions of radial flux machines	10
Fig. 1.3.	Servomotor dimensions (a) housing length and (b) frame size.....	11
Fig. 1.4.	Torque per volume for induction motor and brushless servomotor technologies	12
Fig. 1.5.	Typical torque versus speed curve characteristic of servomotors	13
Fig. 2.1.	Radial and axial sections of inner-rotor radial-flux servomotor with flux and current directions	27
Fig. 2.2.	Lamination and stack of laminations of a stator core with 18 slots design servomotor	28
Fig. 2.3.	Cross-section and definition of the geometrical parameters of a brushless servomotor	29
Fig. 2.4.	Servomotor geometry with fundamental servomotor structure and associated flux path	35
Fig. 2.5.	Simplification of the half of magnetic circuit model for Fig. 2.4	38
Fig. 2.6.	Magnetic field flow in low (a) and high (b) pole number p , with fixed slot number	45
Fig. 2.7.	Brushless servomotor air gap flux density distribution for analytical method and FEA method	46
Fig. 2.8.	Brushless servomotor air gap flux density distribution for improved analytical method and FEA method.....	47
Fig. 2.9.	Electric circuit model for one phase winding	52
Fig. 2.10.	Simplified drive system configuration for brushless servomotor	53
Fig. 2.11.	Induced back EMF of one phase of the current distributed 18-6 slot-pole design	54
Fig. 2.12.	Control block diagram	55
Fig. 2.13.	Inverter drive and prototyped brushless servomotors	56
Fig. 2.14.	Popular winding configurations for brushless servomotor	57
Fig. 2.15.	18-6 slot-pole winding layout	63

Fig. 2.16. 12-10 slot-pole winding layout	63
Fig. 2.17. 12-14 slot-pole winding layout	63
Fig. 2.18. 18-16 slot-pole winding layout	63
Fig. 2.19. Cogging torque cycle for the current conventional with 18-16 slot-pole design	68
Fig. 2.20. Cogging torque full-cycles (a) and peak-to-peak values (b) as a function of magnet width (MW) of 12-10 slot-pole servomotor design	69
Fig. 2.21. Cogging torque full-cycles (a) and peak-to-peak values (b) as a function of slot opening angle (SOAng) of 12-10 slot-pole servomotor design	70
Fig. 2.22. Cogging torque full-cycles (a) and peak-to-peak values (b) as a function of slot opening (SO) of 12-10 slot-pole servomotor design	71
Fig. 2.23. Cogging torque full-cycles (a) and peak-to-peak values (b) as a function of tooth gap depth (TGD) of 12-10 slot-pole servomotor design	72
Fig. 2.24. Cogging torque full-cycles (a) and peak-to-peak values (b) as a function of magnet width (MW) of 12-14 slot-pole servomotor design	73
Fig. 2.25. Cogging torque full-cycles (a) and peak-to-peak values (b) as a function of slot opening angle (SOAng) of 12-14 slot-pole servomotor design	74
Fig. 2.26. Cogging torque full-cycles (a) and peak-to-peak values (b) as a function of slot-opening (SO) of 12-14 slot-pole servomotor design	74
Fig. 2.27. Cogging torque full-cycles (a) and peak-to-peak values (b) as a function of tooth gap depth (TGD) of 12-14 slot-pole servomotor design	75
Fig. 2.28. Cogging torque full-cycles (a) and peak-to-peak values (b) as a function of magnet width (MW) of 18-16 slot-pole servomotor design	76
Fig. 2.29. Cogging torque full-cycles (a) and peak-to-peak values (b) as a function of slot opening angle (SOAng) of 18-16 slot-pole servomotor design	77
Fig. 2.30. Cogging torque full-cycles (a) and peak-to-peak values (b) as a function of slot opening (SO) of 18-16 slot-pole servomotor design	77
Fig. 2.31. Cogging torque full-cycles (a) and peak-to-peak values (b) as a function of tooth gap depth (TGD) of 18-16 slot-pole servomotor design	78
Fig. 2.32. The winding details of SPEED Software template	79
Fig. 2.33. Winding details and winding layout for 12-10 slot-pole design brushless servomotor	80

Fig. 2.34. Torque curves characteristics as function of load/current angle for the new three surface magnets with the segmented stator and concentrated winding design investigated	80
Fig. 2.35. Sensitivity analysis of stator tooth width (TWS) with respect to torque constant for the proposed designs	82
Fig. 2.36. Finite element graphics for flux plot of the new designed brushless servomotors	83
Fig. 2.37. k_t comparison between the new designed brushless servomotors	84
Fig. 2.38. Finite element graphs for torque-ripple of the new designed brushless servomotors	86
Fig. 2.39. Finite element graphs for stall torque of the new designed brushless servomotor	86
Fig. 2.40. FEA and analytical graphs for flux plot of the new designed brushless servomotors	87
Fig. 2.41. FEA stall torque for the new designed brushless servomotor	89
Fig. 2.42. Motor-CAD: Geometry Axial Output Data Temperatures	89
Fig. 2.43. Finite element analysis iron loss calculation	91
Fig. 2.44. Torque constant as function of permanent magnet length	94
Fig. 2.45. New segmented stator core	96
Fig. 2.46. Slot liner insertion machine	97
Fig. 2.47. Lamination stack preparation	97
Fig. 2.48. Insertion of slot liners	97
Fig. 2.49. 18-6 slot-pole design stack	97
Fig. 2.50. Coil winding machine	98
Fig. 2.51. Winding preparation	98
Fig. 2.52. Winding insertion machine	99
Fig. 2.53. Complete winding inserted	99
Fig. 2.54. New segmented stator coil winding	99
Fig. 2.55. Cogging torque levels for conventional no skewed and the new segmented stator not skewed brushless servomotor designs	100
Fig. 2.56. Conventional winding and skew tooling	101
Fig. 2.57. Stator lamination skewing process	101
Fig. 2.58. Glue to maintain the skew angle	101
Fig. 2.59. Skewed stator for conventional winding	101

Fig. 2.60. New stator without need for skewing process	102
Fig. 2.61. Complete new segmented stator	102
Fig. 2.62. Impregnation tooling mounting process	103
Fig. 2.63. Stack insertion process for impregnation	103
Fig. 2.64. Stator impregnation process	103
Fig. 2.65. Impregnated stators ready for the next manufacturing process	103
Fig. 2.66. Different air-gap and the effect on torque constant	105
Fig. 2.67. Rotor manufacturing advantages of new brushless servomotor	105
Fig. 2.68. Rotor shaft mounted for lam insertion	106
Fig. 2.69. Rotor stack laminations	106
Fig. 2.70. Stack lamination insertion process	106
Fig. 2.71. Insertion of the final balancing plate	106
Fig. 2.72. Application of glue to the rotor stack	107
Fig. 2.73. Insertion of permanent magnets to the rotor stack	107
Fig. 2.74. Finalizing the permanent magnet insertion manufacturing process	107
Fig. 2.75. Complete permanent magnet insertion to the rotor	107
Fig. 2.76. Application of glass tape to the rotor to retain permanent magnets	108
Fig. 2.77. Completely taped rotor	108
Fig. 2.78. Cut off the excessive tape material	108
Fig. 2.79. Removal of excessive tape material	108
Fig. 2.80. Tape material turn down machinery	109
Fig. 2.81. Taped rotor after post oven process	109
Fig. 2.82. Tape material turning down	109
Fig. 2.83. Complete rotor assembled	109
Fig. 2.84. Open circuit flux distribution without T-Lams	110
Fig. 2.85. Open circuit flux distribution with T-Lams	110
Fig. 2.86. Cogging torque cycle variation with magnet width without T-lams	111
Fig. 2.87. Cogging torque cycle variation with magnet width with T-lams	112
Fig. 2.88. Signed peak-to-peak cogging torque with and without T-lams	113
Fig. 3.1. Schematic of brushless servomotor with heat transfer modes due to radiation (orange arrow), convection (yellow arrow) and conduction (red arrow)	116
Fig. 3.2. Life vs. temperature curves for insulation systems	117
Fig. 3.3. Traditional motor sizing method based on single thermal resistance ...	120

Fig. 3.4.	The traditional motor sizing method based on single heat transfer coefficient	120
Fig. 3.5.	Example of heat transfer network for an electric motor	122
Fig. 3.6.	FLUX 2D FEA winding thermal image	124
Fig. 3.7.	ANSYS housing water flow	124
Fig. 3.8.	TENV brushless servomotor with main losses to be removed	126
Fig. 3.9.	Hysteresis loop with low loss and high loss	129
Fig. 3.10.	Pipe dimensions and temperature measurement points for modelling of stator	134
Fig. 3.11.	T-equivalent circuit with elementary network components representing back iron	134
Fig. 3.12.	Typical stator section of an inner rotor type brushless servomotor	135
Fig. 3.13.	Trapezoidal conductor bundle cross-section for winding model	139
Fig. 3.14.	One stator slot model	141
Fig. 3.15.	Brushless servomotor main components of the thermal model	156
Fig. 3.16.	Servomotor thermal circuit with air gap convection and rotor losses	156
Fig. 4.1.	Cogging torque test rig system components	162
Fig. 4.2.	Oscilloscope displaying cogging torque and back EMF waveforms	163
Fig. 4.3.	Setup for open circuit iron loss testing	164
Fig. 4.4.	Open circuit iron losses testing torque measurement sensor	164
Fig. 4.5.	Dynamic torque rating test rig	165
Fig. 4.6.	Control Techniques Digitax drive control system and the prototypes ...	166
Fig. 4.7.	Drive control PWM with high frequency carrier and low frequency phase-to-phase components	167
Fig. 4.8.	Test setup for dynamic torque rating of brushless servomotor	167
Fig. 4.9.	(a) Brushless servomotor (b) mounted prototype on the test rig and (c) parts and thermocouple locations on the servomotor under test	171
Fig. 4.10.	LabView visual interface for torque rating	173
Fig. 5.1.	Cogging torque produce by north, south poles and the resultant cogging torque	175
Fig. 5.2.	Comparison of the measured cogging torque with the theoretical predictions using the FEA method and analytical expressions	176
Fig. 5.3.	Measured cogging torque (upper trace) and back EMF (lower trace) for the new servomotor	177

Fig. 5.4.	Expanded measured cogging torque for the new servomotor	177
Fig. 5.5.	Cogging torque signal for servomotor 1000 samples per second	178
Fig. 5.6.	Cogging torque spectrum produced by a FFT for new servomotor	178
Fig. 5.7.	Measured open circuit losses (cold surface) for clockwise and anticlockwise rotation	180
Fig. 5.8.	Measured open circuit losses (hot surface) for clockwise and anticlockwise rotation	181
Fig. 5.9.	Measured open circuit losses with surface temperature variation	182
Fig. 5.10.	Measured open circuit losses for different stator stack lengths	183
Fig. 5.11.	Rotational losses due to the windage and the friction losses	183
Fig. 5.12.	Measured rotational iron losses for different stack lengths	184
Fig. 5.13.	Comparison of measured iron losses and predicted results with analytical and FEA	185
Fig. 5.14.	Frequency, loss per volume, constants and the iron losses equation...	186
Fig. 5.15.	Determination of constants k and n by linear regression	186
Fig. 5.16.	Predicted versus measured iron losses for different stack lengths	187
Fig. 5.17.	The prototype of new concentrated and current distributed design brushless servomotor	190
Fig. 5.18.	Dynamic torque rating test results for the new segmented design	192
Fig. 5.19.	Comparison of dynamic torque rating-speed characteristics for current solid stator core and the new segmented stator design	193
Fig. 5.20.	Dynamic torque rating test results for the new design at increased winding temperature	193
Fig. 5.21.	Dynamic torque rating-speed curve characteristics for different winding temperatures	194
Fig. 5.22.	Variation of servomotor torque level with the winding temperature	195
Fig. 6.1.	Typical peak transition caused by PWM switching in motor with oscilloscope reading 400 Volts per division	198
Fig. 6.2.	Wall insulation materials for the thermal conductivity test	199
Fig. 6.3.	Two-plate system test rig for wall insulation materials	200
Fig. 6.4.	Test setup for paper wall insulation material thermal conductivity	201
Fig. 6.5.	Paper wall insulation material testing for thermal conductivity	204
Fig. 6.6.	Slot insulation system for electric motors	205
Fig. 6.7.	Paper wall insulation Material A flash test	206

Fig. 6.8. Paper wall insulation Material B flash test	206
Fig. 6.9. Paper wall insulation Material C flash test	206
Fig. 6.10. Paper wall insulation Material D flash test	207
Fig. 6.11. Paper wall insulation Material E flash test	207
Fig. 6.12. Conventional stator with paper wall insulation and winding	208
Fig. 6.13. Two stator segments with two paper wall insulation materials	208
Fig. 6.14. Impregnated stator of skewed conventional motor	212
Fig. 6.15. Impregnated segmented stator and rotor of new non-skewed motor....	212
Fig. 6.16. Paper wall insulation material without resin impregnation	213
Fig. 6.17. Paper wall insulation material with resin impregnation	213
Fig. 6.18. System load testing	214
Fig. 6.19. Torque-speed curves for concentrated and distributed winding configurations using wall insulation paper materials A and B	214
Fig. 6.20. Torque-constant, torque performance and current injected to the winding comparison between 12-10 and 18-6 slot-pole combinations	215
Fig. 6.21. SPEED: Outline Editor for new design brushless servomotor cross-section with 12 slots and 10 poles	217
Fig. 6.22. SPEED: WINDING EDITOR for the segmented stator and concentrated windings	218
Fig. 6.23. SPEED: PC-BDC Control Set	218
Fig. 6.24. SPEED: PC-BDC Rotational Losses	219
Fig. 6.25. SPEED: PC-BDC Thermal Information	219
Fig. 6.26. Prototype mounted in the rig system for the performance test	219
Fig. 6.27. Parts of servomotor and rig showing positions of thermocouples	220
Fig. 6.28. Selected test point of delta winding temperature of 80.47 ⁰ C for thermal modelling	220
Fig. 6.29. SPEED: Extract of winding section from DESIGN SHEET	221
Fig. 6.30. SPEED: Extract of static design output from DESIGN SHEET	221
Fig. 6.31. Motor-CAD: Geometry Cross-section with data imported from SPEED PC-BDC	223
Fig. 6.32. Motor-CAD: Geometry Axial Output Data Temperature	223
Fig. 6.33. Motor-CAD: Winding Editor - Winding View Material layer	224
Fig. 6.34. Motor-CAD: Winding Editor - Winding View Conductors	225

Fig. 6.35. Motor-CAD: Geometry Axial View for mounting plate and no encoder model	226
Fig. 6.36. Motor-CAD: Import/Export Losses in SPEED and temperatures in Motor-CAD	227
Fig. 6.37. Motor-CAD: Input Data Losses	228
Fig. 6.38. Motor-CAD: Input Data Cooling Options	229
Fig. 6.39. Motor-CAD: Input Data Radiation	230
Fig. 6.40. Motor-CAD: Input Data Materials & Weights	231
Fig. 6.41. Setup for temperature selection for validation	232
Fig. 6.42. Motor-CAD: Validation Showing predictions versus test steady-state temperatures	232
Fig. 6.43. Motor-CAD: Validation Showing good predictions versus test steady-state temperatures	233
Fig. 6.44. Motor-CAD: Schematic Showing the thermal network and the steady-state temperatures	234
Fig. 6.45. Motor-CAD: Sensitivity analysis of winding temperature vs. air-gap	237
Fig. 6.46. Motor-CAD: Sensitivity analysis of winding hotspot temperature vs. impregnation	237
Fig. 6.47. Motor-CAD: Sensitivity analysis of winding temperature vs. thermal conductivity	238
Fig. A.1. Project structure for the research program	257
Fig. B.1. Position 'A', unstable equilibrium	258
Fig. B.2. Position 'B', motor produces a torque	259
Fig. B.3. Position 'C', stable equilibrium	260
Fig. B.4. Position 'D', unstable equilibrium	260
Fig. B.5. Cogging torque produce by north, south poles and resultant cogging ..	261

NOMENCLATURES

Acronyms

2D	Two-dimensional
3D	Three-dimensional
BM	Beta Magnet (Angle)
BP	Beta Pitch
BPM	Brushless Permanent Magnet
BPMSS	Brushless Permanent Magnet Synchronous Servomotor
CAE	Computer Aided Engineering
CFD	Computational Fluid Dynamics
DAQ	Data Acquisition
EMF	Electromotive Force
FE	Finite Element
FEA	Finite Element Analysis
FEM	Finite Element Method
FFT	Fast Fourier Transform
FSPM	Flux Switching Permanent Magnet
IEA	International Energy Agency
IEC	International Electrotechnical Commission
IEEE	Institute of Electrical and Electronics Engineers
MT	Magnet Thickness
NdFeB	Neodymium Iron Boron
NEMA	National Electrical Manufacturers Association
NTA	Numerical Thermal Analysis
OD	Outer Diameter
PM	Permanent Magnet
PMSM	Permanent Magnet Synchronous Motor
SD	Slot Depth
SM	Surface Mounted
SmCo	Samarium Cobalt

SMRF	Surface Mounted Radial Flux
SO	Slot Open
SOang	Slot Opening Angle
SW	Slot Width
SWI	Slot Width Inner
SWO	Slot Width Outer
TEC	thermal Equivalent Circuit
TEFC	totally Enclosed Fan Cooled
TENV	totally Enclosed Not Ventilated
TGD	tooth Gap Depth
UL	Underwriters Laboratories
UEL	University of East London
YHS	stator Yoke Height
TH	tooth Height
THS	stator Tooth Height
TWS	stator tooth width

List of symbols

A	area
AC	alternating current
A_g	air gap cross-sectional area
A_m	magnet cross-sectional area
A_{sl}	slot area
B	magnetic flux density
B_g	air gap flux density
B_m	magnet flux density
B_{pk}	peak flux density
B_r	remanence flux density
C	capacitance
C	loss coefficient
C_h	loss coefficient due to hysteresis
C_e	loss coefficient due to eddy-current
C_T	stator goodness factor
c	constant

c_p	specific heat capacity
D	bore diameter, diameter of cylinder
D_0	stator outer diameter
d_r	rotor external diameter
D_{rc}	rotor core diameter
F	force
F_a	scalar magnetic potential in the air
F_m	scalar magnetic potential in the magnet
f	frequency
f_s	slot fill factor
Gr	Grashof number
g	air gap length, gravity
\dot{g}	heat generation rate
H	magnetic field intensity
H_c	coercive magnetic field intensity
H_g	magnetic field intensity in the air gap region
H_m	magnet field intensity
h	heat transfer coefficient, hysteresis coefficient
h_c	heat transfer coefficient of convection
h_m	radial thickness of the magnet
h_g	heat transfer coefficient for the air gap
h_R	heat transfer coefficient of radiation
h_{sd}	slot depth
h_{th}	slot opening angle tooth height
h_{yhs}	stator Yoke Height
I	electric current
I_{sp}	sinewave current peak value
i	current, a integer number
i_{ph}	RMS phase current
k	fluid/material thermal conductivity, constant
k_C	carter factor
k_f	constant for peripheral force
k_{open}	ratio between the slot opening and the inner stator slot width
k_{sk}	skew factor

k_t	torque constant
k_{wa}	winding bundle conductivity in the axial direction
L	length
L_d	d-axis inductance of one phase
L_l	leakage inductance
L_{ph}	phase inductance
L_q	q-axis inductance of one phase
LM	magnet length
l_{act}	active length of the rotor
l_m	magnet length
l_{iron}	width of the rotor iron piece
\vec{M}	magnet magnetization
Mn	magnetization throughout the cross-section of the magnets
m	mass, number of phases
MMF	magnetomotive force
N_s	number of slots
Nu	Nusselt number
Nc	least common multiple
n	constant, harmonic number in the air gap flux density
n_s	number of conductors per slot
P	power loss
p	pole pair
P_{ad}	additional power loss
P_{cu}	copper power loss
P_e	hysteresis power loss
P_{fe}	iron loss power
P_h	eddy-current power loss
P_o	power output
P_R	rotor power loss
Pr	Prandtl number
Q_s	number of stator slots
Q_{th}	total heat generated
q	number of slots per pole per phase
R	electrical resistance, thermal resistance

R_a	axial thermal resistance of the housing
R_{aD}	Raleigh number based on the diameter
R_{ag}	thermal resistance due to air-gap
R_{aL}	Raleigh number based on the length
$Rad3$	stator core radius
RC	rotor core diameter
R_{ceh}	contact thermal resistance between housing and encoder housing
R_{cmp}	contact resistance between housing and mounting plate
R_{con}	thermal resistance for conduction heat transfer
R_{csh}	contact resistance between stator laminations and main housing
R_{cws}	contact resistance between windings and stator
Re	Reynolds number
R_{ecf}	front endcap thermal resistance
R_{ecr}	rear endcap thermal resistance
R_{eh}	contact resistance between encoder housing and main housing
R_{er}	radiation resistance between encoder housing and cooling ambient
R_g	air gap reluctance
r_g	air gap radius
R_g	air gap reluctance
R_h	thermal resistance between housing and ambient surrounding
R_{hc}	convection resistance between housing and cooling ambient
R_{hr}	radiation resistance between housing and cooling ambient
R_m	magnet-air gap radius, permanent magnet reluctance
R_{mc}	convection resistance between heat-sink and cooling ambient
R_{mh}	contact resistance between mounting plate and main housing
R_{mp}	mounting plate to ambient total resistance
R_{mr}	radiation resistance between heat-sink and cooling ambient
R_{ph}	phase resistance
R_r	radius to under-side of the magnet
R_{rad}	thermal resistance for radiation heat transfer
R_s	radius to stator-air gap interface, resistance between stator and housing
R_w	thermal resistance between the winding and the stator core
r	section radius
r_r	rotor section radius

r_s	stator section radius
T	torque, temperature
THM	housing thickness
T_0	ambient temperature
T_a	Taylor number
T_{cogg}	cogging torque level
T_{ec}	encoder temperature
T_{eh}	encoder housing temperature
T_h	housing temperature
T_m	mean temperature
T_{mp}	mounting-plate temperature
T_s	stator temperature
T_w	winding temperature
ΔT	delta temperature
t	material mass density, lamination thickness
V	volume
v	velocity
v_{ph}	phase back EMF voltage
W_{cu}	dissipation due to copper loss
w	width
w_{so}	slot open
w_{swi}	inner Slot Width
w_{swo}	outer Slot Width
w_{tws}	stator tooth width
y_{yhs}	stator Yoke Height

Greek letters

α	temperature coefficient of resistivity, thermal diffusivity
α_{sk}	ratio of the total circumferential skew to the slot pitch
β	viscosity of medium
ε	radiation emissivity
η_{rpm}	rotational speed
ρ	resistivity, mass-density
σ	material conductivity

Θ	beta angle
ν	fluid dynamic viscosity
ν_r	rotor peripheral velocity
ϕ	magnet flux
ϕ_e	equivalent arc of the tooth segment
ϕ_p	half stator pole pitch
ψ	magnet flux linkage
ψ_t	total number of flux lines
ψ_{leak}	number of leakage flux lines between permanent magnet poles
ω	angular frequency
ω_m	mechanical angular speed
θ	rotor position
θ_s	slot pitch
θ_m	beta magnet angle
λ_1	specific permeance coefficient
μ	fluid dynamic viscosity
μ_0	permeability of air
μ_m	permeability of material
μ_r	magnet relative recoil permeability

Subscripts

a	air, ambient
ang	angle
C	convection
con	conduction
conv	convection
cu	copper
E	electrical
F	force
fe	iron
g	air gap length (GAP)
ha	shaft axial thermal conductivity
hr	shaft radial thermal conductivity
swi	inner slot width

L	length
<i>leak</i>	leakage
<i>lm</i>	magnet thickness
m	mechanical, magnet
<i>ma</i>	permanent magnet axial thermal conductivity
<i>mma</i>	permanent magnet mean axial thermal conductivity
<i>mr</i>	permanent magnet radial thermal conductivity
<i>mmr</i>	permanent magnet mean radial thermal conductivity
o	outer
out	output
<i>swo</i>	outer slot width
<i>pk</i>	peak
R	radiation
r	radial, rotor
<i>ra</i>	rotor axial thermal conductivity
<i>rad</i>	radiation
rc	rotor core
<i>rma</i>	rotor mean axial thermal conductivity
<i>rmr</i>	rotor mean radial thermal conductivity
<i>rpm</i>	rotations per minute
<i>rr</i>	rotor radial thermal conductivity
s	slot
<i>sa</i>	stator back-iron axial thermal conductivity
<i>sma</i>	stator back-iron mean axial thermal conductivity
<i>sd</i>	slot depth
<i>so</i>	slot open
<i>sr</i>	stator back-iron radial thermal conductivity
<i>smr</i>	stator back-iron mean radial thermal conductivity
<i>stw</i>	stator tooth width
<i>ta</i>	thermal axial
<i>tma</i>	thermal mean axial
<i>tr</i>	thermal radial
<i>tmr</i>	thermal mean radial
<i>th</i>	tooth height

<i>w</i>	winding
<i>wa</i>	winding axial
<i>wma</i>	winding mean axial
<i>wr</i>	winding radial
<i>wmr</i>	winding mean radial
<i>yhs</i>	stator yoke height

ACKNOWLEDGEMENTS

The research has been carried out during the period 2010-2014 as a part of a research programme, "Material Optimisation and Design for Manufacturing of a Brushless Synchronous Servomotor", in the School of Architecture, Computing and Engineering at the University of East London (UEL) and in the Research and Development (R&D) laboratory of Control Techniques Dynamics (CTD) Andover. The programme was financed partially by the Engineering and Physical Sciences Research Council (EPSRC) and by Control Techniques Dynamics Ltd.

The author would like to thank the EPSRC and CTD Ltd for sponsoring the project.

The author would like to express his immense gratitude to Professor Roy Perryman, Professor Stephen Dodds, and Dr Wada Hosny, all from the University of East London, and Dr Sujitha Jayasoma together with Dr Gunaratnam Sooriakumar, both from CTD Ltd, for their guidance at different stages of the research programme.

Thanks also go to Mr Keith Hedges and Mr Brian Smith, both from CTD Ltd, for all their support and the opportunity to undertake a major part of research work on the CTD premises. Special thanks go to Mr Richard Clarke, Mr Brian Smith and Miss Sam Hayter, all from CTD Ltd, for the constant encouragement during the research programme, which was so helpful.

The author would like to extend his special gratitude to Dr Dave Staton from Motor Design Limited for his support throughout the research work.

The author thanks all his family members, especially his parents, Orlando da Silva and Nenita Sá da Silva, for their encouragement, love, belief and indeed everything in life.

Finally the author wishes to extend a special appreciation to his wife, Margarida Gomes da Silva, for her meritorious patience considering that she has been almost the only person looking after the children during the research period. **Thank you.**

Helder Sá, London, September 2014

With love to my daughters Vanessa and Meuhno, and my son Filómeno Sá

CHAPTER 1

INTRODUCTION

1.1. Overview

The increasing needs of modern society, brought about by economic developments and population increase, are requiring mounting numbers of applications requiring electric motors ranging from simple computer fans to printing machines, food mixers, and many others. In view of the need to reduce the contribution to the carbon footprint, advantage needs to be taken of the room for improvement in the electro-mechanical energy conversion efficiency and the torque per unit volume of electric motors. Hence there is an increasing trend of replacing motors that are inferior in these respects, such as induction motors, by types that not only perform better but can be improved further. The BPM synchronous servomotor, which is the focus of the research programme, falls into this category.

The cost and the demand for energy and raw materials have increased considerably in the last 10 years when compared with previous decades, and therefore every meaningful way of saving energy and material usage became key targets in the rotational BPM synchronous servomotor manufacturing industry.

Nowadays the manufacturing and performance advantages associated with the concentrated winding (segmented stator) technology for BPM synchronous servomotors are now well known. The problems of low winding factor, torque ripple, non-synchronous field components and high space MMF harmonics has compromised investment in segmented stator concentrated winding technology in the past. The significant improvements in motor design tools, however, have made it possible to almost eliminate all these problems. This technology is therefore becoming more attractive, not only in increasing

the energy conversion efficiency but also reducing the cost of production and saving material (Boglietti et al., 2014).

A new rotating BPM synchronous servomotor incorporating segmented stator technology is developed in this research program with the aim of improving the performance, simplifying the manufacturing process, and reducing manufacturing cost and waste (Mecrow et al., 2004) (Jack et al., 2000).

It is the objective of the PhD project to design a high efficiency and high torque density three-phase BPM synchronous motor of medium speed for servo application. Also improve the manufacturing process in order to reduce waste and manufacturing time attained to the current servomotor. Higher torque and output power should be achieved from a defined servomotor volume and this volume is of the current distributed winding design model from the manufacturer. This is very convenient from the manufacturing standing point, because this will avoid changes on the tools that are already in place for the particular stator outer diameter and totally enclosed aluminium housing frame. In other words, the new BPM synchronous servomotor with concentrated winding configuration can use the tooling of the long established and available manufacturing processes, and standardized parts such as housing, shaft and bearings. For the current research work the servomotor length can vary but only one frame size is selected, see Fig. 1.3 (a) and (b), for range of frame sizes of the current distributed winding BPM synchronous servomotor. Performance comparison between the current design and new design of the BPM synchronous servomotor is based on 2D FEA and experimental data. The current servomotor rated power is 1.75 kW at 3000 rpm and it is totally enclosed not ventilated (TENV). And the new design is also TENV type and will implement current design split ratio and the torque, cogging torque, iron loss are compared for performance of both technologies.

Current BPM synchronous servomotor with distributed winding has 18-6 slot-pole combination and for the new concentrated winding configuration different slot-pole combinations are analysed for torque performance using 2D FEA.

The experimental work is based on two prototype BPM synchronous servomotors, one with a conventional distributed winding configuration and the other with the new concentrated winding configuration, to facilitate performance comparisons.

1.2. Outline of the Thesis

The following sections of this chapter (Chapter 1) commence with a description of the research motivation. Then the performance characteristics of different motors are compared in order to highlight the importance of the product investigated in this research. Finally the aims and objectives of the research study are laid out.

The interior-rotor surface mounted (SM) brushless permanent magnet (BPM) synchronous servomotor with both distributed and concentrated winding configurations are described in Chapter 2. The design aspects and manufacturing processes are then presented, including a discussion of the performance characteristics and the critical parameters. Analytical and finite element analysis (FEA) tools are then used to define the motor components in terms of performance and a design parameter sensitivity analysis is performed. Other important aspects of chapter 2 are slot-pole combinations, iron loss analysis, permanent magnet descriptions of the active materials used in motor manufacturing and general discussion of the cooling of motors.

Chapter 3 presents thermal analysis of the prototype BPM synchronous servomotor. Different modelling methods are used to describe the thermal behaviour of the BPM synchronous servomotor. Approaches to motor dimensioning are presented and means for cooling are presented. The two prototypes addressed in Chapter 4 are later used in Chapter 6 to calculate and generate the main losses data to be input to the thermal model.

Prototype testing for both conventional distributed winding and the new concentrated winding configurations are described in Chapter 4 together with the experimental procedure. The results from a system rig used to test both prototypes under similar environmental conditions are presented.

Test results for both prototypes are presented in Chapter 5. Conventional J-K type thermocouples are located in different parts of the servomotor and one in a position to monitor the ambient temperature. The maximum winding operating temperature is defined as the reference temperature for both prototypes tested. The main test performed was a dynamic torque rating test in order to obtain the torque-speed curves for each prototype. Also, cogging torque and iron loss were tested for comparison and analysis carried out in this Chapter. Different performance results are compared with those obtained from the corresponding simulations, where possible, for the new prototype servomotor. Discussion of the results is mainly focused on torque-speed curve, cogging torque and level of the stator iron loss.

An offshoot of the research work is described in Chapter 6. This is the development of a better understanding of the influence of the electrical wall insulation paper on the BPM synchronous servomotor performance for both the distributed and the concentrated winding configurations. This has been included as an important part of the research programme. Fundamental mechanical and heat transfer characteristics of the most popular and commercially available electrical insulation paper materials have been investigated regarding torque performance and also safety. A special prototype with a water jacket for cooling has been produced to determine where to concentrate manufacturing effort to reduce the temperatures within the servomotor. Here what-if analysis is performed for the main thermal wall component using Motor-CAD, i.e. the main thermal resistance values in the simulations are changed within certain limits to determine the boundaries of performance and efficiency enhancement. This knowledge is offered to BPM synchronous servomotor manufacturers to predict performance improvements through improved thermal conductivity of the wall insulation paper, also taking into account increased slot-fill, principally for the segmented stator, concentrated winding configuration.

Finally, the conclusions of the research work are presented in Chapter 7 and important points are highlighted for further work.

1.3. Background

There is much discussion today about the adverse effect of various domestic and industrial systems' emission on the environment, from the amount of energy used by appliances in everyday household operations, to the energy consumption in industry. There have been, in addition to this pressing issue, the possible avenues with which individuals and corporations could reduce these emissions and the effects they have on the environment.

Manufacturing still plays a major role in economic growth worldwide and indirect carbon dioxide emission is as a result of the demand for products. An example is in the manufacture of BPM synchronous servomotors. There is a continuous demand for servomotors of various sizes and varying performance characteristics due to the numerous application potential in areas such as aerospace, specialised military applications, automotive industry and in domestic products.

With this demand comes the demand for energy required for its manufacture, which in turn generates excessive waste if efficient manufacturing is not applied. Waste emissions, especially carbon dioxide (CO₂) emission from energy usage have been on the increase as an outcome of rising product demand. This can be trimmed down however, by the introduction of energy and resource efficiency techniques and measures in manufacturing processes.

According to research by the International Energy Agency (IEA), technical improvement efficiency for manufacturing industries could be achieved if the best available technology were applied. According to their study, there would be savings of 5%-7% of total energy use and a noteworthy reduction in carbon dioxide emissions worldwide (IEA, 2008) (IEA, 2007). The Carbon Trust in addition, states that applications using electric motors consume an estimated two-third of electrical energy use by industry, so even modest efficiency gains in the machine design can deliver substantial savings (The Carbon Trust, 2011). Indeed, one of the objectives of the proposed research programme is to discover available ways to achieve these reductions in the amount of

energy used and wasted in the production process of BPM synchronous servomotors.

The proposed research programme stems from previous research into the development of a new generation of synchronous servomotors for motion control and drive applications, by increasing the operating performance and efficiency- through the development of methods to reduce the effect of cogging with the use of improved cogging calculations for surface mounted permanent magnet synchronous servomotors (Sooriyakumar et al., 2007a).

This showed that substantial improvement can be made by the use of a combination of analytical calculations and finite element analysis (PMSMAnalyser and Opera_2D). Previous work has also included the development and analysis of a new generic steady state and transient thermal model for mapping the heat transfer throughout a permanent magnet synchronous motor by considering its individual components as elements of an overall thermal equivalent circuit.

The results obtained from the model were compared with corresponding experimental tests for the stall and rated performance with natural and forced cooling for two different motors, one with a rated speed of 1500 r/min and 130 Nm stall torque having 30 slots and 10 poles, and the other with a rated speed of 3000 r/min and 15 Nm stall torque having 18 slots and 6 poles (Sooriyakumar, 2009).

Initially, the manufacturing process of synchronous servomotors with conventional construction will be reviewed to identify the limits of any improvements that can be made. The research programme will then be carried forward by considering a new modular segmented stator construction that has the potential of bringing about further improvements beyond those attainable with the conventional construction. Each stator segment will consist of integrated yoke segment and stator tooth with its own insulated copper winding (Libert et al., 2006).

Significant advantages of this arrangement will be

- a) a much simplified assembly and less costly winding operations,

- b) significant reduction of the winding overhang and therefore reducing the machine length and the overall envelope size, providing an improved power/weight ratio, torque/volume ratio and efficiency, and
- c) a much increased slot-fill ratio compared with the conventional distributed windings thus providing an associated flux increase. The assembled stator modules will be held in place within a conventional motor frame.

The research programme will also address issues such as

- a) stator module interlocking profiles that minimise the reluctance across each module yoke interface,
- b) investigation of the potential for reducing eddy current, hysteresis and stray losses.
- c) suitable coil end connection for ease of assembly and reliability.

In order to present a standard three phase connection interface to the user, the individual stator module windings will have to be interconnected to one another and the three phases so as to produce a similar MMF function to the conventional distributed windings. This will require three coils per stator module, in order for each stator tooth to share the three phases.

There are a number of factors that lead to effective design and manufacture of brushless servomotors including the choice of materials and the geometry in which they are assembled. The proposed research programme will review the current materials used in the manufacture of synchronous servomotors including the method by which they are being applied to the manufacturing process, in order to identify the limits of any improvement that can be made. The prospects of improvement may include the reduction of waste in the manufacturing process, research into new motor construction materials and the successful use of such materials to bring about the desired performance characteristics.

A key requirement for servomotor operation over continuous periods of elevated temperatures is the thermal distribution within the motor and efficient dissipation of heat from the motor. This is ideally required due to the fact that as more heat is able to escape into the surroundings results in the motor running at cooler temperatures, hence ensuring better performance characteristics for customer satisfaction. The opposite of this may include the probable demagnetising of the permanent magnets, the burn-out of the windings due to excessive temperature peaks, the presence of localised hot spots and consequent reduction in the operating life of the servomotor.

This research programme will study current constituent materials of servomotor design to identify their shortcomings with the plan to incorporate better materials especially regarding effective thermal conductivity. Impregnation of the windings will also be used to improve the winding insulation, protection, and thermal contact for improved heat distribution and cooling, thereby reducing localised hot-spots.

The maximum attainable performance improvements such as maximising the torque constant (kt), minimising the cogging torque and torque ripple, enabled by changes to the servomotor construction will be assessed by means of sensitivity analysis with respect to the variable design parameters, such as the magnet dimensions and slot-pole combinations, using 2-D FEA packages to provide the results before prototyping.

A major factor to consider is the *manufacturing process* of synchronous servomotors which greatly influences the quality and quantity of the motors being produced. An approach that will be employed in the proposed programme will be to review the current design and manufacturing process with the aim of a) reducing the amount of materials being used b) reducing the manufacturing time and c) reducing the hours of manual labour.

The benefits associated with these aims and objectives will be an increase in energy saving through cleaner and more environmentally friendly manufacturing techniques, the ability to satisfy production targets and customer demands as a result of reduced motor assembly time. To every form

of waste, there is a cost attached and this programme will tackle the key point, which is to discover where and how waste is being created.

1.4. Classification of Brushless Motors

A brushless motor is a motor such as AC induction motor. Other example of motors that can be included in such class of motors are stepping motor, brushless DC motor and brushless AC motor (Hanselman, 2003). And a servomotor is the motor controlled by an external drive based on the rotor position information from a feedback.

The word “servo” is a Latin word and it means slave and the master is the external control device. According to (Hendershot et al., 1994) (Hanselman, 2003) there are different construction possibilities for motors, but all motors contain two primary parts. These are the non-moving or stationary part is called the stator and the moving or rotating part is called the rotor. And the most common motor shape is inner-rotor cylindrical as shown in Fig. 1.1 (a).

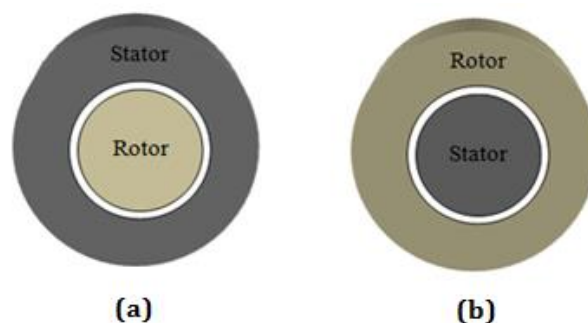


Fig. 1.1. Inner-rotor (a) and outer-rotor (b) motor construction possibilities.

Due to the advantages attained to this construction, for the present research work all the prototypes are of the inner rotor and cylindrical type BPM synchronous servomotor construction. First of all, this is the current manufacturer construction method and secondly the construction is the same as those of popular AC induction motors (Hendershot et al., 2010). From the thermal standing point it is easier to cool down something stationary compared to something that it is rotating, and also it is true that is easier to cool something outside than hidden component within a structure. From safety point it is more advisable to keep the rotating components within a structure rather than exposing them for easy contact.

All these advantages associated to the inner-rotor motor make this construction possibility the preferable choice in motor manufacturing. Both constructions are radial flux motor types and for some special application such as rim motor for electric powered wheelchair the outer-rotor type of Fig. 1.1 (b) is the best choice in terms of motor construction (Yang et al., 2007).

The rotor of an inner-rotor type can take many shapes but the most popular configurations shown in the Fig. 1.2. and where a) Surface mounted magnets, b) inset rotor with surface magnets, c) surface magnets with pole shoes producing a cosine flux density, d) buried tangential magnets, e) buried radial magnets, f) buried inclined magnets with cosine shape pole shoe and g) permanent magnet assisted synchronous reluctance motor with axially laminated construction (Salminen, 2004).

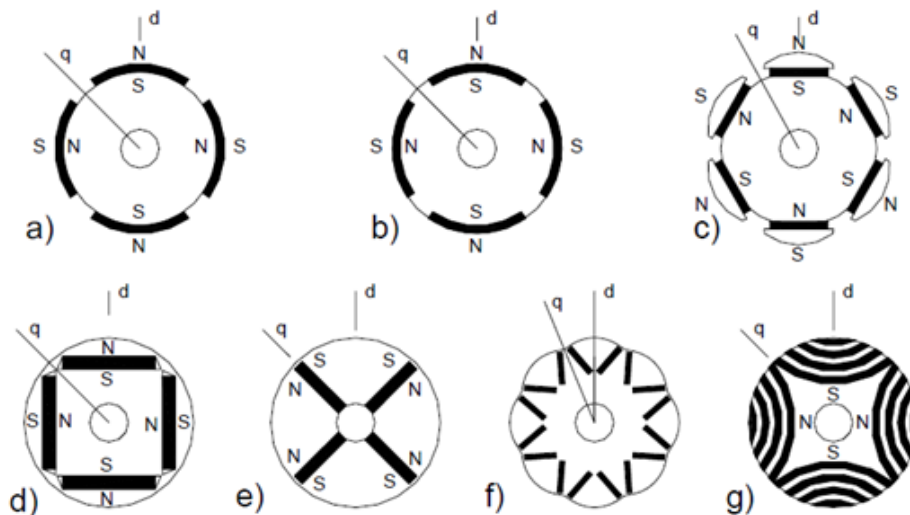


Fig. 1.2. Different rotor constructions of radial flux machines (Salminen, 2004).

For this research work the surface magnet types, as shown in the Fig. 1.2 a) and b), are used for all electromagnetic designs and prototypes. After definition of the brushless servomotor shape, survey is performed on more popular brushless motor technologies mainly used for position control in order to compare their respective stall torque per volume performance level.

This was achieved by visiting the web pages of the main players in servomotor manufacturing, such as Siemens, YASKAWA or ROCKWELL Automation, in order to gather the data that is presented in this section that

compares the two more popular brushless servomotor technologies in terms of performance. The approach taken in order to quantify the performance level for each brushless motor was to calculate the volume and divide the stall torque (Nm) value given on the catalogue to the corresponding volume.

Fig. 1.3 shows three dimensions and these are A, B and T.

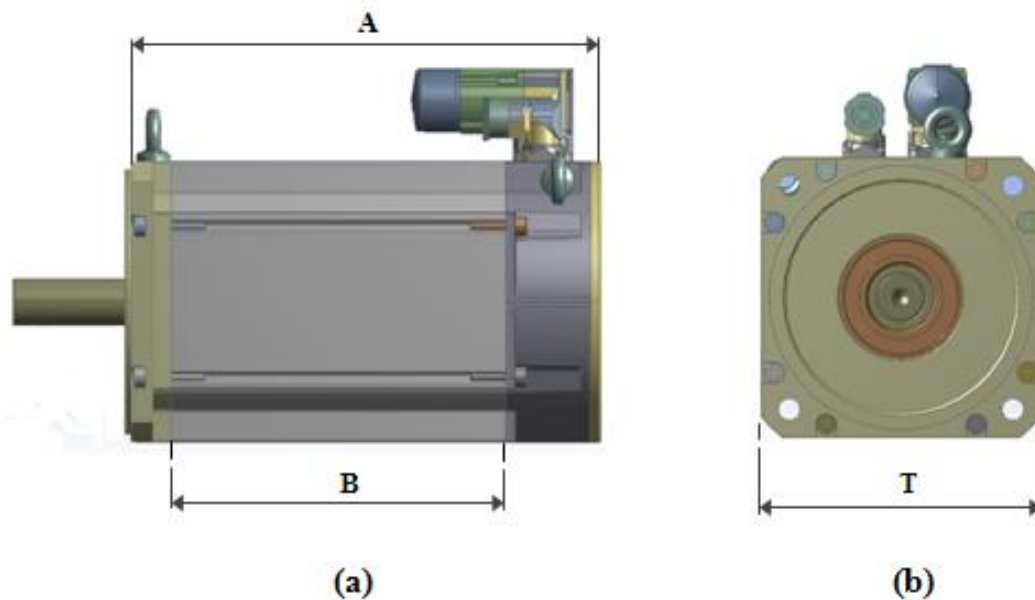


Fig. 1.3. Servomotor dimensions (a) housing length and (b) frame size.

The dimension A and B in the Fig. 1.3 (a) represent motor length and housing length respectively, the dimension T in the Fig. 1.3 (b) represents the motor frame size. Therefore the volume for each motor is roughly calculated as $V = T^2 \times B$, and there the performance (Per) value is calculated as stall torque divided by the volume as $Per = Nm / V$, in our case volume in dm^3 .

Normally the manufactures catalogues do not give the active material length. However this can be approximated to the housing length. The value of housing length is not directly given but it can be obtained with reasonable accuracy from other dimensions given, but the value of the frame size T is always given since it is the reference value for the standard sizes such as NEMA.

The results represented in the Fig. 1.4 show clearly the advantages of using the motor with BPM rather than using for example the popular induction motor (IM).

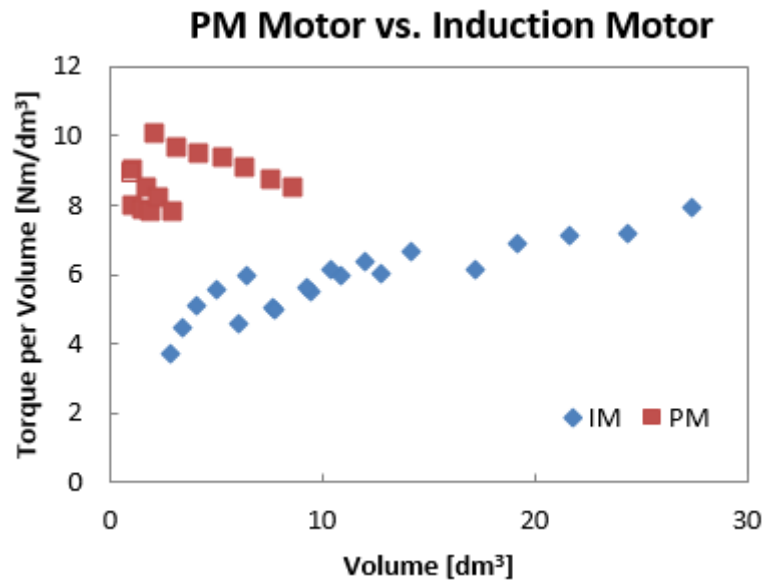


Fig. 1.4. Torque per volume for induction motor and brushless servomotor technologies.

According to (Libert, 2004), permanent magnet synchronous motors (PMSM) are well suitable for new adjustable speed AC inverter drives, and the reasons been that both efficiency and power factor of these motors are not depending on the pole pair number and speed near to the level of the case of Induction motors. Induction motor is normally coupled to a mechanical gearbox and all this system can be replaced with a direct drive BPM motor. This will help to save space, increase the efficiency and decrease the maintenance cost. The above mentioned aspects are making the BPM servomotors very attractive solutions and they have continuously replacing the induction motors in many industrial applications.

1.5. Research Aim and Objectives

What this research programme aims to achieve is to indirectly influence the current global problem with harmful emissions, by considering the key areas to research in servomotor manufacture that would ultimately lead to a product of improved performance, as shown in Fig. 1.5, and efficiency together with an improvement in efficiency in the production process.

The more important torque performance points (A, A', B, B', C, D, E and F), and two operating limit zones defined by the torque-curves (orange, dashed yellow and brown) represented in the Fig. 1.5.

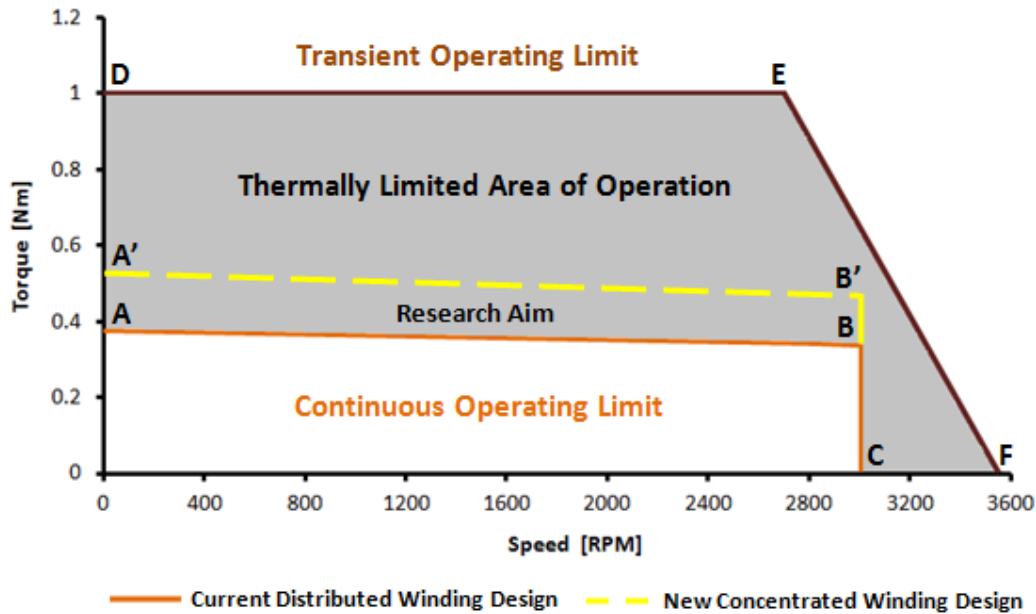


Fig. 1.5. Typical torque versus speed curve characteristic of servomotors.

This proposed research programme contributes to the establishment of a new generation of synchronous motors for motion control and drive applications that advance the state of the art by:

- a) research towards the design optimisation of brushless servomotors using a segmented stator construction
- b) increasing the operating performance and efficiency of this design using methods including finite element analysis, simulation tools and experimental data and
- c) implementation of the design methodology in the manufacturing processes, focussing on reducing energy, production time and minimising waste.

Research methodologies that will be utilised in this research will include literature reviews that will be employed to determine market analysis of current technologies involving an investigation of design and manufacturing technologies which are implemented in modern machines. Prototype components and assemblies will be utilised in developing knowledge about machine design, operation and performance. Experimental data will be obtained from laboratory testing under different load applications for a fixed environmental condition. This approach will enable design, development,

simulation and testing to be undertaken in order to investigate and verify optimal machine design.

Fig. 1.5 presents the overall project aim performance graphically, depicting different thermal operating limits of a BPM synchronous servomotor. From the yellow dashed line it can be observed that the new servomotor will have greater continuous operating limit when compared to the current distributed servomotor.

Points A, B and C represent the continuous operating limit or inner envelope of the current BPM synchronous servomotor with distributed windings and points A', B' and C' represent the aimed torque-speed curve performance for the new concentrated design. Point A and point A' represent stall torque points of the servomotors, this is the available continuous torque when the servomotor is in standstill or near zero speed, and at these points there is no rotational losses (only copper loss). Point B and point B' represent rated torque points of the servomotors, this is the available continuous torque when the servomotor is running at rated speed, and at these points, both copper loss and rotational losses are considerable. Point C represents the rated speed, the speed where the servomotor maximum continuous power is defined due to drive rated voltage limit defined by point E and point F. Point D represents the peak torque, this is limited by current and the magnet temperature (demagnetisation of magnets can occur), the torque constant (kt) drop is quite significant and this is shown in the later chapter. Point E represents end peak torque, this is the end of peak torque curve limited by current and start of peak torque curve limited by control drive rated voltage. And final point F represents the no-load speed, the speed of the servomotor when it is running without load, and this point depends on back EMF constant and control drive rated voltage.

It is proposed to achieve increased performance with improved manufacturing process and reduced production cost. Project structure is shown in Appendix A, where machine design tools for both electromagnetic and thermal design are used to evaluate different servomotor material components. After optimising the materials, the impact of the implemented manufacturing

process is evaluated in terms of different servomotor performance characteristics such as torque constant (k_t), cogging torque or the level of the losses.

Therefore this research work is focussed on evaluations of active materials, machine design tools, improved manufacturing process and reduced manufacturing cost in order to achieve its goals.

1.6. Literature Review

In this research project literature review it was found that the brushless permanent magnet (BPM) synchronous servomotors are one of the high torque variable speed motor types. With the improvements made in the last 30 years on the permanent magnet in terms of performance, quality and price, these factors have made permanent magnet motors more attractive than field wound machines. Research has been undertaken on how permanent magnets mounted on the rotor can give more advantages when compared to the classical field wound synchronous motors and further improvement to the magnetic performance and how the improved thermal management can bring further gains to the motor efficiency, performance, size and cost.

The research is aimed at developing a new high torque density, high efficiency BPM synchronous servomotor incorporating segmented stator technology with thermal control using mounting flange naturally cooled system. This involved design, sensitivity analysis for optimisation, prototype construction and testing procedures. The proposed design is for an inner rotor surface mounted BPM synchronous servomotor with concentrated winding using segmented stator topology which will provide a new generation of servomotors.

Inner rotor surface mounted BPM synchronous servomotors are one of the high torque permanent magnet synchronous servomotor types as shown in Fig. 1.2 (a). They used low to high number of pole-pairs and in terms of operation they are very similar to other rotary synchronous permanent magnet servomotors. With the improvements made in permanent magnet materials in terms of performance, quality and price, these factors have made the

permanent magnets more attractive than field wound motors for many applications. Research has been undertaken on how permanent magnet on the moving part of a synchronous servomotor can give more advantages when compared to field wound synchronous/asynchronous or any other servomotors. (Overshoot, 1991), showed that regarding to PM materials there is a continuous increase of energy density and the capacity to withstand temperature. Therefore handling demagnetisation much better and these aspects are allowing BPM synchronous servomotor competing for variety of servo applications.

Later (Jokinen, 2004), showed that brushless with permanent magnets costs less than the traditional field wound motors with the outer diameters up to 150 mm. This is true for the larger motors however the number of magnet poles has to be kept low due to iron loss increase with the poles.

Regardless of the progress that has been made in recent years on improving the quality of permanent magnet electric motors, demagnetisation is still a problem when seeking improved motor performance.

Two solutions to reduce iron loss and magnet eddy current that causes demagnetisation were presented by (Toda et al., 2005), and consist on, laminating the stator core and segment the magnets. However, both solutions bring extra cost to the manufacturing and handling of the magnetic components and therefore from manufacturing standing point the segmentation of magnets bring difficulties to the processes.

For various possible slot-pole combinations BPM synchronous servomotors, one particular configuration has been gaining special attention on many practical medium speed applications, which are those concentrated windings related by:

$$2p = N_s \pm 2 \quad (1.1)$$

(Zhu, 2009) (Hanselman, 2003) where p is the pole pair combination and N_s is number of slots. The more appropriate $N_s/2p$ combinations for a balanced

3-phase is 6/4, 6/8; 12/10, 12/14; 18/16, 18/20; 24/22, 24/26, etc... Increasing pole numbers results in high winding factor (Salminen, 2004) and high flux linkage, however as mentioned previously increase pole limit the speed, increases flux leakage and increase losses.

With the current high environmental concerns, focus has been put on reducing energy consumption and therefore the efficiency of the electric motor became a critical factor. And in this area currently high efficiency electric motors with inner rotor surface mounted permanent magnets with the slot-pole combinations of $N_s/2p$ can play a critical role in terms of energy saving.

The popularity of these electric motors is increasing considerably also in high-torque/low-speed applications where high poles are not very critical to the losses due to speed. For these applications the motor shaft tends to be hollow to reduce inertia due to high split ratio. Traditionally high-torque/low-speed is an application created by combining a considerable high speed motor such as induction motor or switch reluctance motor with a gearbox and transmission train that have the capability of reducing the speed and increasing torque in the same ratio. This will result in regular maintenance to the gearbox and to the transmission train and also significant losses will occur in the gearbox which will reduce the efficiency of the system. The gearbox and the installation are expensive, and also it consumes a significant amount of space. Therefore the idea of replacing this system with an arrangement that can mount directly to the application is becoming a very attractive solution. Inner rotor hollow shaft surface mounted BPM synchronous servomotors are becoming very popular in industrial applications due to their high-torque/low-speed characteristic and better performance when compared to the conventional method (Magnusson, 2004). The applications range from wind turbines to machine tools and transportation vehicles, where high-torque and high precision are required at relatively low speeds.

The inner-rotor radial flux permanent magnet (RFPM) configuration, as shown in Fig. 1.1 (a) for different constructions, the structure is the classical type for BPM synchronous servomotor and the most common due to the similarity in

terms of structure to the classical synchronous motors or induction motors (IM). When the structure is hollow, mainly for the surface mounted magnets there are two popular varieties: the complete servomotor and the built-in servomotor. For the first type the servomotor can be connected directly to the application shaft, but for the built-in type servomotor the components need to be directly integrated into the application mechanics because the stator and the rotor are supplied as individual components.

There are a number of research activities mainly on the large PMSMs currently being undertaken in the Nordic countries (Krovel et al., 2004). In these works special attention is been given to the axial and transverse flux permanent magnet motors. The development of large permanent magnet synchronous motors in these countries is due to the long traditions of ship building and wind turbines. Research is also happening in UK, France, Germany and US on small and medium size permanent magnet motors, for both solid and hollow shafts configurations, for machine tools (packaging, printing, extruding, papermaking, plastic film and materials handling machines). The desire is to increase the torque density, reduce the size, and reduce the thermal dissipation problems due to the high power and rotational losses due to smaller size motor.

The implementation of force cooling designs makes the system more expensive and difficult to manufacture. However this is best cooling method and enables higher power density at reduced motor size, and even the low speed permanent magnet motors can operate at significantly higher speed (around 1000 rpm) due to improved removal of stator iron losses. When applied to the stator, force cooling system seems to be effective in removing the heat caused by the PM rotating field (Yang et al., 2009), however not so effective with removing heat due to the copper losses and this is mainly due to the wall insulation materials between the copper winding and the stator core, and also between windings of different phases (Sá et al., 2013).

Different techniques are used for wall insulation systems and this is described on the following chapters. However from the manufacturing point of view the one with wall insulation paper system and impregnation/potting offers more

benefits. Also this combined insulation system is the one used for the original BPM synchronous servomotor subject to research on this project, therefore for simplicity and manufacturing process similar technology is chosen for the new servomotor. Therefore research is undertaken on the more popular commercially available electric wall insulation materials and the more suitable materials were selected for testing of heat transfer characteristics, mechanical and electrical properties. Research is therefore progress to find a new electric wall insulation material with the similar or improved electric insulation capabilities and also with improved thermal conductivity.

The major challenge of this research is to bring improved manufacturing processes, improve performance, efficiency, and optimise the material usage and selection. Remove all non-value added servomotor components to the torque from the original BPM synchronous servomotor in order to reduce waste.

Continuous literature review, including web pages, is undertaken in this project in order to keep up to date with the different research points. Research papers, articles and books on the electromagnetic and thermal aspects of electric motor design have been identified and studied that date back to 1950's. The number of references obtained is 95 and 12 of the key research papers reviews are as follows:

(Nategh et al., 2014) introduced a study of impregnation materials for thermal management for high-performance liquid cooled electrical machines. The thermal impact of using different impregnation materials on the stator side of the machine is investigated. Three impregnation materials were evaluated and an advanced thermal model of the machine was developed to investigate the thermal impact of these impregnation materials, their manufacturability and maximum attainable torque density.

(Boglietti et al., 2014) presented a study of fractional-slot concentrated-winding machines and their related problems and challenges to be solved by engineers. In this study it is shown that despite electrical machine design being considered mature from a technical and technological standing point,

significant progress and new steps forward have been continuously made throughout the years. Progress in terms of design tools, innovations in the manufacturing processes, together with improved magnetic and electrical insulation materials are presented.

(Popescu et al., 2013) described the main thermal phenomena in the BPM synchronous servomotor. The complexity of the loss process is pointed out and different analytical methods are applied to calculate the losses. The demagnetization of the magnets is the prime concern together with the losses causing this, i.e., the magnet loss and AC copper loss, which are investigated. Reviews on various cooling systems are presented, including the results of several experimental investigations.

(El-Refaie et al., 2013) carried out a study promoted by the increased interest in fractional-slot concentrated-winding electrical machines in view of their advantages when compared with non-fractional machines. The paper gives a complete review of the state of the art of the fractional-slot concentrated-winding machine. A good update is given on current research activities and research trends on the subject.

(Dajaku et al., 2012) introduced a flux-barrier in the stator yoke of a BPM synchronous motor with a 12-10 slot-pole combination to reduce the permanent magnet losses experienced with concentrated windings. This flux barrier introduces strategically located magnetic saturation in the stator yoke to reduce or even cancel some space harmonics of low order in the air-gap, thereby reducing the rotor losses and the demagnetization of the permanent magnets.

(Hendershot et al., 2010) presented an extensive study on different slot-pole combinations for brushless permanent magnet motors. They show that machines with fractional slot windings have lower cogging torques than those with integer slot windings, through reducing the alignment between the magnet poles and minimum magnetic reluctance paths between the slots. This is achieved by calculating the winding pitch as the nearest integer to the number of slots divided by the number of magnet poles. This brings the further

benefit of minimising the need for skewing and therefore eliminating this stage of the manufacturing process.

(Wu et al., 2010) investigated the optimal split ratio in fractional slot interior permanent magnet machines with non-overlapping windings. They developed an analytical model to optimise the flux density ratio by finding the optimal split ratio for maximum torque density. The analytical results were verified by finite element analysis and the influence of pole-slot combinations, tooth-tips and other issues on optimal split ratio and flux density ratio were presented. They also proposed that the preferred air-gap flux density should be around 0.5-0.7 times the maximum stator tooth flux density.

(Sooriyakumar et al., 2007b) presented a new and efficient design methodology for the specification, development and manufacture of permanent magnet synchronous motors. A genetic algorithm based design optimisation technique was developed where the multi-criteria components considered were the electromagnetic performance, the thermal performance and the material cost. This resulted in the development of a Permanent Magnet Synchronous Motor (PMSM) Analyser where motor dimensions and topology are input to the programme in order to provide an optimised design.

(Toda et al., 2005) analysed the losses in brushless synchronous servomotors using finite element analysis (FEA) software and they were able to accurately evaluate the stator iron loss and the rotor eddy current loss for both the conventional brushless synchronous servomotor and the modular/segmented brushless synchronous servomotor. In this research two solutions were implemented to improve the iron loss and eddy current loss that can cause demagnetization. For the iron loss reduction the solution was to reduce the thickness of the stator laminations and the eddy current loss could be reduced significantly by segmenting the permanent magnets circumferentially.

(Mecrow et al., 2004) undertook research on simplifying the manufacturing process for electrical machines and introduced the segmented stator construction technique in which the stator teeth are split to allow a pre-wound coil with a thick wire and having good thermal and mechanical characteristics,

to be wound around the tooth after which the teeth are interlocked to form the electrical machine stator. The method of winding conventional electrical machines where the core is made of a stack of stamped laminations and the coils are inserted around the teeth makes the insertion process very difficult due to the small slot opening and normally specialised machines are required for this purpose. This highlights that the single tooth technique simplifies manufacturing methods, therefore reducing the cost of production, and the need for specialist staff. Using the single tooth winding, the winding overhang is reduced and the slot fill percentage is much higher than conventional synchronous servomotors and will allow a much more compact machine with improved power/weight ratio.

(Jokinen, 2004) later showed that it is more economical to use magnets than wound poles for motors with diameters up to 150 mm, and this is also still true for larger diameters as long as the poles are kept small. Regardless, the progress that has been made in recent years on improving the quality of permanent magnets, demagnetization is still a problem when seeking improved motor performance, also the speed is limited due to the high pole number which increases the iron losses.

(Overshott, 1991) showed that apart from the reduced cost, the permanent magnet energy density has been increased and the magnets can withstand higher temperatures, showing that the permanent magnets are becoming more resistant to demagnetization, and allowing these motors to compete with the traditional field wound motors for high torque/power, low/high speed applications.

In the applications where there is a requirement for high energy consumption and high dynamic operation, the inner rotor surface mounted permanent magnet synchronous servomotor can be a good solution because of the high efficiency and power density. Also whenever space-saving is necessary these motors are a good solution, the maintenance level is very low of these motors when compared to other electric motors due to fewer mechanical parts and reduced mechanical losses due to elimination of gearbox and transmission system.

This current switching to the electric motors with permanent magnet material is causing high increasing demand for these materials and at the present there is a big debate on materials scarce and supply issues due to dominance of China in terms of the main permanent magnet materials.

The very fast expansion of the PMSM for many applications justifies the effort that is being undertaken to find a low cost solution which is efficient and provides significant energy and materials saving in both operating performance and manufacturing process.

1.7. Research Contributions

A new design procedure for permanent magnet synchronous servomotors is presented in this thesis based on the world leading SPEED, Motor-CAD, ANSYS and OPERA-2D software. The SPEED software is used for fast geometrical modelling and then combined with the Motor-CAD software and ANSYS for thermal analysis. Opera-2D is the FEA software used for parameter optimisation in the electromagnetic design. This new combination of design aids renders the thesis an important reference for electrical machine designers in the servomotor design industry, especially enabling those joining this challenging field to climb the learning curve fast and advance the state of the art.

Significant research contributions on material saving and a systematic FEA design approach that enables torque performance optimisation are presented in Chapter 2. Main contribution is a new notch based T-Lam permanent magnet retaining device is introduced, referred to as the T-Lam and is shown in Fig. 2.85. This allows material saving due to the elimination of glue, glass taping and a balancing plate and also increases the torque constant. A new optimisation technique based on a systematic FEA approach is taken to overcome high cogging torque problem that occurred as a side effect of the T-Lam introduction. The optimisation has been carried out with respect to four design parameters, which are the magnet width (MW), the slot opening (SO), the slot open angle (SOAng) and the tooth gap depth (TGD). This systematic FEA approach takes into account the effects of punching on the magnetic properties of the laminations for the stator design parameter selection. A

reduction of approximately 15% on non-value added material usage is achieved using the above techniques together with the stator segmentation that allows a shorter winding overhang. In the conventional servomotor, the rotor requires oven treatment for approximately 60 minutes after the tape application shown in Chapter 2, Fig. 2.76 to Fig. 2.79. After this, a glue and tape setting time of approximately 5 minutes is needed for each of the 12 rotors, one after the other, amounting to an additional 60 minutes. Hence the adoption of the new notch based T-Lam permanent magnet retaining method eliminates this 120 minute manufacturing process, replacing this with manufacturing operations occupying approximately 70% of the original time. Also, the torque performance increases by approximately 7% due to the effective air-gap reduction.

Matrix thermal model solver equations are derived for the new BPM synchronous servomotor in Chapter 3 for fast thermal analysis to predict the temperatures of the main Control Techniques Dynamics (CTD) servomotor components, including the copper winding, the stator surface and the mounting plate. The thermal resistance values needed for this thermal analysis are obtained from prototype servomotor test data.

The results presented in Chapter 5 for open circuit iron loss using the test procedure of Chapter 4 are applied for different servomotor lengths to develop a simplified iron loss equation. The graph of power per unit volume [in W/m^3] vs. the frequency [in *Hertz*], from the open circuit iron loss test data is obtained using a least-squares process to determine the constants for the frequency dependent equation. This equation can be used to reliably calculate any length within the defined motor frame size without the need for prototyping.

In Chapter 6, thermal design aspects of BPM synchronous servomotors are studied that can be adopted to improve the thermal design. The thermal model is implemented in the Motor-CAD software and the results compared with those from the matrix solver presented in Chapter 3. Chapter 6 presents the thermal impact of the electrical wall insulation paper material on the servomotor thermal management. Five commercially available materials are tested to ascertain the real thermal impact of this insulation in a totally closed

non ventilated (TCNV) motor. Both experimental investigation and software simulation are performed. The motor simulation was carried out using the Motor-CAD software, enabling servomotor designers to predict the thermal performances of different wall insulation materials for different impregnation qualities and gaps within the stator.

The development of the new high dynamic range of motors for automation applications helped to enhance the sponsoring company's sales by approximately 20%.

CHAPTER 2

BRUSHLESS PM SYNCHRONOUS SERVOMOTOR DESIGN AND MANUFACTURE

2.1. Introduction

This second chapter initially highlights the manufacturing and performance advantages associated with the interior-rotor surface-mounted radial-flux (SMRF) BPM synchronous servomotor. These advantages are the same for both distributed and concentrated winding configurations when compared with other electric motor topologies. Therefore an alternative configuration is not considered in this research. Hence the motors investigated have the configuration of Fig. 2.1, the work concentrating on increasing performance for a given frame size.

The geometric parameters of the BPM synchronous servomotor that are critical regarding its electromagnetic performance which are used for its modelling both analytically and numerically are defined. Extensive references to the published literature on this subject can be found in Hendershot et. al., 2010 and Hanselman, 2003. The mathematics developed for the servomotor sizing and performance calculations are presented and some analytical results compared with those obtained using finite element analysis (FEA). The work of numerous researchers on the design of surface mounted radial flux BPM synchronous servomotors with both the conventional distributed and the new concentrated windings have already been described in Chapter 1. The advantages and drawbacks of both winding configurations are discussed in this chapter. Geometric, magnetic and electric characteristics that affect the torque performance constitute the main focus.

Slot-pole combinations are analysed aiming for higher torque density, i.e., torque per unit volume. Sensitivity analysis is applied for cogging torque

performance with respect to some design parameters. FEA is used together with thermal modelling software to obtain the torque performance level for each new servomotor design within practical thermal constraints. Their iron losses are also compared. Permanent magnet material characteristics are defined and their selection is discussed with a view to reduced material usage without penalising the torque performance.

Both the new and conventional servomotors are studied and compared in terms of their manufacturing processes. Finally prototypes are built for testing with both distributed winding and concentrated winding configurations based on analyses and experimental results presented in the following chapters.

2.2. Radial-Flux BPM Synchronous Servomotor

The interior-rotor radial-flux surface mounted BPM synchronous servomotor as shown in Fig. 2.1 is the most common type of brushless permanent magnet servomotor.

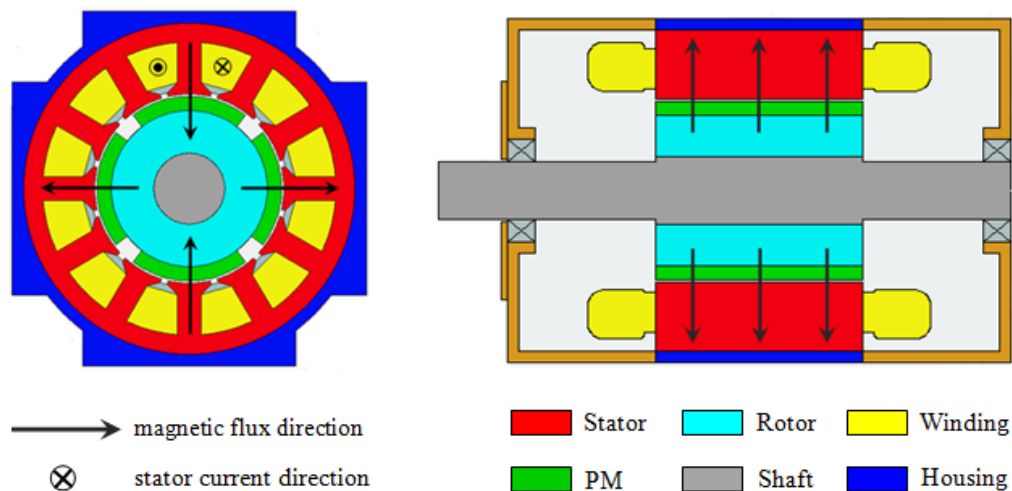


Fig. 2.1. Radial and axial sections of inner-rotor radial-flux servomotor with flux and current directions.

According to Hendershot et al., 2010 the principal reason for its establishment is its advantages over other configurations relating to manufacturing and magnetic properties.

When compared with well-established motors such as induction motors (IM) or stepping motors the stator configuration is exactly the same. Therefore all

the standardized infrastructure for manufacturing parts of this mature technology can be used for manufacturing inner-rotor BPM synchronous servomotors. This means that tooling, materials, winding methods and other available manufacturing processes do not need to change.

Depending on the slot-pole combination, nearly all the electromagnetic forces in this type of motor contribute to the useful torque, consequently imparting less vibration to the shaft and improving the bearing lifetime, as well as helping to reduce acoustic noise. Surface mounted magnets are favourable as this maximises the torque/inertia ratio due to possibility for inertia-holes. Also the torque/current ratio, referred to as the K_t value, obtained with this motor configuration is generally higher when compared with other configurations for given overall dimensions and mass. For demanding motion control applications these features are critical for high dynamics, i.e., high acceleration and deceleration, and high torque performance.

The torque for this servomotor is proportional to the length, as shown in Fig. 2.2.

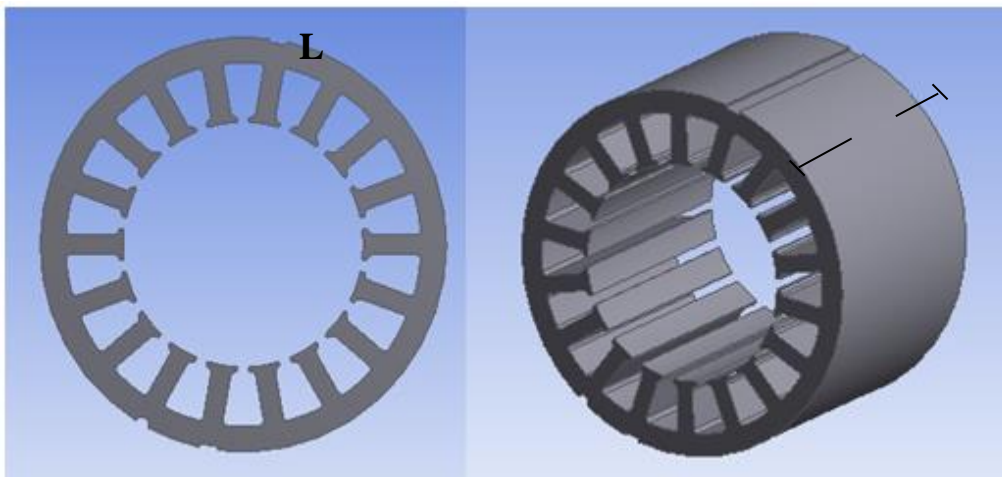


Fig. 2.2. Lamination and stack of laminations of a stator core with 18 slots design servomotor.

Different stator stack lengths of an interior-rotor BPM synchronous servomotor can easily be manufactured for different ratings by increasing the number of laminations and permanent magnet segments in the same proportion without changing lamination profile. Stator and rotor laminations can be punched from

something rotating inside to avoid hazards. Different techniques for magnet retention can be applied to the motor configuration of Fig. 2.3. The most popular methods employed in the servomotor industry are gluing and the application of glass retaining tape. Glass tape, however, tends to increase the air-gap and consequently reduce the torque performance.

Henceforth, for conciseness, the new interior rotor radial-flux surface mounted BPM synchronous servomotor with the concentrated winding configuration under investigation in this research programme will be referred to simply as the *new servomotor* and the conventional interior rotor radial-flux surface mounted BPM synchronous servomotor with the segmented stator and distributed winding configuration will be referred to as the *conventional servomotor*. The term, *servomotor*, on its own refers to either the conventional or new servomotor.

2.3. Basic Design Parameters

2.3.1. Overview

This section deals principally with the properties of servomotors in terms of their dimensional, magnetic and electric properties. In order to facilitate the manufacturability and the commercialisation of the new servomotor, a significant number of features were kept the same as those of the conventional servomotor. These comprise the stator lamination diameter, split-ratio, high quality lamination, sinusoidal phase current, axial length L , and housing diameter as shown in Fig. 2.2 and Fig. 2.3. The maximum winding temperature reference is equal for both servomotors. This will ultimately enable conventional motors in service to be easily replaced with the new servomotors. However, there are also significant differences between the conventional and new servomotors, including the magnet width, the slot-pole number, the conductor current density, the stator tooth width, absence of stator skew, different winding configuration.

Comparative performance and cost analyses are carried out with respect to the adjustable parameters in the new and conventional servomotors. Variation of dimensional, magnetic and electric parameters are all considered. The most important dimensional parameters are thereby identified. The

parameters of magnetic circuit components that realise the specified air-gap flux density are calculated analytically and then compared with the results obtained from FEA. Finally the most relevant electrical components are identified.

2.3.2. Dimensional Parameters

The main dimensional component in this research work is the stator lamination diameter that defines the servomotor frame size. This is best indicated in Fig. 2.3 as D_o , where $D_o/2$ is the radius of the stator core as shown in Fig. 2.2 for the conventional stator technology. The current conventional servomotor frame sizes available from manufacturers have to be retained in the proposed new servomotors. The reasons for this are mainly due to the existing manufacturing tooling, standard sizes and experience developed with the current manufacturing processes. Also for the same reason the stator stack housing, stator lamination and bore diameters cannot be changed from the previous generation of conventional servomotors and therefore only changes of the internal rotor and stator dimensions shown in Fig. 2.3 are allowed. This enables different slot-pole combinations to be investigated to find the best performance in terms of torque density, torque ripple and efficiency. The only significant change in the stator dimensions is the stator-tooth-width coupled with variations in the number of stator slots.

The performance indicators and selling points such as continuous torque rating, dynamic torque output, torque constant and cogging torque of the conventional and new servomotors are all sensitive to the geometrical parameters shown in Fig. 2.3. Each characteristic behaves in a certain manner depending on which geometrical parameter is changed. For example, if the stator-tooth-width is changed, the torque constant is affected but the cogging torque is not affected significantly. In this research work, the sensitivity analysis is applied with respect to all the geometrical design parameters in order to find the best possible design point using FEA.

The parameters in Fig. 2.3 are the lamination outer diameter ($2 \cdot \text{Rad3}$ or D_o), stator yoke height (YHS or h_{yhs}), stator tooth height (THS), stator tooth width

(TWS or w_{tws}), slot opening tooth height (TH or h_{th}), slot open (SO or w_{so}), slot depth (SD or h_{sd}), slot width (SW), inner slot width (SWI or w_{swi}), outer slot width (SWO or w_{swo}), slot opening angle (SOang), air-gap length (GAP or g), tooth gap depth (TGD), magnet thickness (LM or l_m), beta magnet angle (BM or θ_m), slot pitch or beta slot pitch (BP or θ_s), housing thickness (THM), rotor core diameter (RC or D_{rc}) and bore diameter (D).

According to (Hanselman, 2003) the fundamental question in motor design is “How large does a motor have to be to produce a required torque?” For radial-flux motors the answer to this question is often stated by means of the relationship,

$$T = kD^2L \quad (2.1)$$

where T is the maximum possible torque, k is a constant, D is the bore diameter, and L is the axial rotor length, measured perpendicular to the page when viewing Fig. 2.3. As shown in equation (2.1), the torque of a servomotor is directly proportional to the bore diameter due to small air-gap as shown in Fig. 2.3 and the rotor length. Equation (2.1) indicates that a given percentage increase in D produces a much larger increase in T than the same percentage increase.

The square law with respect to D is well explained in Hanselman, 2003. Explained simply, the torque produced and the maximum force are linearly proportional to the diameter. When the radius is increased less force is required to produce a given torque.

And therefore D ($T = F \times r$ where F is force and $r = D/2$ radius) causes torque to increase due to increase of radius and also when the diameter as D is increased, the capacity for more magnets around the rotor periphery increases giving an increase in the maximum attainable peripheral force, F that is proportional to D , i.e., $F = k_f D$, where k_f is a constant. Then the maximum attainable torque per unit length is $T = FD = k_f D^2/2 = kD^2$.

As already pointed out, the stator lamination diameter ($2 \times Rad3$) in Fig. 2.3, i.e., the outer diameter (OD) is fixed in this investigation. Also, due to the

losses and the magnetic circuit saturation, the maximum available torque will not increase with D at the same rate as predicted by (2.1) for the same application. In this research programme, the performance optimisation is carried out for different slot-pole combinations for both the new and conventional servomotors. The design selection will take into account the material cost and the torque performance.

With some approximations the dimensions of Fig. 2.3 can be expressed mathematically in order to calculate the areas of the servomotor. The slot area and core area are very critical to the servomotor performance, because they are current and flux paths respectively.

When these equations are defined, the performance and material usage sensitivity with respect to different parameters can be analysed to arrive at an acceptable trade off regarding the overall cost of the servomotor. The equations are as follows (Libert, 2004a). The bore diameter or the inner stator diameter is

$$D = D_{rc} + 2l_m + 2g \quad (2.2)$$

where D_{rc} is the rotor core diameter, l_m is the magnet thickness and g is the air gap length. The slot pitch θ_s can be calculated as

$$\theta_s = \pi \frac{D}{Q_s} \quad (2.3)$$

where Q_s is the number of stator slots and D is given by equation (2.2). The inner slot width (SWI or w_{swi}), the outer slot width (SWO or w_{swo}) are given by

$$w_{swi} = \pi \frac{D + 2h_{th}}{Q_s} - w_{tws} \quad (2.4)$$

$$w_{swo} = \pi \frac{D + 2h_{sd}}{Q_s} - w_{tws} \quad (2.5)$$

$$h_{yhs} = \frac{1}{2}(D_o - D - 2h_{sd}) \quad (2.6)$$

where h_{th} is the slot opening tooth height, w_{twS} is the stator tooth width, h_{sd} is the slot depth height, h_{yhs} is the stator yoke height and D_O is the stator outer diameter. Therefore the slot area A_S is given using equations (2.4), (2.5) and (2.6) as

$$A_S \approx \frac{1}{2}(w_{swi} + w_{swo}) \cdot (h_{sd} - h_{th}) \quad (2.7)$$

Therefore by adding the number of poles p and considering only the stack length or the active length L , all the 3D stator geometry can be defined using the above equations.

When sizing a BPM synchronous servomotor, one of the most important components to consider is the split ratio as it can significantly influence the servomotor torque performance and efficiency. This can be defined as the ratio of the bore diameter to the stator lamination diameter as shown in Fig. 2.3, i.e.

$$\text{split - ratio} = \frac{\text{bore diameter}}{\text{stator lam diameter}} = \frac{D}{D_O} \quad (2.8)$$

The optimal split ratio for a BPM synchronous servomotor is normally based on how the stall torque and thermal performance vary with the bore diameter variation. The objective is basically to find the optimal split ratio as a trade-off between lower active material cost, minimum copper loss, maximum efficiency and maximum available torque.

This is very important aspect of servomotor design mainly because the active material cost is more than 80% of the total servomotor construction cost. So in this research programme the split ratio of the new prototype servomotor is maintained constant and equal to that of the conventional servomotor with which it is to be compared. This decision has been influenced by CTD report (Sá et al., 2010-2013), the supporting company, and by (Wu et al., 2010) who have proven the current split ratio to be the best for the current frame sizes. The split ratio for the current design is 0.5794. This is further justified by the

reasonable assumption that the winding technology (distributed or concentrated) has no effect on the split ratio factor.

As already stated, a rotor geometry with surface mounted permanent magnets (SMPM) with an inner rotor is used, as shown in Fig. 2.3. This design configuration is the same as used currently for the current conventional servomotor with an 18-6 slot-pole combination. In this topology the protection of the magnets against demagnetisation is low. Hence the maximum flux density of the stator needs to be well controlled. Also in terms of mechanical strength there is a significant problem due to the centrifugal force being proportional to the square of the speed.

A good reason for selecting the surface mounted permanent magnet design, however, is that there is a low leakage flux associated with this topology as shown in Fig. 2.4, and regarding production, assembly is relatively straightforward (Hendershot et. al., 2010) compared with interior permanent magnet (IPM) type servomotors.

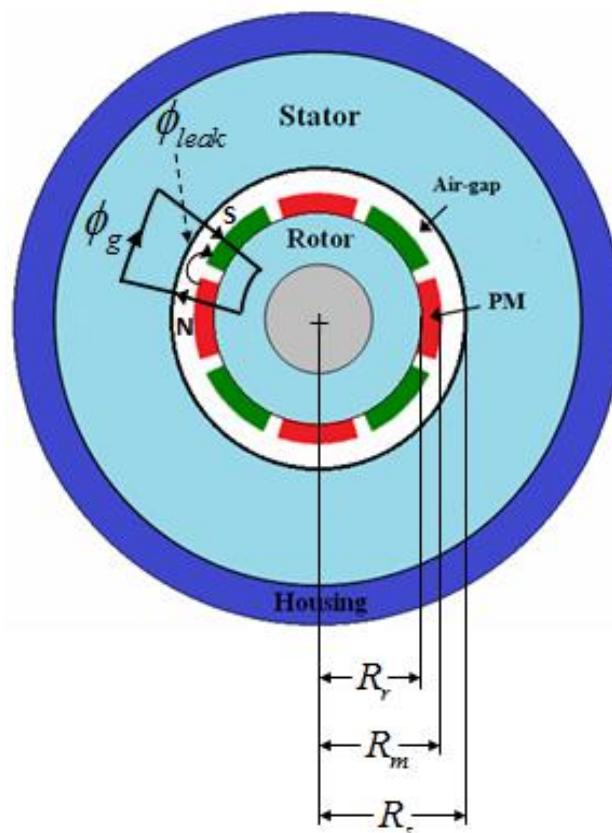


Fig. 2.4. Servomotor geometry with fundamental servomotor structure and associated flux path.

For the new slot-pole combinations an AC star connected winding is used for the stator as is the case for the predecessor design with an 18-6 slot-pole combination. The exterior of the stator back iron is enclosed similarly with a conventional aluminium housing. The basic motor configurations of the current conventional servomotor shown in TABLE 2.1 are used for FEA magnet initial circuit model in order to perform the initial calculations for the new servomotor designs.

TABLE 2.1. Dimensions and parameters of current distributed winding.

Dimensions and parameters	Value
Housing diameter (mm)	115
Outer diameter of stator stack (mm)	107
Bore diameter (mm)	62
Permanent magnet thickness (mm)	2.95
Air gap (mm)	0.75
Tooth gap depth (mm)	0.83
Slot opening (mm)	2.5
Slot opening angle (Deg)	28
Slot tooth width (mm)	5.2
Stator tooth depth (mm)	15.5

This covers determination of the shape of different magnetic circuit components using mainly a 2D FEA model for electromagnetic designs and use FEA with thermal lumped model for torque performance calculation.

In order to obtain the *Optimal Design* as defined previously, the performance of the BPM synchronous servomotor is evaluated by its performance indicators. In the case of this research work these are the stall torque, cogging torque, torque ripple and torque constant. At this stage *sensitivity analysis* to *optimise* is performed. The variables with the least sensitivity to torque, cogging torque, torque ripple and torque constant can be disregarded.

The design with the linear sensitivity or low parameter variation can be kept constant to the more appropriated value based on safety or manufacturability and then all other variables are optimised. This process provides graphs to provide a clear picture of performance in terms of the cogging torque, output torque, and torque constant.

2.3.3. Magnetic Parameters

A 2D FEA electromagnetic tool is used in order to obtain an optimal design and this done by considering all nonlinear characteristics of the BPM synchronous servomotor. If the performance is not in the expected range, some adjustments can be made to the servomotor geometry to improve the servomotor performance. When this stage finishes prototype servomotors are built and tested and all the results obtained are presented and compared with those obtained from FEA model where is necessary.

This section is mainly related to the methods of definition of magnetic circuits with focus on air gap flux density and distribution for the conventional servomotor with the 18-6 slot-pole combination. This flux density is very critical for BPM synchronous servomotor design since it can quantify the level of flux required to pass through the air-gap as shown in Fig. 2.4. It links the stator to the rotor magnetically and it is the main flux in the motor, participating in energy conversion. There is another portion of flux that does not cross the air-gap as shown in Fig. 2.4, and this leakage flux does not contribute to the energy conversion. Equations for the air-gap flux density due to the magnets in a surface mounted BPM synchronous servomotor are later presented for Fig. 2.4.

A prediction of the open circuit magnetic field based on the 2-D model in the cylindrical coordinates is carried out analytically and compared with the FEA calculations. These calculations are critical to the calculated torque predictions. Assuming tangentially magnetized permanent magnets, the air gap flux density level is assumed to have a rectangular shape with a constant value, between B_g . This rectangular shape is as wide as the permanent magnet width, ω_m , and with a maximum value B_m . In the inner-rotor BPM

synchronous servomotor, the magnet flux leaves the north poles via air-gap and then passes to the stator where it splits equally into opposite directions and crosses the air-gap once more towards the neighbouring South poles. Fig. 2.4 shows half of the North and South poles facing the air gap and the flux main flow, ϕ_g , is illustrated. Apart from this main flux path, there is flux jumping from one magnet to another without passing into the stator core, and this is the magnet leakage flux ϕ_{leak} already mentioned.

Assuming infinite permeability of the iron materials in both the stator and the rotor, a simple magnetic circuit model for the half permanent magnet and air-gap is presented in Fig. 2.5 with B/H curve (a) and magnetic circuit (b).

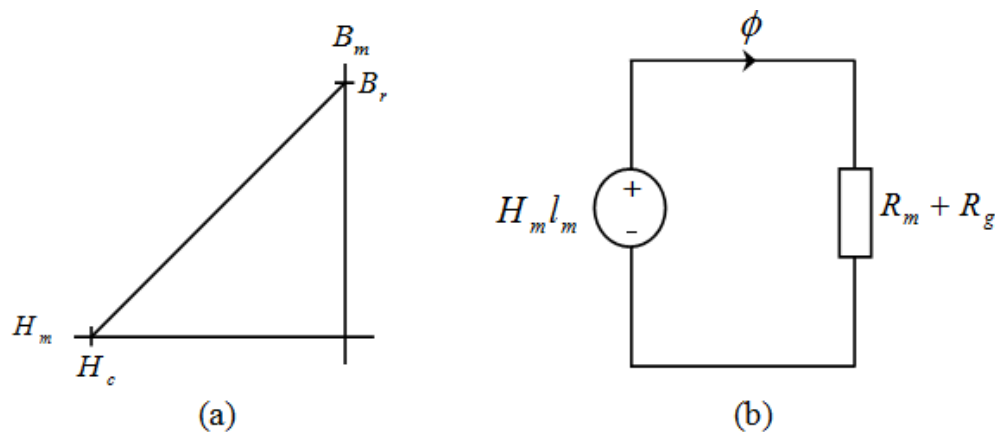


Fig. 2.5. Simplification of the half of magnetic circuit model for Fig. 2.4.

The circuit for a half iron width of the servomotor structure as shown in Fig. 2.4 can be developed as shown in Fig. 2.5. This equivalent lumped circuit allows for calculation of the maximum flux density B_m using Ampere's law.

Conventionally it is assumed that any magnetising force or field intensity, H , produces a flux density, B . In the absence of currents in the winding, the permanent magnet is the only source of flux in the circuit. Therefore in the lumped circuit above, the permanent magnet is assumed as a constant magneto-motive force source of value, $H_m l_m$, that causes flux to flow in the fashion shown in Fig. 2.4. In series with the flux source there is an associated permanent magnet reluctance of R_m plus the air gap reluctance R_g . It is assumed that the majority of the flux crosses the air gap region and the

reluctances of the stator core, R_s , and rotor core, R_r , are negligible when compared with the reluctance, R_g , to flux due to the air gap.

Permanent magnets such as NdFeB or SmCo have linear second quadrant demagnetization curves as shown in Fig. 2.5 (a). When the servomotor windings are energized, from this characteristic curve it is possible to calculate the permanent magnet operating flux density, B_m , as a function of the permanent magnet external field intensity.

The linear relationship on the second quadrant demagnetization curve between the flux density, B_m , and the field intensity, H_m , can be written as

$$B_m = B_r + \mu_m H_m \quad (2.9)$$

where $\mu_m = \mu_0 \mu_r$ and since the gradient of the curve in Fig. 2.5 (a) is

$$\mu_m = \frac{B_r}{H_c} \quad (2.10)$$

therefore with some manipulations the magnet field intensity can be written as

$$H_m = \frac{B_m}{\mu_m} - H_c \quad (2.11)$$

where H_c is the coercive magnetic field intensity of the permanent magnet.

Applying Ampere's law that states

$$\sum MMF = 0 \quad (2.12)$$

this can be written for the reluctance model shown in Fig 2.5 (b) as

$$H_m l_m + H_g g = 0 \quad (2.13)$$

where H_g is the magnetic field intensity in the air gap region.

Introduction of equation (2.11) into equation (2.13) leads to the following.

$$\left(\frac{B_m}{\mu_m} - H_c \right) l_m + H_g g = 0 \quad (2.14)$$

from which

$$H_c l_m = H_g g + \frac{B_m}{\mu_m} l_m. \quad (2.15)$$

Applying the constitutive relation as

$$\mu_m = \mu_0 \mu_r \approx \mu_0 \quad (2.16)$$

is a valid assumption. Then

$$H_c l_m = \frac{B_g}{\mu_0} g + \frac{B_m}{\mu_0} l_m \quad (2.17)$$

Total flux in the circuit is

$$\phi = B_g A_g = B_m A_m \quad (2.18)$$

where A_g and A_m are the air gap area and the permanent magnet area, respectively.

Therefore introducing equation (2.18) into equation (2.17) by setting $B_g = \phi/A_g$ and the magnet flux density as $B_m = \phi/A_m$ as follows,

$$H_c l_m = \phi \frac{g}{\mu_0 A_g} + \phi \frac{l_m}{\mu_0 A_m} \quad (2.19)$$

Finally, since the air gap reluctance is $R_g = g/(\mu_0 A_g)$ and the permanent magnet reluctance is $R_m = l_m/(\mu_0 A_m)$, equation (2.19) reduces to the following.

$$H_c l_m = \phi (R_g + R_m) \quad (2.20)$$

Furthermore, at open circuit the permanent magnetic field intensity, H_m , is equal to the coercive magnetic field intensity of the permanent magnet, H_c , and then (2.20) may be written as

$$H_m l_m = \phi (R_g + R_m). \quad (2.21)$$

In a similar fashion to the above, (Libert, 2004a) presented the air gap reluctance, R_g , and the permanent magnet reluctance, R_m , as functions of length, area and permeability as follows.

$$\left. \begin{aligned} A_g &= L \times l_{iron} \\ A_m &= L \times \omega_m \end{aligned} \right\} \quad (2.22)$$

Therefore

$$R_m = \frac{l_m}{\mu_0 \mu_r L \omega_m} \quad (2.23)$$

where L is the active length of the servomotor and ω_m is the magnet width.

The air gap reluctance is presented as

$$R_g = \frac{g \cdot k_C}{\mu_0 L l_{iron}} \quad (2.24)$$

with the width of the rotor iron piece l_{iron} as

$$l_{iron} = \left(\frac{\pi - \theta_m}{2} \right) \frac{D_{rc}}{p} \quad (2.25)$$

and k_C is the Carter factor given by

$$k_C = \frac{\theta_s}{\theta_s - \frac{(k_{open} w_{swi})^2}{k_{open} w_{swi} + 5g}} \quad (2.26)$$

where k_{open} is the ratio between the slot opening, w_{so} , and the inner stator slot width, w_{swi} , as follows.

$$k_{open} = \frac{w_{so}}{w_{swi}} \quad (2.27)$$

and finally B_m is written as

$$B_m = \frac{B_r}{1 + \frac{\mu_r g k_c \omega_m}{l_m \cdot l_{iron}}} \cdot \frac{\omega_m}{l_{iron}} \quad (2.28)$$

where B_r is the flux density of the magnet and μ_r the relative magnet permeability.

The leakage flux between two neighbouring permanent magnets is taken into account by the factor k_{leak} that is formulated as

$$H_c l_m = H_g g + \frac{B_m}{\mu_m} l_m \quad (2.29)$$

Applying the constitutive relation as

$$\mu_m = \mu_0 \mu_r \approx \mu_0 \quad (2.30)$$

is a valid assumption. Then

$$H_c l_m = \frac{B_g}{\mu_0} g + \frac{B_m}{\mu_0} l_m \quad (2.31)$$

Total flux in the circuit is

$$\phi = B_g A_g = B_m A_m \quad (2.32)$$

where A_g and A_m are the air gap area and the permanent magnet area, respectively.

Therefore introducing equation (2.32) into equation (2.31) by setting $B_g = \phi/A_g$ and the magnet flux density as $B_m = \phi/A_m$ as follows,

$$H_c l_m = \phi \frac{g}{\mu_0 A_g} + \phi \frac{l_m}{\mu_0 A_m} \quad (2.33)$$

Finally, since the air gap reluctance is $R_g = g / (\mu_0 A_g)$ and the permanent magnet reluctance is $R_m = l_m / (\mu_0 A_m)$, equation (2.33) reduces to the following.

$$H_c l_m = \phi (R_g + R_m) \quad (2.34)$$

Furthermore, at open circuit the permanent magnetic field intensity, H_m , is equal to the coercive magnetic field intensity of the permanent magnet, H_c , and then (2.34) may be written as

$$H_m l_m = \phi (R_g + R_m). \quad (2.35)$$

In a similar fashion to the above, (Libert, 2004a) presented the air gap reluctance, R_g , and the permanent magnet reluctance, R_m , as functions of length, area and permeability as follows.

$$\left. \begin{aligned} A_g &= L \times l_{iron} \\ A_m &= L \times \omega_m \end{aligned} \right\} \quad (2.36)$$

Therefore

$$R_m = \frac{l_m}{\mu_0 \mu_r L \omega_m} \quad (2.37)$$

where L is the active length of the servomotor and ω_m is the magnet width.

The air gap reluctance is presented as

$$R_g = \frac{g \cdot k_C}{\mu_0 L l_{iron}} \quad (2.38)$$

with the width of the rotor iron piece l_{iron} as

$$l_{iron} = \left(\frac{\pi - \theta_m}{2} \right) \frac{D_{rc}}{p} \quad (2.39)$$

and k_C is the Carter factor given by

$$k_C = \frac{\theta_s}{\theta_s - \frac{(k_{open} w_{swi})^2}{k_{open} w_{swi} + 5g}} \quad (2.40)$$

where k_{open} is the ratio between the slot opening, w_{so} , and the inner stator slot width, w_{swi} , as follows.

$$k_{open} = \frac{W_{so}}{W_{swi}} \quad (2.41)$$

and finally B_m is written as

$$B_m = \frac{B_r}{1 + \frac{\mu_r g k_c \omega_m}{l_m \cdot l_{iron}}} \cdot \frac{\omega_m}{l_{iron}} \quad (2.42)$$

where B_r is the flux density of the magnet and μ_r the relative magnet permeability.

The leakage flux between two neighbouring permanent magnets is taken into account by the factor k_{leak} that is formulated as

$$k_{leak} = \frac{\psi_t - \psi_{leak}}{\psi_t} \quad (2.43)$$

where ψ_t is the total number of flux lines plotted using the finite element method and ψ_{leak} is the number of leakage flux lines between PM as shown in Fig. 2.6.

According to (Libert, 2004a) for surface mounted permanent magnet motors the equation is

$$k_{leak} = \frac{\psi_t - \left(\frac{7p}{60} - 0.5\right)}{\psi_t} \quad (2.44)$$

for a total number of flux lines, $\psi_t = 100$, and where p is the number of permanent magnet poles of the servomotor.

Taking leakage into account for the surface mounted motors, B_m , can be written as

$$B_m = \frac{B_r \cdot k_{leak}}{1 + \frac{\mu_r g k_c}{l_m}} \quad (2.45)$$

Based on equations (2.30) and (2.31) the maximum air gap flux density, B_m , decreases with increase of the number of permanent magnet poles.

Fig. 2.6 shows the FEA predicted flux pattern of two BPM synchronous servomotors with different rotor pole numbers but with the same number of slots.

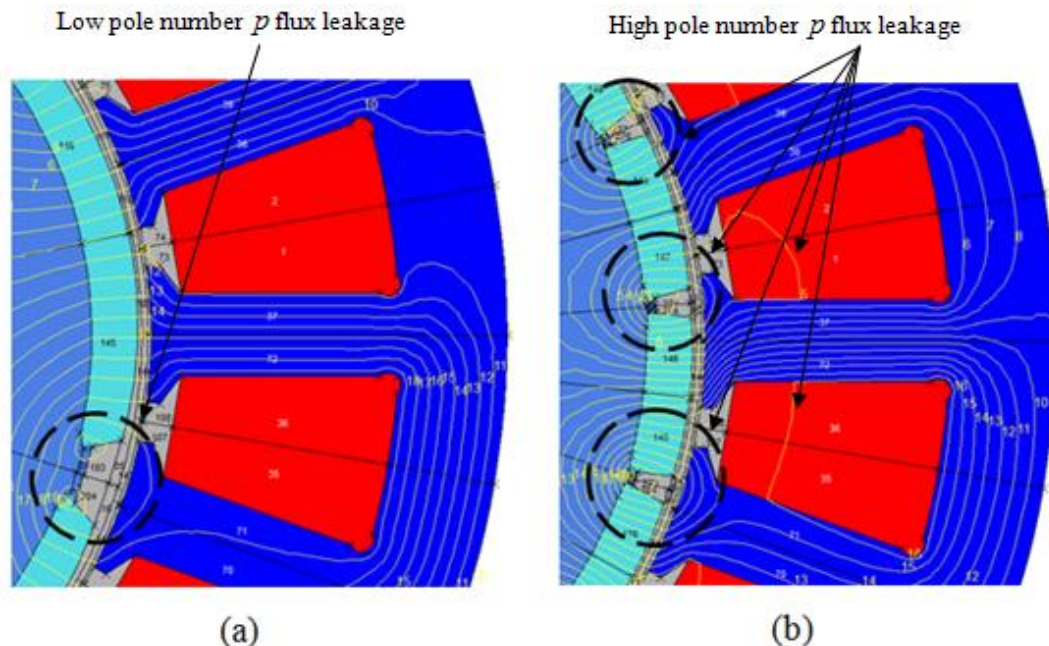


Fig. 2.6. Magnetic field flow in low (a) and high (b) pole number p , with fixed slot number.

The servomotor of Fig. 2.6 (a) has six permanent magnets and (b) has sixteen permanent magnets, and both servomotors have a current servomotor design slot number of eighteen. The FEA figures indicate that there is a considerable increase of flux leakage due to the increase of the number of permanent magnets.

Fig. 2.7 shows a typical air-gap flux density distribution for an 18-6 slot-pole combination used for the current conventional servomotor design. By defining the geometry of the servomotor into the FEA software, as shown in Fig. 2.6, it is possible to perform the calculation open circuit air-gap flux due to the permanent magnet poles. This allows for an accurate calculation of flux density level in the air-gap and also takes into account the stator slotting effects, as shown in Fig. 2.7. In Fig. 2.7 it is shown the air gap flux density calculated using FEA and analytical method for the 18-6 slot-pole servomotor. Note that the FEA counts for the stator slotting effects while the analytical

method is more of an ideal air-gap flux density distribution. However the analytical method allows for the calculation of the maximum flux density level in the air-gap as shown in Fig. 2.7, here it assumes maximum flux density along the permanent magnet width.

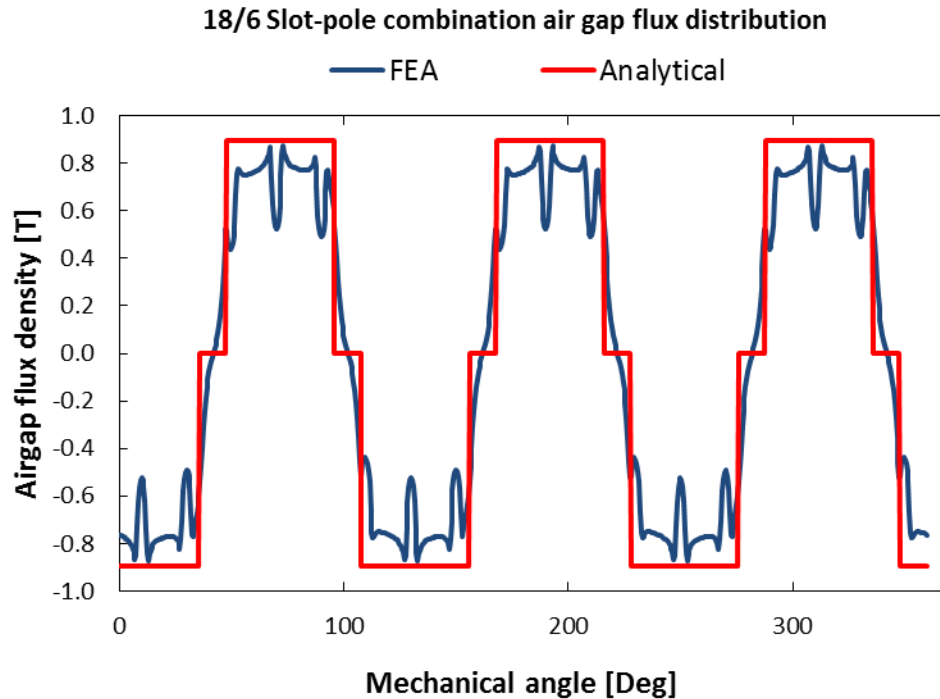


Fig. 2.7. Brushless servomotor air gap flux density distribution for analytical method and FEA method.

Therefore at design stage, it is always preferable to go for lower poles, if the performance is not affected, since the effectiveness of permanent magnetic material used tends to be higher and from manufacturing standing point it is more convenient to have fewer magnets to insert in the rotor rather than an increase number of magnets. This is one of the critical criteria to consider later on this research work for servomotor design selection.

Different approaches were taken by different authors (Hanselman, 2003) (Zhu et al., 1993) with more sophisticated mathematics for prediction of magnetic field in the air-gap and permanent magnet regions of surface mounted machines. The analytical expressions for flux density and the field intensity in the air-gap and the permanent magnet of a BPM synchronous motor with radial flux surface mounted with inner-rotor as shown in Fig. 2.4 are presented.

The same analytical expressions are also applied to the radial flux servomotor with the outer-rotor configuration. The radius under side of the permanent magnet pole in Fig. 2.4 is $R_r = D/2 - g - l_m$, magnet air-gap radius is $R_m = D/2 - g$ and the radius to stator air-gap interface or bore radius is $R_s = D/2$.

These parameters can be used together with a simple approach to formulate the magnetic field distribution based on a scalar magnetic potential. Therefore mathematical expressions can be developed for the flux density and field intensity in the air-gap and permanent magnets of a BPM synchronous servomotor with radial flux as shown in Fig. 2.8 for the conventional servomotor.

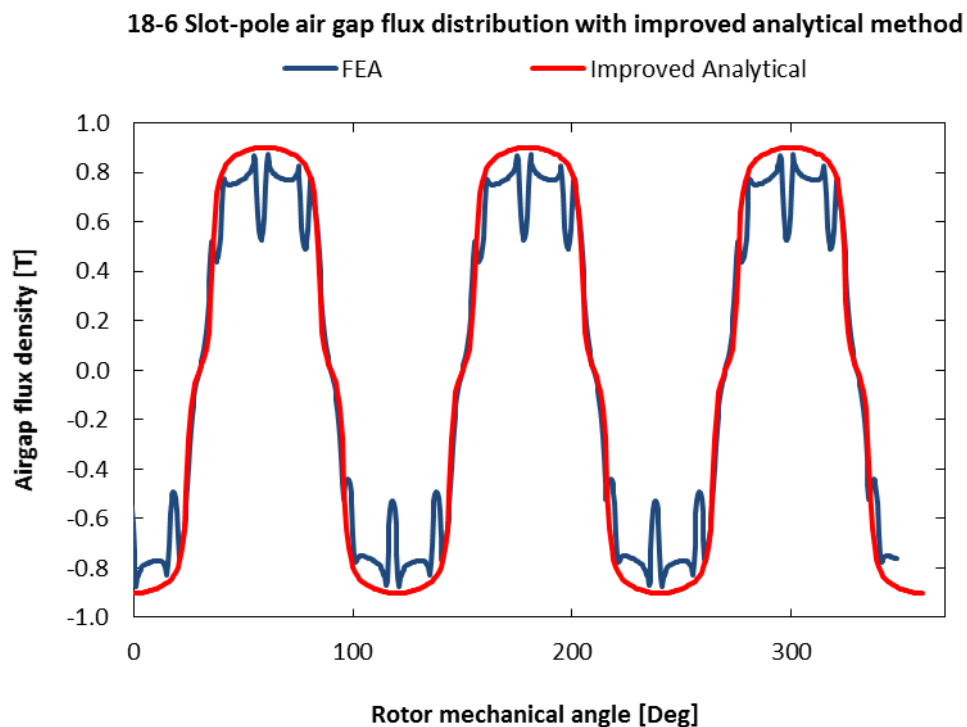


Fig. 2.8. Brushless servomotor air gap flux density distribution for improved analytical method and FEA method.

If it assumed that the magnetic distribution of Fig. 2.4 is uniform in the axial direction (deep into the page). Then magnetic distribution for the servomotor becomes a simple 2D problem. If there are no currents going through the windings, then the magnetic fields can be modelled as the solutions of partial differential equation (Laplace's equation) (Hanselman, 2003) as follows.

$$\nabla^2 F_a = 0, \quad (2.46)$$

where F_a is the scalar magnetic potential in the air. By the quasi-Poisson partial differential equation, the regions with permanent magnet material can be modelled for the magnetic fields as follows,

$$\nabla^2 F_m = \frac{\vec{\nabla} \cdot \vec{M}}{\mu_r} \quad (2.47)$$

where F_m is the scalar magnetic potential in the magnet, μ_r is the magnet relative recoil permeability, and \vec{M} is the magnet magnetization (Hanselman, 2003).

In absence of the servomotor winding current, then magnet magnetization is the only magnetic field source of the problem that causes flux to flow in the fashion that is shown in figures (2.8) and (2.9).

According to (Hanselman, 2003), if above equations are treated as scalar potential with solution, therefore the vector field intensity can be found as following,

$$\vec{H} = -\vec{\nabla} F \quad (2.48)$$

where F can be either F_a or F_m .

Then the vector flux densities for both air-gap and the permanent magnet regions can be obtained from the vector field intensity of equation (2.34) as

$$\left. \begin{aligned} \vec{B}_a &= \mu_0 \vec{H} \\ \vec{B}_m &= \mu_r \mu_0 \vec{H}_m + \mu_0 \vec{M} \end{aligned} \right\} \quad (2.49)$$

where μ_0 is the permeability of free space that is very low when compared with the negligible reluctance of stator core area. And the subscripts a and m are related to air and magnet.

The term \vec{M} is the magnetization that has components along the radial and tangential directions, and the magnetization can be written as

$$\vec{M} = M_r \vec{i}_r + M_\theta \vec{i}_\theta \quad (2.50)$$

where r and θ are the cylindrical coordinates.

This method is of a sophisticated 2-D analytical open circuit calculation method for the normal component or air gap flux density is presented by Zhu [Zhu]. And this is the magnetic field calculation method performed using Microsoft Office Excel sheet in this thesis. This *conventional open circuit field calculation* method applied to Fig. 2.4 according to (Zhu et al., 1993) states the following.

In the air space:

$$B_r(r, \theta) = \sum_{n=1,3,5,\dots}^{\infty} \frac{\mu_0 M_n}{\mu_r} \frac{np}{(np)^2 - 1} R_m^{-(np-1)} \left\{ \frac{(np-1)R_m^{2np} + 2R_r^{np+1}R_m^{np-1} - (np+1)R_r^{2np}}{\frac{\mu_r+1}{\mu_r} [R_s^{2np} - R_r^{2np}] - \frac{\mu_r-1}{\mu_r} \left[R_m^{2np} - R_s^{2np} \left(\frac{R_r}{R_m} \right)^{2np} \right]} \right\} \left[r^{np-1} + R_s^{2np} r^{-(np+1)} \right] \cos np\theta \quad (2.51)$$

In the magnets:

$$B_r(r, \theta) = \sum_{n=1,3,5,\dots}^{\infty} \mu_0 M_n \frac{np}{(np)^2 - 1} R_m^{-(np-1)} \left\{ \frac{\left(np - \frac{1}{\mu_r} \right) R_m^{2np} + \left(1 + \frac{1}{\mu_r} \right) R_r^{np+1} R_m^{np-1} - \left(np + \frac{1}{\mu_r} \right) R_s^{2np} - \left(1 - \frac{1}{\mu_r} \right) \left(\frac{R_r}{R_m} \right)^{np+1} R_s^{2np}}{\frac{\mu_r+1}{\mu_r} [R_s^{2np} - R_r^{2np}] - \frac{\mu_r-1}{\mu_r} \left[R_m^{2np} - R_s^{2np} \left(\frac{R_r}{R_m} \right)^{2np} \right]} \right\} \left[r^{np-1} + R_s^{2np} r^{-(np+1)} \right] \cos np\theta \\ + \sum_{n=1,3,5,\dots}^{\infty} \mu_0 M_n \frac{np}{(np)^2 - 1} \left(\frac{R_r}{r} \right)^{np+1} \cos np\theta \quad (2.52) \\ + \sum_{n=1,3,5,\dots}^{\infty} \mu_0 M_n \frac{(np)^2}{(np)^2 - 1} \left(\frac{R_r}{r} \right)^{np+1} \cos np\theta$$

$$\begin{aligned}
B_\theta(r, \theta) = & \sum_{n=1,3,5,\dots}^{\infty} -\mu_0 M_n \frac{np}{(np)^2 - 1} R_m^{-(np-1)} \\
& \left\{ \frac{\left(np - \frac{1}{\mu_r} \right) R_m^{2np} + \left(1 + \frac{1}{\mu_r} \right) R_r^{np+1} R_m^{np-1} - \left(np + \frac{1}{\mu_r} \right) R_s^{2np} - \left(1 - \frac{1}{\mu_r} \right) \left(\frac{R_r}{R_m} \right)^{np+1} R_s^{2np}}{\frac{\mu_r + 1}{\mu_r} \left[R_s^{2np} - R_r^{2np} \right] - \frac{\mu_r - 1}{\mu_r} \left[R_m^{2np} - R_s^{2np} \left(\frac{R_r}{R_m} \right)^{2np} \right]} \right. \\
& \left. \left[r^{np-1} - R_s^{2np} r^{-(np+1)} \right] \sin np\theta \right. \\
& + \sum_{n=1,3,5,\dots}^{\infty} \mu_0 M_n \frac{np}{(np)^2 - 1} \left(\frac{R_r}{r} \right)^{np+1} \sin np\theta \quad (2.53) \\
& \left. - \sum_{n=1,3,5,\dots}^{\infty} \mu_0 M_n \frac{np}{(np)^2 - 1} \sin np\theta \right.
\end{aligned}$$

for $np = 1$:

in the air-gap

$$B_r(r, \theta) = \frac{\mu_0 M_1}{2\mu_r} \left\{ \frac{\left(\frac{R_m}{R_s} \right)^2 - c_1 \left(\frac{R_r}{R_s} \right)^2 + \left(\frac{R_r}{R_s} \right)^2 \ln \left(\frac{R_m}{R_r} \right)^2}{\frac{\mu_r + 1}{\mu_r} \left[1 - \left(\frac{R_r}{R_s} \right)^2 \right] - \frac{\mu_r - 1}{\mu_r} \left[\left(\frac{R_m}{R_s} \right)^2 - \left(\frac{R_r}{R_m} \right)^2 \right]} \right\} \left[1 - \left(\frac{R_s}{r} \right)^2 \right] \cos \theta \quad (2.54)$$

and

$$B_\theta(r, \theta) = \frac{\mu_0 M_1}{2\mu_r} \left\{ \frac{\left(\frac{R_m}{R_s} \right)^2 - c_1 \left(\frac{R_r}{R_s} \right)^2 + \left(\frac{R_r}{R_s} \right)^2 \ln \left(\frac{R_m}{R_r} \right)^2}{\frac{\mu_r + 1}{\mu_r} \left[1 - \left(\frac{R_r}{R_s} \right)^2 \right] - \frac{\mu_r - 1}{\mu_r} \left[\left(\frac{R_m}{R_s} \right)^2 - \left(\frac{R_r}{R_m} \right)^2 \right]} \right\} \left[1 - \left(\frac{R_s}{r} \right)^2 \right] \sin \theta \quad (2.55)$$

In the magnets

$$B_r(r, \theta) = \frac{\mu_0 M_1}{2} \left\{ \frac{\left(\frac{R_m}{R_s} \right)^2 - 1 + \ln \left(\frac{R_m}{R_r} \right) \left[\frac{\mu_r + 1}{\mu_r} \left(\frac{R_r}{R_s} \right)^2 - \frac{\mu_r - 1}{\mu_r} \left(\frac{R_r}{R_m} \right)^2 \right]}{\frac{\mu_r + 1}{\mu_r} \left[1 - \left(\frac{R_r}{R_s} \right)^2 \right] - \frac{\mu_r - 1}{\mu_r} \left[\left(\frac{R_m}{R_s} \right)^2 - \left(\frac{R_r}{R_m} \right)^2 \right]} \right\} \left[1 + \left(\frac{R_r}{r} \right)^2 \right] \cos \theta$$

$$+ \frac{\mu_0 M_1}{2} \left[1 - \ln \left(\frac{r}{R_m} \right) + \left(\frac{R_r}{r} \right)^2 \ln \left(\frac{R_m}{r} \right) \right] \cos \theta \quad (2.56)$$

$$B_\theta(r, \theta) = \frac{\mu_0 M_1}{2} \left\{ \frac{\left(\frac{R_m}{R_s} \right)^2 - 1 + \ln \left(\frac{R_m}{R_r} \right) \left[\frac{\mu_r + 1}{\mu_r} \left(\frac{R_r}{R_s} \right)^2 - \frac{\mu_r - 1}{\mu_r} \left(\frac{R_r}{R_m} \right)^2 \right]}{\frac{\mu_r + 1}{\mu_r} \left[1 - \left(\frac{R_r}{R_s} \right)^2 \right] - \frac{\mu_r - 1}{\mu_r} \left[\left(\frac{R_m}{R_s} \right)^2 - \left(\frac{R_r}{R_m} \right)^2 \right]} \right\} \left[1 - \left(\frac{R_r}{r} \right)^2 \right] \sin \theta$$

$$+ \frac{\mu_0 M_1}{2} \left[-\ln \left(\frac{r}{R_m} \right) - \left(\frac{R_r}{r} \right)^2 \ln \left(\frac{R_m}{r} \right) \right] \sin \theta \quad (2.57)$$

where

$$M_n = M_m + npM_{\theta n} \quad (2.58)$$

$$\text{and } M_m = \begin{cases} 2 \frac{B_{res}}{\mu_0} \alpha_p \frac{\sin \frac{n\pi\alpha p}{2}}{\frac{n\pi\alpha p}{2}} & \text{for radial magnetization} \\ \frac{B_{res}}{\mu_0} \alpha_p (a_n + b_n) & \text{for parallel magnetization} \end{cases} \quad (2.59)$$

$$M_{\theta n} = \begin{cases} 0 & \text{for radial magnetization} \\ \frac{B_{res}}{\mu_0} \alpha_p (a_n - b_n) & \text{for parallel magnetization} \end{cases} \quad (2.60)$$

$$a_n = \frac{\sin \left[(np+1) \alpha_p \frac{\pi}{2p} \right]}{(np+1) \alpha_p \frac{\pi}{2p}} \quad (2.61)$$

$$b_n = \begin{cases} 1 & \text{for } n = 1 \\ \frac{\sin \left[(np-1) \alpha_p \frac{\pi}{2p} \right]}{(np-1) \alpha_p \frac{\pi}{2p}} & \text{for } np \neq 1 \end{cases} \quad (2.62)$$

for internal rotor:

$$\left. \begin{aligned} R_m &= R_s - g \\ R_r &= R_s - g - h_m \end{aligned} \right\} \quad (2.63)$$

for external rotor

$$\left. \begin{aligned} R_m &= R_s + g \\ R_r &= R_s + g + h_m \end{aligned} \right\} \quad (2.64)$$

where g is a constant, n is the harmonic number and r, θ are the cylindrical coordinates.

2.3.4. Electric Parameters

2.3.4.1. Overview

The main electrical components properties to be chiefly considered in design stage of a BPM synchronous servomotor with a radial flux are stator winding resistances, inductances, the external voltage, induced voltage or back EMF, and current loading as represented in Fig. 2.9 (Hanselman, 2003).

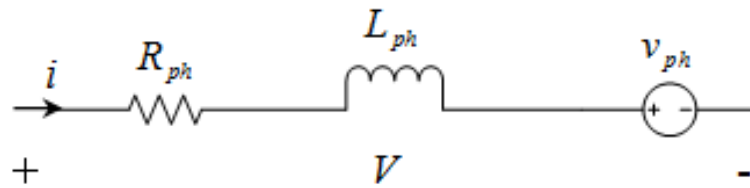


Fig. 2.9. Electric circuit model for one phase winding.

In this research work only the AC synchronous motor drive is considered, and these motors are normally controlled with the use of sinusoidal current using popular pulse width modulation (PWM) techniques with inverter drives.

2.3.4.2. The AC Line Voltage

A simplified form of the overall system drive that starts a BPM synchronous servomotor is shown in Fig. 2.10.

For this investigation all the servomotors operation is controlled using pulse width modulation (PWM) techniques. Power electronic devices (normally 6-transistor inverter) are essentially used to start the servomotor and also define the current, the direction of rotation and the speed. The 3-phases with fixed frequency from the mains are converted to DC fixed voltage across filter

capacitor of $V_d = 300\text{ V}$ by combining diode rectifier circuit with filter capacitor.

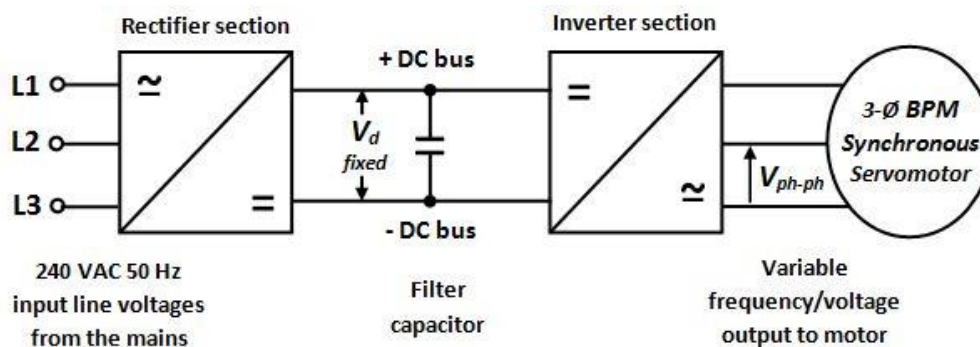


Fig. 2.10. Simplified drive system configuration for brushless servomotor.

Then the positive and negative DC bus voltages can be obtained as +DC bus voltage as 300 volts and as –DC bus voltage as -300 volts. Switching techniques are used in the inverter circuit to obtain the output voltages at different frequencies from the fixed DC line. According to (Miller, 2013) the inverter should be able to produce an AC voltage waveform with the fundamental RMS line voltage around $0.9 \times \sqrt{6} / \pi$ times the DC source voltage, and therefore $0.9 \times \sqrt{6} / \pi \times 300 = 210.5\text{ V}$. Normally in order to maintain the PWM control of current the 0.9 factor must be achieved. And if it is assumed that the servomotor is operating at 0.85 power-factor, then the classical AC power equation to estimate the servomotor line current can be applied as following

$$P = \sqrt{3} VI \cos \phi \quad (2.65)$$

2.3.4.3. Current Loading

Torque is proportional to current, the electric current component of Fig. 2.9 is the current supplied to the servomotor by the inverter section of Fig. 2.10.

The inverter is essentially an electronic control circuit that regulates current into the servomotor in order to maximise the torque. There are different types of current-regulators for these AC servomotors, mainly controlling the quality of current waveform and provide the needed voltage to the three-phases. The more popular controllers are space-vector controller and direct torque control

(DTC). However, inclusion of the theory of these sophisticated control strategies would deviate primary focus of this thesis, which is the BPM synchronous servomotor design, performance characteristic and manufacturing.

The function of the inverter drive is mainly to provide AC output with different frequency and match the polarity of the current to the polarity of the back EMF in order to obtain maximum possible torque. All the 3-phase servomotors used in this research work have sinusoidal back EMF and one phase of the 3-phase back EMF is shown in Fig. 2.11 for the current design with the 18-6 slot-pole combination. In Fig. 2.11, the back EMF shape is mainly the fundamental component. Almost not much harmonic contends to the back EMF but it is not a perfect sinusoidal voltage.

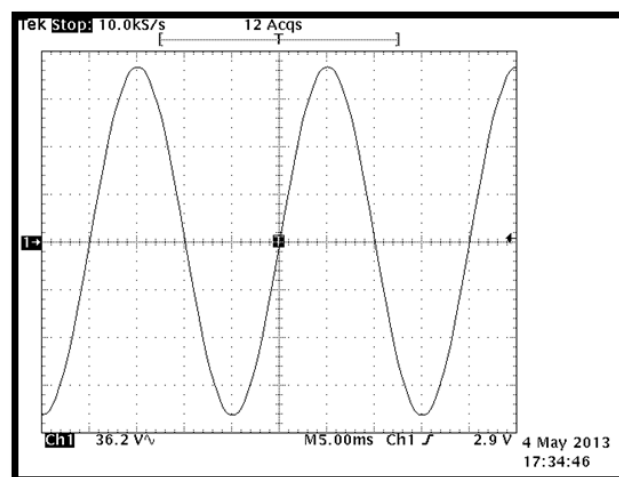


Fig. 2.11. Induced back EMF of one phase of the current distributed 18-6 slot-pole design.

When the voltage V is applied across the circuit shown in Fig. 2.9, the current i flows in the circuit. This flow creates copper losses or heat losses in the resistive component R_{ph} and creates a magnetic field that stores energy in the inductance L_{ph} . The same current goes through the back EMF voltage source v_{ph} that absorbs instantaneous power due to product of $v_{ph} \times i$. Because this power does not create heat or magnetic field that stores energy, then this must go somewhere. This power is converted to mechanical power in the shaft $T\omega$ in order to satisfy conservation of energy (Hanselman, 2003).

Therefore the following equation is used for the power of the servomotor

$$v_{ph} \times i = T\omega \quad (2.66)$$

where ω is rotational speed in rad/s.

From equation (2.66) the torque performance of a BPM synchronous servomotor is directly proportional to the current and the back EMF voltage source (v_{ph}) and v_{ph} is directly proportional to the air-gap flux density as previously stated. Therefore the current regulator it is needed together with the PWM inverter as shown in Fig. 2.12 to generate sinusoidal current to matches the back EMF shown in Fig. 2.11.

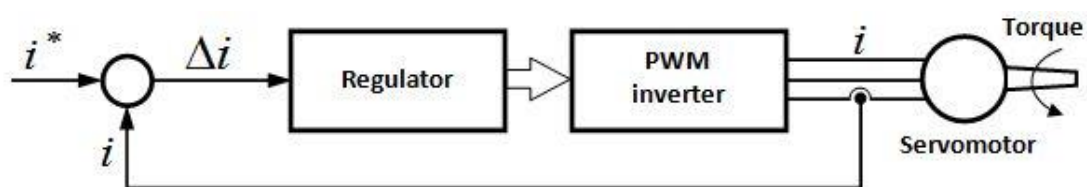


Fig. 2.12. Control block diagram (Hendershot et. al., 2010).

When the number of turns is defined, then the back EMF constant is fixed and therefore the torque becomes essentially dependent on the current matching. Then it can be assumed that the torque waveform is dependent on current waveform. However, independently from the current waveform, the servomotors shown in Fig. 2.12 are designed to produce a smooth shaft torque. All the servomotors in this research work have nearly sinusoidal wave-shape and therefore they all can be considered “sinewave” servomotor types. These servomotors are usually associated with high performance that requires smooth torque, rapid response, and a constant kt or linear relationship between the torque and current.

According to (Hendershot et. al., 2010) the peak value of the current I_{sp} , its fundamental frequency f and its phase angle γ relative to the back EMF defines the sinewave of the current. And if $\gamma > 0$, the back EMF is lacking relatively to the phase current. The shaft position information is required in order to control the current phase angle. In this research work, this position information is obtained by means of electronic encoder connected to the shaft.

The inverter drive used operates fundamentally in switched mode, the transistors are switched on and off in a very fast rate. The switching pulses of the DC bus are timed conveniently for different widths in order to obtain a current waveform in the servomotor that matches the back EMF waveform for maximum torque performance. Fig. 2.12 shows a basic model of a closed-loop current-regulator, and the model is enough to show how the inverter applies PWM voltage waveform to the servomotor. Provided the DC bus voltage is relatively greater than the back EMF voltage and the servomotor impedance allows for the demanded current. In Fig. 2.12 the current sensing reads the input current i to the servomotor phases and feedback to a comparator that generates a current error Δi corresponding to the difference between the demanded current i^* and the actual current i . Then according to (Hendershot et. al., 2010), the combination of the regulator and the PWM inverter in Fig. 2.12 operates as a high-gain amplifier in order to force the current error value to zero. And where the reference current is given by the following equation

$$i^* = I_{sp} \sin \omega t \quad (2.67)$$

The inverter drive system used in this research work is shown in Fig. 2.12, this device contents a closed-loop current-regulated pulse width modulated (PWM) inverter capable of supplying current waveform shape close to the sinusoidal waveform shown in Fig. 2.13.

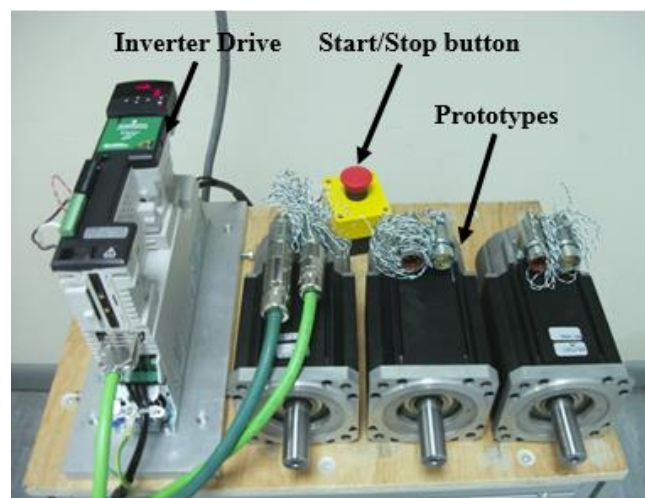


Fig. 2.13. Inverter drive and prototyped brushless servomotors.

2.3.4.4. Stator Winding Resistance

The power of the servomotor is limited mainly by the ability of the conductors in the windings to carry certain amount of current without overheating.

Assuming that there is series connection between all coils in one phase then the phase resistance is calculated as

$$R_{ph} = \rho_{cu} \frac{(pL + (D + h_{ss})\pi k_{coil})n_s^2 q}{f_s A_{sl}} \quad (2.68)$$

where f_s is the slot fill factor, n_s is the number of conductors per slot, A_{sl} slot area, q is number of slots per pole per phase, p is number of poles, ρ_{cu} copper resistivity and the $D\pi k_{coil}$ is introduced as term to take into account the end-winding or overhang (Libert, 2004a).

Three winding configurations are shown in Fig. 2.14, the winding configuration for a BPM synchronous servomotor can be of the different types.

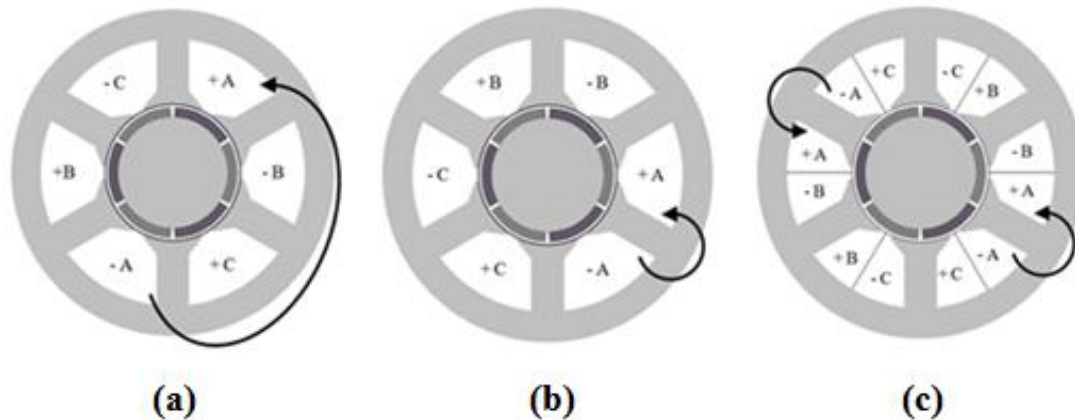


Fig. 2.14. Popular winding configurations for brushless servomotor.

The three types shown on the figure are the most popular. The configuration shown in (a) is a distributed type of winding with the single-layer. The configurations of (b) is also a single-layer with the concentrated winding type and more popular where safety is a concern. The configuration (c) is a double layer of the concentrated winding type and it is the most popular when looking for high torque density and good thermal performance.

Up to now, the most popular winding configuration is the distributed winding type, for this case the winding of each phase overlap as shown in Fig. 2.14(a). The major problems associated with this winding configuration in terms of manufacturing are the material waste and relatively low slot-fill factor.

The material is wasted mainly due to significant length of the overhang that not contributes to torque, and consequently requires a longer housing. The faster manufacturing process of this configuration is normally associated with poor slot-fill as described in the following sections.

From manufacturing and thermal standing point configuration (c) is more attractive and this is the configuration selected for new designs instead of current design configuration (a). All the characteristics of the new designs are presented in later sections.

2.3.4.5. Inductances

The surface mounted permanent magnet (SMPM) as shown Fig. 2.13 has the magnets almost covering all the peripheral area of the rotor core, and the space between the magnet poles has no material.

Because the reluctance of a permanent magnet is close to that of the air, therefore the reluctance to the flux can be taken as been equal all around the components associated to the air gap.

This means that there is no reluctance component to the torque, this is a non-salient type permanent magnet machine and therefore the inductances can be assumed to be equal around the air gap region as

$$L_d / L_q = 1 \quad (2.69)$$

where L_d is d-axis winding inductance and L_q is q-axis winding inductance. According to (Libert, 2004a)

$$L_d = L_q = L_l + L_{md} = L_l + L_{mq} \quad (2.70)$$

where L_l is leakage inductance and, L_{md} and L_{mq} represent the d- and q- axis magnetizing inductances. And they can be represented for the rated speed as

$$L_l = p q n_s^2 L \mu_0 \lambda_1 \quad (2.71)$$

$$L_{md} = \frac{3}{\pi} (q n_s k_{w1})^2 \frac{\mu_0}{gk_C + \frac{l_m}{\mu_r}} (D - g)L \quad (2.72)$$

where q is the number of slots per pole per phase, λ_1 is the specific permeance coefficient of the slot opening and it depends on the slot geometry and k_{w1} is the fundamental winding factor. In this case when $q=1$ then $k_{w1}=1$ and this is discussed in more details on the next subsection of slot-pole combinations.

For the case of salient PM machines the inductances that have the contributions of both d- and q- axis inductances, therefore the equation for the d-axis in this case can be the same as for the SMPM motor type. The calculation for the q-axis magnetizing inductance is calculated using the following equation

$$L_{mq} = \frac{3}{\pi} (q n_s k_{w1})^2 \frac{\mu_0}{gk_C} (D - g)L \quad (2.73)$$

2.3.4.6. Back E.M.F.

When winding current is zero or at open-circuit condition, the flux linkage due to the permanent magnets in the rotor induces voltage across the stator windings whenever the flux linkage varies with time. Induced back electromotive force EMF voltage v_{ph} in the BPM synchronous servomotor windings is given by Faraday's law, which states the following

$$v_{ph} = \frac{\partial \psi}{\partial t} = \frac{\partial \psi}{\partial \theta} \cdot \frac{d\theta}{dt} = \omega \frac{\partial \psi}{\partial \theta} \quad [\text{V}] \quad (2.74)$$

where ψ is magnet flux linkage of the winding, θ is the rotor position and $\omega = 2\pi f$ is the radian frequency. In order input current to the winding, this

induced voltage cannot be greater than V_d . EMF waveform is critical in defining the BPM synchronous servomotor operation in terms of drive current control and the torque ripple (Hendershot et. al., 2010). Phase back EMF for the current design 18-6 slot-pole servomotor is shown in Fig. 2.14.

2.4. Slot-Pole Combination

The decision of number of permanent magnet poles to use is primarily done because the speed of servomotor defined by the fundamental supply frequency f as:

$$\eta_{rpm} = \frac{60 \times f}{p} \quad (2.75)$$

where p is the number of pole-pair. For the current servomotor with six poles and with the speed of 3000 rotations per minute (η_{rpm}), it would be needed a frequency of 150 Hz, which is three times higher than mains frequency of 50 Hz shown in Fig. 2.10. The inverter drive used in this research work is shown in Fig. 2.12 and has a maximum switching frequency of 12 KHz and can generate output frequencies well beyond of 150 Hz. Then there is no problem of rotor pole number to the speed frequency limit. The main reason for speed limit is due to the limited DC line voltage for the back EMF.

Due to constrain imposed by the frame size of current distributed winding design. Therefore the split-ratio for this servomotor is used for the new segmented concentrated winding design configurations selected for analysis.

Extensive work on performance characteristics of different slot-pole combinations for inner-rotor radial-flux BPM synchronous servomotors with concentrated windings can be found on research performed by (Libert et al., 2004b) (Cistelecan et al., 2007). Different winding layouts and winding factors are presented for the concentrated winding machines with the slot number varying from 6 to 90 and the pole number varying from 4 to 80. Therefore due to frame size constraint value imposed by the value 115 mm shown in TABLE 2.1, it is obvious that high slot number or pole number would not be practical. Significantly high number of slots would force to a very small stator tooth width

which in turn suffers significant degradation when punched and causes increased magnetic saturation and consequently performance drop.

Another problem with the high slot number is the increase of the number of segmented teeth to be wound and consequently slowing down the manufacturing process. High number of poles for the current bore diameter shown in TABLE 2.1 would force significant small magnet poles. From the manufacturing standing point, a small magnet is difficult to handle and also increase of number of magnet poles to be fitted on rotor makes manufacturing process slower. All new design servomotors in this research work are 3-phase motors. The placement of the conductors of each phase in the slots for the new balanced concentrated winding machines is determinate according to the method proposed by (Cros et al., 2002). Relatively complex method for winding factor k_w calculations is presented by (Libert et al., 2004b), where k_w is the number of slots per pole per phase. TABLE 2.2 presents different slot-pole combinations up to 30-18 slot-pole combinations and their respective winding factors.

TABLE 2.2. Winding factors for different slot-pole pair combinations.

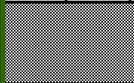
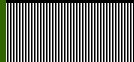
$Q_s \setminus 2p$	4	6	8	10	12	14	16	18
6	0.866		0.866	0.500		0.500	0.866	
9	0.617	0.866			0.866	0.617	0.328	
12	1		0.866				0.866	
15			0.621	0.866				
18		1	...	0.647	0.866			
21				0.866	0.890	
24			1	...		0.760	0.866	
27				0.866
30				1		

0.866	$k_w = 0.866, q = 1/2, 1/4$		$k_w = 0.945, q = 3/8, 3/10$
	$k_w = 0.902, q = 3/7, 3/11$		$k_w = 0.951, q = 5/14, 5/16$
	$k_w = 0.933, q = 2/5, 2/7$	not allowed	... $k_w < 0.866$

The electromagnetic torque of a BPM synchronous servomotor is proportional to the generated winding factor. Therefore the higher winding factors slot-pole combinations are selected from TABLE 2.2 in order to achieve reduced input current to the servomotor at reduced number of turns and increased torque.

Three high k_w slot-pole combinations of 12-10, 12-14 and 18-16 are selected for design simulations using FEA and thermal model for performance torque evaluation. TABLE 2.3 shows the number of slot per pole per phase q and the winding pattern for the selected slot-pole combinations.

TABLE 2.3. Winding layout for the selected slot-pole pair combinations.

Slot-pole combination or number of slot per pole per phase q	Winding layout
 $q = 2/5, 2/7$... C'A A'A' AB' BB B'C C'C CA' AA A'B B'B' BC CC...
 $q = 3/8$... C'A A'A' AA A'B B'B' BB B'C C'C CC...

The winding layouts are defined as shown in TABLE 2.3 and method presented by (Cros et al., 2002) for the calculation of q is as follows:

$$q = \frac{Q_s}{2p \times m} \quad (2.76)$$

where Q_s is the number of slots, p is the number of pairs of poles and m is the number of phase. The conventional servomotor has a through of 3 teeth that causes a relatively long winding overhang as shown in Fig. 2.15. Fig. 2.16, 2.17 and 2.18 in contrast show the segmented servomotors that allow a much shorter overhang.

In the winding layout of TABLE 2.3, as example for all other phases, A' represents the return conductor corresponding to go conductor A .

The $q = 2/5$ and $q = 2/7$ have similar winding layout and the unique winding difference been the shifting between phase B and the phase C, and this can be observed in the Fig 2.16 and Fig. 2.17.

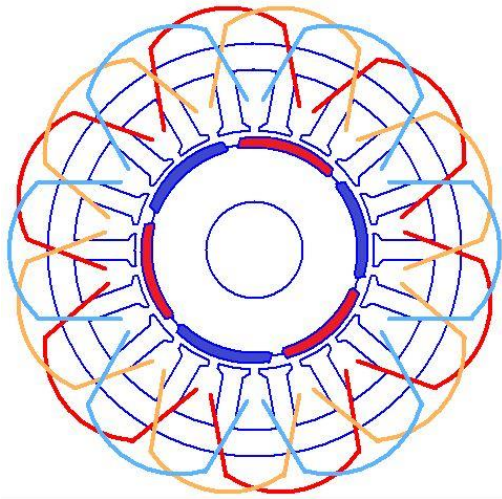


Fig. 2.15. 18-6 slot-pole winding layout.

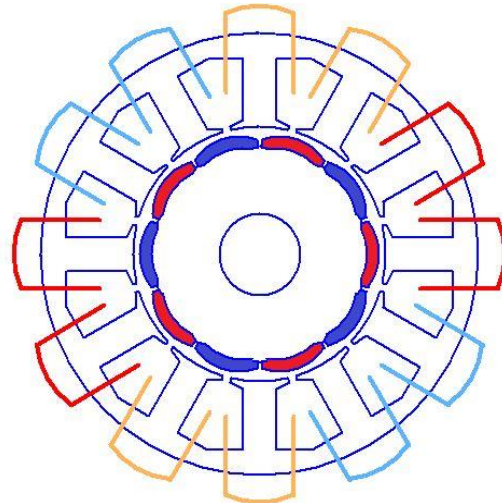


Fig. 2.16. 12-10 slot-pole winding layout.

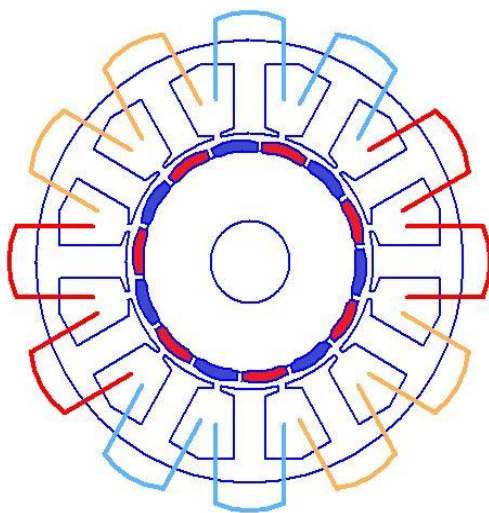


Fig. 2.17. 12-14 slot-pole winding layout.

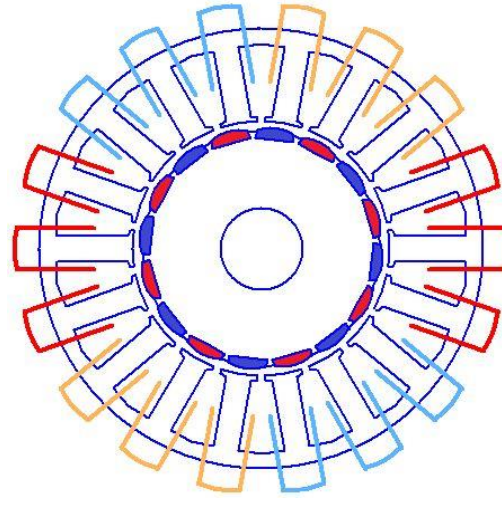


Fig. 2.18. 18-16 slot-pole winding layout.

2.5. Torque Performance Analysis

2.5.1. Overview

The performance indicators for the new segmented stator designs with concentrated windings and the current design with distributed windings are graphically plotted and the results are compared in the following sections using FEA and thermal modelling tools. In this section the servomotors are compared in terms of their cogging torque, torque constant, torque ripple, torque performance.

It has been proven that the selected slot-pole combinations allow for good torque density on medium speed medium size servomotors (Zhu, 2009) (El-Refaie, 2013). The standard 18-6 servomotor will be used to compare its performance with the performance of the new design configurations. Due to the imposed boundary of frame size of 115 mm of current design with distributed winding, then split-ratio is kept equal for the new servomotors. At no load condition design parameters affecting cogging torque are analysed for optimal value.

Then best current angle is obtained for the analysis of performance characteristics of each new segmented stator concentrated winding design presented. Torque constant k_t characteristics are compared between the designs. Torque ripple for design is analysed for each design and compared. And finally torque performance levels are compared between the servomotor designs.

2.5.2. Cogging Torque

Cogging torque is due to desire of the permanent magnets on the rotor to align at minimum opposition to magnetic flux or reluctance. From Fig. 2.3 the stator ferromagnetic surrounding around the air gap forms a variable magnetic resistance because of the cycled ferromagnetic poles carrying the windings that have air gaps between them. If these air gaps did not exist as shown in Fig. 2.4 the cogging torque would be zero. This means that it would have a uniform air gap between the bar magnet rotor and the ferromagnetic stator (stator yoke or back iron) and any position could be taken as an *unstable equilibrium* position. This means that the cogging torque is purely the interaction between the bar magnet rotor and the ferromagnetic stator as shown in Fig. 2.6 and it does not need any current to the winding of the servomotor.

Cogging torque is one of the main contributors to the torque ripple in the BPM synchronous servomotor and for servo application this is normally not desirable.

According to (Dosiek et al. 2007) cogging torque can be cancelled by making the air-gap reluctance to be constant with respect to the rotor position. But according to (Hanselman, 1994), in practice the cogging torque can be greatly reduced but it cannot be eliminated. This can be achieved mainly by optimal pole arc or magnet/stator tooth shifting or by parameters optimisation.

Mathematical solution for exact cogging torque quantification is based on the rotor position and the material properties of the servomotor components. This relationship is written as:

$$T_{cogg} = -\frac{1}{2} \Phi^2 \frac{dR}{d\theta} \quad (2.77)$$

where

T_{cogg} [Nm]	cogging torque.
Φ [Wb]	magnet flux crossing the air gap.
R [A/Wb]	total reluctance through which the flux passes.
θ [rad]	rotor angular position.

The fundamental form equation (2.77) shown that cogging torque is a function of air-gap flux density, air-gap reluctance and the rotor position. Therefore the use of an increased air-gap length would help to reduce the cogging torque.

The problem of this design solution is that the torque produced by the servomotor would drop considerably if the same current is applied to the windings. Also (Moravec, 2008) (Keyhani, 1999) highlighted that the only reason that the equation (2.77) cannot be often applied because most of the time the knowledge of the material property that causes reluctance R is unavailable due to manufacturing secret and therefore effectively the best way is to measure the cogging torque from the prototype.

Cogging torque is an undesirable component and theoretically it can be eliminated via machine design, from equation (2.77), if the air-gap flux (Φ) or rate of change of the air gap reluctance ($dR/d\theta$) is forced to zero the cogging torque will be zero. The air-gap flux cannot be zero since the gap is needed

for the windings and also without it the machine would not be able to rotate when current is applied to its windings.

A special relation can be observed between the number of pair-poles p and number of stator slots Q_s . Their least common multiple ($LCM = N_c$) will be equal to the number of cogging cycles per complete rotation or full mechanical revolution.

And this LCM is defined by (Salminen, 2004) for concentrated winding fractional slot machines in the range of the servomotors investigated in this research work and results are shown in TABLE 2.4.

TABLE 2.4. The least common multiplier N_c (for Q_s and N_p) values for concentrated wound fractional slot machines

$Q_s \setminus 2p$	2	4	6	8	10	12	14	16	20	22	24	26
3	6	12	6	24	30	12	42	48	60	66	78	84
6		12	18	24	30	36	42	48	60	72	78	84
9			18	72	90	36	126	144	180	198	234	252
12				48	60	72	84	48	60	132	156	168
15					30	60	210	240	60	330	390	420
18						36	126	144	180	198	234	252
21							42	336	420	462	546	84
24								96	120	264	312	168

This reinforces the idea that cogging torque is the interaction between the magnet (the source of flux that passes through the air gap) and the stator teeth (the source of the varying air-gap reluctance), and also this interaction is periodic therefore cogging torque can be represented in general form as a Fourier series

$$T_{cogg} = \sum_{i=1,2,3,\dots}^{\infty} T_i \sin(iN_c\theta) \quad (2.78)$$

(Zhu et al., 2000) used the fundamental equation (2.78) with an introduction of a skew factor and the equation became

$$T_{cogg} = \sum_{i=1,2,3,\dots}^{\infty} K_{sk} T_i \sin(iN_c \theta) \quad (2.79)$$

where

$$K_{sk} = \frac{\sin(iN_c \pi \alpha_{sk} / Q_s)}{iN_c \pi \alpha_{sk} / Q_s} \quad (2.80)$$

and

- i an integer
- K_{sk} skew factor
- Q_s slot number
- N_c least common multiple
- α_{sk} ratio of the total circumferential skew to the slot pitch

Observe Table 2.4, both researchers (Dosiek et al. 2007) and (Zhu et al., 2000) mentioned the fact that generally cogging torque (T_{cogg}) amplitude is lower when the least common multiple (N_c) is large and the number of servomotor stator slots (Q_s) or number of rotor pair-poles (p) is small.

Therefore in order to help on the selection of Q_s and N_p for certain cogging at design stage for both overlapping and non-overlapping, they introduced a new factor C_T named “goodness” of slot and pole number combination as following

$$C_T = \frac{2pQ_s}{N_c} \quad (2.81)$$

They also highlighted that there is no formal basis for relating C_T to the amplitude of cogging torque but it was found that this factor is proportional to the cogging torque peak value.

Therefore this investigation is on the influence of BPM synchronous servomotor dimensional parameters on cogging torque.

The complete cogging torque cycle for the current conventional distributed winding with 18-6 slot-pole design is shown in Fig. 2.19.

This FEA result is obtained for comparison with the cogging torque of new concentrated winding configuration designs.

The selected slot-pole combination designs of new servomotors are of 12-10, 12-14 and 18-16 combinations.

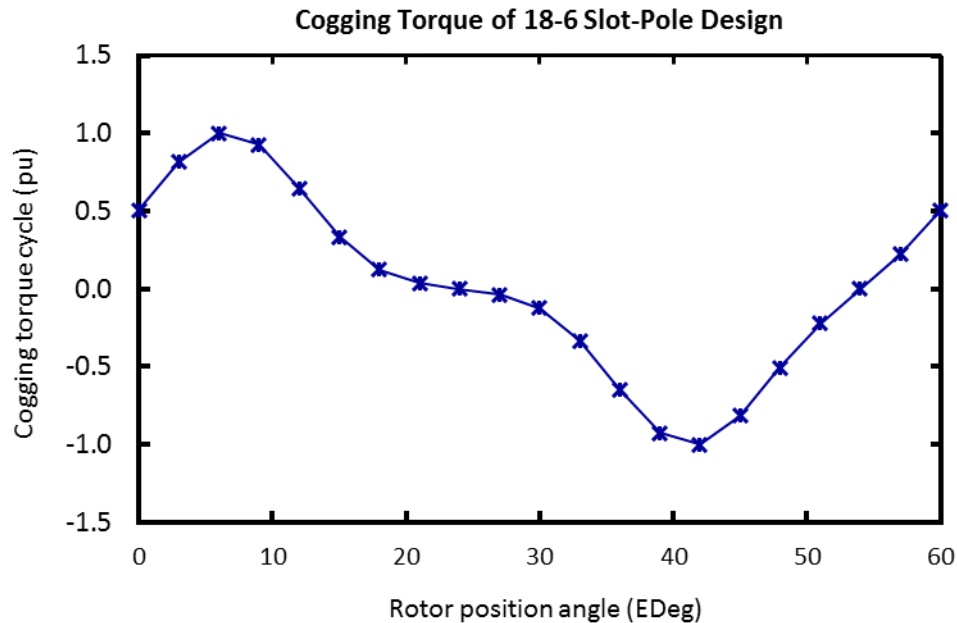


Fig. 2.19. Cogging torque cycle for the current conventional with 18-16 slot-pole design.

Full cogging torque cycle for the current conventional design is obtained after 60 electrical degrees rotor angle as shown in Fig. 2.19. The full cogging torque electrical cycle for any slot-pole combination is calculated as $(360 / LCM) \times p$.

Based on sensitivity analysis of current 18-6 slot-pole design FEA model it was found that cogging torque is mainly sensitive to magnet width MW, slot opening angle SOAng, slot opening SO and tooth gap depth TGD shown in Fig. 2.3. Here BM in Fig. 2.3 is the permanent magnet pole angle corresponded to magnet width MW. FEA design models are developed for the new concentrated winding designs. Then sensitivity analysis is performed using FEA for the new concentrated design models.

The main focus is on the effect of design components such as MW, SOAng, SO and TGD on the cogging torque developed by the new 12-10, 12-14 and 18-16 slot-poles combination FEA design models.

The major task of the investigation is to reduce the peak-to-peak value of the cogging torque component. Or to make it come to the specification and in this case this is less than 1% of the stall torque of the new selected designs where the stall torque is the torque at 0 speeds. The number of rotor poles, stator slots, stator tooth width (TWS) and all other design parameters are fixed and only MW, SOAng, SO and TGD are the changeable parameters.

The computation of the design characteristic is made using Opera 2D FEA Software. The initial parameter values of MW, SOAng, SO and TGD for the all the new servomotor designs are equal to those values of the current conventional distributed winding design and the parameters values are shown in TABLE 2.1.

Therefore it is assumed that a single major cogging torque contributor is from the rotor side which is only the MW and the remaining significant cogging torque contributors (SOAng, SO and TGD) are from the stator side of the servomotor.

2.5.2.1. Sensitivity Analysis of 12-10 Slot-Pole Design

The cogging torque from FEA results as function of MW for the new concentrated windings segmented stator design with 12-10 slot-pole combination are presented in Fig. 2.20 (a) and 2.20 (b).

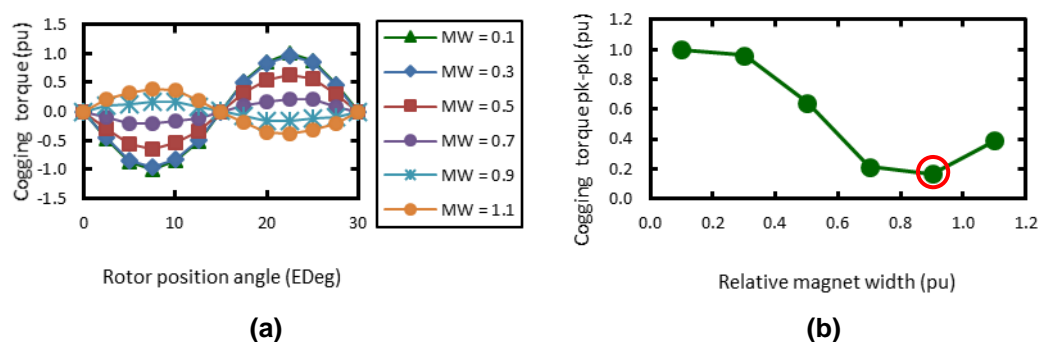


Fig. 2.20. Cogging torque full-cycles (a) and peak-to-peak values (b) as a function of magnet width (MW) of 12-10 slot-pole servomotor design.

With standard gap between the permanent magnets, a maximum MW length that represents 100% is defined in order to accommodate the 10 rotor pole number.

Then the magnet length variation is carried within a minimum magnet length and the 110% of the defined maximum length as shown in Fig. 2.20 (a), and this is called *variable factor*. The cogging torque cycles for different magnet lengths are obtained with their respective magnitude as shown in Fig. 2.20 (b). From the figure it can be observed that the cogging torque is not linear and it is very sensitive to the MW variation. From Fig. 2.20 (b) it can be observed that from the cogging torque standing point, the best design point is around 90% of *variable factor*. Reducing MW increases the cogging torque significantly and increasing MW beyond 100% also increases the cogging. Therefore the relative magnet width of 90% is used for the new design with the 12-10 slot-pole combination.

Significant cogging torque occurs due to the variation of the slot opening angle SOAng as shown in Fig. 2.21 (a) and (b).

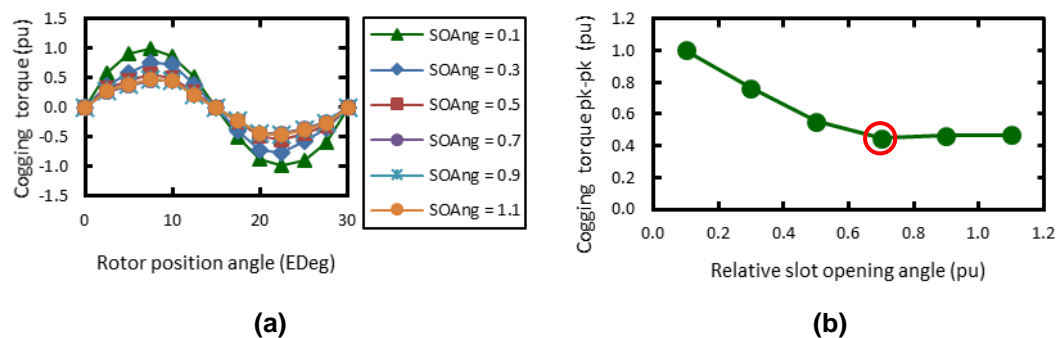


Fig. 2.21. Cogging torque full-cycles (a) and peak-to-peak values (b) as a function of slot opening angle (SOAng) of 12-10 slot-pole servomotor design.

Similar percentages variation range applied to the MW is also applied here to the SOAng for sensitivity analysis. Both figures show that reduced SOAng increase significantly the cogging torque. However Fig. 2.21 (b) shows that increasing SOAng up to around 70% of its *variable factor*, the cogging torque reduces in a linear manner. However the figure shows that continuous increase of SOAng above 70% does not improve cogging torque. And consequence is that the SOAng increase starts affecting the slot fill capacity of the servomotor and consequently the torque performance. Therefore value near 70% of SOAng variable factor is selected for final design modelling of the new 12-10 slot-pole design since further increase does not reduce cogging torque significantly and the slot-fill reduces due to SOAng increase.

Slot opening SO is another design parameter that has great influence on the reluctance variation of the BPM synchronous servomotor magnetic system.

Similarly to the previous sensitivity analysis performed for cogging torque due to the MW and the SOAng, here the cogging torque cycles and the peak-to-peak values as functions of SO relative values are shown in Fig. 2.22 (a) and (b). It can be observed that decreasing SO significantly reduces the cogging torque peak-to-peak value. And increasing the value above 70% of *variable factor* does not bring significant gain or change regarding to the cogging torque amplitude.

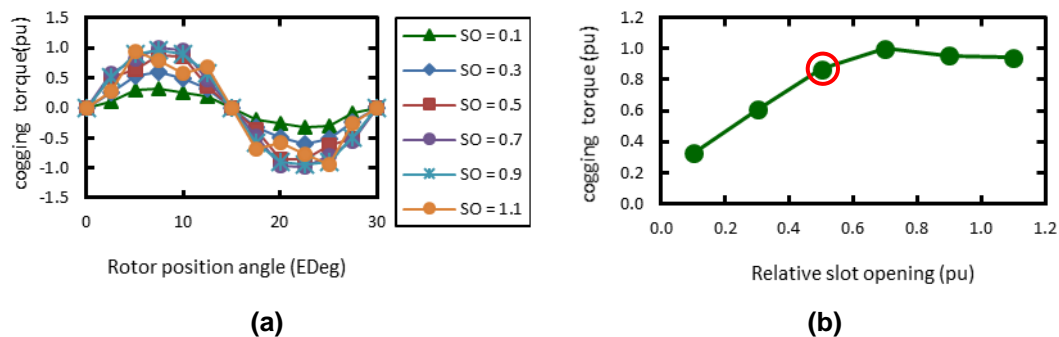


Fig. 2.22. Cogging torque full-cycles (a) and peak-to-peak values (b) as a function of slot opening (SO) of 12-10 slot-pole servomotor design.

Due to the industrial safety standards based on UL Standards (Underwriters Laboratories - global independent safety Science Company) for the frame size used in this research work the SO value cannot go below the size representing 50% of *variable factor*.

However large SO is not very convenient when looking for high density level BPM synchronous servomotor. Large SO is mainly avoided in order to reduce the flux saturation levels on the tips and consequently higher heat to the permanent magnets that affects the servomotor performance. And therefore the selected value for the SO for the new 12-10 slot-pole design is 50% of *variable factor* indicated in Fig. 2.22 (b).

The last design parameter analysed for sensitivity analysis of 12-10 slot-pole is tooth gap depth TGD and the results shown in Fig. 2.23 (a) and (b).

From the figures it can be observed that for the case of 12-10 slot-pole design the cogging torque variation due to TGD is negligible. And since the cogging is not sensitive to any TGD within the *variable factor* then the design point is selected purely based on performance and safety grounds. The method of punching used for the production of laminations causes degradation to the laminations and therefore worsening the magnetic quality of the laminations.

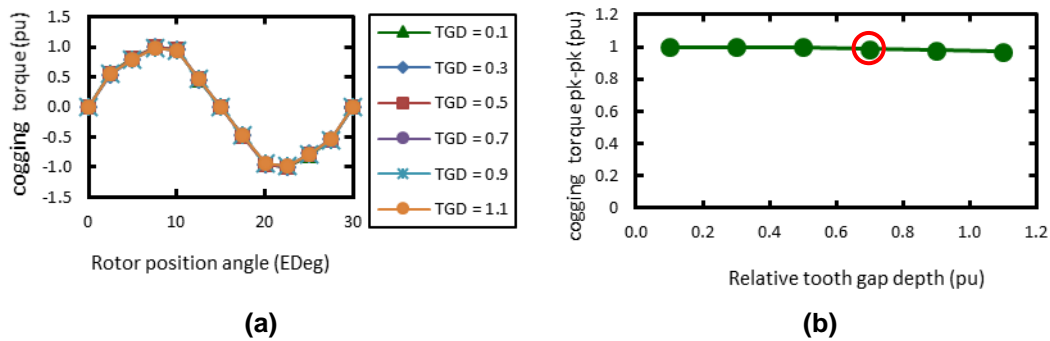


Fig. 2.23. Cogging torque full-cycles (a) and peak-to-peak values (b) as a function of tooth gap depth (TGD) of 12-10 slot-pole servomotor design.

Therefore relatively small TGD would cause significantly high degradation due to the punching effect to the tooth tips and consequently reduce the magnetic performance due to the saturation. From the safety point is not convenient to have relatively small TGD since it can make tips to be very sharp when the lamination stack is formed and this can cause cuts to the operator during the manufacturing. And for this design of 12-10 slot-pole combination the TGD selected value is approximately 70% of value of TGD *variable factor*.

2.5.2.2. Sensitivity Analysis of 12-14 Slot-Pole Design

The second new designed FEA model for sensitivity analysis on cogging torque for MW, SOAng, SO and TGD is performed here. The new servomotor with the 12-14 slot-pole combination is shown in Fig. 2.17.

This alternative concentrated winding design differs to the 12-10 slot-pole design in two aspects, and these are the rotor poles number and winding phase placement. This can be observed from Fig. 2.16 and Fig. 2.17 where the blue phase and orange are changed in terms of their mechanical position and also have different rotor pole number.

The maximum magnet width for 14 pole design that could be incorporated in the current servomotor design bore radius with the standard gap between the magnets is found before performing sensitivity analysis to MW. The cogging torque from FEA results as function of MW for the new concentrated windings segmented stator design with 12-14 slot-pole combination are presented in Fig. 2.24 (a) and 2.24 (b).

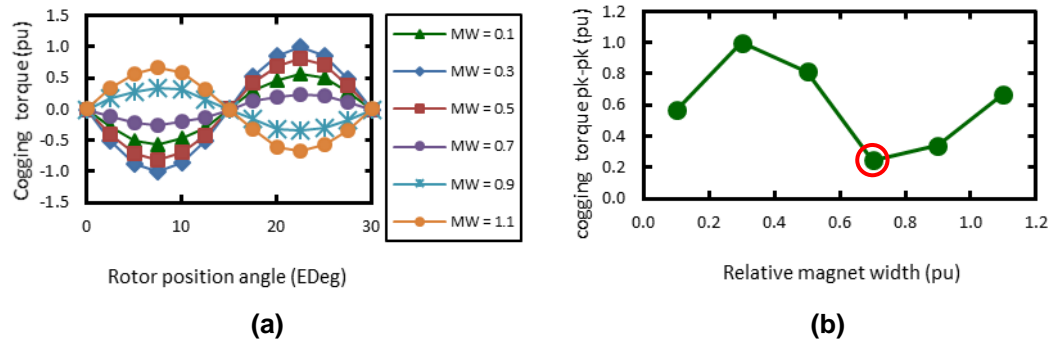


Fig. 2.24. Cogging torque full-cycles (a) and peak-to-peak values (b) as a function of magnet width (MW) of 12-14 slot-pole servomotor design.

In the similar fashion to the MW sensitivity analysis of 12-10 slot-pole design, here also a portion of the permanent magnet width is taken as 100% *variable factor*. Then different percentages of the permanent magnet portion are used to vary the MW and the cogging torque characteristics for these variations are obtained as shown in Fig. 2.24 (a). The peak-to-peak cogging torque characteristics of the 12-14 slot-pole design as function of MW is shown in Fig. 2.24 (b). Increasing the MW from 10% up to 110% of *variable factor*, the peak-to-peak cogging signal takes a sinusoidal shape. The best cogging torque for this particular 12-14 slot-pole design is around 70% increase of the variable factor as indicated in Fig. 2.24 (b). Therefore for this design the cogging torque is selected to be the relative magnet width of 70%.

The influence of slot opening angle SOAng in the cogging torque is clearly shown in Fig. 2.25 (a) for the 12-14 slot-pole design. Cogging torque cycles of several points corresponded to the percentage variable factor SOAng are shown in the figure. The peak-to-peak value for each cogging cycle is presented in Fig. 2.25 (b). It can be observed that the cogging torque is non-

linear, and where increasing slot opening angle up to 50% increase of *variable factor* helps reducing the cogging torque.

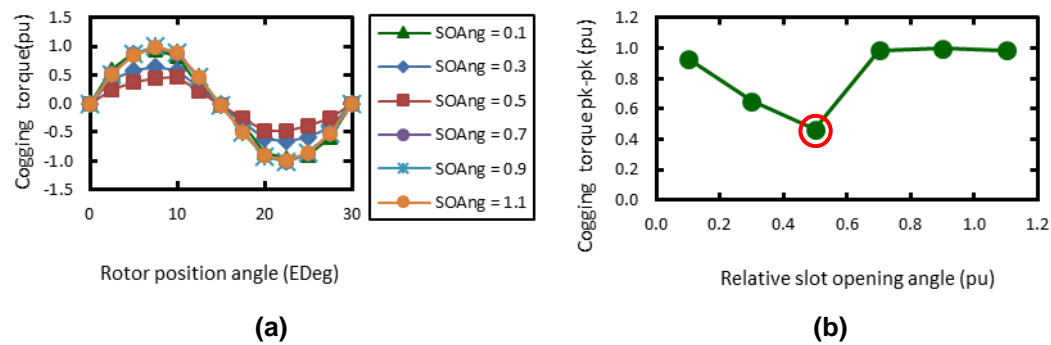


Fig. 2.25. Cogging full-cycles (a) and peak-to-peak values (b) as a function of slot opening angle (SOAng) of 12-14 slot-pole servomotor design.

However increasing SOAng above 50% will cause significant increase of cogging torque. With the significant rise of the cogging torque peak-to-peak value between 50% and 70% increase of *variable factor*. And the cogging torque value was constant from 70% up to 110% of *variable factor* as shown in Fig. 2.25 (b). Therefore 50% of *variable factor* is selected for the SOAng value of the servomotor with the 12-14 slot-pole combination as indicated in Fig. 2.25. Slot opening SO is computed from FEA for the 12-14 slot-pole design in the similar fashion of the analysis performed previously with the 12-10 slot-pole design model.

The results for the cogging torque variation as function of slot opening variations is shown in Fig. 2.26.

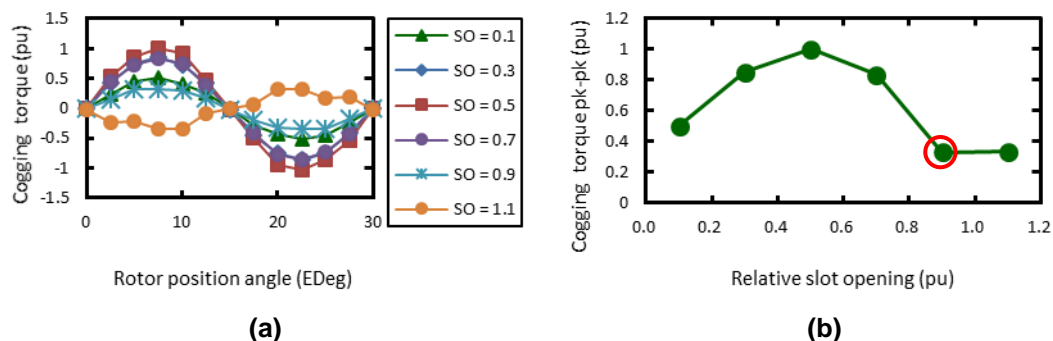


Fig. 2.26. Cogging torque full-cycles (a) and peak-to-peak values (b) as a function of slot-opening (SO) of 12-14 slot-pole servomotor design.

It can be verified a significant cogging torque cycle variation due to the variation of *variable factor* change of the slot-opening. Increasing *variable factor* up to 50% increases the peak-to-peak value of cogging torque. Then any percentage increase above 50% and below 90% causes decreasing towards the minimum value of cogging torque. And further increase of slot opening keeps the cogging torque peak-to-peak value constant. And due to similar UL standards on safety mentioned from the previous 12-10 slot-pole design FEA model, here the slot opening is selected for the value of 90% of *variable factor* of Fig. 2.26.

The minimum UL required value unfortunately represents the maximum cogging torque around 90% of *variable factor*. There is minimum increase of saturation due to the SO increase but the cogging is significantly reduced when compared with 50% of *variable factor*. The influence of tooth gap depth for the 12-14 slot-pole design is very similar to the one of previous FEA design model with 12-10 slot-pole design configuration.

The variation of TGD does not affect much the cogging torque level as shown in Fig. 2.27 (a) and (b). However, it is noticeable a reduction of cogging torque peak-to-peak value with the increase of TGD.

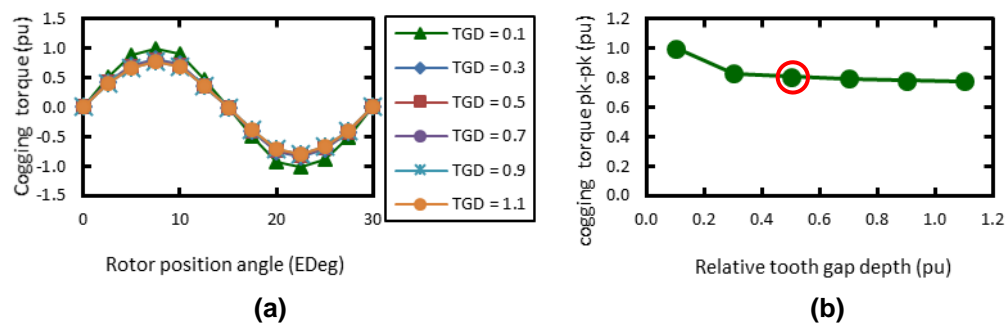


Fig. 2.27. Cogging torque full-cycles (a) and peak-to-peak values (b) as a function of tooth gap depth (TGD) of 12-14 slot-pole servomotor design.

The increase is not very significant but cannot be neglected as the case of the TGD effect of the previous FEA design model. Therefore the selected TGD for this particular design is equal to 50% *variable factor* for the same reason presented for the first FEA design model with 12-10 slot-pole combination. And this selection is due to magnetic saturation and to avoid cuts to the operator during manufacturing, then the TGD cannot be made very small.

2.5.2.3. Sensitivity Analysis of 18-16 Slot-Pole Design

A study is now made to the third new proposed FEA designed model for sensitivity analysis on cogging torque for MW, SOAng, SO and TGD. The analysis is performed to the servomotor of 18-16 slot-pole combination shown in Fig. 2.18. This alternative concentrated winding design differs to the both slot-pole designs proposed previously. This new design has high number of rotor poles and same number of stator poles compared with the current distributed winding 18-6 slot-pole design.

The cogging torque cycle and the respective peak-to-peak values due to the MW for 18-16 slot-pole design are presented in Fig. 2.28 (a) and (b).

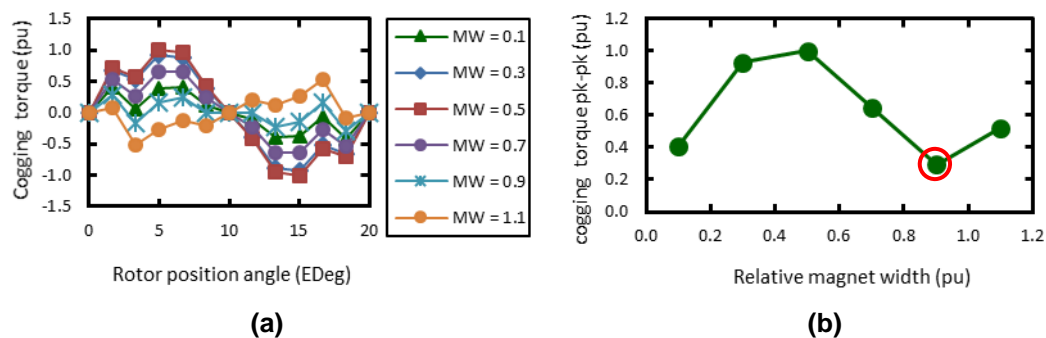


Fig. 2.28. Cogging torque full-cycles (a) and peak-to-peak values (b) as a function of magnet width (MW) of 18-16 slot-pole servomotor design.

It can be observed from Fig. 2.28 (a) that the cogging torque is less sinusoidal when compared with the current distributed design and the new proposed designs with 12-10 and 12-4 slot-pole combinations. This is mainly due to the reduced magnet width used in order to incorporate higher pole number into a fixed bore radius. Both results Fig. 2.28 (a) and (b) show that this new design cogging torque is very sensitive to the MW change and the effect is non-linear. Lowest peak-to-peak cogging torque is around 90% *variable factor*, and therefore this magnet width is selected for the new servomotor.

Slot opening angle variation of 18-16 slot-pole design sensitivity analysis does not show significant variation of cogging torque when compared with previous designs.

This can be observed in Fig. 2.29 (a) for different cogging torque cycles and the also from their peak-to-peak values as shown in Fig. 2.29 (b).

Therefore the determination of the value of SOAng is purely based on avoiding magnetic saturation without compromising slot fill significantly. For this new design the selected value for SOAng is approximately 70% of *variable factor* and this is shown in Fig. 2.29 (b).

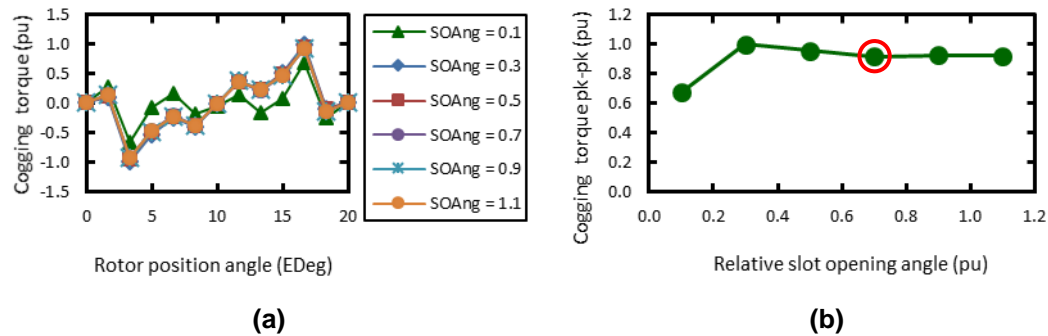


Fig. 2.29. Cogging torque full-cycles (a) and peak-to-peak values (b) as a function of slot opening angle (SOAng) of 18-16 slot-pole servomotor design.

The lowest cogging torque value from the figure is for the 10% of *variable factor*, however this would cause increased saturation and manufacturing issues. Therefore higher *variable factor* is selected without much slot-fill area been taken. The determination of slot opening SO of the design incorporating 18-16 slot-pole combination is similar to the previous two concentrated winding design variations. The UL minimum SO required must be taken into account.

The cogging torque cycles and their respective peak-to-peak values for different percentages of *variable factor* of 18-16 slot-pole design are presented in Fig. 2.30. The cycles of cogging torque shown in Fig. 2.30 (a) are very instable. The resulting peak-to-peak values of cogging torque are shown in Fig. 2.30 (b).

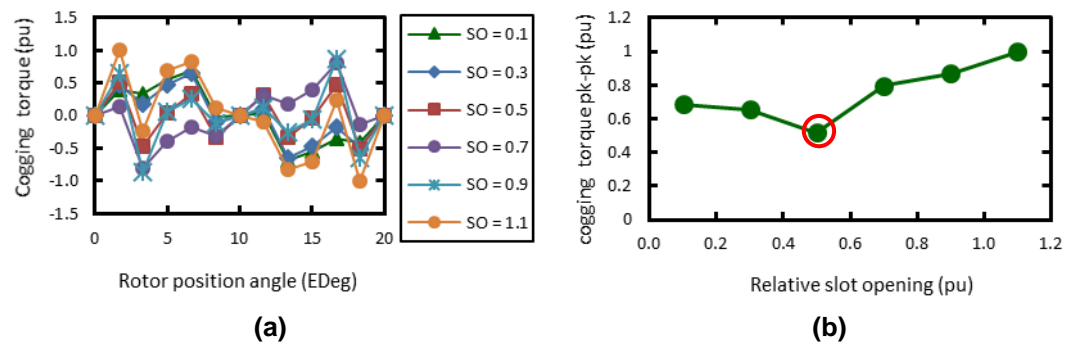


Fig. 2.30. Cogging torque full-cycles (a) and peak-to-peak values (b) as a function of slot opening (SO) of 18-16 slot-pole servomotor design.

The second figure indicates that increasing the percentage of variable factor up to 50% helps to reduce peak-to-peak cogging torque. Any further increase will consequently increase the cogging torque peak-to-peak value. Therefore the lowest peak-to-peak value is selected for this final design variation with 18-16 slot-pole design. This value is 50% *variable factor* and it is correspondent to the minimum required UL slot opening due to the safety reasons.

The tooth gap depth changing effect on cogging torque cycle is almost negligible as shown in the FEA results of Fig. 2.31 (a). Therefore similarly to the previous design, the determination of TGD is based only on performance and operator safety.

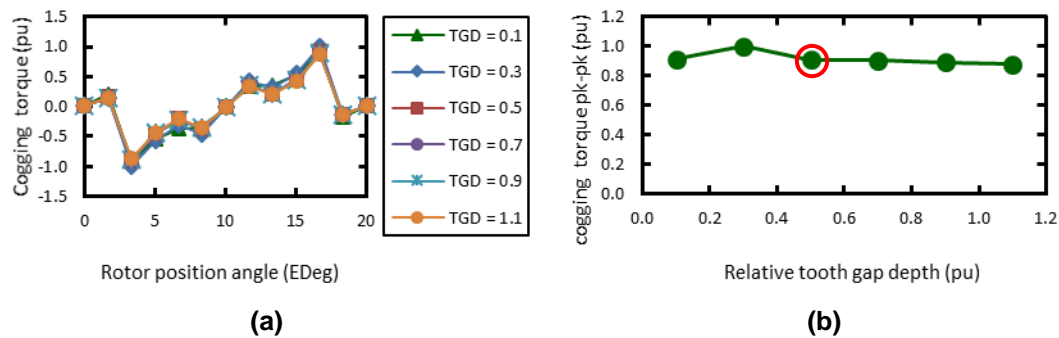


Fig. 2.31. Cogging torque full-cycles (a) and peak-to-peak values (b) as a function of tooth gap depth (TGD) of 18-16 slot-pole servomotor design.

Performance issues can be rise due to magnet saturation and the safety side is that the stator tooth tip can became very sharp with the small TGD, risking cutting the operator when assembling the stator. Therefore, the selected TGD for the 18-16 slot-pole design new variation is around 50% of *variable factor* as shown in Fig. 2.31. Further increase of TGD will not bring significant reduction of cogging torque as it is shown in Fig. 2.31 (b). In the other hand this increase of TGD would reduce the slot area and therefore reduce slot fill capacity of the 18-16 slot-pole design.

2.5.3. Torque Constant

By using the current set of voltage driven computations for the current conventional servomotor with 18-6 slot-pole combination, it is possible to use

FEA to obtain the optimal torque constant (k_t) and the k_t characteristics for each of the new concentrated winding designs.

The k_t is one of the more useful performance indicators of a servomotor. The values for k_t are given as follows:

$$k_t = \frac{T}{i} \quad (2.82)$$

where T is the torque in Nm and i is equals to input current to the servomotor in A.

Larger torque constant means that more torque can be obtained from the servomotor for the same amount of input current.

However in order to calculate k_t it is important to find the current/load angle first for each design.

The split ratio for the new designs is defined to be equals to the split ratio of current design.

The slot-fill percentage of new designs must be within 52% to 55% and number of turns (TC) of each design must be fixed to the value of k_e (V/krpm) obtained from SPEED software. This TC is the maximum turns for defined back EMF at speed of 1000 rpm.

Therefore the k_t of the servomotor becomes dependent mainly on the stator tooth width (TWS) and the back iron thickness (BIT) saturation. The winding detail for SPEED software model for the 12-10 slot-pole design is shown in Fig. 2.32 and Fig. 2.33 as examples.

Therefore after finding the best current/load angle for each new designs, the sensitivity analysis is performed for TWS and BIT for the optimal k_t .

Template Editor							
Windings							
Connex	Wye	Throw	1	Offset	8	TC	124
WdgType	Custom	PPATHS	2	PCWire	0.0000	TCCWire	0.3930
NSH	1	NSH2	1	NSHA	1	WireDens	8890.0000
WireSpec	BareDia	Wire	0.7500	wb	2.0000	InsThick	0.0332
WireSpec2	None	Wire2	2.0000	wb2	2.0000	InsThk2	0.0000
WireSpecA	None	WireA	2.0000	wbA	2.0000	InsThkA	0.0000
WireCR	0.0000	WireCR2	0.0000	WireCRA	0.0000		
Ext	0.0000	XET	1.4000	EndFill	0.5000	CoilFill	1.0000
X_R	1.0000	Rext	0.0000				

Fig. 2.32. The winding details of SPEED Software template.

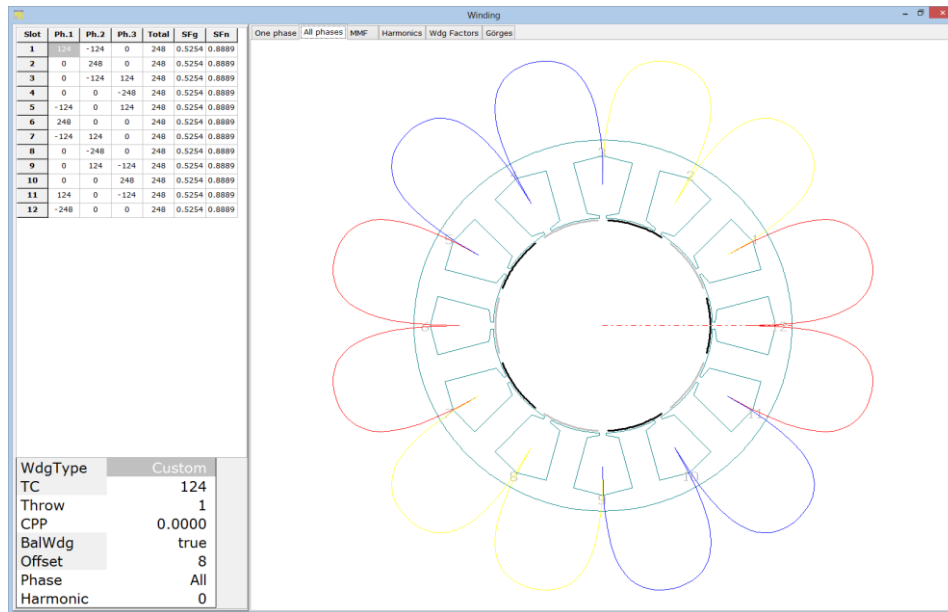


Fig. 2.33. Winding details and winding layout for 12-10 slot-pole design brushless servomotor

2.5.4. Current Angle

In the Fig. 2.34, the torque curve characteristics are presented for the proposed new servomotors incorporating 12-10, 12-14 and 18-16 slot-pole combinations. The FEA is performed using voltage drive model, where torque levels are calculated from 0 degree to 180 degrees load/current angle.

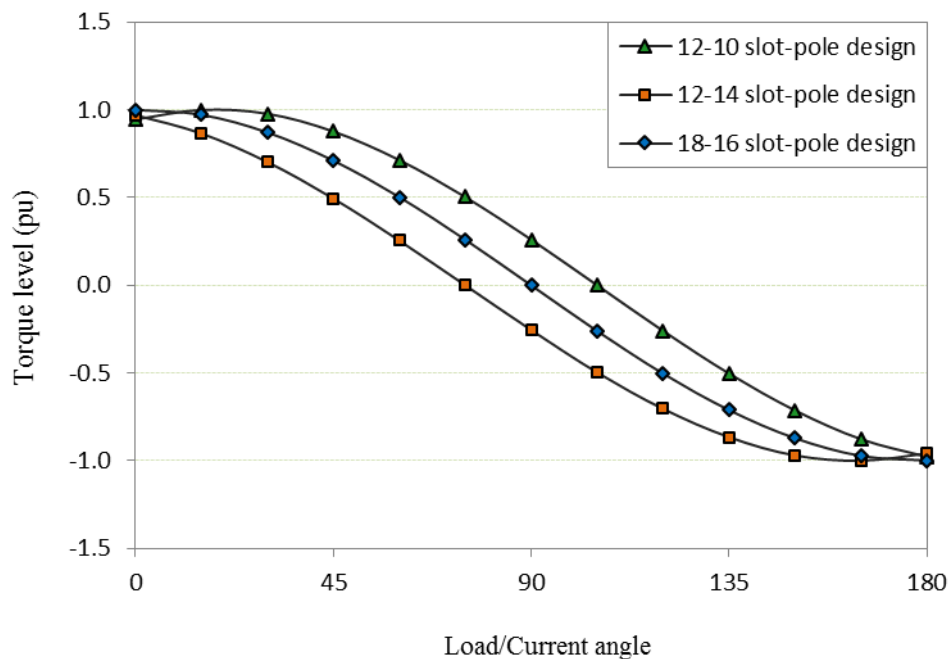


Fig. 2.34. Torque curves characteristics as function of load/current angle for the new three surface magnets with segmented stator and concentrated winding design investigated.

The values given for the stator tooth width (TWS) and for the back iron thickness (BIT) are not the optimal values of these servomotor design parameters.

Their optimal values are not very important at this design stage since the current values are kept constant for the all range current angles from 0 to 180 degrees of each design. Therefore this means that the best current angle does not change when TWS or BIT are changed. These two design parameters tend to vary significantly the k_t of the servomotor. But by rule of thumb, sensitivity analysis can be performed to obtain optimal TWS and make BIT 56% of the TWS. It can be observed from Fig. 2.34 that the best load/current angle for the 12-10 slot-pole servomotor design is approximately 15 degrees, and however if the current angle is 105 degrees then this would reduce the torque level to approximately zero. For the 12-14 slot-pole servomotor design, the best firing angle is equal to 165 degrees and the resulting torque is negative.

In reality, using this current angle the servomotor would simple rotate in reverse direction. However, incrementing 180 degrees would give 345 degrees correspondent to the positive torque with the same magnitude. The performance of the 18-16 slot-pole servomotor design in Fig. 2.34 shows that the best load/current angle is 0 degree. However, using current angle equals to 15 degrees would not penalise significantly the torque level.

Therefore the selected current angles for the 12-10, 12-14 and 18-16 slot-pole designs are of 15, 345 and 0 degrees respectively for k_t analysis as function of TWS. The k_t analysis for BIT is not presented here. Now sensitivity analysis is performed for the TWS for the all three servomotors containing segmented stators with concentrated windings and results shown in Fig. 2.35.

For this case the torque constant (k_t) value is the performance indicator rather than the cogging torque. After defining the number of turns of each servomotor as function of the back E.M.F. using SPEED software, the sensitivity analysis is performed to the TWS by varying its value. In this case initial reasonable value is given to the maximum TWS and the BIT is made approximately half of that maximum TWS value.

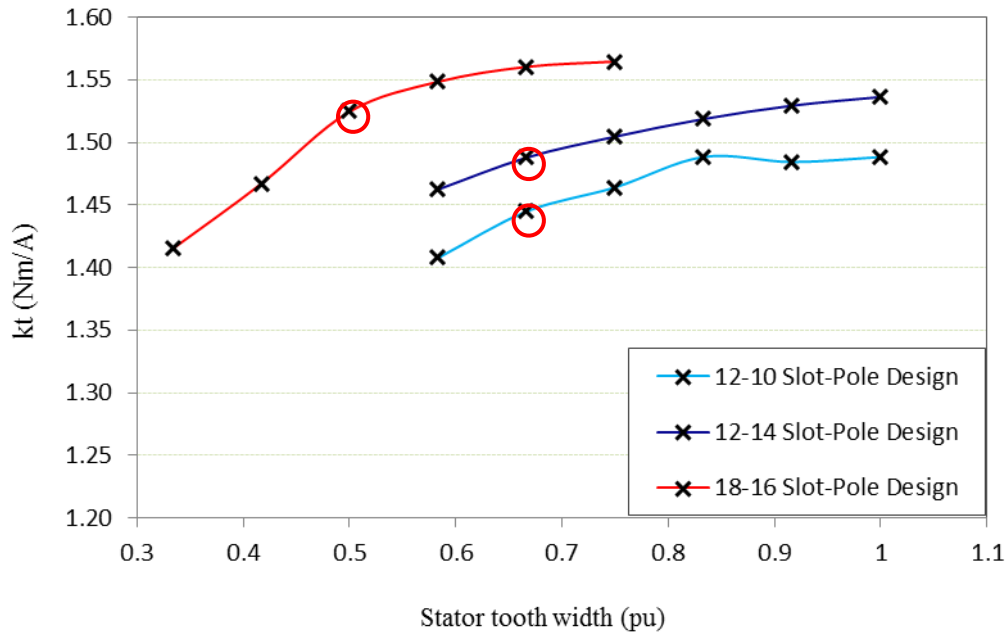


Fig. 2.35. Sensitivity analysis of stator tooth width (TWS) with respect to torque constant for the proposed designs.

Therefore since the flux level does not change due to fix TC and fix current, then changing TWS affects the k_t due to the saturation of the stator tooth as shown in Fig. 2.35 and Fig. 2.36. The figures show the curve characteristics as function of TWS and the FEA flux density level for all three new servomotor designs. Maximum and minimum TWS density levels are compared in terms of tooth saturation in Fig. 2.36. This saturation point needs to be defined between these two extremes and then the best BIT can be also found for the design in the same fashion. Or alternatively this saturation point can be consider the optimal TWS and the typical rule of thumb is to make the BIT 56% of the value of optimal TWS as previously indicated.

Fig. 2.35 shows that the designs with higher number of poles have better k_t , and the figure also shows that the k_t drops with reduction of TWS. This is mainly due to reluctance increase caused by decreasing TWS as shown in Fig. 2.36. At maximum TWS the saturation level is relatively low as shown in Fig. 2.36 (a), (c) and (e). With minimum TWS, the saturation levels are quite high as shown in Fig. 2.36 (b), (d) and (f). The 12-10 slot-pole design and the 12-14 slot-pole design have similar trend because the number of slots are the same and TWS is changed in similar manner for both designs. The 12-14 slot-pole design has higher k_t due to its higher number of poles.

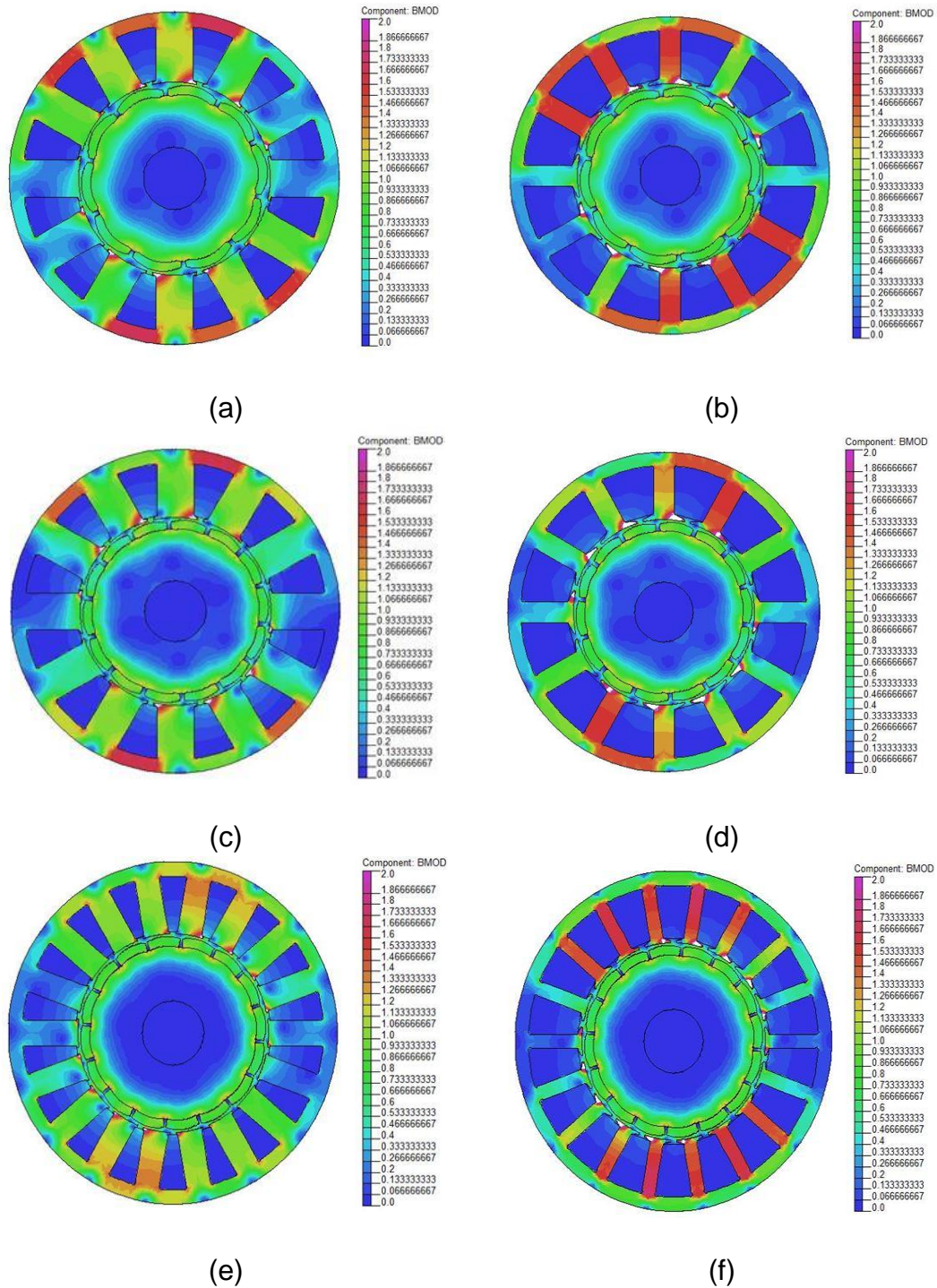


Fig. 2.36. Finite element graphics for flux plot of the new designed brushless servomotor.

The 18-16 slot-pole design has significantly higher k_t when compared with other two designs. However its characteristics curve is different, here the design does not allow for significant change of TWS. It can be observed from Fig. 2.35 that the k_t drops significantly when TWS is less than 0.5. This is mainly due to the increase number of slots for a relatively small frame size.

The corresponding TWS selected for both 12-10 and 12-14 slot-pole design combinations is approximately equals to 0.66 as shown in Fig. 2.35.

The corresponding TWS for the 18-16 slot-pole design is equal to 0.5 from Fig. 2.35. The corresponding dimensional value of BIT for each design is equals to approximately 56% of the respective TWS by making use of rule of thumb. Or similar sensitivity analysis to the one performed here for TWS can be perform for BIT, and using the selected value of TWS from Fig. 2.35 as a fixed value.

After definition of design parameters, the k_t curve characteristics for the new servomotors are investigated. The k_t curve characteristics are plotted for design comparison in Fig. 2.37.

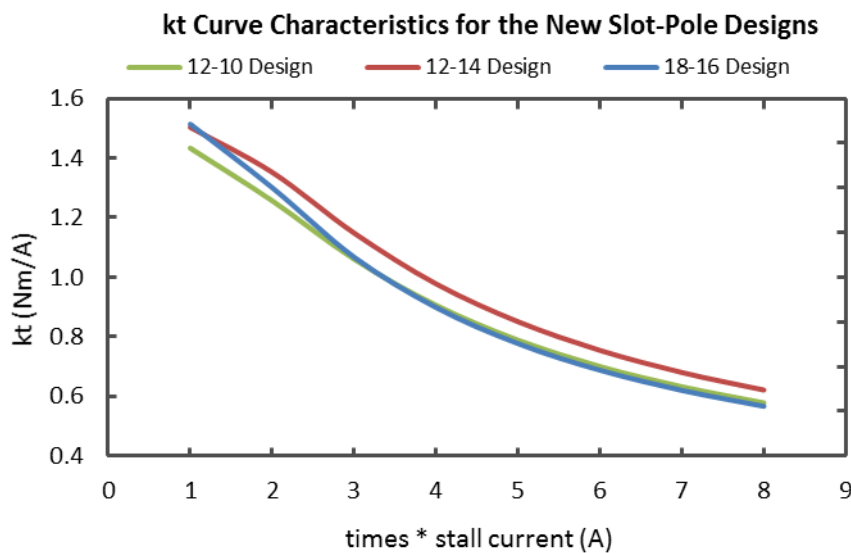


Fig. 2.37. k_t comparison between the new designed brushless servomotors.

These curve characteristics are important due to nonlinear nature of the k_t and these characteristics vary from one design to another. From Fig. 2.37 it can be observed that the designs with 12 slots have similar curve characteristics, and the 18 slot design has different curve characteristic. This is understandable since the TWS and BIT selected from the design points of Fig. 2.35 are equal for the designs with 12 slots.

Therefore their capability of conducting flux is exactly the same. It can be observed that decay of the k_t for the 18-16 slot-pole design is much significant with the increase of current. The Figure shows that at 1 times stall current the

18-16 design configuration has highest k_t . And this was previously shown in Fig. 2.35. However, this superior torque constant vanishes with the increases of the input current to the servomotor. Fig.2.37 shows that at 2 times stall current the k_t value of 18-16 slot-pole design is below the k_t value of 12-14 slot-pole design and very close to the k_t value of 12-10 slot-pole design. At 3 times stall current the k_t values for 12-10 and 18-16 slot-pole designs are the same. However, test results from the current 18-6 slot-pole design shows that 4 times stall current correspond to real 3 times stall torque due to k_t drop.

The 3 times stall torque is one of the key specifications in the BPM synchronous servomotor industry in terms of performance. And when 4 times stall current is applied, Fig. 2.37 shows that the k_t value of 18-16 slot-pole design is lower than the k_t value of 12-10 slot-pole design. Therefore the best k_t for the range of performance requirements of BPM synchronous servomotor is of the 12-14 slot-pole design. However the significant k_t advantage for 18-16 slot-pole design cannot be ignored.

2.5.5. Torque Ripple

Ideally, generating a sinusoidal current from the inverter drive of Fig. 2.12 capable of matching the sinusoidal back EMF of the BPM synchronous servomotor as shown in Fig. 2.14 would lead to almost constant torque with no torque ripple just cogging.

In the real case there is always a phase difference between the input current and the back EMF. In this case the torque ripple can be minimized by providing position information required for best current possible sinusoidal current. The other sources of torque ripple are reluctance torque (cogging), mismatch between amplitude signals of the phases (back EMF of current) and the high harmonic contents within the back EMF or sinusoidal current.

From Fig. 2.38 it can be observed that the torque ripple is similar for the new designs with the segmented stator and concentrated winding. The 12-10 slot-pole design is the one with highest peak-to-peak ripple and therefore will have lower electromagnetic average torque when compared with the 12-14 and 18-16 slot-pole designs.

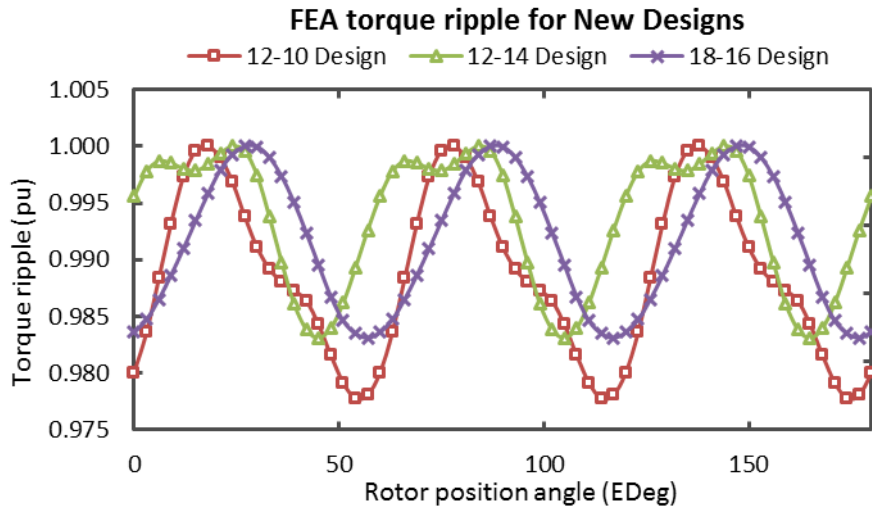


Fig. 2.38. Finite element graphs for torque-ripple of the new designed brushless servomotors.

Because the torque ripple is not very significant between the proposed designs, therefore the final design selection will not depend too much on torque ripple characteristics of the BPM synchronous servomotor.

However in terms of torque performance shown in Fig. 2.39, at stall the 12-10 slot-pole design performance is around 7% below 18-16 slot-pole design in terms of torque.

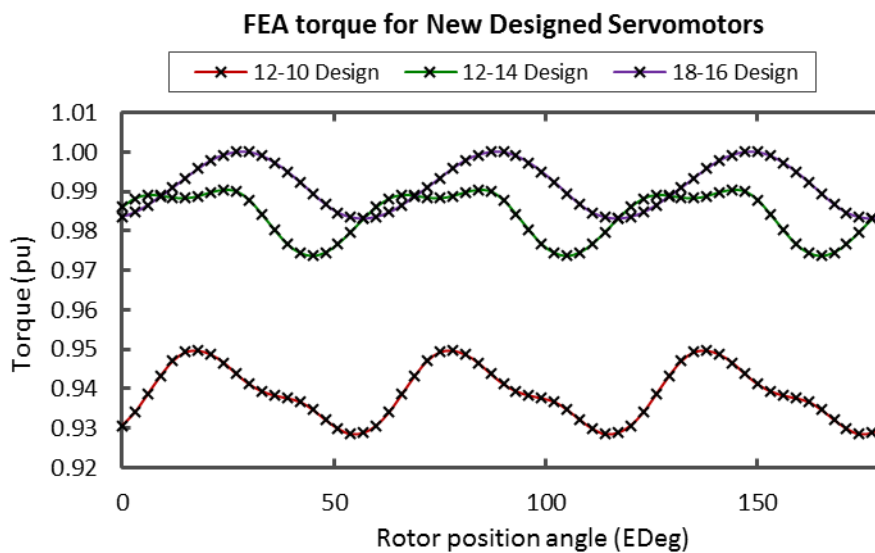


Fig. 2.39. Finite element graphs for stall torque of the new designed brushless servomotors.

This is mainly due to the K_t difference at 1 times stall condition previously discussed. The open circuit air-gap flux density for the proposed slot-pole designs are presented in Fig. 2.40.

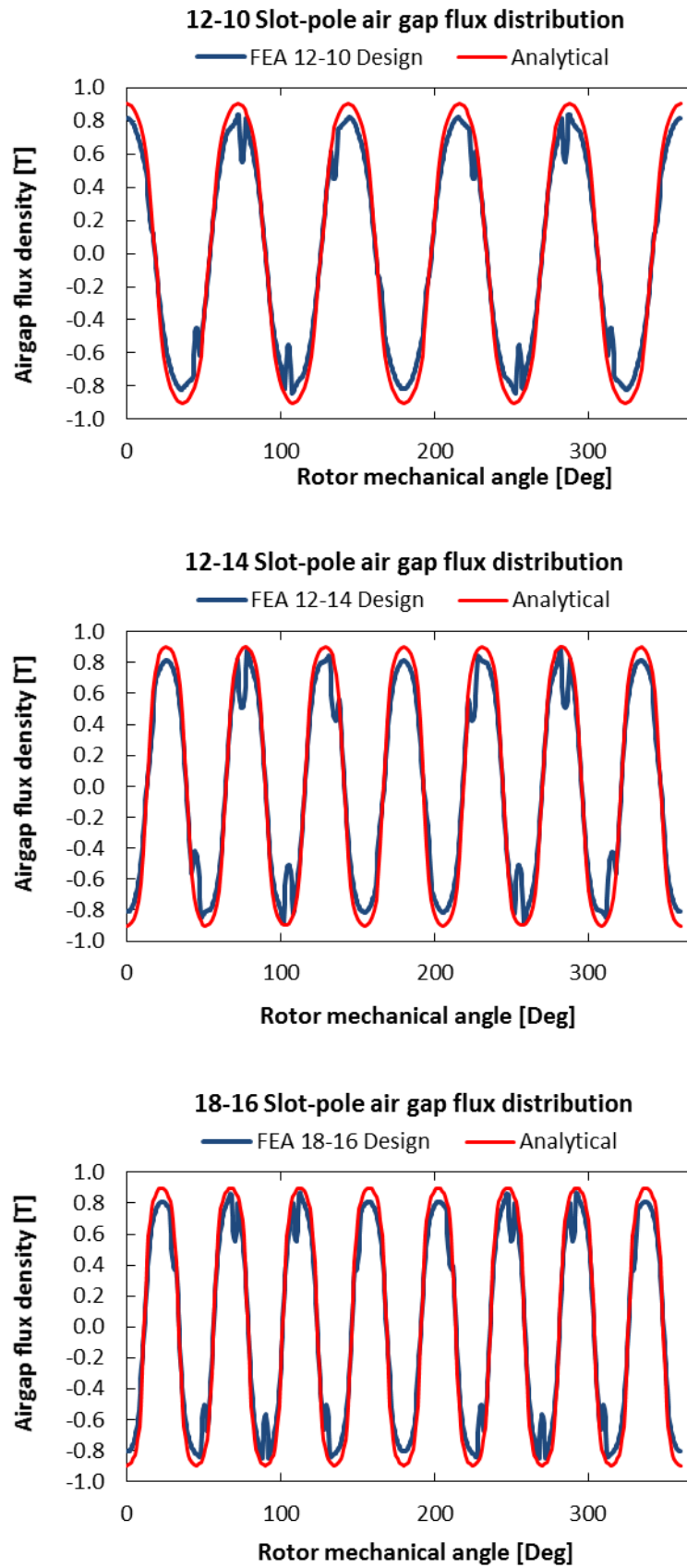


Fig. 2.40. FEA and analytical graphs for flux plot of the new designed brushless servomotors.

Both FEA and analytical calculation results are plotted for comparison and verification. The figure shows excellent agreement in the calculation of air-gap flux density for all new designs. The flux density in the air-gap is proportional to the torque and therefore a good indicator in terms of servomotor performance.

2.5.6. Torque Rating

In order to obtain the performance characteristics, the electromagnetic torque analyses have been performed and so far neglecting the losses in the BPM synchronous servomotor.

However losses do occur, analytic expressions exist for analysis of losses in the BPM synchronous servomotors and they are given in the following chapters. After obtaining the K_t values, the BPM synchronous servomotors stall torque performance levels are computed analytically with thermal model.

The combination of FEA and analytical thermal model leads to a maximum torque for a reference temperature limit. This is very important factor since it defines the thermal efficiency of the BPM synchronous servomotor. Which is the BPM synchronous servomotor's power output for a given maximum temperature rise. And since the speed limit due to back EMF is constant for all new designs.

Then torque is the only power output P_o variable that can differentiate the new slot-pole designs from the following equation

$$P_o = T\omega \quad (2.83)$$

where T is the electromagnetic torque produced due to current in the winding and ω is the angular velocity.

Therefore torque performances are analysed and compared for new designs for a maximum reference temperature. Details of thermally efficient servomotors are given in more detail in the coming chapters.

Fig. 2.41 shows the stall torque performance comparison between the three slot-pole design combinations proposed in this research work.

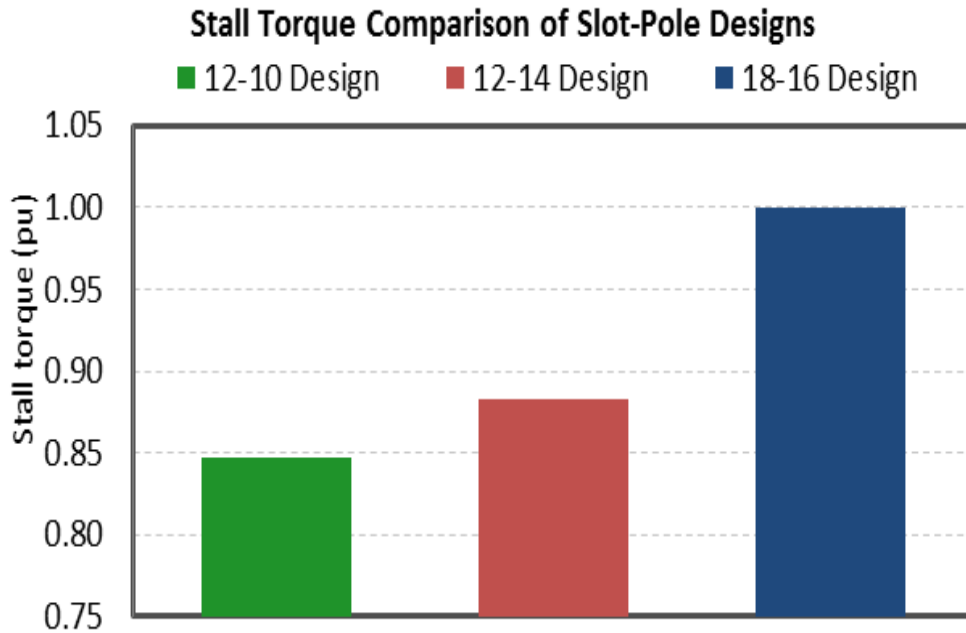


Fig. 2.41. FEA stall torque for the new designed brushless servomotors.

The maximum winding temperature is fix, and the based on input data and material data, losses are calculated and loaded to thermal model.

Motor-CAD software is used to iterations and obtains the thermal distribution and Fig. 2.42 shows steady-state temperatures for different parts of the BPM synchronous servomotors.

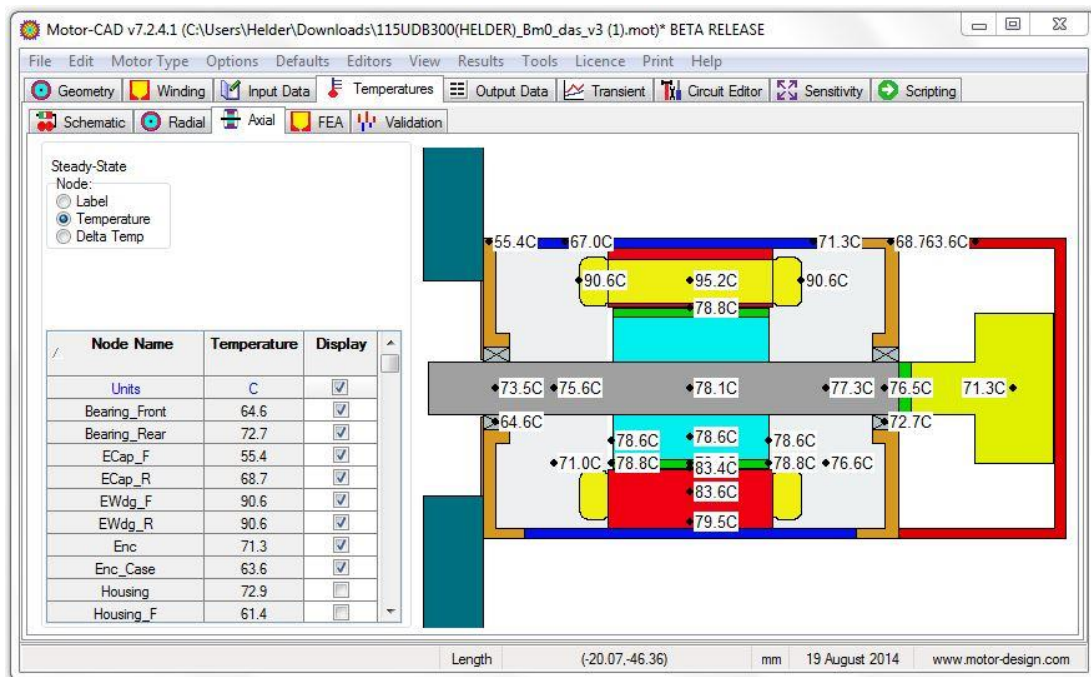


Fig. 2.42. Motor-CAD: Geometry Axial Output Data | Temperatures.

2.6. Iron Loss

Iron loss, also known as core loss, is normally the second largest component of power loss in the BPM synchronous servomotor. This loss is mainly made of ‘classical’ eddy current and hysteresis losses. It is reduced mainly by means of core lamination and the use of special materials (i.e. silicone). It is difficult to calculate accurately mainly due to the loss data obtained from manufacturers typically differing from those of real machines (Clerc et al., 2012). Also the waveforms of the currents and fluxes in the machine during tests to measure the losses can be very different to those occurring in service.

Also, lamination stresses occurring during manufacture change their magnetic and electrical characteristics. Therefore tests on a physical servomotor are preferable.

FEA software is used to obtain an accurate estimate of the iron losses in all the BPM synchronous servomotors presented in this research work. This is done here by calculating the orthogonal X and Y components.

The loss components associated with the magnetic flux components, B_x and B_y , are calculated and then added together separately (Hargreaves et al., 2012).

This theory gives an expression for the magnetic losses as a function of frequency, f , and peak magnetic flux density, B_m , as

$$\text{Power Loss Density} = c_1 B_m^2 f + c_2 (B_m f)^2 + c_3 (B_m f)^{1.5} \quad (2.84)$$

where c_1 is the hysteresis loss coefficient, c_2 is the classical eddy current loss coefficient that is a function of the electric conductivity and the thickness of the lamination, and c_3 is the excess loss coefficient that is a function of the cross-section of the lamination and the constant field. The loss predictions using the FEA based method are compared between the designs for different speeds as shown in Fig. 2.43 for speeds up to 6000 r/min. It can be observed that the rate of iron losses increase with speed in the 18-16 slot-pole design is considerably higher than that of the 12-10, 12-14 and 18-6 slot-pole designs.

This, however, is mainly due to the increased numbers of rotor poles. The 18-16 slot-pole configuration has a higher magnetic frequency causing higher iron losses.

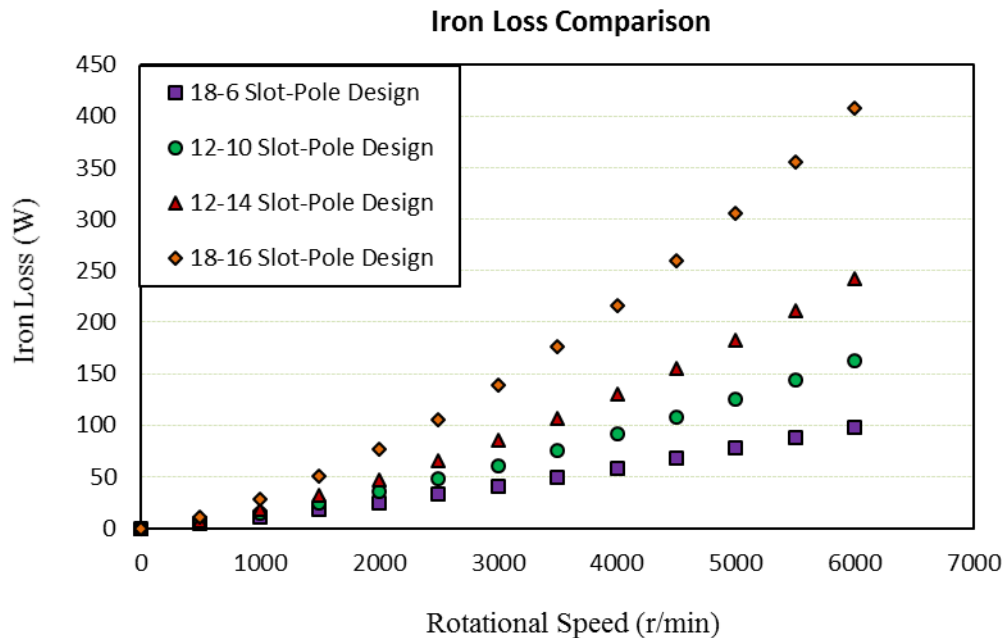


Fig. 2.43. Finite element analysis iron loss calculation.

The 12-14 slot-pole design also has significantly high iron loss, at maximum rotational speed (6000 r/min) the iron losses are more than double of that from the current 18-6 slot-pole design. The 12-10 slot-pole design is the design presenting the losses level closer to the current design losses.

2.7. Design Selection

The final design selection is highly influenced by the level of iron losses. With the restriction on frame size increase, then it is important to minimise the losses to be dissipated within the frame. There is a maximum power that can be dissipated by the defined frame for a reference temperature.

The aim is to maximise the torque within this maximum possible power dissipation of the BPM synchronous servomotor. For the rated torque of results presented in Fig. 2.41 the maximum speed for the new BPM synchronous servomotors is limited to 3000 RPM due to back EMF. Reducing the number of turns to half would allow doubling the speed servomotor to 6000 RPM to maintain the output power. Therefore the BPM synchronous

servomotors with high pole number are not recommended for this application. From Fig. 2.41 it can be observed that the performance difference between the 12-10 design and 12-14 design is not very significant. The torque difference between the two designs is about 3%. However the iron losses in the 12-14 design is quite significant compared with 12-10 design. From the manufacturing standing point is better to have low number of poles to feed to the rotor in order to accelerate the rotor manufacturing process. Increased size magnets are easier to handle and have larger manufacturing tolerances.

Therefore 12-10 slot-pole design is the best option since the servomotor needs to operate up to 6000 RPM. The 18-16 slot-pole design is also selected due to its high performance characteristics associated to this configuration and this is shown in Fig. 2.41. The 18-16 slot-pole combination is not prototyped in this research work but it will be used in the future applications requiring high torque with low speed only. Then the proposed design to be prototyped is the design with 12-10 slot-pole combination.

But before prototyping, the sensitivity analysis needs to be performed for optimal permanent magnet material usage. This is done next by fixing the permanent magnet width MW and varying the permanent magnet length LM or thickness.

2.8. Permanent Magnet Material usage

The most popular permanent magnet materials used in the servomotor manufacturing industry are neodymium iron boron (NdFeB), samarium cobalt (SmCo) and ferrite magnets.

Permanent magnet material is the crucial part in the brushless servomotor. In recent years a lot of focus has been on permanent magnet materials and power loss calculation in permanent magnet (Beckley, 2002) (Fan, 2009) (Ibrahim, 2012).

This is mainly because permanent magnets materials play a vital role in any permanent magnet machine performance. Better understanding and improvements of materials played an important role on the evolution of the electrical motors witnessed in the last century. If the dimensions and

parameters are fixed, the magnetic materials are main contributors to the torque constant of a BPM synchronous servomotor. Their property and dimension changes add value to the output torque and the efficiency of the servomotor.

Since Alnico, the first “modern” hard magnet or permanent magnet material according [www.http://www.thompsonrd.com] was developed in 1940. The permanent magnet materials have experienced considerable changes in products quality, manufacturing and marketing. Never the less the permanent magnet industry never experienced before the current increasing demand, politicisation and uncertainty mainly for the rare earth (RE) permanent magnet.

As previously mentioned, permanent magnets play a vital role in any permanent magnet machine. In servomotors as shown with equation (2.12), the magnet MMF interacts with the stator MMF to produce torque. Usually permanent magnet BPM synchronous servomotors are operated at relatively high speed therefore special attention needs to be given in selection of permanent magnet material depending on machine operation and application. Because at eddy currents due to asynchronous travelling flux harmonics induces power loss in permanent magnets.

Though the loss is less compared with core and copper loss but it may cause demagnetization in permanent magnets.

There are currently following three types of permanent magnets which represent about 85% of all permanent magnets used in the BPM synchronous servomotor industry:

a. Neodymium

Neodymium magnet or neodymium iron boron (NdFeB) magnet is the most widely used type of rare-earth magnet in BPM synchronous servomotor. Made from an alloy of neodymium, iron and boron to form the $Nd_2Fe_{14}B$, it is fully dense (sintered) permanent magnet with highest magnetic output. It has maximum energy product for magnet size and weight.

It is limited to simple geometries and due to brittleness requires careful handling.

b. Samarium Cobalt

SmCo can stand much higher temperatures than NdFeB. In terms of magnetic energy product or B_r , as shown in Table 2.5, SmCo is not very far from NdFeB. Hence there is a current interest on researching and exploit this good thermal characteristic of SmCo in order to help enhance the performance of the BPM synchronous servomotor to the level of performance of the BPM synchronous servomotors using NdFeB magnets in the servomotor industry.

c. Ferrite

Ferrite Magnet show good resistance to demagnetization, excellent corrosion resistance and low price per pound. In fact, measured by weight, ferrite represents more than 75 percent of the world magnet consumption. It is the first choice for most types of DC motors, magnetic separators, magnetic resonance imaging and automotive sensors. Ferrite magnets are extensively used in applications requiring flexible magnet. On a tonnage basis, these are primarily used for sound- deadening and casketing applications. Flexible ferrite is used for low energy-low cost servomotors.

Fig. 2.44 shows the kt curve characteristics as function of permanent magnet length LM . From the figure, there is a good proportionality between LM and the kt up to $LM = 3$.

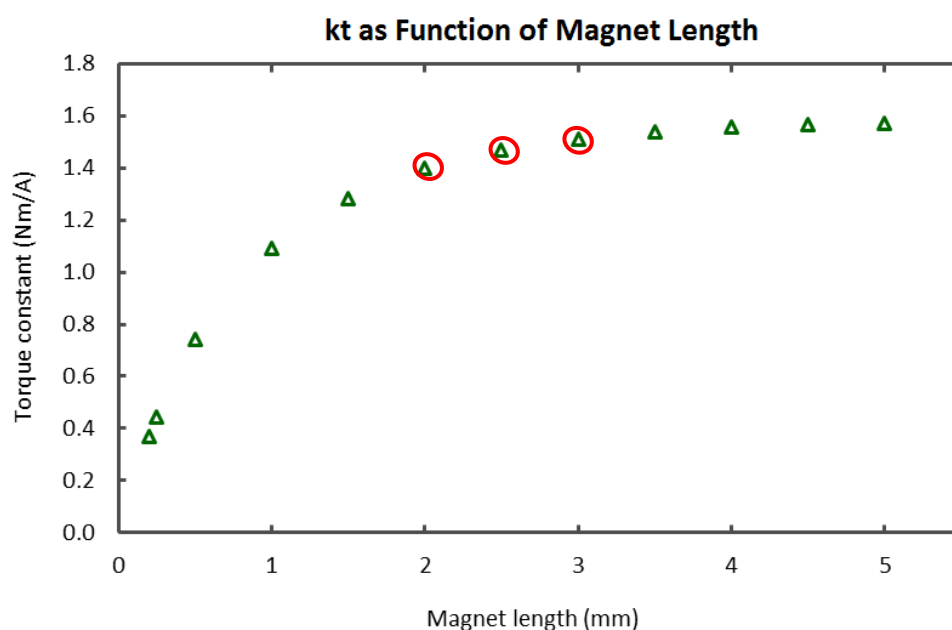


Fig. 2.44. Torque constant as function of permanent magnet length.

Increase of the magnet length from $LM = 3$ do not show significant increase of k_t and the permanent magnet material is wasted. Since the designer wish to maximize the torque of the servomotor frame at lower cost, then the three best selection points ($LM = 2$, $LM = 2.5$ and $LM = 3$) are indicated in Fig. 2.44. In the present research work the value of $LM = 3$ mm is selected in order to improve the demagnetization characteristics of the BPM synchronous servomotor.

2.9. Manufacturing Process of Brushless Motors

This section examines more important production methods for both BPM synchronous servomotors with conventional distributed windings and new segmented stator design with concentrated windings. The two most important servomotor parts are stator and the rotor, and all the value added components to the servomotor torque are incorporated within these two components. Therefore this makes the manufacturing process of these components extremely important when aiming for higher torque without increasing servomotor frame size as it is the case of the current research work. The segmented technique for the new stator is introduced and the advantages associated to this technique in terms of manufacturing are presented.

Continuous increase in international competition in the servomotor industry is driving BPM synchronous servomotor manufacturers to seek improvements on their manufacturing processes. This is needed in order maximise the production, improve quality, minimise waste and labour cost on production of servomotors. In the coming pages some of the most important manufacturing processes of BPM synchronous servomotor are described with corresponding illustrations to enhance the readers understanding.

2.9.1. Stator Core Assembly

2.9.1.1. Overview

The stator core assembly is described mainly with the lamination stacking process, stator insulation system, winding insertion, skew and impregnation processes.

The methods of lamination stacking are described for both stator technologies (non-segmented and segmented).

2.9.1.2. Stack and Electric Wall Insulation Process

For segmented stator the single laminations as shown in Fig. 2.45 (a) can be glued from the supplier to form the segmented teeth as shown in Fig. 2.45 (b).

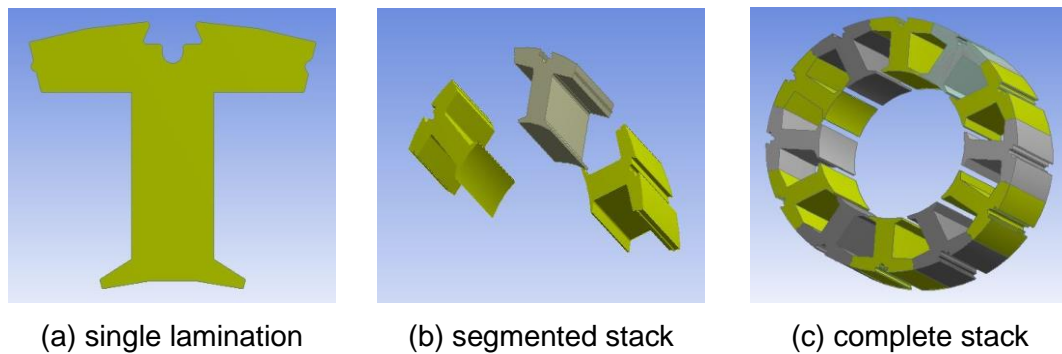


Fig. 2.45. New segmented stator core.

Then the teeth can be put together as shown in Fig. 2.45 (c) to form the stator core. This is a good solution to accelerate the manufacturing process of BPM synchronous servomotors.

However this pre-glued solution is not very practical with the conventional full core stator stacks due to significant weight per unit stator lamination core.

This makes it difficult to manage during transportation and manufacturing, and good example is during the insulation insertion process as shown from Fig. 2.46 to Fig. 2.49. The process for stacking laminations can be implemented using different methods. The most popular methods are by hand selection and by automated selection system.

The hand selecting lamination stacking method can be performed by weight or by height as shown in Fig. 2.47 and Fig. 2.48. This is by far the most popular method for lamination stacking in the BPM synchronous servomotor industry.

The reason had been that this is the most secure lamination stacking method since the operator can detect specific problems related to a particular lamination batch and therefore compensate accordingly to compensate for the correct stack length. And therefore accurate BPM synchronous servomotor

active length can be achieved due to high consistence by using this technique.



Fig. 2.46. Slot liner insertion machine.

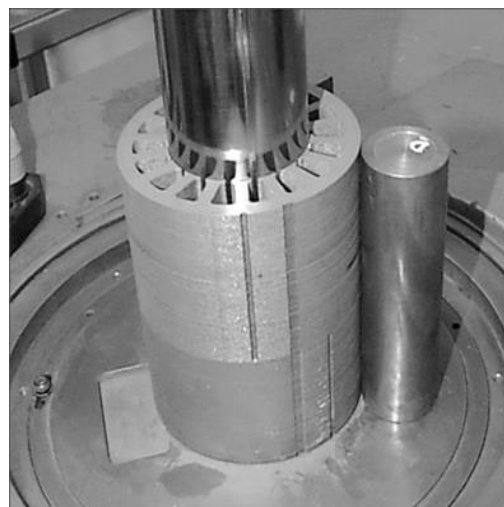


Fig. 2.47. Lamination stack preparation.

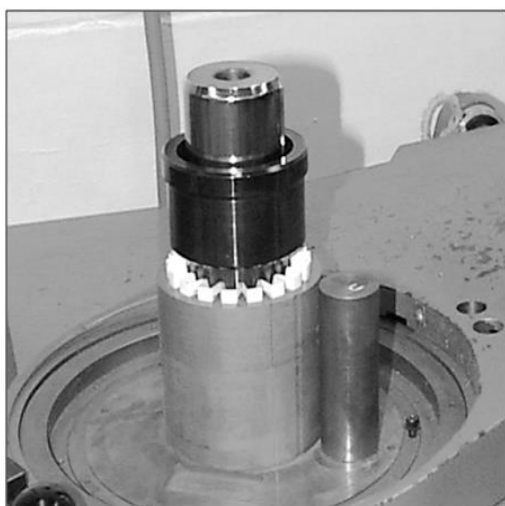


Fig. 2.48. Insertion of slot liners.

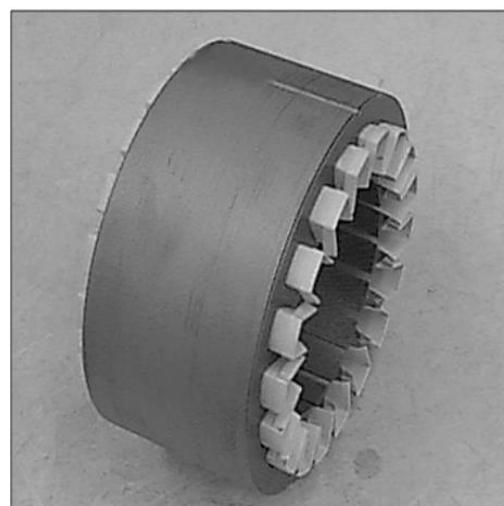


Fig. 2.49. 18-6 slot-pole design stack.

Fig. 2.46 shows typical slot liner or insulation insertion machine for inner-rotor non-segmented stator or full core.

The laminations are inserted in the machine-head up to the level of measurement tool for the BPM synchronous servomotor active stack length as shown in Fig. 2.47.

A semiautomatic system under the machine-head is used to cut the electrical insulation material into the size and then inserted the insulation material in the stator slots as shown in Fig. 2.48. Finally, Fig. 2.49 shows a non-skewed

stator stack for the conventional BPM synchronous servomotor just after the electrical insulation paper insertion manufacturing process.

This manufacturing process using the slot liner insertion machine can be eliminated if the segmented stator system as shown in Fig. 2.45 is used for stator production. Insulation paper can be cut to size and then glued to the slot surfaces without difficulties.

This is better than having insulation insertion machine that requires adjustments for each servomotor length. The machine also requires maintenance and a specialized person to perform all the required adjustments related to the insertion machine operation.

2.9.1.3. Coil Winding and Insertion Process

The current winding process for conventional BPM synchronous servomotor involves mainly two steps. First step uses a tapered coil-form to wrap the wire around and then push the wire into a transfer-tool as shown in Fig. 2.50.

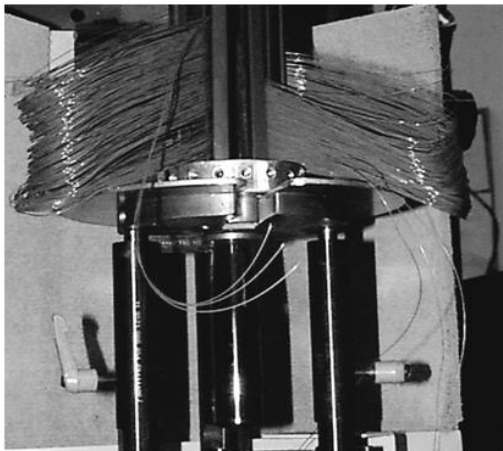


Fig. 2.50. Coil winding machine.



Fig. 2.51. Winding preparation.

The problem with this step is that the process only can be performed with relatively small gauge size and flexible wire. The number of turns cannot be too high to avoid damaging the wire or its insulation during the insertion process, and this causes low slot-fill factor that does not favours the cooling of the Servomotor. The second step is shown in Fig. 2.51 and Fig. 2.52, in this step the operator manually transfers the tool with the coils to the injection machine shown in Fig. 2.51. Then the injection machine is used to insert the

coils to the stator core as shown in Fig. 2.45. Finally the stator is ready for skewing process as shown in Fig. 2.53, significant overhang can be observed from the figure.

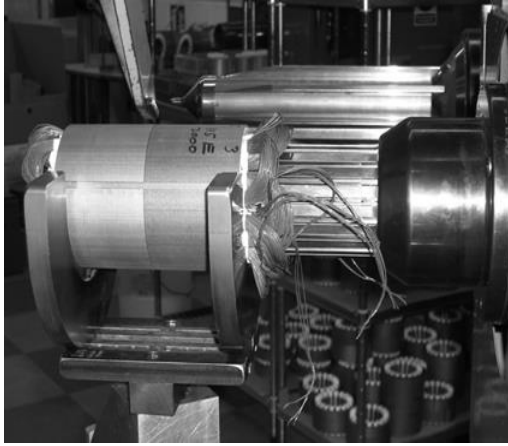


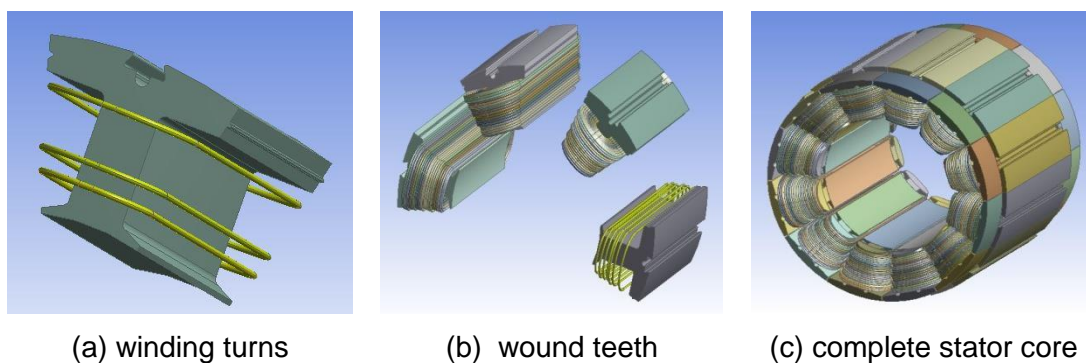
Fig. 2.52. Winding insertion machine.



Fig. 2.53. Complete winding inserted.

Need for skewing brings other non-value added processes to the stator manufacturing and the increased overhang forces to a longer servomotor. And this means that extra aluminium material need to be used for servomotor manufacturing.

However with segmented stator technology almost all the mentioned difficulties related to the winding process of the full core servomotors are eliminated. With the new stator coil winding method the stator lamination stacks are split as shown in Fig. 2.54 (a).



(a) winding turns

(b) wound teeth

(c) complete stator core

Fig. 2.54. New segmented stator coil winding.

This segmental construction technique allows for wrapping the wire around of each single tooth of the stator as shown in Fig. 2.54 (b). Thicker wire and

tightly wound coil can be obtained with this technique and these will favourite thermal performance of the servomotor and consequently the torque. And when the segments are put together as shown in Fig. 2.54 (c), good contact is achieved between the coil and the slot surface.

This winding process does not require complex dedicated machinery or specialist staff as shown in Fig. 2.51 and Fig. 2.52. A high slot fill factor can be achieved with this technique even when the coil is wound manually. Obviously this is not the best manufacturing process, since it would be very slow and costly in terms of time for production to produce servomotors in this fashion. However, very simple system can be constructed to wound around the teeth shown in Fig. 2.54.

2.9.1.4. Skewing Process

After complete winding insertion of current 18-6 slot-pole design as shown in Fig. 2.53, the stator core needs to be skewed in order to reduce the cogging torque. The new slot-pole combinations are almost cogging torque free when compared with the current servomotor, and this can be observed from Fig 2.55. In the figure, the cogging torque values of the new designs with 12-10, 12-14 and 18-16 slot-pole combinations are multiply by 100 in order to get comparable values of cogging of the current 18-6 slot-pole design.

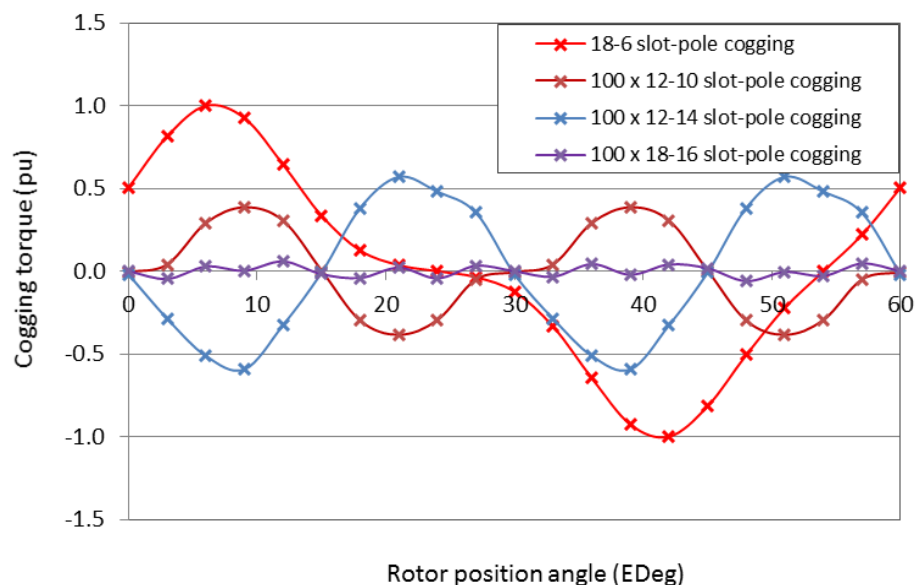


Fig. 2.55. Cogging torque levels for conventional no skewed and the new segmented stator no skewed brushless servomotor designs.

From Fig. 2.55 it can be observed that the selected new servomotors have low cogging torque. That for the 18-16 slot-pole design is much lower than with the 12-10 and 12-14 slot-pole combinations, the latter having the worst cogging torque. The 18-6 slot-pole design has a significantly high cogging torque when it is not skewed and therefore a skewing process as shown from Fig. 2.56 to Fig. 2.59 must be applied.

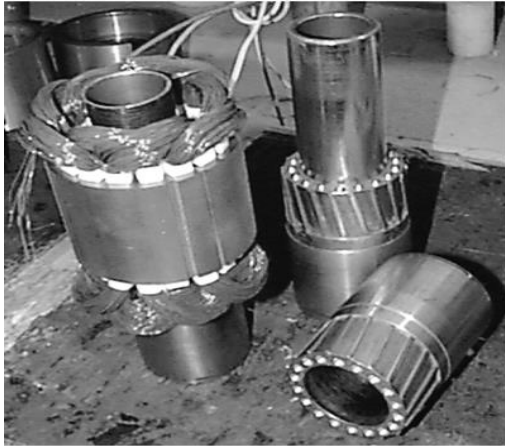


Fig. 2.56. Conventional winding and skew tooling.

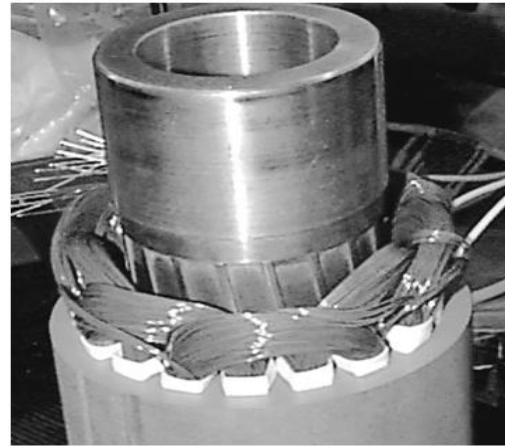


Fig. 2.57. Stator lamination skewing process.

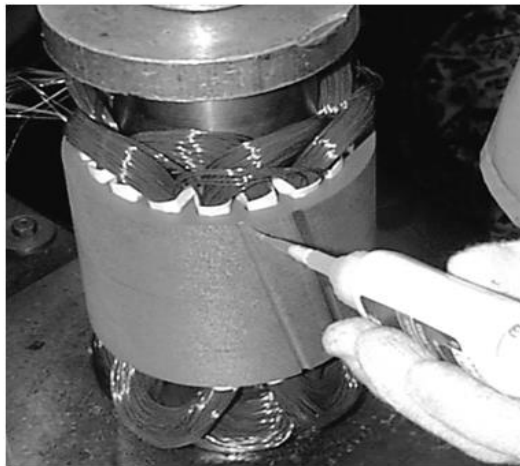


Fig. 2.58. Glue to maintain the skew angle.

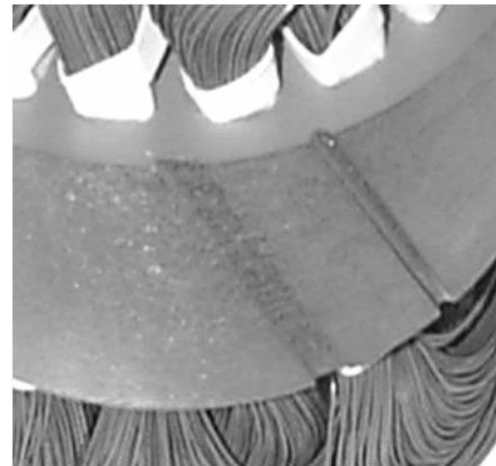


Fig. 2.59. Skewed stator for conventional winding.

Tools need to be developed to twist the core to the minimum cogging angle. Or an alternative solution is to skew the permanent magnet. However, the process would make the permanent magnets extremely expensive.

The new designs with concentrated windings selected in this research work does not require any skew due to the very low cogging torque level associated

to these servomotors. Just design parameters optimisation is required in order to almost totally eliminate the cogging torque. Or bring the cogging torque below 1% of the stall torque. With the new segmented design the stator lamination are punched as shown in Fig. 2.60 (a).

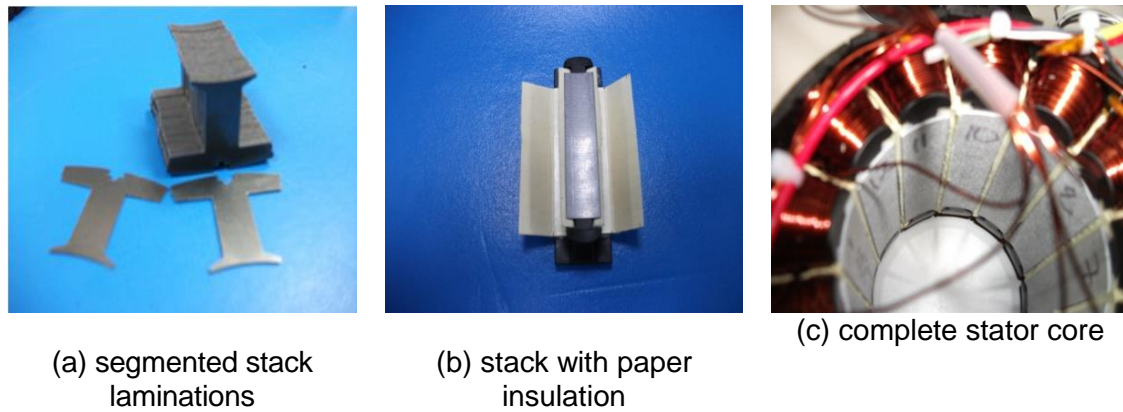


Fig. 2.60. New stator without need for skewing process.

Then the laminations are put together to form the segment that needs to be electrically insulated as shown in Fig. 2.60 (b) using wall insulation paper on the slot surface. And finally wound and put together as shown in Fig. 2.60 (c) without any need for skew. Therefore a much simpler manufacturing process solution when compared with current process and without need for any skewing tools or station in the production line.

2.9.1.5. Impregnation Process

When the stacks are put together as shown in Fig. 2.61 (a) the servomotor can be housed without need for any skewing as shown in Fig. 2.61 (b). After the housing process the servomotor stator can be impregnated and the resulting stator is shown in Fig. 2. 61 (c).

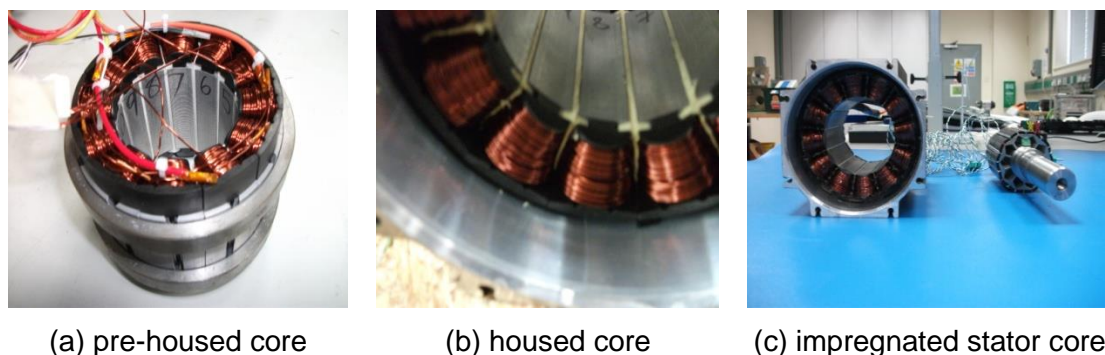


Fig. 2.61. Complete new segmented stator.

Resin is applied mainly to the windings in this impregnation system. Together with wall insulation material, this is considerate part of secondary insulation of the BPM synchronous servomotor. This impregnation process also helps to improve the winding structure.

The trickle resin impregnation manufacturing process as shown from Fig. 2.62 to Fig. 2.65 is used for both concentrated and distributed winding technologies.

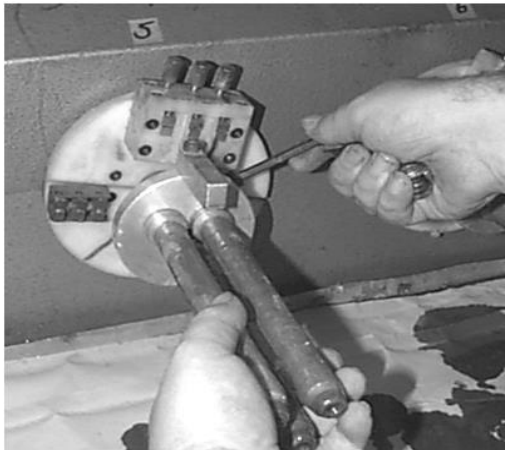


Fig. 2.62. Impregnation tooling mounting process.

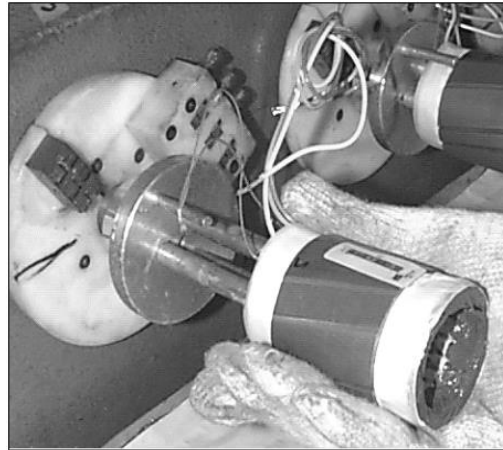


Fig. 2.63. Stack insertion process for impregnation.

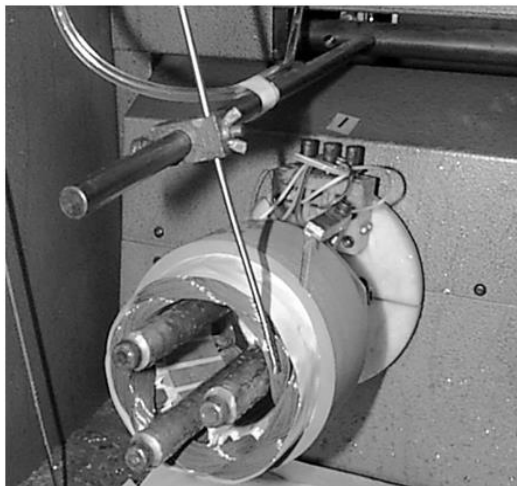


Fig. 2.64. Stator impregnation process.

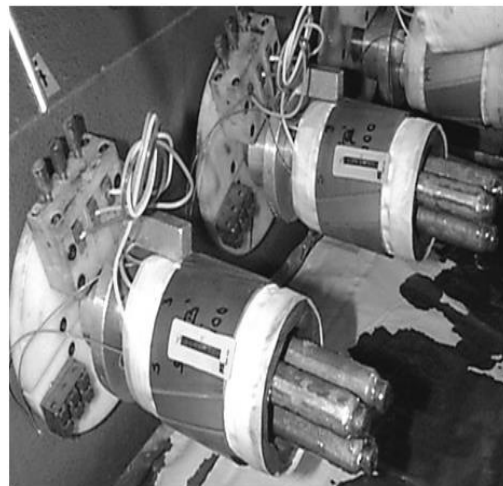


Fig. 2.65. Impregnated stator ready for the next manufacturing process.

This automatic system greatly increase the amount of resin applied to the stator winding and improve stator thermal conductivity. The trickle machines are expensive but they can really be effective in terms of amount of material to be used and where to apply without much emission. Therefore reducing waste

and improving the quality of the BPM synchronous servomotor. The principle of the trickle machine can be described with the support of Fig. 2.62 to Fig. 2.65. The impregnation tooling is mounted as shown in Fig. 2.62. Then for the conventional BPM synchronous servomotor the stack is inserted before housing as shown in Fig. 2.63.

The winding phases are then connected to a DC power in order to preheat the stator winding area with DC current. Then the dispensing nozzle is used to apply the resin as shown in Fig. 2.64. And finally the stack is removed from trickle machine as shown in Fig. 2.65 to a post-heat area to set the resin. This process helps to solidify the winding and improve the heat distribution within the BPM synchronous servomotor and consequently the overall torque performance.

2.9.2. Rotor Side

The rotor manufacturing can greatly affect the air gap length. Then the more significant components of rotor assembly processes are highlighted mainly with rotor lamination stacking process, magnet assembly process, rotor taping and rotor turning down processes. The manufacturing processes for the rotor used in the conventional servomotor are shown in Fig. 2.68 to Fig. 2.83.

A significant air gap length must be allowed with the conventional method of rotor manufacturing due to the glue and the glass tape. The significant effect of air gap in the performance of the BPM synchronous servomotor is shown in Fig. 2.66. Fig. 2.66 shows that there is a linear proportionality between the air gap and the k_t level of the BPM synchronous servomotor. Therefore the research work will focus on the manufacturing techniques for the rotor of the new segmented stator with concentrated winding design in order to avoid increased air gap. By aiming to eliminate all non-value added components of the current manufacturing method. The glue or the glass tape do not add value to torque, they simple used to hold the magnet poles in place. However, when they are applied in the servomotor manufacturing process they tend to take significant space in the air gap. In these processes the balancing plate, the glue and glass tape are non-value added to torque but they are necessary to retain the magnetic structure in place. However removal of these materials

would reduce the manufacturing cost and the material cost and waist related to the rotor construction.

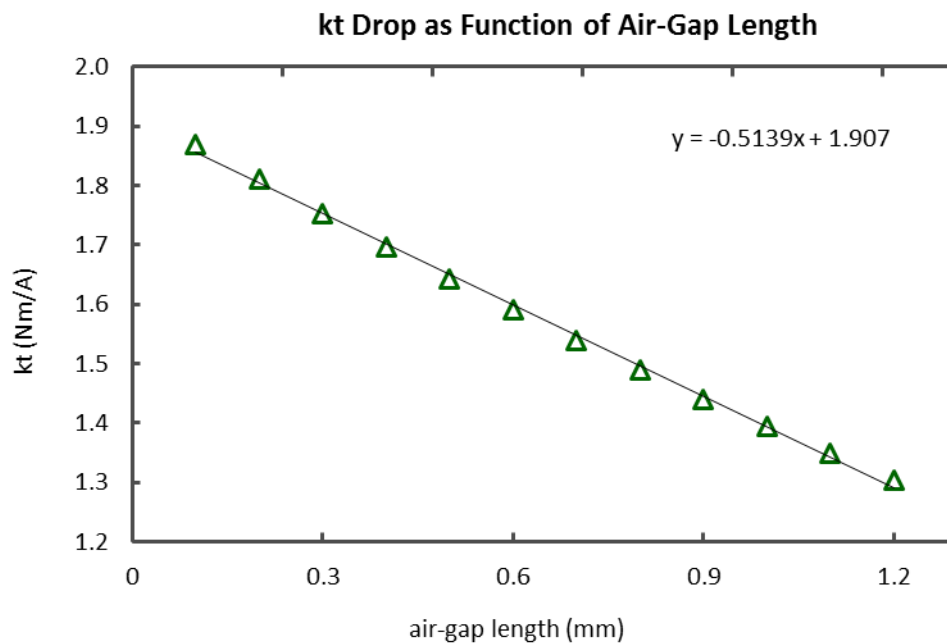


Fig. 2.66. Different air-gap and the effect on torque constant.

The removal of these non-value added materials can be eliminated as shown in Fig. 2.67.

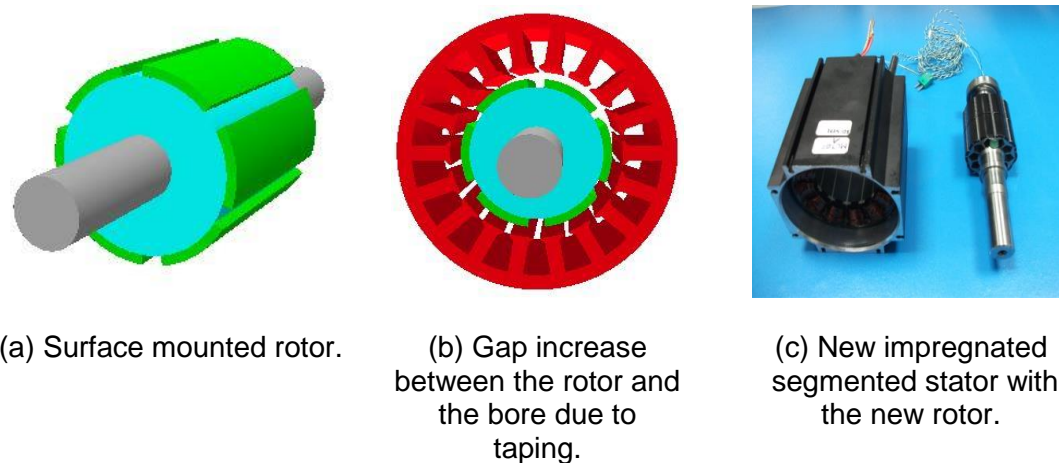


Fig. 2.67. Rotor manufacturing advantages of new brushless servomotor.

The magnets need to be inserted and retained without glue or tape. When the permanent magnets are mounted in the rotor stack surface as shown in Fig. 2.67 (a), the magnets need to be secure and then ready to be inserted in the

stack iron as shown in Fig. 2.67 (b). This is achieved with the new BPM synchronous servomotor as shown in Fig. 2.67 (c).

2.9.2.1. Rotor Lamination Assembly

In process of rotor lamination assembly the rotor shaft is mounted as shown in Fig. 2.68 and then the stack laminations shown in Fig. 2.69 are inserted into shaft just after the first balancing plate. The rotor stack lamination insertion process is shown in Fig. 2.70. Finally the second balancing plate is inserted as shown in Fig. 2.71 to hold the laminations together.

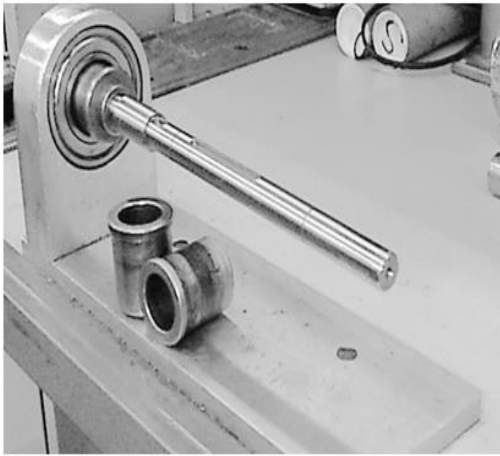


Fig. 2.68. Rotor shaft mounted for lamination insertion.

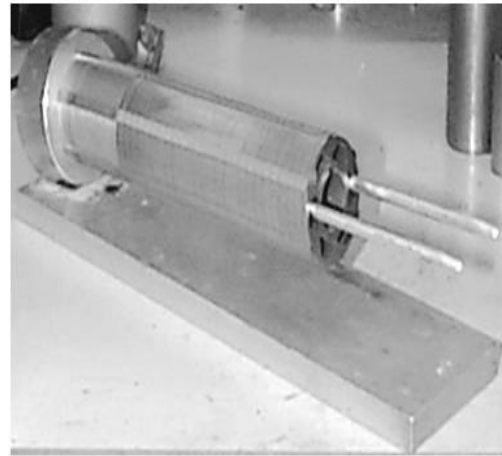


Fig. 2.69. Rotor stack laminations.

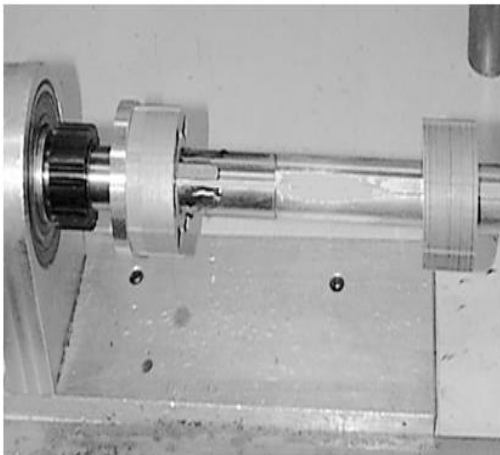


Fig. 2.70. Stack lamination insertion process.

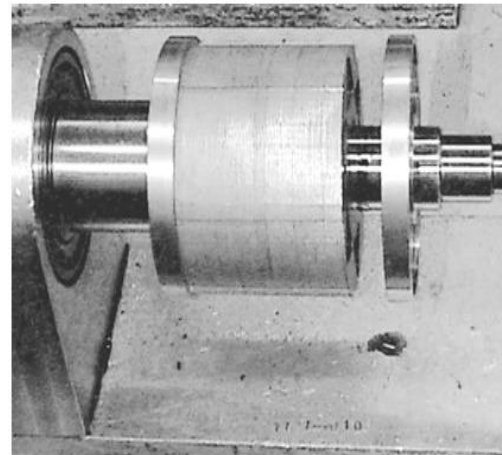


Fig. 2.71. Insertion of the final balancing plate.

2.9.2.2. Magnet Assembly

The permanent magnets are mounted on the rotor lamination stack surface as shown in Fig. 2.66 (a). After insertion of the second balancing plate, glue is

applied to the rotor stack surface as shown in Fig. 2.72. Then the magnet poles are located as shown in Fig. 2.73 to Fig. 2.75.



Fig. 2.72. Application of glue to the rotor stack.



Fig. 2.73. Insertion of permanent magnets to the rotor stack.



Fig. 2.74. Finalizing the permanent magnet insertion manufacturing process.

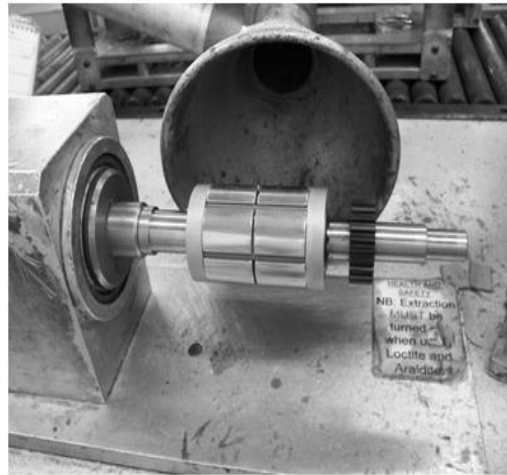


Fig. 2.75. Complete permanent magnet insertion to the rotor.

2.9.2.3. Rotor Taping

The next manufacturing process is to apply the glass tape as shown in Fig. 2.76.

The excessive glass tape as shown in Fig. 2.77 need to cut off and removed as shown in Fig. 2.78 and Fig. 2.79.

After removing the excessive tape, the rotor is taken to the oven before turning down process and all the excessive permanent magnet rotor tape is wasted.

Glass tape does not add value to the torque, it is just used to retain the permanent magnet poles to the rotor structure.

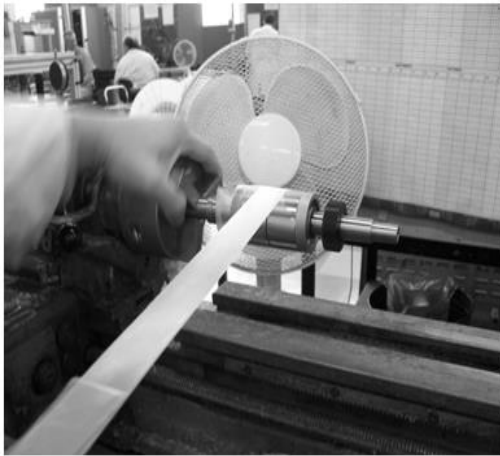


Fig. 2.76. Application of glass tape to the rotor to retain permanent magnets.

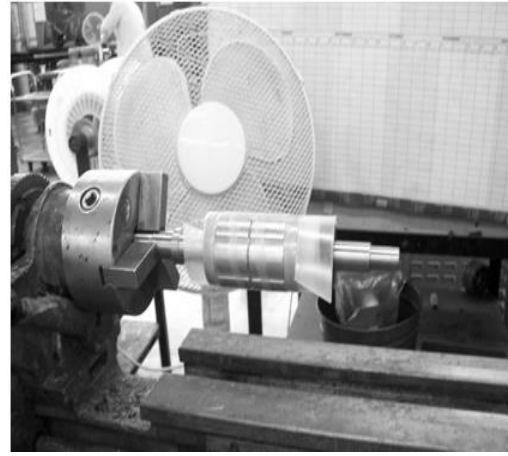


Fig. 2.77. Completely taped rotor.

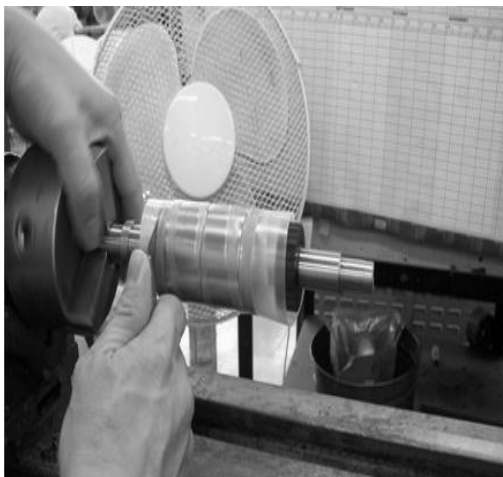


Fig. 2.78. Cut off the excessive tape material.

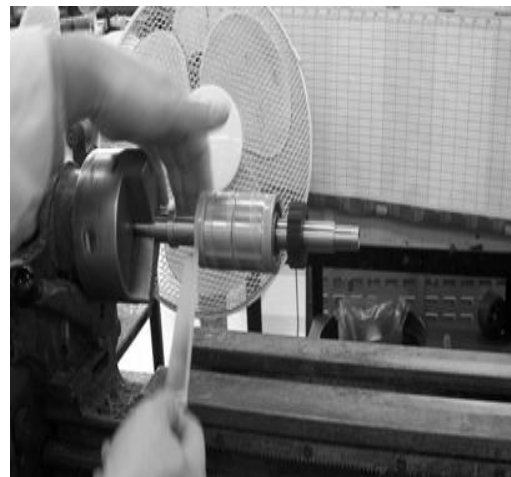


Fig. 2.79. Removal of excessive tape material.

2.9.2.4. Turning Down

The permanent magnet tape material turn down machinery is shown in Fig. 2.80 and the taped rotor after post oven manufacturing process is shown in Fig. 2.81.

The tape material turning down process removes the excessive glass tape as shown in Fig. 2.82 and the resulting rotor is shown in Fig. 2.83.

Excessive time is wasted with this manufacturing process does not add value to the BPM synchronous servomotor.



Fig. 2.80. Tape material turn down machinery.

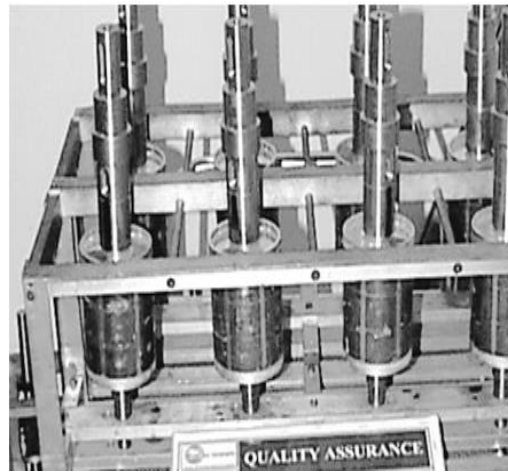


Fig. 2.81. Taped rotor after post oven process.

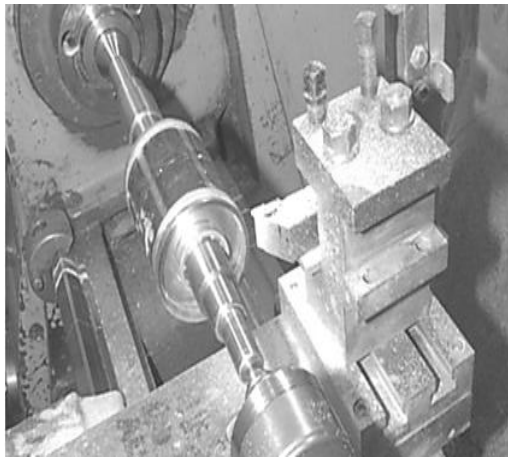


Fig. 2.82. Tape material turning down.

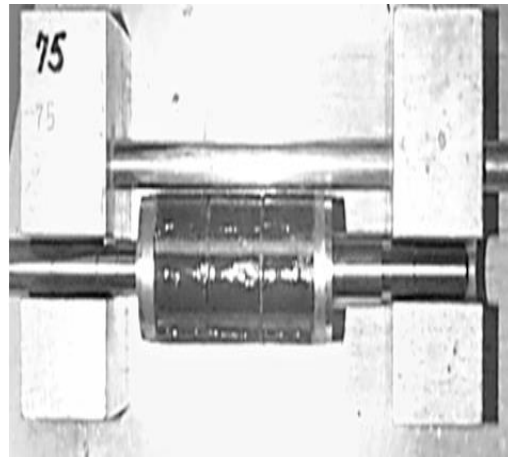


Fig. 2.83. Complete rotor assembled.

2.10. Design for PM Retention of New Servomotor

The prototype rotor shown in Fig. 2.67 (c) has no balancing plate or glass-tape to hold the permanent magnets in place. This is achieved instead by implementing a magnetic notch. This, however, results in cogging torque pattern change, this becoming more complex. This is a non-linear problem that cannot be solved analytically, leaving open only numerical approaches, FEA being applied here.

If the retention notches, referred to as T-lams, are introduced without changing any other design parameters, then the cogging torque tends to change significantly. Sensitivity analysis of the cogging torque with respect to the four main design parameters (MW, SOAng, SO and TGD) that affect the

cogging torque can be performed, however, to obtain optimal design parameters that minimise the cogging torque using FEA.

The FEA images of the open-circuit (zero stator current) flux pattern for the conventional configuration without T-lams is shown in Fig. 2.84 and that with the T-lams is shown in Fig. 2.85.

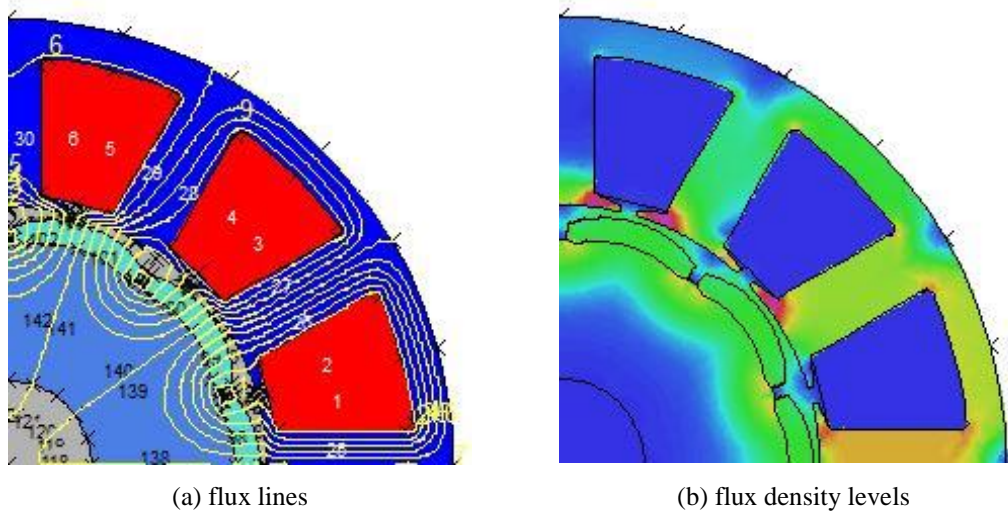


Fig. 2.84. Open circuit flux distribution without T-Lams.

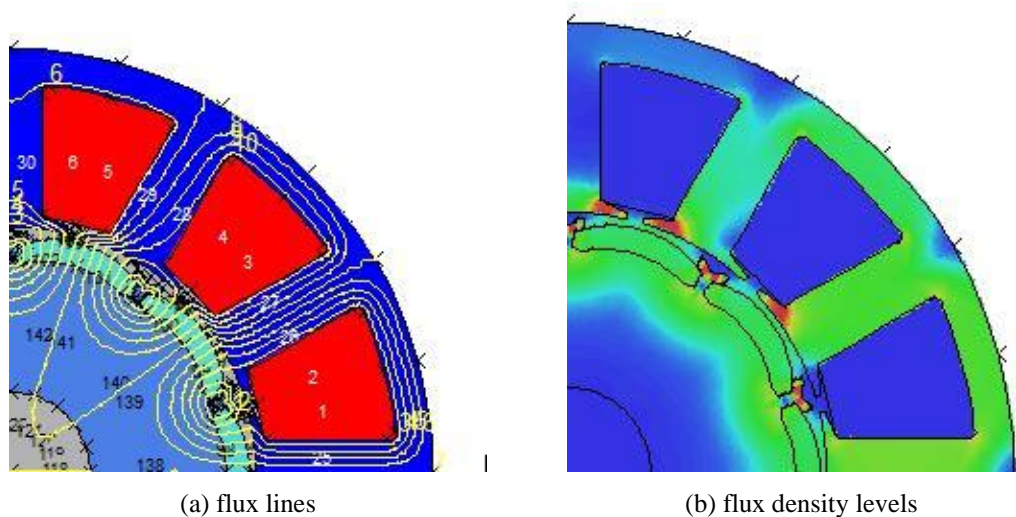


Fig. 2.85. Open circuit flux distribution with T-Lams.

When the T-Lams are introduced, it is evident by comparing Fig. 2.84 with Fig. 2.85, that it causes considerable changes in the flux pattern in the region of the T-lams. Fig. 2.84 (b) shows a higher stator tooth saturation level than that

of Fig. 2.85 (b). This means that there are more flux lines travelling through the teeth. A significant level of saturation can be observed in the region of the T-Lams in Fig. 2.85 (b), indicating that an increasing number of flux lines are taking the notch path as shown in Fig. 2.85 (a). This tends to increase the cogging torque and make it significantly non-sinusoidal as a function of the rotor angle. Hence there is a need to carry out optimisation with respect to the design parameters that affect the cogging torque.

Fig. 2.86 and Fig. 2.87 show, respectively, one cycle of the cogging torque waveforms for different magnet widths with and without the T-Lams.

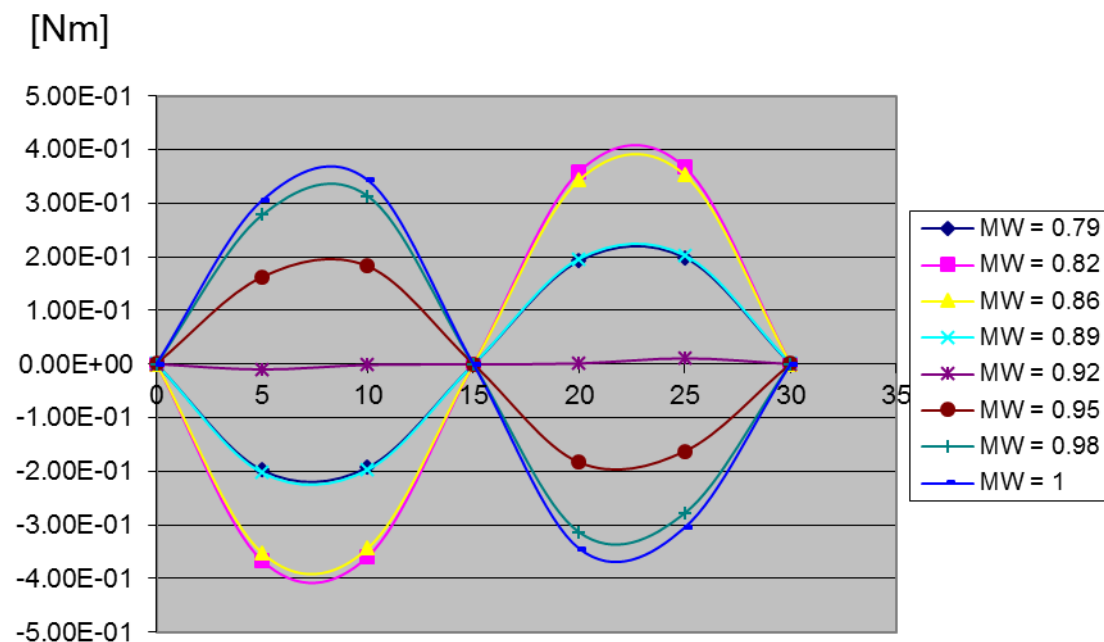


Fig. 2.86. Cogging torque cycle variation with magnet width without T-lams.

The design point is selected in a different fashion than for the conventional method presented in Subsections 2.5.2.1 to 2.5.2.3. Here, the optimal design point for cogging is chosen taking into account the punching effect on the rotor lamination notch (Boglietti et al., 2001) and also the FEA cogging torque waveform signal as described in Appendix B and FEA sample script in Appendix C. When the cogging torque opposes the direction of rotation, its sign is negative and when aiding the direction of rotation it is positive.

The peak-to-peak cogging torque is defined using the waveforms of Fig. 2.86 and Fig. 2.87 in such a way that it can be positive or negative, as follows.

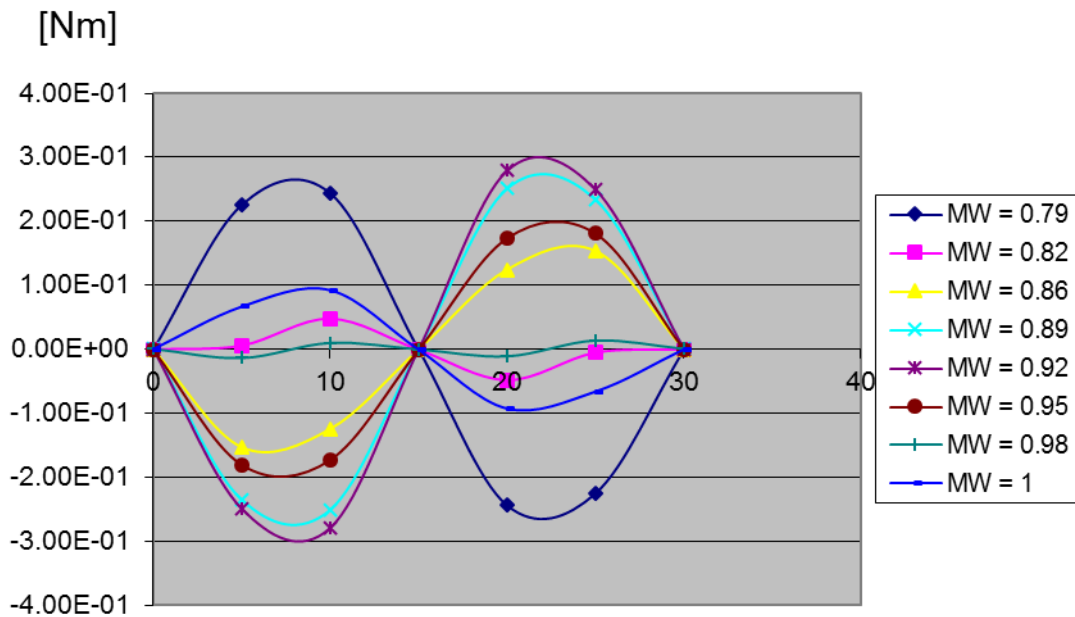


Fig. 2.87. Cogging torque cycle variation with magnet width with T-lams.

If the cogging torque rises from zero angle to a maximum peak, the peak-to-peak cogging torque is taken as positive and if it falls from zero to negative peak the peak-to-peak cogging torque is taken as negative. In this section only one design parameter selection is shown as an example.

The optimal point for all the other design parameters can be obtained using the same process iteratively, cycling through the design parameters until the peak-to-peak cogging torque is minimised in magnitude. The peak-to-peak value according to the above definition is obtained for each waveform and plotted as shown in Fig. 2.88.

Now the designer must select the optimal point based on the two characteristic curves shown in Fig. 2.88. An interesting observation is the 'T-lam' curve has two optimal points where the peak-to-peak cogging torque passes through zero, one for about $MW=0.83$ [pu] and the other for about $MW=0.98$ [pu]. This raises the question of which one is best.

The logical choice would be the point yielding the highest torque constant, in this case the one with the largest magnets, i.e., $MW=0.98$ [pu]. But when observing the 'No T-Lam' curve the two points have significantly large cogging torque.

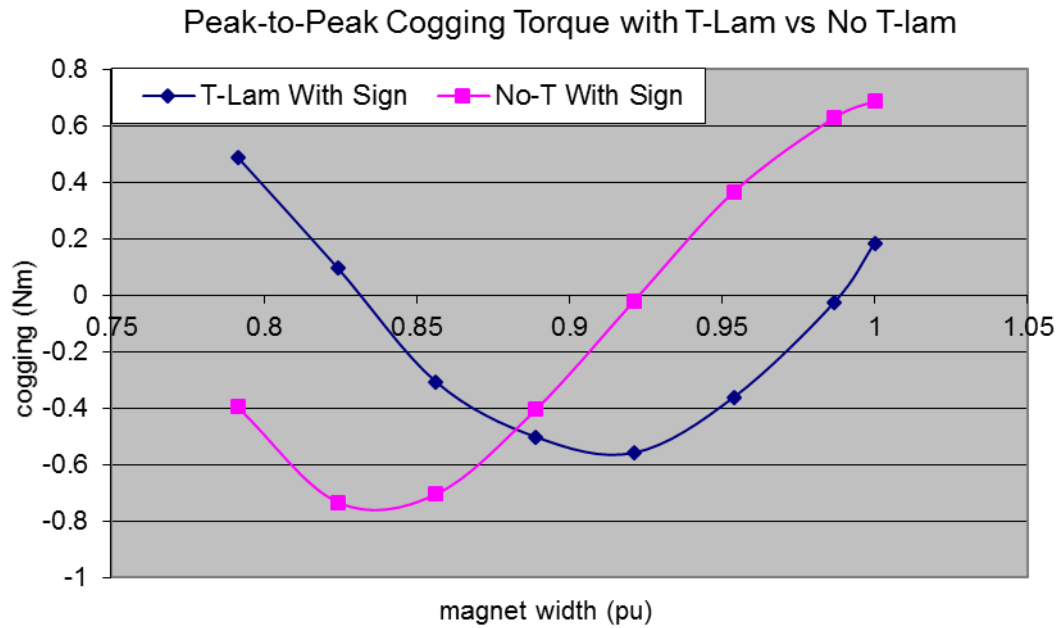


Fig. 2.88. Signed peak-to-peak cogging torque with and without T-lams.

A magnet width of 1 [pu] is not a good design point since the peak-to-peak cogging torque can only get worse. Due to random errors in the notch dimensions due to imperfect punching will cause the 'T-Lam' curve in Fig. 2.88 to shift and therefore affect the optimal design points. Then knowing how much the notch is affected due to manufacturing (Boglietti et al., 2001) (Boglietti et al., 2003a) helps to decide the design point for the magnet width.

If a MW of 0.92 [pu] is selected, the peak-to-peak cogging torque is very low without the T-Lams. However, the peak-to-peak value with the T-Lams is at its maximum negative value at that point. Hence lowest cogging point without the T-Lams is the worst cogging point with the T-Lams. At this stage a good observation must be made to the curve characteristics of No T-Lam and the T-Lam of Fig. 2.88. Some level of experience with the material characteristics as well as ingenuity will help the designer select the best design point.

Imperfect manufacturing will cause errors in dimensions and imperfect mechanical interfacing of components, some of which are critical in that the 'T-Lam' curve of 2.88 is very sensitive with respect to them and that a degree of experience is required to select design points that will not be too sensitive,

thereby guaranteeing a batch of motors leaving the production line with an acceptable spread in the performance characteristics such as cogging torque.

Summarising, the first observation that may be made in Fig. 2.88 is that there are two optimal design points with respect to the magnet width for the new rotor with the T-Lams but only one optimal design point for the conventional rotor without the T-Lams.

An interesting but less important observation is that the optimal design points for the rotor with the T-Lams are the very worst ones for the rotor without the T-Lams, while the optimal design point for the rotor without the T-Lams is the very worst one for the rotor with the T-Lams.

As indicated earlier, however, this is only an illustration and a true optimisation with respect to all four design parameters (MW, SOAng, SO and TGD) will yield different values of MW from the ones that are optimal in Figure 2.88. Even if including these four design parameters in the optimisation produces two sets of parameters for which the cogging torque is minimised, one set will undoubtedly produce a higher torque constant than the other and will therefore be the optimal set of parameters.

Another important practical consideration is the random variations in component dimensions and imperfect mechanical interfaces between these components. Performance measures such as the peak-to-peak cogging torque and the torque constant may be sensitive to some of these imperfections and under these circumstances a degree of experience on the part of the designer may be needed to select an optimal design point for which a batch of servomotors leaving a production line will exhibit an acceptable statistical spread of the performance measures.

CHAPTER 3

THERMAL ANALYSIS OF BRUSHLESS SERVOMOTORS

3.1. Introduction

The power output of a brushless PM synchronous servomotor for a given temperature defines its thermal efficiency. When natural cooling is used, the temperature rise critically determines the maximum allowed power dissipation inside the servomotor during its operation.

Improving the heat dissipation and heat distribution reduces the hotspots and contributes to the thermal efficiency improvement of the servomotor. It follows that how and where the main heat losses are generated in the servomotor is an important part of this research work.

This is very critical due to the necessity of predicting the thermal distribution within the machine components at critical operation points. For example how it is very important to know how much iron loss occurs at different speeds. The thermal model of a brushless servomotor is defined using existing calculations and software tools. Traditional and new methods for thermal analysis using a thermal equivalent circuit with lumped parameters are described and their limitations are presented. Calculations for thermal circuits are presented for the important servomotor components. Predominance of stator losses is highlighted and the iron losses are investigated using analytical expressions and FEA. Cooling aspects and orientation of the prototype servomotors are described and the mounting plate/flange does influence significantly the performance of a TENV BPM synchronous servomotor. A matrix solver for the thermal model is developed based on the test data and the analyses are performed and compared with the test results in Chapter 6.

3.2. Importance of Thermal Analysis

The main factors to consider when designing a brushless servomotor as shown in Fig. 3.1 are the cost, durability, compliance with the performance specification according to the standards (IEC, UL, etc.) and the customer requirements.

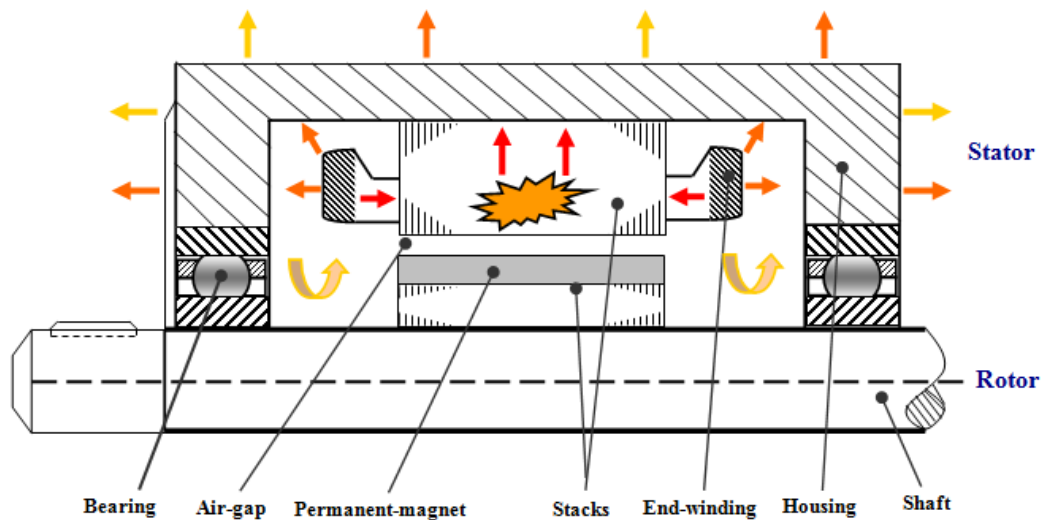


Fig. 3.1. Schematic of brushless servomotor with heat transfer modes due to radiation (orange arrow), convection (yellow arrow) and conduction (red arrow).

Optimised designs are required nowadays due to the current requirements for smaller and cheaper servomotors with maximised efficiency due to material scarcity and the environmental impact.

The life of a brushless servomotor is ultimately dependent on the heat dissipation and temperature limit, as shown in Fig.3.2 (Staton, 2012).

Also many components used in a servomotor have different temperature limits. Therefore it is very important to be able to estimate the temperatures at different locations in order to be able to estimate the servomotor operating performance and life time.

Operating a brushless servomotor causes heat to be generated due to power losses occurring such as copper losses due to current, iron losses due to the magnets and rotational losses due to friction and windage. Therefore to ensure that the servomotor components such as winding insulation materials, encoders, bearings and permanent magnets do not operate above their

temperature limits, the losses must be distributed and removed efficiently to ensure a long operational life. Also lowering the operating temperature reduces the copper winding resistance and consequently the copper loss.

The stall torque and rated torque of a brushless servomotor are the most important performance indicators for continuous operation and therefore it is important to know at what cost (thermally) the design achieves a specified torque value.

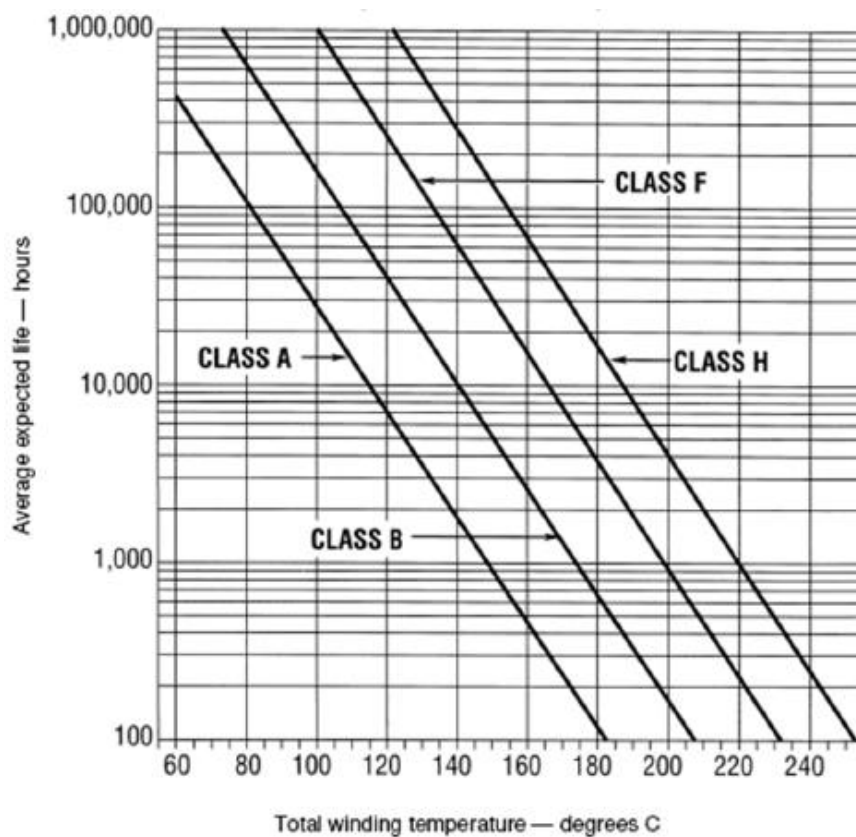


Fig. 3.2. Life vs. temperature curves for insulation systems (per IEEE 117 & 101).

The graph shown in Fig. 3.2 is the one typically used in the industry to estimate the servomotor average expected life time.

These temperature limits define the torque-speed characteristic curve and the output power of the servomotor. Fig. 3.2 from the IEEE standards shows four categories of rating temperature rise in the winding. According to these graphs, the temperature limits for different categories for longer average expected life hours are as follows

- Class A = 60⁰ C (105⁰C IEC temperature of insulation)
- Class B = 75⁰ C (130⁰C IEC temperature of insulation)
- Class F = 100⁰ C (155⁰C IEC temperature of insulation)
- Class H = 125⁰ C (180⁰C IEC temperature of insulation)

It can be observed from Fig. 3.2 that the average expected life of the brushless servomotor doubles for a 10⁰ C winding temperature drop. The temperature rise limitation is applied to the winding in order to protect the winding insulation system. However in the BPM synchronous servomotor used in this research work the critical components regarding limited temperature may be different. The optical encoder electronic circuit has a temperature limit that is normally lower than that of the winding insulation. Another problem of excessive temperature rise can be the loss of flux in the PM and this will cause increased MMF and copper loss (I^2R) for a fixed torque and demagnetization may occur. Also the bearing life, the housing safety limit or the use of a plastic cover can all be temperature limiting components of a BPM synchronous servomotor.

It follows from the above that thermal analysis is crucial for prediction of the rated torque of a BPM synchronous servomotor for a specified thermal rating performance class.

3.3. Thermal Aspects of Prototype Brushless Servomotors

The BPM synchronous servomotors studied in this research programme have a cylindrical inner rotor surface with mounted PM as described in chapter 2 and are all naturally cooled. All the servomotors are mounted on a vertical flat plate, i.e., mounting flange, and are horizontally orientated for testing as shown in Chapter 4.

Therefore all the existing natural convection calculations for a vertical flat plate and for horizontal cylinder can be used in order to predict the thermal behaviour of the prototyped servomotors. For testing results only steady state analysis is performed, and steady state simulation solutions are obtained

using thermal lumped circuit models for the concentrated winding configuration servomotor.

To facilitate a fair comparison, the current design uses trickle impregnation and therefore the new design is also impregnated with the same material in order to avoid any thermal advantage. The same electric wall insulation is applied to both prototypes and therefore maintains the same wall thermal conductivity between the windings and the stator core.

The new design has a significantly shorter overhang and therefore the housing length is considerably smaller, making the overall volume of the new servomotor smaller. However this increases the thermal resistance between housing surface and the surroundings. The prototyped servomotors have similar bore radii, the same outer diameter, and identical housing surface and material.

3.4. Traditional Design Methods

The traditional design method for the BPM synchronous servomotor is based mainly on designer experience, pre-defined sizing methods based on graphs and tables, and some rules of thumb (Staton, 2012). Traditionally the electromagnetic design has received much more attention than thermal design.

The main reason for this is that electric motor designers usually have an electrical, rather than mechanical engineering background. Also, the tools available for thermal design normally require an in-depth understanding and experience of heat transfer processes for their effective use. Consequently the designer tends to produce an oversized servomotor for a given application, occasionally under-designed with dire consequences.

3.4.1. Traditional Sizing Methods

The traditional sizing method is based on a single parameter as shown in Fig. 3.3 and Fig.3.4. This is the thermal resistance defined between the winding surface and the ambient surroundings. Other thermal data such as the

housing heat transfer coefficient illustrated in Fig.3.4 or the winding current density are all obtained using simple rules of thumb.

Test results of existing BPM synchronous servomotors can be used and the competitor catalogue data can be very useful (Staton, 2012).

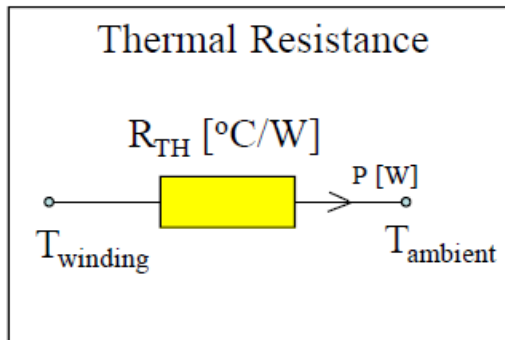


Fig. 3.3. Traditional motor sizing method based on single thermal resistance.

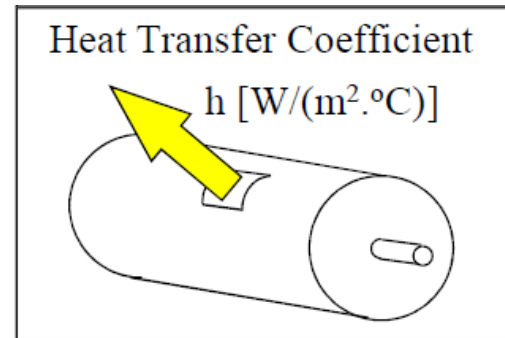


Fig. 3.4. The traditional motor sizing method based on single heat transfer coefficient.

This model is over simplified for a relatively complex thermal system such as the BPM synchronous servomotor and obviously creates problems in terms of accuracy of the model. The designer simply has no idea of where to concentrate design effort due to a poor understanding of the thermal behaviour between the winding and its surroundings.

3.4.2. Typical Rules of Thumb

Rules of thumb are based on the dimension values of electric motors data gained from tests on existing motors.

Different selected data sets can result in the predictions of the required motor sizes being very different for a given application.

Consequently the designer will over-design resulting in an unnecessarily large and heavy thereby wasting material. Occasionally under-designing can result due to inaccurate data resulting in an undersized servomotor that will overheat.

Some important rules of thumb exist for the winding current densities and for the heat transfer coefficients as shown in TABLE 3.1 and TABLE 3.2.

TABLE 3.1. Typical current densities (continuous operation) (Staton, 2012).

Condition	A/mm ²	A/in ²
Totally enclosed	1.5 - 5	1000 - 3000
Air-over, fan-cooled	5 - 10	3000 - 6000
Liquid cooled	10 - 30	6000 - 20000

TABLE 3.2. Typical heat transfer coefficients (continuous operation) (Staton, 2012).

Cooling	W/m ² °C
Air natural convection	5 - 10
Air forced convection	10 - 300
Liquid cooled	50 - 20000

The large ranges of values presented for each running condition shows clearly the difficulty of this approach and that considerable experience is required to use the data effectively.

3.5. Modern Design Methods

The difficulties of sizing and selecting parameters for electric machines are very much reduced by the available modern design methods such as thermal lumped circuit models (Motor-CAD) and numerical thermal analysis (FEA).

Thermal lumped circuit models are analogous to electric circuits, comprising resistances, sources, capacitances connected between nodes but heat power flows through the circuit rather than current. This greatly helps a designer with an electrical background. This analytical method is extremely fast when compared with FEA or CFD numerical methods due to the relatively small number of numerical calculations entailed. FEA and CFD however, are more accurate but are generally more time consuming due to the difficulty in preparing appropriate modelling information for their use.

3.5.1. Thermal Lumped Circuit Model

A thermal lumped circuit network is shown in Fig. 3.5 and this comprises:

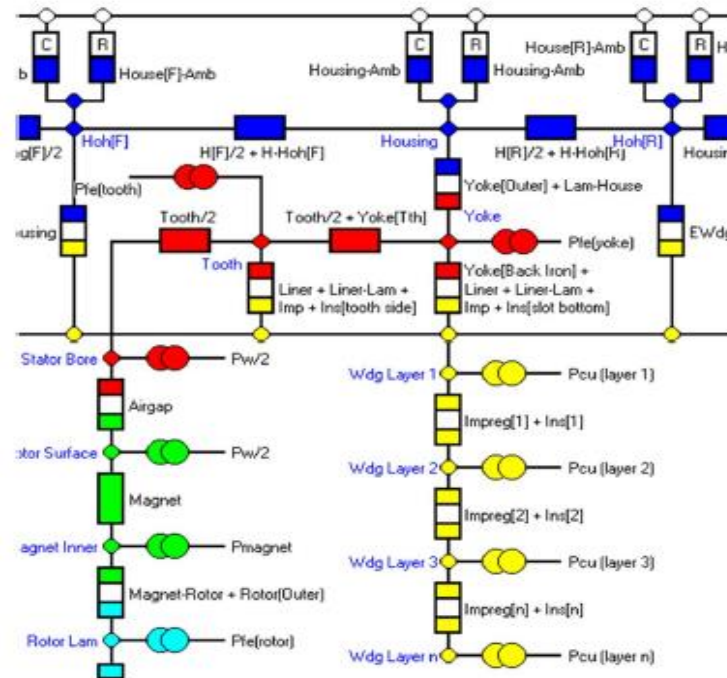


Fig. 3.5. Example of heat transfer network for an electric motor.

- thermal resistances analogous to electrical resistances,
- power sources analogous to current sources,
- thermal capacitances analogous to electrical capacitances,
- nodal temperatures analogous to nodal voltages, and
- power flow through resistances analogous to current flow through resistances.

As shown in Fig. 3.5, thermal resistances are placed in the circuit to model heat transfer paths in the servomotor, due to conduction, convection and radiation.

The conduction heat transfer equation for a thermal resistance is written as

$$R_{con} = \frac{L}{kA} \quad (3.1)$$

where L [m] and A [m²] are, respectively, the length and area obtained from the motor geometry and k is the thermal conductivity of the material in watts per meter per degree Celsius.

The convection heat transfer equation for a thermal resistance is written as

$$R_{conv} = \frac{1}{h_c A} \quad (3.2)$$

where h_c [W / m² · °C] is the heat transfer coefficient of convection obtained from the empirical dimensionless analysis formulation.

The radiation heat transfer equation for a thermal resistance is

$$R_{rad} = \frac{1}{h_r A} \quad (3.3)$$

where h_r [W / m² · °C] is the heat transfer coefficient of radiation.

The power inputs are located on the nodes where the losses occur, examples being windings and stator core components where copper and iron losses occur. Their detailed calculations are described in the coming pages.

Thermal capacitances are important for transient analysis. The capacitance, C , of a servomotor component is simply calculated as follows:

$$C = m \times c_p \quad (3.4)$$

where m is the mass of the component and c_p is specific heat capacity of its material.

3.5.2. Numerical Thermal Analysis

There are two basic types of numerical thermal analysis (NTA) available for BPM synchronous servomotors, i.e., finite element analysis (FEA) and computational fluid dynamics (CFD).

Each of which has pros and cons as listed in TABLE 3.3. Fig.3.6 and Fig.3.7 show colour shade results with corresponding quantity (temperature) and scale (colour) for the numerical thermal analysis using FEA and CFD, respectively. The key requirement is to know and define the geometric details in order for the FEA to predict the conduction heat transfer accurately. This is difficult to achieve due to the complexity of the structures comprising components of different materials in a BPM synchronous servomotor.

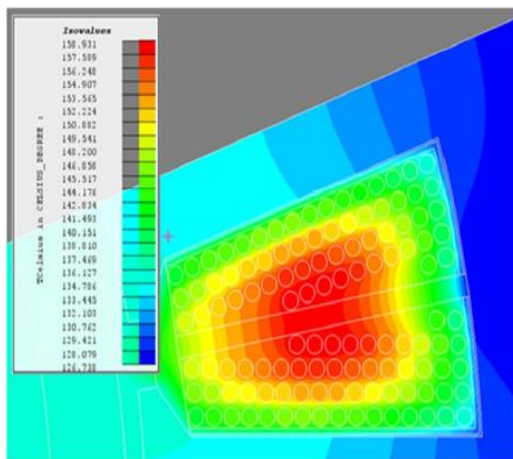


Fig. 3.6. FLUX 2D FEA winding thermal image.

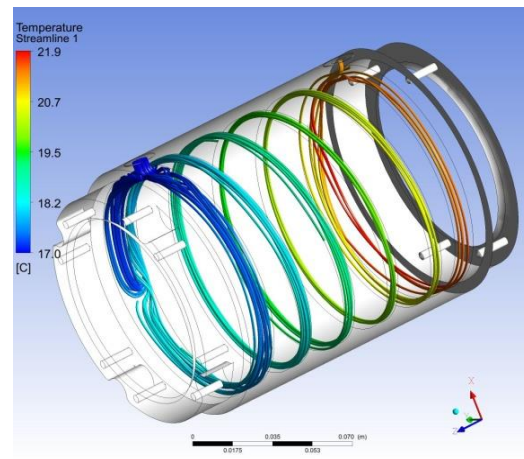


Fig. 3.7. ANSYS housing water flow.

Similar to the problems faced in lumped circuit analysis, the gaps between the servomotor components and windings are unknown but can be modelled in FEA and good data can be collected to tune the analytical thermal lumped circuit models. Some level of tuning is required in order to produce a good model and this can be time consuming, but the time saved in fast computation using the accurately tuned lumped circuit model can compensate for this.

For visualization of heat flow, CFD is the best option. This, however, can only be relied upon for this visualisation as the numerical results can be very inaccurate due to the difficulty of inputting the correct modelling information to the package. Similarly to FEA thermal modelling using CFD and the computations take several days rather than seconds as is the case with the lumped circuit method. Thus the lumped circuit method is the main tool used in this research work for rapid thermal modelling analysis.

TABLE 3.3. Numerical thermal analysis (NTA) and the respective strengths and weaknesses

NTA	PROs	CONs
FEA	<ul style="list-style-type: none"> • Accurate calculation of conduction heat transfer • Good for tuning and checking design solutions • Good visualization of temperature rise in the servomotor components • Good to model difficult part of the thermal design • Good data can be generated to aid thermal lumped circuit model for fast analysis 	<ul style="list-style-type: none"> • Slow in the process when compared with thermal lumped circuit model • Difficult to model interface gap or gaps in the windings • The boundary conditions for convection and radiation have to be input by the user • Generally difficult in thermal calculations • Need for calibration of model to increase accuracy
CFD	<ul style="list-style-type: none"> • With experience, an accurate solution can be obtained • Heat transfer trend is calculated correctly • Excellent for visualization of flow in difficult parts • Low error in fluid flow thermal distribution • Good to model difficult part of the thermal design • Good to calibrate analytical thermal lumped circuit 	<ul style="list-style-type: none"> • When predicting heat transfer the errors tend to be very large compared with FEA • Not specific to electric motors and therefore a general purpose CAE and therefore very difficult to model servomotor • Extended time for data input for the geometry • The computation time can take hours if not days rather than seconds

3.6. Heat Sources in Brushless Servomotor

According to (Staton, 2012) (Hendershot et al., 2010) in a BPM synchronous servomotor, fortunately the two highest losses occur on the stator side, as shown in Fig. 3.8, and not in the rotor as is the case with DC motors or induction motors.

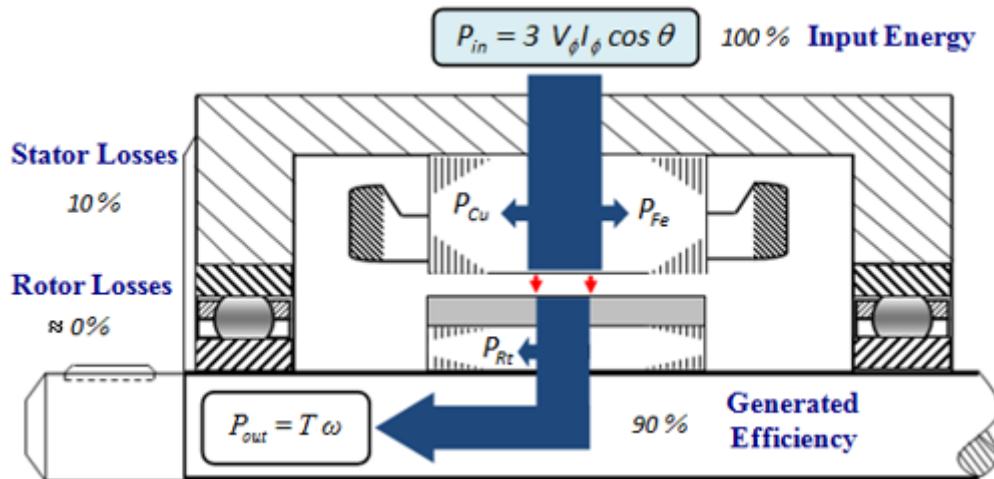


Fig. 3.8. TENV brushless servomotor with main losses to be removed.

These losses that cause heat that need to be distributed and removed from the servomotor are copper losses (I^2R loss) and iron losses proportional to $(flux \cdot frequency)^2$. The efficiency and temperature of a servomotor depend mainly on these two loss components.

Copper loss tends to be dominant at low speeds and the iron losses at high speeds. The significant losses in surface mounted BPM synchronous servomotors are as follows:

- In the stator copper windings (Copper Loss)
- In the stator iron (Iron Losses)
- In the permanent magnets (Eddy Current Loss)
- Windage loss due to rotation
- Friction loss due to rotation (negligible in BPM)

3.6.1. Copper Loss Calculation

According to (Hendershot et al., 2010) the copper loss, also referred to as Joules loss, is the largest component of power loss in BPM synchronous

servomotors. Neglecting AC current effects, the calculation of this loss is based upon the expression,

$$m i_{ph}^2 R_{ph} , \quad (3.5)$$

where m , i_{ph} and R_{ph} are, respectively, the number of phases, the RMS phase current and the phase resistance. When current is passed through the windings, the temperature of windings increases, causing the resistivity also to increase according to

$$\rho = \rho_a [1 + \alpha(\Delta T)] \quad (3.6)$$

where ρ_a [Ohm-m] is the resistivity at ambient temperature, α is temperature coefficient of resistivity and ΔT is the thermal differential potential between the winding temperature and the ambient temperature that causes the flow of heat energy.

The converted mechanical power or the output power, P_{out} , is the product of the torque, T , in [Nm] and the rotational speed ω in [rad/s] as shown in Fig. 3.8.

3.6.1.1. Copper Loss and Winding Temperature

As shown by equation (3.6), the copper resistivity increases linearly with the winding temperature, which ultimately limits the motor torque. The temperature coefficient is $\alpha = 0.00393 / ^\circ C$ for the copper winding and therefore

- A 50°C temperature rise causes a 20% increase in resistance.
- A 140°C temperature rise causes a 55% increase in resistance.
- If the current remains constant, the increase in the copper loss is proportional to the increase in resistance.

3.6.1.2. Copper Loss and Permanent Magnet Temperature

Increased magnet temperature affects the remanence flux density level, B_r , of the magnet and according to (Staton, 2012) this relationship is equivalent to

torque being proportional to the current. However an increase in current will cause an increase in copper loss proportional to I^2 and any increase in the magnet temperature will lead to a loss of flux and the current needed for a given torque must therefore be increased, meaning a higher I^2R loss. Typical temperature coefficients of B_r for different permanent magnet materials are as follows:

- Ferrite: $\alpha_r = -0.2 \text{ \%/}^\circ\text{C}$ (-20% flux for 100 °C rise)
- Sm-Co: $\alpha_r = -0.03 \text{ \%/}^\circ\text{C}$ (-3% flux for 100 °C rise)
- Nd-Fe-B: $\alpha_r = -0.11 \text{ \%/}^\circ\text{C}$ (-11% flux for 100 °C rise)

Proximity losses can influence the copper loss when the current in a conductor is influenced by the current flowing in neighbouring conductor. This is an AC effect and FEA is used for the calculations.

3.6.2. Iron Loss Calculation

Iron losses, or the core losses, are normally the second largest component of power loss in the BPM synchronous servomotor. These losses are principally 'classical' eddy current and hysteresis losses. They are usually reduced by means of laminations and use of special materials (i.e., silicone).

They are difficult to calculate accurately using loss data obtained from the manufacturer mainly due to the inaccuracy of this data, which is derived from sinusoidal waveforms that are very different to those obtained from a servomotor experimentally. Also the stress of manufacture on the laminations changes their characteristics.

Hence calibration using tests on the physical servomotor is the best solution when available. Analytical and numerical methods are used for calculation of the losses based on these measurements.

3.6.2.1. Iron Loss Calculation (Analytical)

The losses are mainly dependent on the flux density and the frequency. The hysteresis loss is due to the reluctance of the steel or soft magnetic alloy to

change its magnetic state in the complete electrical cycle represented by a pair of magnets.

The energy loss per cycle is proportional to the area enclosed by the B/H loop and therefore the power loss is proportional to the product of this area and the frequency. Typical B/H loops of high and low hysteresis loss materials are illustrated in Fig. 3.9.

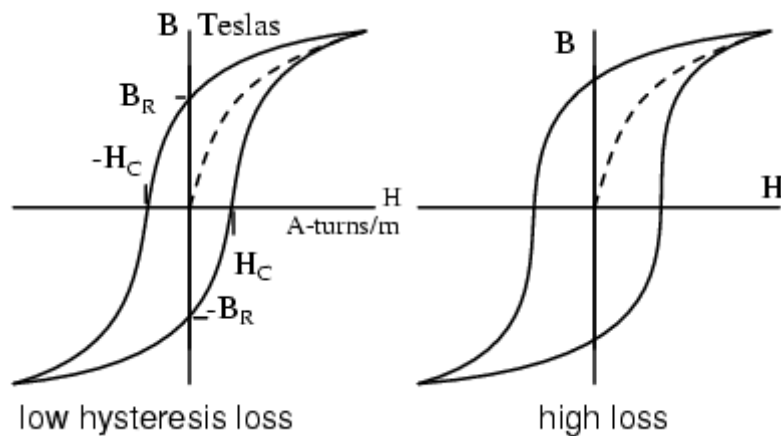


Fig. 3.9. Hysteresis loop with low loss and high loss.

The hysteresis loss is calculated as

$$P_h = C_h B_{pk}^n \quad [W/Kg] \quad (3.7)$$

where n is dependent on the type of material and according to (Hendershot et al., 2010) this value falls between 1.6 and 2.2, it is not constant and varies with peak flux density level B_{pk} and frequency f .

The eddy-current loss component is due to circulating current paths due to e.m.f.s induced by the changing field and varies with the square of peak flux density and the square of the frequency. The formula is similar to the classical one with frequency and flux density dependence, and is as follows:

$$P_e = C_e f^2 B_{pk}^2 \quad [W/Kg] \quad (3.8)$$

where the coefficient C_e is calculated as

$$C_e = \frac{\pi^2 t^2 \sigma}{6 \rho_m} \quad (3.9)$$

where t is the lamination thickness, σ is the material conductivity and ρ_m is the material mass density (Hendershot et al., 2010).

To calculate the combined eddy current and hysteresis losses, equations (3.7) and (3.8) may be combined.

The loss coefficients, C_h and C_e need to be found first using data from steel manufacturers. Then

$$P_c = C_h f B_{pk}^n + C_e f^2 B_{pk}^2 \quad (3.10)$$

Curve fitting from test data can be used to obtain the following:

$$P_c = C_h f B_{pk}^{a+bB_{pk}} + C_{e1} [dB/dt]^2 \quad (3.11)$$

and coefficient C_h is found as

$$C_h = \frac{h P_c}{B_{pk}^n f} \quad (3.12)$$

where h is the fraction of the total loss attributable to hysteresis. In (3.11),

$$C_{e1} = \frac{C_e}{2\pi^2} \quad (3.13)$$

and in (3.10),

$$C_e = \frac{P(1-h)}{f^2 B_{pk}^2} \quad (3.14)$$

A more sophisticated algorithm is that of Bertotti, which includes an iron loss term as a function of frequency and the peak magnetic flux density, as follows:

$$\text{Power Density} = C_1 B_m^2 f + C_2 (B_m f)^2 + C_3 (B_m f)^{3/2} \quad (3.15)$$

where the C_1 term is due to hysteresis, the C_2 term is due to eddy currents, the C_3 term is due to excess losses. The three coefficients can be calculated based on manufacturer's data. The coefficient, C_2 , is a function of the stator magnetic lamination thickness and its electric conductivity. The coefficient, C_3 , is a function of the cross sectional area of the lamination sheet and the field density level.

3.6.2.2. Iron Loss Calculation (Numerical)

FEA software can be used to get a more accurate estimate of the iron losses in the machine. The calculation is based on similar equations as used in the analytical method but applied to each element.

3.6.3. Magnet Loss Calculation

Analytically, the current density in the magnets is calculated according to Maxwell's second equations, as follows:

$$\oint E \cdot ds = -\frac{d}{dt} \iint_s B \cdot d\alpha \quad (3.16)$$

The eddy current losses in the magnets can be estimated empirically using the following equation:

$$P_m \approx \frac{V_m b_m^2 B_m^2 \omega^2}{6\rho_m} \quad (3.17)$$

where ω , ρ_m , V_m and B_m are angular frequency, magnet resistivity, total volume of the magnets, and the magnetic flux density in the air gap.

The magnet loss calculation requires the following

- Some level of experience will help for better tuning of the FEA
- Each magnet is modelled as a separate solid conductor
- Need to take into account the switching and slot opening effects

3.6.4. Windage Loss Calculation

The hydrodynamic losses for a fluid medium can be approximated by (Staton, 2012)

$$P_{hydr} = 0.5 C_m \rho \pi l_{act} (d_r/2)^4 \Omega \quad (3.18)$$

Where

- ω is speed in [rad/s]
- ρ mass density [Kg/m³]
- d_r rotor external diameter [m]
- l_{act} active length of the rotor [m]
- C_m loss coefficient

The dimensionless loss coefficient C_m is determined by:

$$C_m = e^\gamma / 1000 \quad (3.19)$$

where γ is a function of Taylor's number (Staton, 2012).

For Taylor's number, $T_a > 400$, γ is given by

$$\gamma = \ln(6.3) - 0.141 \cdot [\ln(T_a) - \ln(400)] \quad (3.20)$$

and when $T_a < 400$, γ is given by

$$\gamma = \ln(23) - 0.351 \cdot [\ln(T_a) - \ln(10)] \quad (3.21)$$

The following equation defines the Taylor's number

$$T_a = \frac{\delta \cdot \frac{d_r}{2} \cdot \Omega}{\frac{\beta}{\rho}} \cdot \sqrt{\frac{\delta}{\frac{d_r}{2}}} \quad (3.22)$$

where δ is the fluid gap [m] and β is the viscosity of medium [Pa.s].

Means of estimating losses in electrical machines are available but must be used with care. Both analytical and numerical methods can be used, the latter being more accurate. It is impossible to get exact results due to many uncontrollable factors being introduced due to component preparation and manufacturing processes.

3.7. Lumped Parameter Thermal Model of a Brushless Servomotor

Thermal lumped circuit modelling for inner rotor radial-field brushless servomotors with T-equivalent circuits as basic elements of network is frequently presented to estimate heat removal (Mellor, 1983). When the prototypes are naturally cooled, heat is removed by convection, conduction and radiation.

This is the cheapest form of cooling when compared with other cooling methods such as air blow (fan), liquid or steam, which also bring challenges in the servomotor manufacturing and its applications.

However, when forced cooling is applied, for example via external flow of air or direct water over the stator, both efficiency and performance increase considerably.

In this research work all the BPM synchronous servomotors are plate or flange mounted, and therefore a considerable amount of heat is transferred to the surrounding air through the mounting plate.

The mounting plate and the servomotor surface are painted black in order to promote the heat transfer by radiation.

Networks and equations are presented for modelling conduction of different components of a BPM synchronous servomotor. In the coming pages, the T-equivalent circuit is used to represent different components of the BPM synchronous servomotor.

The mean temperature, T_m , which is the average temperature of a whole component is obtained from the node marked Tm, as shown in Fig. 3.10

(pipe) and in Fig. 3.11 (network) that used a cylindrical pipe structure to model the stator core of the servomotor.

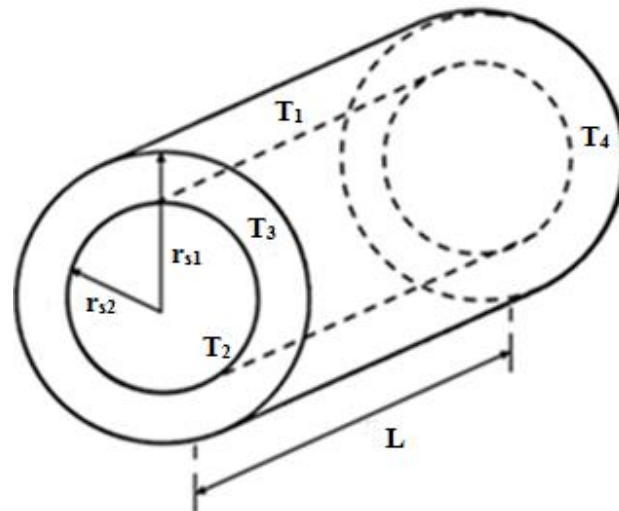


Fig. 3.10. Pipe dimensions and temperature measurement points for modelling of stator.

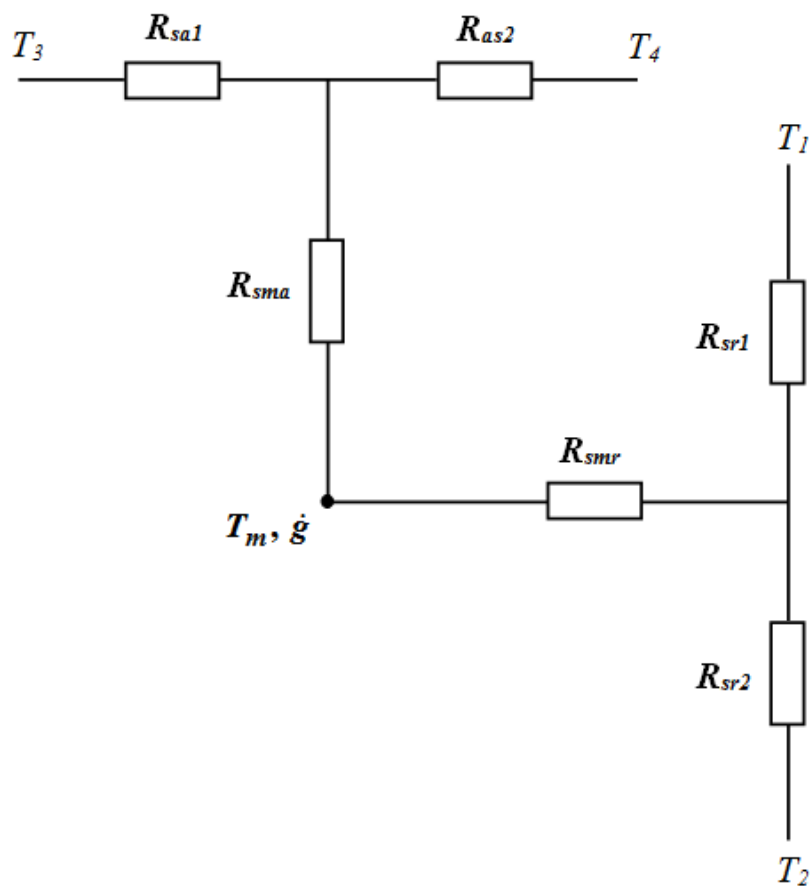


Fig. 3.11. T-equivalent circuit with elementary network components representing back-iron.

As an example, this modelling concept can be applied to the copper winding as shown in Fig. 3.12 for slot 1 with thermal resistances, R_1 , R_2 , R_m , and a copper average temperature, T_{cu} , if the heat flow in the axial direction is neglected.

The convection and radiation thermal resistances are obtained using existing calculations (Staton et al., 2008). Then a matrix solver or thermal equivalent circuit based on test data for the BPM synchronous servomotors thermal analysis is presented.

So in this research work thermal analysis is performed using the matrix solver and Motor-CAD. Then the results are compared with the results obtained from the testing of prototyped servomotors with concentrated winding technologies developed in this research programme.

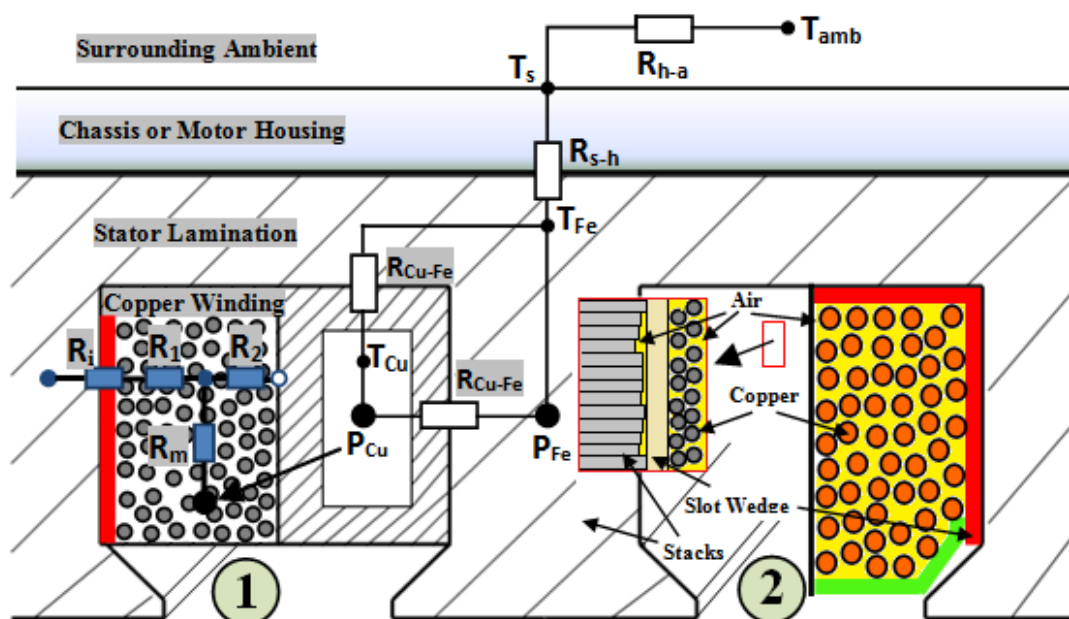


Fig. 3.12. Typical stator section of an inner rotor type brushless servomotor.

3.7.1. General Concepts

Heat transfer is estimated by first defining the loss distribution within a BPM synchronous servomotor. The stator losses are dominant in this type of machine, the copper loss being dominant at low speeds and the iron losses dominant at high speeds. However, the frictional losses and Windage losses are also considered.

The copper loss, P_{Cu} , in a servomotor stator is also known as resistive loss or Joules loss and is due to the copper resistance as explained previously. The subscript Cu is, of course, used to identify the power loss as being in the copper winding.

A typical stator section of a rotating inner rotor type motor and the main components are the motor housing, the laminations and the coil as shown in Fig. 3.12. Slot 1 shows two types of thermal equivalent circuit used to model the stator windings. Slot 2 illustrates the physical winding configuration and limitations from the heat transfer standing point.

The slot clearly shows a poor surface contact between the different stator components. There are gaps between the soft iron stacks and the electrical insulation material. There are also gaps within the winding, and also between the winding and the electrical insulation. All these gaps will reduce the motor thermal efficiency by contributing higher thermal resistances in the stator between the copper windings and the stator parts. An aim of this research work is to further investigate this efficiency problem in order to present solutions to mitigate the thermal efficiency of cylindrical inner-rotor electric motors.

For the purpose of this research work a simple uniform cylinder surface area is assumed and no cooling fins are provided for any prototype. The entire frame is assumed to have the same temperature. In practice, however, the middle point temperature reading in the servomotor housing is taken as the reference temperature. The prototyped servomotors are all naturally cooled and therefore the dissipation of heat to the surroundings through the frame housing occurs via convection and radiation thermal resistances. Thermal

conduction takes place via thermal resistances between the housing and the mounting plate, and the encoder housing. In order to use T-equivalent circuits to form a network of thermal resistances modelling conduction for the cylinder, various assumptions and simplifications are made. Good contact is assumed between the aluminium servomotor housing and the stator iron laminations. The laminations have perfect contact in axial direction.

3.7.2. Conduction Heat Transfer

Some thermal resistances, such as the resistances between the copper conductors and the thermal resistances between the slot conductors and the slot wedge as shown in Fig. 3.12, Slot 2, are very difficult to determine due to 3D effects.

According to (Incropera et al., 2011) (Holman, 1981) the steady-state temperature distribution is treated as a diffusion problem where it is essential to find the hottest temperature in the servomotor based on a given distribution of losses and a known rate of heat removal. In 3D space, the heat conduction or the heat diffusion can be represented by the following equation:

$$\nabla \cdot k \nabla T + \dot{Q} = \rho c_p \frac{\partial T}{\partial t} \quad (3.23)$$

where T is the temperature, k is the thermal conductivity of the material in W/m^0C , \dot{Q} is the power loss per unit area, ρ is the material density and c_p is the specific heat capacity of the material.

Equation (3.23) assumes no convection in the medium and density variation within the medium and is therefore only applicable to incompressible mediums. If the variation of k is small, the equation can be written as follows

$$\nabla^2 T + \frac{1}{k} \frac{\partial \dot{Q}}{\partial t} = \frac{1}{\alpha} \frac{\partial T}{\partial t} \quad (3.24)$$

where

$$\alpha = \frac{k}{\rho c_p} \quad m^2/s \quad (3.25)$$

Using a Cartesian coordinate system, $\nabla^2 T$ can be represented as (Hendershot et al., 2010)

$$\nabla^2 T = \frac{\partial^2 T}{\partial x^2} + \frac{\partial^2 T}{\partial y^2} + \frac{\partial^2 T}{\partial z^2} \quad (3.26)$$

and can be applied in cylindrical coordinates as

$$\nabla^2 T = \frac{1}{r} \frac{\partial}{\partial r} \left(r \frac{\partial T}{\partial r} \right) + \frac{1}{r^2} \frac{\partial^2 T}{\partial \theta^2} + \frac{\partial^2 T}{\partial z^2} \quad (3.27)$$

Many researchers (Sooriyakumar, 2007c) (Simpson, 2013) (Mellor et al., 1991) used the T-equivalent lumped thermal network for the thermal modelling of electric motors with inner rotor radial flux conduction thermal resistances. For example, the general cylindrical component as shown in Fig. 3.10 can be modelled as the thermal circuit shown in Fig. 3.11. Here the thermal resistances and temperature nodes are applied with some assumptions regarding the stator back iron. The conduction thermal resistance equations for a hollow cylindrical component are derived assuming that the axial and radial heat flow directions are independent as shown in Fig. 3.11. Also from Fig. 3.11 it is assumed that the mean or average temperature, T_m , is the one defining the heat flow in both the radial and the axial directions. It is assumed that there is no heat flowing in any other direction. For example, there is no heat circulating around the stator core. The heat generated, Q , and the capacitance, C , are assumed to be uniformly distributed over the body.

According to (Sooriyakumar, 2009) the total heat generation, Q_{th} , is defined as

$$Q_{th} = \dot{Q} \times V \quad (3.28)$$

where V is the volume of the cylindrical pipe shown in Fig. 3.10. In Fig. 3.11 the T-equivalent circuit is formed by using two thermal resistances to represent both radial and axial directions, and a third thermal resistance representing the mean thermal resistances in the radial and axial directions.

There are two temperature values representing specific surface temperatures in each of the radial and axial directions, and where also there is a third temperature representing the average temperature of the component for both radial and axial directions.

Losses near zero on the rotor of the BPM synchronous servomotor are assumed as already indicated in Fig. 3.8. The thermal resistances for the air gap, permanent magnet and rotor are included without heat sources since it is assumed that all the heat is generated in the stator and dissipated via the motor housing and the mounting plate.

Therefore the heat generation and transfer occur principally in the stator windings, the stator teeth, and the stator back iron, as shown in Fig. 3.12. The thermal resistance formulations are described in the coming pages.

3.7.2.1. Winding Modelling

For the winding thermal resistance formulation for both axial and radial heat flows, it is assumed that the stator slots 1 and 2 of Fig. 3.12 contain conductor bundles with trapezoidal cross sections as shown in Fig. 3.13 (Staton, 2012).

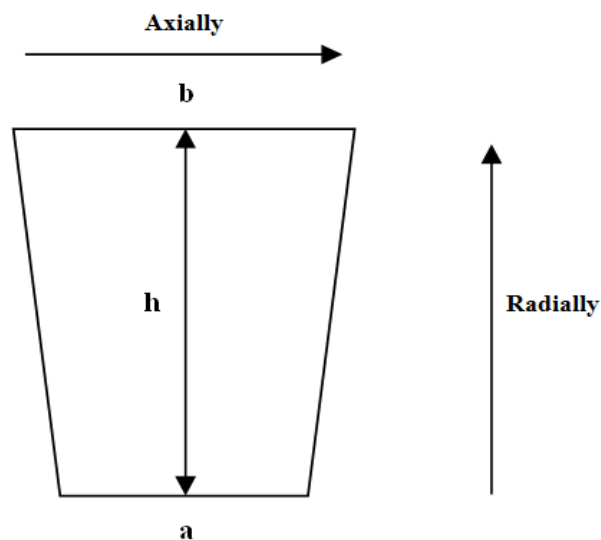


Fig. 3.13. Trapezoidal conductor bundle cross-section for winding model.

Hence the thermal resistances, R_{wa1} and R_{wa2} , for the axial heat flows are formulated in the similar fashion to Fig. 3.12 as follows:

$$R_{wa1} = R_{wa2} = \frac{b-a}{k_{wa} h L \ln(b/a)} \quad (3.29)$$

where k_{wa} is the winding bundle conductivity in the axial direction, a is the inner slot width, b is the outer slot width, $h = SD - TH$ slot depth minus slot opening angle tooth height as shown in Fig. 2.3 and L the stack perpendicular to the page.

The mean axial thermal resistance for the round wire windings is modelled as

$$R_{wma} = \frac{1}{3} R_{wa1} \quad (3.30)$$

The thermal resistances modelling the radial heat flows for the windings are

$$R_{wr1} = \frac{h}{2k_{wr}(b-a)} \left[1 - \frac{2a^2 \ln(b/a)}{(b^2 - a^2)} \right] \quad (3.31)$$

and

$$R_{wr2} = \frac{h}{2k_{wr}(b-a)} \left[\frac{2b^2 \ln(b/a)}{(b^2 - a^2)} - 1 \right] \quad (3.32)$$

Different mean radial thermal resistance formulations for the round wire windings have been proposed by several researchers (Mellor, 1983) (Staton et al., 2005a) (Demetriades et al., 2010) (Boglietti et al., 2003b) (Gerling et al., 2005), and according to (Mellor, 1983) this thermal resistance is modelled as

$$R_{wmr} = \frac{2}{\pi c L k_{wr} n} \quad (3.33)$$

where c is a constant and n is the number of stator slots.

Also (Liu et al., 1993) presented a simple analytical expression for the mean radial thermal resistance as

$$R_{wmr} \approx -\frac{R_{wr1} + R_{wr2}}{6} \quad (3.34)$$

which is a good approximation and according to (Liu et al., 1993), the problem may be solved by a conformal transformation but this results in a very complex analytical solution.

3.7.2.2. Stator Teeth Modelling

The modelling of the stator teeth is performed by the cylindrical segmentation technique (Simpson, 2013).

In this case the stator teeth are modelled as segments of a cylinder, as shown in Fig. 3.14. All of the segments are thermally connected in parallel.

The thermal resistance representing the stator teeth can be obtained by defining the equivalent arc ϕ_e of the tooth segment and then the segment cross-sectional area equal to that of the actual tooth dimension can be calculated (Sá et al., 2010-2013).

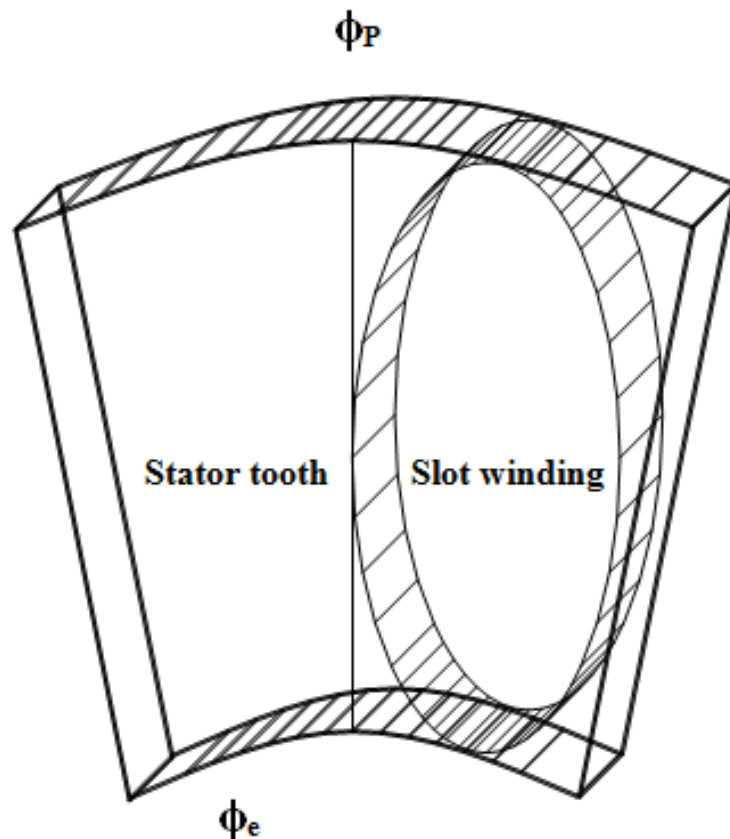


Fig. 3.14. One stator slot model.

Thus the axial thermal resistances representing the T-equivalent circuit for the stator teeth can be formulated as follows

$$R_{ta1} = R_{ta2} = \frac{\phi_p L}{2\pi k_{ta} \phi_e (r_{s2}^2 - r_{s3}^2)} \quad (3.35)$$

where ϕ_p is the half stator pole pitch, k_{ta} is the axial thermal conductivity and r_{s3} is half of the stator bore diameter as shown in Chapter 2 on Fig. 2.3.

The mean axial thermal resistance for the servomotor stator teeth is formed as

$$R_{ma} = -\frac{1}{3} R_{ta1} \quad (3.36)$$

The radial thermal resistances are given by

$$R_{tr1} = \frac{\phi_p}{4\pi k_{tr} L \phi_e} \left[1 - \frac{2r_{s3}^2 \ln(r_{s2}/r_{s3})}{(r_{s2}^2 - r_{s3}^2)} \right] \quad (3.37)$$

and

$$R_{tr2} = \frac{\phi_p}{4\pi k_{tr} L \phi_e} \left[\frac{2r_{s2}^2 \ln(r_{s2}/r_{s3})}{(r_{s2}^2 - r_{s3}^2)} - 1 \right] \quad (3.38)$$

where k_{tr} is the radial thermal conductivity of the stator teeth.

The mean radial thermal resistance is given by

$$R_{mr} = \frac{-1}{8\pi (r_{s2}^2 - r_{s3}^2) k_{tr} L} \left[r_{s2}^2 + r_{s3}^2 - \frac{4r_{s2}^2 r_{s3}^2 \ln(r_{s2}/r_{s3})}{(r_{s2}^2 - r_{s3}^2)} \right] \quad (3.39)$$

3.7.2.3. Stator Back Iron Modelling

The T-equivalent circuit thermal resistances representing the stator back iron of the servomotor have already been presented in Fig. 3.11 with their respective temperature nodes.

The mean temperature that is the average temperature of the whole cylindrical component is T_m .

The axial thermal resistances representing the T-equivalent circuit for the stator back iron are given by

$$R_{sa1} = R_{sa2} = \frac{L}{2\pi k_{sa} (r_{s1}^2 - r_{s2}^2)} \quad (3.40)$$

where k_{sa} is the axial thermal conductivity of the stator back iron.

The mean axial thermal resistance for the stator back iron is given by

$$R_{sma} = \frac{1}{3} R_{sa1} \quad (3.41)$$

The heat conduction in the radial direction is governed by Poisson's equation (Mellor et al., 1991) in one-dimension and this is given by

$$\frac{d^2T}{dr^2} + \frac{1}{r} \frac{dT}{dr} + \frac{\dot{Q}}{k_r} = 0 \quad (3.42)$$

where k_r is the thermal conductivity of the component in the radial direction.

The equation is subject to the radial boundary conditions for Fig. 3.10 as

$$T = T_1 \quad \text{at} \quad r = r_{s1}$$

$$T = T_2 \quad \text{at} \quad r = r_{s2}$$

where T_1 and T_2 are the outer and inner cylinder surface temperatures and where r_{s1} and r_{s2} are outer and inner surfaces of the hollow cylinder as shown in Fig. 3.10.

The radial thermal resistances for the stator back iron are given by

$$R_{sr1} = \frac{1}{4\pi k_{sr} L} \left[1 - \frac{2r_{s2}^2 \ln(r_{s1}/r_{s2})}{(r_{s1}^2 - r_{s2}^2)} \right] \quad (3.43)$$

and

$$R_{sr2} = \frac{1}{4\pi k_{sr} L} \left[\frac{2r_{s1}^2 \ln(r_{s1}/r_{s2})}{(r_{s1}^2 - r_{s2}^2)} - 1 \right] \quad (3.44)$$

where k_{sr} is the radial thermal conductivity of the stator back iron.

The mean radial thermal resistance is given by

$$R_{smr} = \frac{-1}{8\pi (r_{s1}^2 - r_{s2}^2) k_{sr} L} \left[r_{s1}^2 + r_{s2}^2 - \frac{4r_{s1}^2 r_{s2}^2 \ln(r_{s1}/r_{s2})}{(r_{s1}^2 - r_{s2}^2)} \right] \quad (3.45)$$

3.7.2.4. Air-Gap Modelling

The air gap heat transfer characteristics in the BPM synchronous servomotors are the least well defined, but it is assumed that the heat generated in the stator crosses the air gap directly to the rotor.

The experimental data for heat flow between concentric cylinders exist (Gazley, 1958) and this is normally what is adapted with some adjustments to the air gap heat emitted from the stator and the winding surfaces to the rotor and the permanent magnets. For example,

it is assumed that any heat emitted from the stator and the winding surface is transferred directly to the rotor through the air gap.

Hence the axial heat flow is negligible and it is assumed that there is no heat flowing axially from the air gap into the surrounding endcap air (Saari, 1998).

All modes of heat transfer occur across the air gap region, however, conduction and convection can be neglected due to the relatively small temperature difference between the rotor and stator surface.

(Gazley, 1958), however, suggested an increase of approximately 10% of the coefficients of the Taylor number (Ta) to compensate for the radiation effect as shown in TABLE 3.4 and Table 3.5.

TABLE 3.4. Evaluation of Nu according to the range of Ta

Nusselt Number (Nu)	Taylor Number (Ta)
$Nu = 2$	$Ta < 41$
$Nu = 0.212 Ta^{0.63} Pr^{0.27}$	$41 < Ta < 100$
$Nu = 0.386 Ta^{0.5} Pr^{0.27}$	$Ta > 100$

TABLE 3.5. Evaluation of Nu according to the range of Ta with 10% increase due to radiation

Nusselt Number (Nu)	Taylor Number (Ta)
$Nu = 2.2$	$Ta < 41$
$Nu = 0.233 Ta^{0.63} Pr^{0.27}$	$41 < Ta < 100$
$Nu = 0.425 Ta^{0.5} Pr^{0.27}$	$Ta > 100$

The heat transfer due to convection is highly dependent on the surface ruggedness of the rotor and the stator plus the peripheral speed of the rotor surface. In practice there will also be additional fluid disturbances due, for example, to the slot openings.

However, in order to simplify the calculations, both the rotor and stator surfaces are assumed to be smooth and therefore according to (Kylander,

1995) (Saari, 1998), the critical transition between laminar and turbulent flow is characterized by the modified Taylor number,

$$Ta = \frac{\omega_m^2 r_g g^3}{\nu_a^2}, \quad (3.46)$$

where ω_m is the mechanical angular speed of the rotor, r_g is the air gap radius, g is the air gap length and ν_a is the kinematic viscosity of the air.

Based on Becker and Kaye measurements, the Nusselt number, Nu , is equal to 2 assuming laminar flow in the air gap and for this particular case, Ta is less than 1740, which is the critical value of the Taylor number.

When this value is exceeded, turbulent flow occurs. Then the Nusselt number is given by the following empirically derived expression (Becker et al., 1962).

$$N_u = 0.409Ta^{0.241} - 137Ta^{-0.75} \quad (3.47)$$

(Staton et al., 2005b) proposed a more traditional approximation to the Taylor number that is based on a dimensionless convection correlation developed from testing on concentric rotating cylinders by (Gazley, 1958).

This work was based on the work developed by (Taylor, 1935) and in both works the Taylor number is used to judge if the flow is laminar, vortex or turbulent as the following functions of Reynolds number, Re , as

$$Ta = Re \sqrt{\frac{g}{r_g}} \quad (3.48)$$

and

$$Re = \frac{g v_r}{\nu_a} \quad (3.49)$$

where v_r is the rotor peripheral velocity.

The Nusselt number can be evaluated according to the range of calculated Taylor values as summarised in TABLE 5.4 and TABLE 5.5 according to Taylor and Gazley, respectively where Pr is the Prandtl number defined as

$$Pr = \frac{\nu}{\alpha} = \frac{c_p \mu}{k} \quad (3.50)$$

where α is the thermal diffusivity, c_p is the fluid specific heat capacity, μ is the fluid dynamic viscosity and k is the fluid thermal conductivity.

As shown in TABLE 3.4 and TABLE 3.5, Ta less than 41 indicates that the air gap flow is below *critical vortex*, the flow is *laminar* and only heat transfer by conduction takes place.

According to (Kylander, 1995) both conduction and convection take place in the air gap and the heat transfer coefficient for the air gap h_g is calculated as

$$h_g = \frac{Nu k_a}{2g} \quad (3.51)$$

where k_a is the thermal conductivity of air and g is the air gap length.

The radial thermal resistance of the air gap R_g located between the rotor and the stator surfaces is

$$R_g = \frac{1}{h_g 2\pi r_g L} \quad (3.52)$$

As shown in the above equations, the air gap thermal resistance is a temperature dependent component mainly due to the variation of the kinematic viscosity, ν_a , of air and the thermal conductivity, k_a , of air with the temperature.

Therefore these variations need to be taken into account when modelling the air gap thermal resistance.

Also the thermal expansion of both the rotor and the stator materials need to be compensated in order to obtain the effective air gap length g (Lindstrom, 1999).

3.7.2.5. Permanent Magnets Modelling

In the inner rotor surface mounted BPM synchronous servomotor configuration shown in Fig. 2.3, for simplicity, the permanent magnets are assumed to be concentric cylinders as shown in Fig. 3.10.

Then the formulation of thermal resistances can be performed in a similar fashion to the stator back iron.

Hence the axial thermal resistances for the permanent magnets are given by

$$R_{ma1} = R_{ma2} = \frac{L}{2\pi k_{ma} (r_{s1}^2 - r_{s2}^2)} \quad (3.53)$$

where k_{ma} axial thermal conductivity of the permanent magnet poles.

The mean axial thermal resistance for the permanent magnet is given by

$$R_{mma} = -\frac{1}{3} R_{ma1} \quad (3.54)$$

Hence the radial thermal resistances for the permanent magnet can be presented as

$$R_{mr1} = \frac{1}{4\pi k_{mr} L} \left[1 - \frac{2r_{s2}^2 \ln(r_{s1}/r_{s2})}{(r_{s1}^2 - r_{s2}^2)} \right] \quad (3.55)$$

and

$$R_{mr2} = \frac{1}{4\pi k_{mr} L} \left[\frac{2r_{s1}^2 \ln(r_{s1}/r_{s2})}{(r_{s1}^2 - r_{s2}^2)} - 1 \right] \quad (3.56)$$

where k_{mr} is the radial thermal conductivity of the permanent magnet, and the mean radial thermal resistance is given by

$$R_{mmr} = \frac{-1}{8\pi(r_{s1}^2 - r_{s2}^2)k_{mr}L} \left[r_{s1}^2 + r_{s2}^2 - \frac{4r_{s1}^2 r_{s2}^2 \ln(r_{s1}/r_{s2})}{(r_{s1}^2 - r_{s2}^2)} \right] \quad (3.57)$$

3.7.2.6. Rotor Modelling

The rotor without the shaft can be modelled in exactly similar way as the stator back iron and the permanent magnet. Therefore the axial thermal resistances for the rotor are given by

$$R_{ra1} = R_{ra2} = \frac{L}{2\pi k_{ra}(r_{s1}^2 - r_{s2}^2)}, \quad (3.58)$$

where k_{ra} is the axial thermal conductivity of the rotor.

The mean axial thermal resistance for the rotor is given by

$$R_{rma} = -\frac{1}{3} R_{ra1} \quad (3.59)$$

Hence the radial thermal resistances are given by

$$R_{rr1} = \frac{1}{4\pi k_{rr}L} \left[1 - \frac{2r_{r3}^2 \ln(r_{r2}/r_{r3})}{(r_{r2}^2 - r_{r3}^2)} \right] \quad (3.60)$$

and

$$R_{rr2} = \frac{1}{4\pi k_{rr}L} \left[\frac{2r_{r2}^2 \ln(r_{r2}/r_{r3})}{(r_{r2}^2 - r_{r3}^2)} - 1 \right] \quad (3.61)$$

where k_{rr} is the radial thermal conductivity of the rotor and the mean radial thermal resistance can be formulated by

$$R_{rnr} = \frac{-1}{8\pi(r_{r2}^2 - r_{r3}^2)k_{rr}L} \left[r_{r2}^2 + r_{r3}^2 - \frac{4r_{r2}^2 r_{r3}^2 \ln(r_{r2}/r_{r3})}{(r_{r2}^2 - r_{r3}^2)} \right] \quad (3.62)$$

Here, r_{r3} is the shaft radius and r_{r2} is half of the rotor core diameter.

3.7.2.7. Shaft Modelling

The shaft can be modelled as a solid cylindrical component without internal heat generation, where the axial and the radial resistances are given by

$$R_{ha1} = R_{ha2} = \frac{L}{k_h A} \quad (3.63)$$

and

$$R_{hr} = \frac{\ln(r_{ha1}/r_{ha2})}{2\pi k_h L} \quad (3.64)$$

3.7.3. Calculation for Prediction of Convection and Radiation Heat Transfer from Housing Surface

All the prototyped BPM synchronous servomotors in this research work are TCNV and have similar housing surfaces as shown in Fig. 1.3 (a) and therefore no cooling fins are taken into consideration when modelling the housing surface heat transfer.

Due to the stator lamination cylindrical structure as shown in Fig. 1.1 (a) and Fig. 2.3, the servo housing frame can be assumed to have a simple uniform cylindrical surface.

Uniform temperature is assumed over the entire housing frame and the total heat dissipation from the servomotor frame is found to be a combination of convection and radiation from the external surface to the surroundings, and conduction heat transfer to the mounting plate and the feedback housing is as shown in Fig. 1.3 (a).

The most sensitive parameters regarding accuracy of the prediction of heat transfer via convection and radiation are their respective heat transfer coefficients.

Convection heat transfer is governed by Newton's Law (Hendershot et al., 2010) as follows

$$\frac{\dot{Q}}{A} = h\Delta T \quad [\text{w/m}^2] \quad (3.65)$$

Radiation heat transfer is governed by the Stefan-Boltzmann equation

$$\frac{\dot{Q}}{A} = e \sigma (T_1^4 - T_2^4) \quad [\text{w/m}^2]. \quad (3.66)$$

In the case of the BPM synchronous servomotor, both heat transfer modes are significant when natural cooling is implemented. If however, force cooling is applied the convection tends to be very dominant, and radiation negligible depending on the air temperature.

3.7.3.1. Convection from Housing Surface

The cylindrical shape is assumed for the servomotor housing for which empirical data can be found for convection within the heat transfer technical literature (Incropera et al., 2007) (Holman, 1981).

The method of convective thermal analysis for the convective thermal resistances modelling the housing follows the earlier work of (Staton et al., 2008), (Powell, 2003) (Dajaku, 2006).

In this method of calculation, the problem is significantly simplified by introducing several approximations, assumptions and compensation factors to the analytical solutions.

The convection thermal resistance, R_{conv} , is determined as a function of the surface area, A , and the convection heat transfer coefficient, h_c as in (Staton et al., 2008). Thus

$$R_{conv} = \frac{1}{h_c \cdot A} \quad (3.67)$$

According to (Sooriyakumar et al., 2007c), natural convection heat transfer on a surface depends on the geometry of the surface as well as its orientation, the surface temperature and thermo-physical properties of the fluid, i.e., the air.

The simple empirical calculations for the average Nusselt number, N_u , in natural convection are of the form,

$$N_u = \frac{h_c \delta}{k} \quad (3.68)$$

where δ is the characteristics length of the motor geometry and k is the thermal conductivity of air.

From equation (3.68) in natural convection, N_u is a function of the surface temperature, which causes a non-linearity in the governing heat flow equation.

(Churchill et al., 1975a) provided a more sophisticated relationship for Natural convection from horizontal isothermal cylinders from their experimental data with the Raleigh number based on the diameter D of the cylinder. Thus

$$N_{uD} = 0.36 + \frac{0.518R_{aD}^{1/4}}{\left(1 + (0.559/P_r)^{9/16}\right)^{4/9}} \quad (3.69)$$

for $10^{-6} \leq R_{aD} \leq 10^9$ (Normally CTD motors have this range)

and

$$N_{uD} = \left\{ 0.60 + 0.387 \left[\frac{R_{aD}}{\left[1 + \left(\frac{0.559}{P_r}\right)^{9/16}\right]^{16/9}} \right]^{1/6} \right\}^2 \quad (3.70)$$

for $10^{-5} \leq R_{aD} \leq 10^{12}$

The Raleigh number as a function of the cylinder diameter is

$$R_{aD} = G_r P_r = \frac{g \beta \Delta T D^3}{\alpha \nu} \quad (3.71)$$

$$G_r = \frac{g \beta \Delta T D^3}{\nu^2} \quad (3.72)$$

$$P_r = \frac{\nu}{\alpha} \quad (3.73)$$

where D is the diameter of the cylinder.

3.7.3.2. Convection from Heat Sink Plate

(Churchill et al., 1975b) also proposed two equations on the basis of their experiments for a different range of the Raleigh number based heat sink plate or mounting flange length, L , as

$$N_{uL} = 0.68 + 0.67 R_{aL}^{1/4} \left(1 + \left(\frac{0.492}{Pr} \right)^{9/16} \right)^{-4/9} \quad \text{for } R_{aL} < 10^9 \quad (3.74)$$

$$R_{aL} = G_r P_r = \frac{g \beta \Delta T L^3}{\alpha \nu} \quad (3.75)$$

where L is the height of the vertical surface of mounting flange.

3.7.3.3. Radiation from Housing and Heat Sink Plate

The heat transfer rate equation for radiation is based on the Stefan-Boltzmann law and where the thermal resistance due to radiation is dependent on the material of the body, the condition of its surface and the temperature and is given by

$$\dot{q} = \sigma \varepsilon (T_2^4 - T_1^4) \quad (3.76)$$

and thermal resistance, R_{rad} , due to radiation is given by

$$R_{rad} = \frac{1}{h_{rad} \cdot A} \quad (3.77)$$

where h_{rad} is the radiation coefficient,

$$h_{rad} = \sigma \varepsilon F_{1-2} (T_0 + T_8) (T_0^2 + T_8^2) \quad (3.78)$$

where $\sigma = 5.67 \times 10^{-8}$ is the Stefan-Boltzmann constant, F is the view factor from surface finish and ε is the radiation emissivity.

T_0 and T_8 are, respectively, the room temperature and the radiation body temperature. The radiation surface emissivity is taken as unity in case of a 'black body'.

Test results show that the best value for the radiation emissivity is around 0.85. The view factor is taken as 1 due to the absence of cooling fins.

3.8. Matrix Thermal Model Solver

Fig. 3.15 shows the BPM synchronous servomotor components relevant to the thermal model and the corresponding simple thermal resistance network shown in Fig. 3.16 is used for the steady-state thermal analysis.

According to (Stening, 2006) (Boglietti et al., 2009) the temperature of each node in the network circuit is calculated as the solution to a set of linear simultaneous equations.

Thermal resistances and nodes are used to represent convection and radiation heat transfer and temperatures outside of the BPM synchronous servomotor. Internal resistances due to heat conduction from the winding to the stator core and the stator core to the housing are shown in Fig. 3.16. R_{ec} , R_{er} , R_{hc} , R_{hr} , R_{mc} and R_{mr} are the thermal resistances representing convection and radiation from the encoder housing, convection and radiation from the housing top middle surface to the ambient surroundings and

convection and radiation mounting plate to the ambient surroundings, respectively. R_{eh} and R_{mh} are resistances due to the contact between the main housing and the encoder housing and from the main housing to the mounting plate. R_{csh} and R_{cws} are contact resistances due to conduction from the stator core to the main housing and from the copper winding to the stator core. R_{ag} is the thermal resistance due to the air gap, which involves conduction and convection heat transfer modes. The powers, P_{fe} , P_{cu} , P_R and P_{ad} , represent, respectively, the iron loss, copper loss, rotor loss and additional loss within the servomotor. The steady-state thermal modeling can be used to predict the temperature distribution in the critical sections of Fig. 3.15 at different operating points. The temperatures, T_0 , T_h , T_{mp} , T_{ec} , T_s and T_w , of Fig. 3.16 are, respectively, the ambient, housing, mounting plate, encoder, stator and the winding temperatures.

Use of this lumped thermal model leads to accurate results for bodies when correct adjustments factors are applied. In natural convection, the surrounding air has a thermal conductivity around $k_{air} = 0.026W / m^0C$ and therefore the convection heat transfer tends to offer a significantly higher thermal resistance when compared with the conduction heat transfer mode in the servomotors.

This increased thermal resistance due to convection and favors radiation heat transfer mode, however radiation heat transfer mode is negligible when force convection is applied. The heat flow caused by the rotor loss is neglected in the thermal networks since it is small in comparison to the iron loss, copper loss and additional loss.

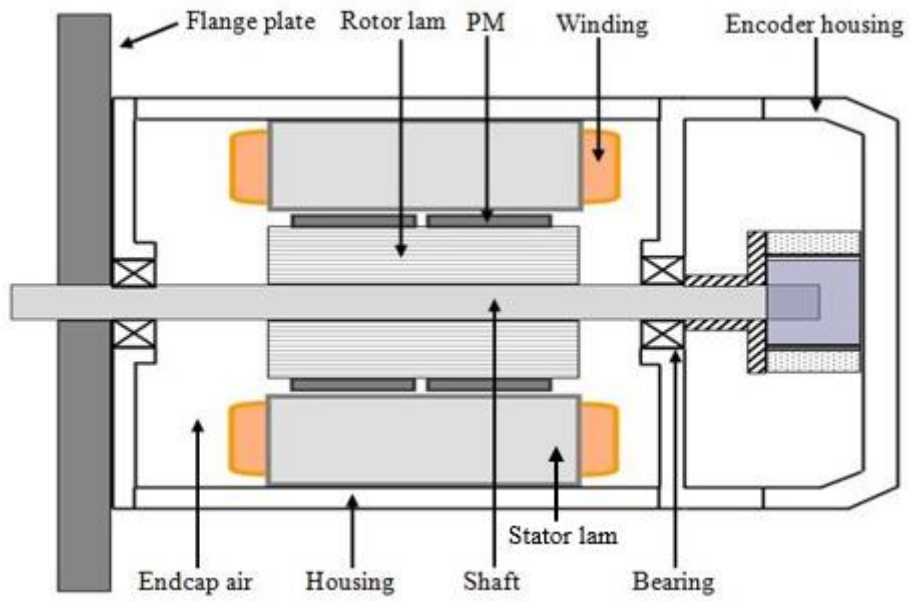


Fig. 3.15. Brushless servomotor main components of the thermal model.

This models the stator housing, flange plate and the encoder housing.

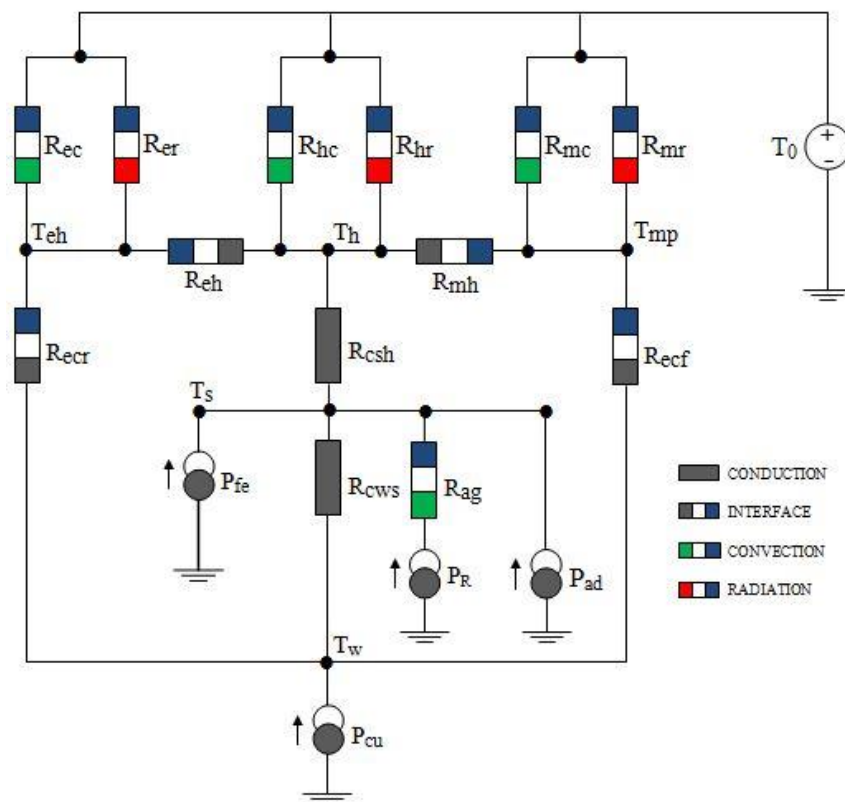


Fig. 3.16. Servomotor thermal circuit with air gap convection and rotor losses.

Also it is convenient to hold the number of components small in order to reduce the complexity of the thermal circuit and obtain fast thermal simulation results.

By applying nodal equations to the network model shown in Fig. 3.16, the following equations are obtained

$$\frac{T_h - T_{mp}}{\frac{R_a}{2} + R_{cmp}} + \frac{T_h - T_{eh}}{\frac{R_a}{2} + R_{ceh}} + \frac{T_h - T_0}{R_h} + \frac{T_h - T_s}{R_s} = 0 \quad (3.79)$$

Here, R_a is the axial thermal resistance of the housing component, R_{cmp} is the thermal resistance due to contact between the housing and the mounting plate, R_{ceh} is the thermal resistance due to contact between the housing and the encoder housing, R_h is the total thermal resistance between the housing and the ambient surroundings, and R_s is the thermal resistance between the stator core and the housing. Equation (3.79) can be written as

$$\left(\frac{1}{\frac{R_a}{2} + R_{cmp}} + \frac{1}{\frac{R_a}{2} + R_{ceh}} + \frac{1}{R_h} + \frac{1}{R_s} \right) T_h - \left(\frac{1}{\frac{R_a}{2} + R_{cmp}} \right) T_{mp} - \left(\frac{1}{\frac{R_a}{2} + R_{ceh}} \right) T_{eh} - \frac{T_s}{R_s} = \frac{T_0}{R_h} \quad (3.80)$$

Equation (3.81) is obtained from Fig. 3.16 as

$$\frac{T_{mp} - T_0}{R_{mp}} + \frac{T_{mp} - T_h}{\frac{R_a}{2} + R_{cmp}} + \frac{T_{mp} - T_w}{R_{ecf}} = 0 \quad (3.81)$$

where R_{ecf} is the front endcap thermal resistance and rewritten as:

$$\left(\frac{1}{R_{mp}} + \frac{1}{\frac{R_a}{2} + R_{cmp}} + \frac{1}{R_{ecf}} \right) T_{mp} - \left(\frac{1}{\frac{R_a}{2} + R_{cmp}} \right) T_h - \frac{1}{R_{ecf}} = \frac{T_0}{R_{mp}} \quad (3.82)$$

The expression for the thermal resistance for the encoder/feedback device is obtained as

$$\frac{T_{eh} - T_0}{R_{eh}} + \frac{T_{eh} - T_h}{\frac{R_a}{2} + R_{ceh}} + \frac{T_{eh} - T_w}{R_{ecr}} = 0 \quad (3.83)$$

where R_{ecr} is the rear endcap thermal resistance. This can be rewritten as

$$\left(\frac{1}{R_h} + \frac{1}{\frac{R_a}{2} + R_{ceh}} + \frac{1}{R_{ecr}} \right) T_{eh} - \left(\frac{1}{\frac{R_a}{2} + R_{ceh}} \right) T_h - \frac{1}{R_{ecr}} T_w = \frac{T_0}{R_{eh}} \quad (3.84)$$

The equation of the thermal resistance between the winding node temperature, T_w , and the housing node temperature, T_h , is the sum of the contributions from the windings, contact resistances, paper wall insulation material, impregnation material, stator steel, and the aluminium housing. These can be simplified to

$$\frac{T_s - T_h}{R_s} - P_{fe} - P_{ad} + \frac{T_s - T_w}{R_w} = 0 \quad (3.85)$$

where R_w is the thermal resistance between the winding and the stator core.

This equation can be re-arranged as follows:

$$\left(\frac{1}{R_s} + \frac{1}{R_w} \right) T_s - \frac{T_h}{R_s} - \frac{T_w}{R_w} = P_{fe} + P_{ad} \quad (3.86)$$

The dissipation due to copper loss is

$$\frac{T_w - T_{mp}}{R_{ecf}} + \frac{T_w - T_{eh}}{R_{ecr}} + \frac{T_w - T_s}{R_w} = W_{cu} \quad (3.87)$$

and can be rewritten as

$$\left(\frac{1}{R_{ecf}} + \frac{1}{R_{ecr}} + \frac{1}{R_w} \right) T_w - \frac{T_{mp}}{R_{ecf}} - \frac{T_{eh}}{R_{ecr}} - \frac{T_s}{R_w} = W_{cu} \quad (3.88)$$

Equations (3.79) to (3.88) can be written in the matrix-vector form and solved as follows to calculate the temperature rise in the nodes relative to a reference temperature.

$$[T] = [A]^{-1} [P] \quad (3.89)$$

Here $[P]$ is the vector of dissipation losses assigned to the nodes given by

$$[P] = \begin{bmatrix} \frac{T_0}{R_h} \\ \frac{T_0}{R_{mp}} \\ \frac{T_0}{R_{eh}} \\ P_{fe} + P_{ad} \\ P_{cu} \end{bmatrix} \quad (3.90)$$

and $[T]$ is the required temperature rise vector,

$$[T] = \begin{bmatrix} T_h \\ T_{mp} \\ T_{eh} \\ T_s \\ T_w \end{bmatrix} \quad (3.91)$$

The thermal conductance matrix, $[A]$, is formed using the thermal resistances of the model as

Due to the temperature dependence of the components in $[A]$ and $[P]$ an interactive mathematical solution must be used with regular updates in order to obtain the resulting thermal resistances.

$$\left[\begin{array}{ccccc}
 \frac{1}{\frac{R_a}{2} + R_{cmp}} & -\frac{1}{\frac{R_a}{2} + R_{cmp}} & -\frac{1}{\frac{R_a}{2} + R_{ceh}} & -\frac{1}{R_s} & 0 \\
 +\frac{1}{\frac{R_a}{2} + R_{ceh}} + \frac{1}{R_h} + \frac{1}{R_s} & & & & \\
 -\frac{1}{\frac{R_a}{2} + R_{cmp}} & \frac{1}{R_{mp}} + \frac{1}{\frac{R_a}{2} + R_{cmp}} + \frac{1}{R_{ecf}} & 0 & 0 & -\frac{1}{R_{ecf}} \\
 -\frac{1}{\frac{R_a}{2} + R_{ceh}} & 0 & \frac{1}{R_{eh}} + \frac{1}{\frac{R_a}{2} + R_{ceh}} & 0 & -\frac{1}{R_{ecr}} \\
 -\frac{1}{R_s} & 0 & 0 & \frac{1}{R_s} + \frac{1}{R_w} & -\frac{1}{R_w} \\
 0 & -\frac{1}{R_{ecf}} & -\frac{1}{R_{ecr}} & -\frac{1}{R_w} & \frac{1}{R_{ecf}} + \frac{1}{R_{ecr}} + \frac{1}{R_w}
 \end{array} \right] \quad (3.92)$$

3.9. Summary

A thermal model has been developed for the design of BPM synchronous servomotors. The model is based on a thermal network with lumped parameters represented by equivalent thermal resistances. A steady-state calculation can be performed for a constant reference temperature. The importance of thermal modelling and analysis of BPM synchronous servomotors is highlighted in terms of servomotor lifetime, sizing and performance. Different thermal modelling techniques are presented with their pro and cons. The heat transfer taking place in the servomotor due to conduction, radiation and convection is addressed in some detail. Means of estimating losses in electric machines are presented to be used with some level of care when modelling a BPM synchronous servomotor. Different component modelling is performed for individual parts of the servomotor by presenting the analytical expression and considering the component conductivity and heat transfer coefficients.

CHAPTER 4

EXPERIMENTAL RIG AND TEST PROCEDURES

4.1. Introduction

This chapter describes the experimental apparatus used to verify the theoretical predictions of the prototype servomotor performances together with the experimental procedures and the data acquisition methods required to achieve this. The tests are designed to determine the cogging torque, the open circuit iron losses and the dynamic torque rating. This is only a subset of all the BPM synchronous servomotor characteristics that can be determined using the apparatus, others being, for example, back E.M.F., torque-ripple, peak torque or friction.

A DC motor is coupled to the servomotor under test and used to turn its rotor in the cogging torque test and the rotational speed is controlled by a 5V supply. The apparatus for the iron loss test is operated up to 6000 r/min in both cold (ambient temperature) and hot (80⁰C housing surface temperature) to compare the cold and hot iron losses.

The speed for the dynamic torque rating test rotating speed is limited by the number of winding turns defined at the electromagnetic design stage in Chapter 2. Finally, the temperature data acquisition and the associated software are described.

4.2. Experimental Setup

For the measurement of the cogging torque, the key test equipment comprises a DC drive motor, a vibrometer, an oscilloscope, a DC supply and a shaft encoder for position measurement.

To determine the open circuit iron losses, the key test equipment comprises a motor drive system, a torque transducer, a digital voltmeter and a drive controller. To determine the dynamic torque rating, the key test equipment comprises a drive controller, a motor loading system, a power analyser, and a

thermometer. All the test equipment described above are the standard equipment used for current conventional BPM synchronous servomotors and have been adapted for the prototype servomotors under investigation.

4.2.1. Cogging Torque Test Setup

The main components of the cogging torque testing rig are shown in Fig. 4.1 and Fig. 4.2. These comprise a vibrometer with its sensor, feedback device, DC motor, supply cable, feedback and an oscilloscope.

The servomotor under test is fitted to the sensor as shown in Fig. 4.1 and the servomotor shaft is connected to the DC motor shaft.

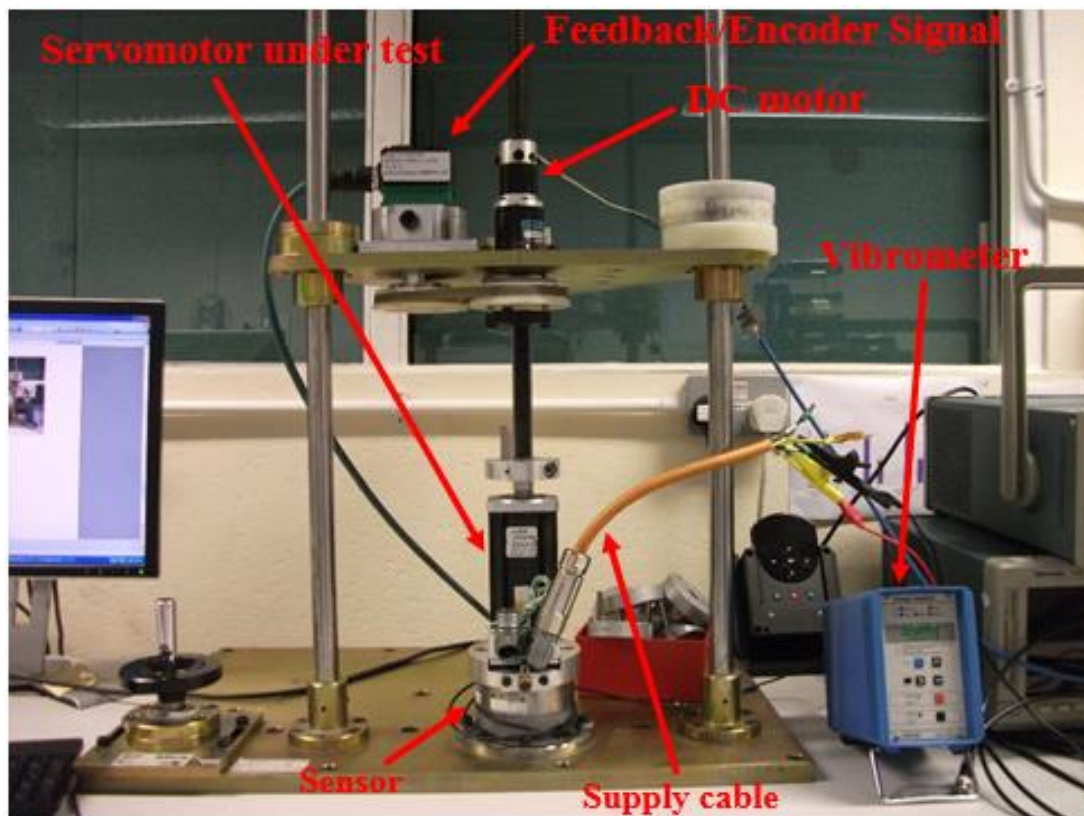


Fig. 4.1. Cogging torque test rig system components.

The servomotor supply cable is used to obtain the back EMF information for each pole of the servomotor as shown in Fig. 4.2.

The cogging torque signal can be obtained directly from the vibrometer. Also the rotor position information can be obtained from the feedback device if necessary.

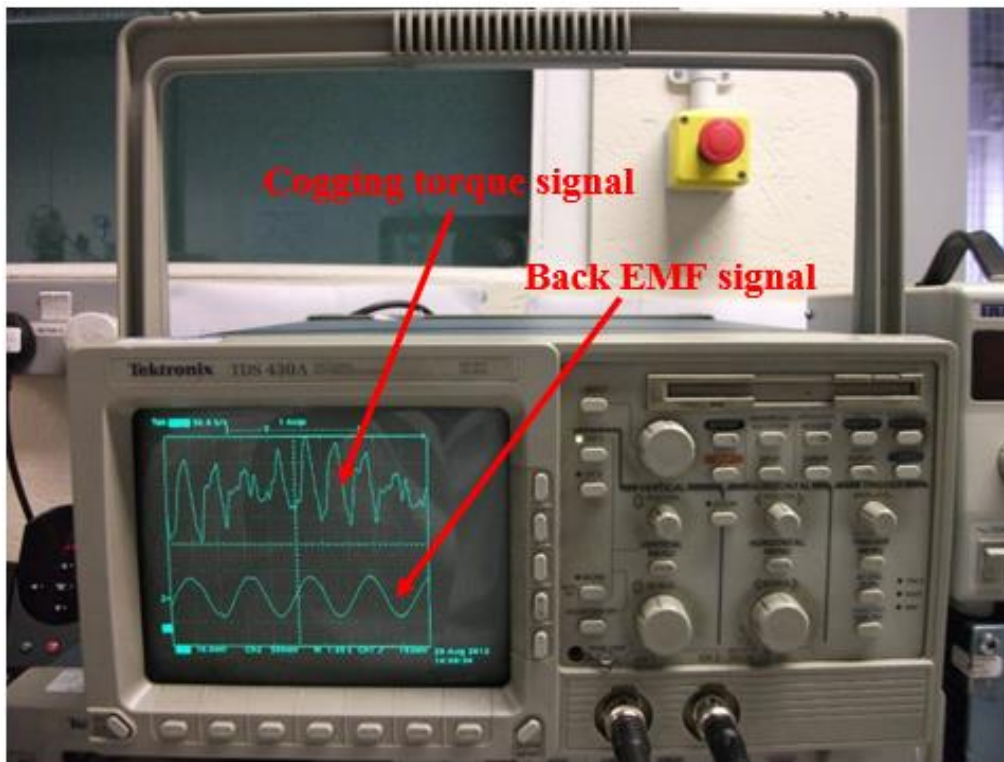


Fig. 4.2. Oscilloscope displaying cogging torque and back EMF waveforms.

4.2.2. Open Circuit Iron Loss Test Setup

It is shown in Chapter 2 and Chapter 3 that the iron losses are proportional to the number of poles and since the number of poles of the new prototype is greater than that of the current design, the open circuit iron loss test shown in Fig. 4.3 is very important in this research work.

From Fig. 4.3 it can be observed that the power cable is not connected to the BPM synchronous servomotor under test.

However, the power cable and the feedback cable are connected for the drive servomotor for speed control.

The torque transducer shown in Fig. 4.4 is mounted between the shafts of the motor drive system and the servomotor under test and therefore measures the torque applied to the servomotor by the motor drive system.

The measurements from the torque transducer, which are voltages, are obtained using a digital multimeter as shown in Fig. 4.3. Also a 24 V DC power supply provides the excitation voltage for the torque transducer.

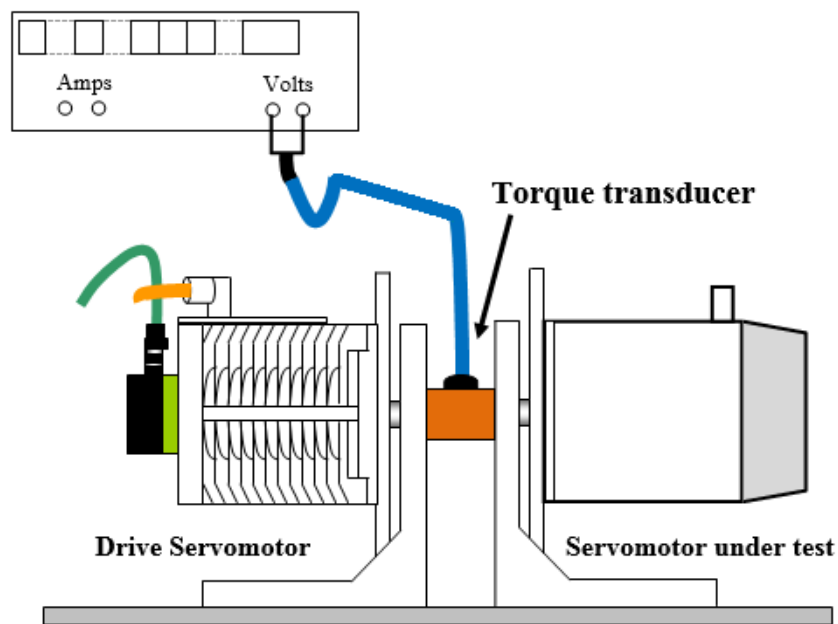


Fig. 4.3. Setup for open circuit iron losses testing.

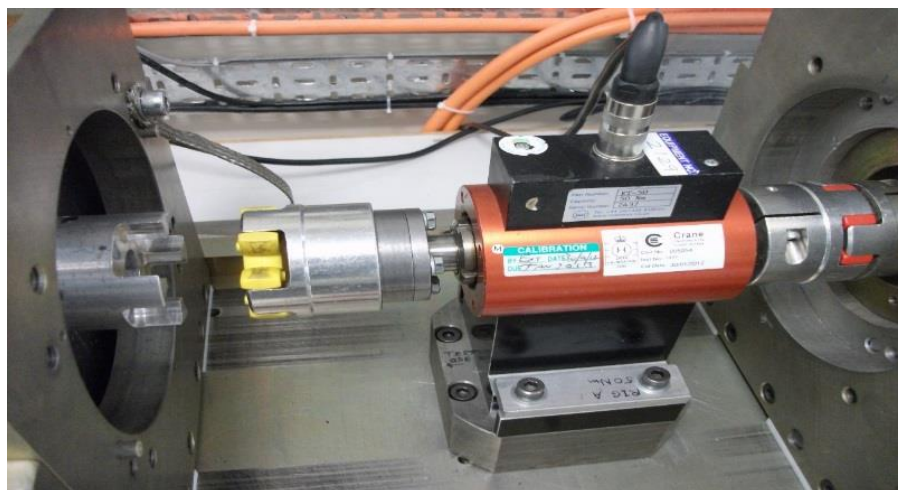


Fig. 4.4. Open circuit iron losses testing torque measurement sensor.

4.2.3. Dynamic Torque Rating Test Setup

Fig. 4.5 shows the dynamic torque rating rig with drive input, DC bus, 3-phase output measurements that are fed to a power analyser, the dynamometer load machine with its controller, temperature measurement device and BPM synchronous servomotor under test.

The drive input circuitry shown in Fig. 4.5 is essentially a 3-phase diode rectifier bridge with capacitor filter.

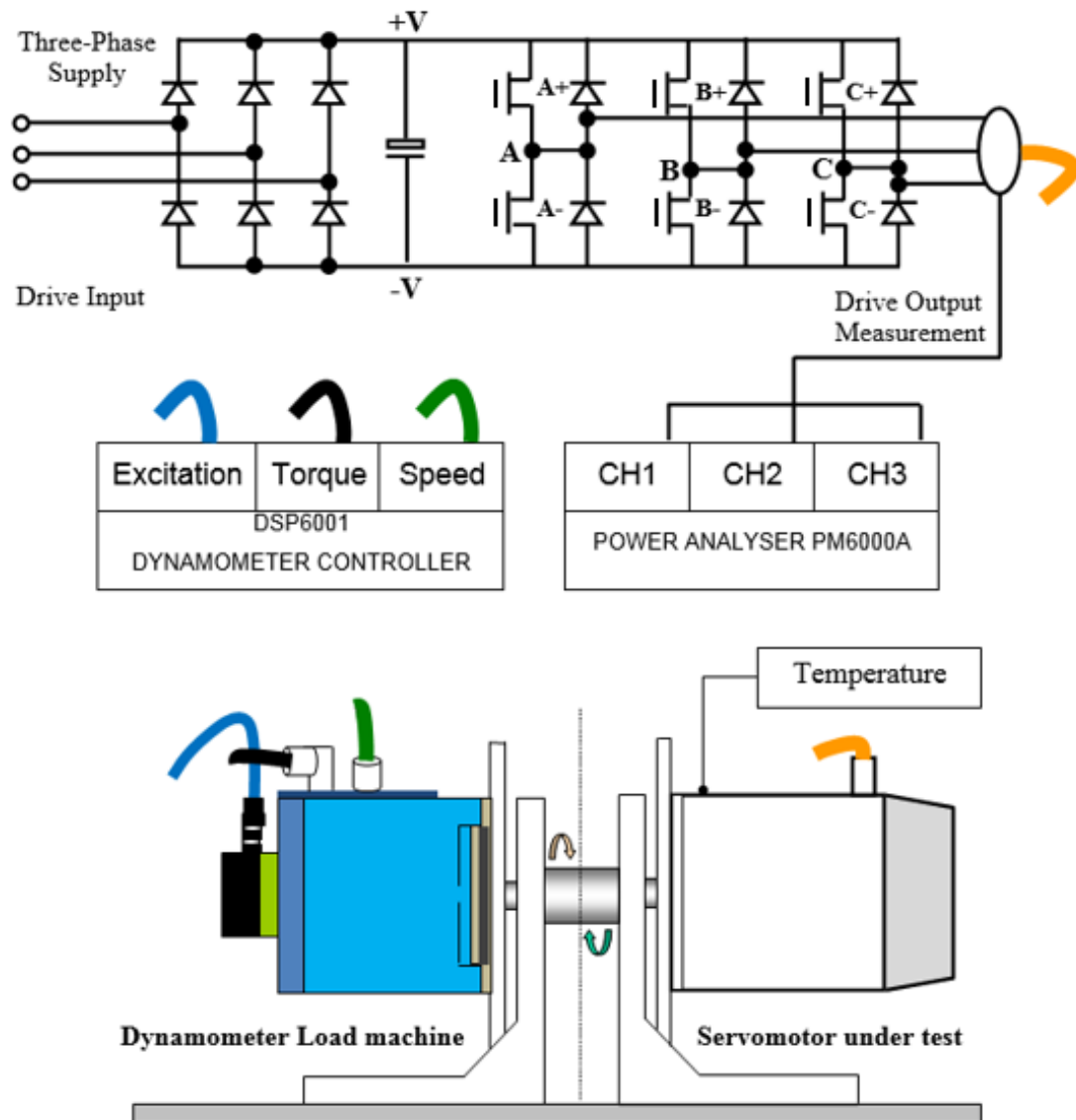


Fig. 4.5. Dynamic torque rating test rig.

All these components are incorporated in the high efficiency Control Techniques Digitax drive control system shown in Fig. 4.6 (Control Techniques, 2014). Relying on its high efficiency the drive input is not measured for the purpose of the dynamic torque rating test. The drive controller has the capability of displaying the value of the DC bus voltage using one of the control drive parameters.

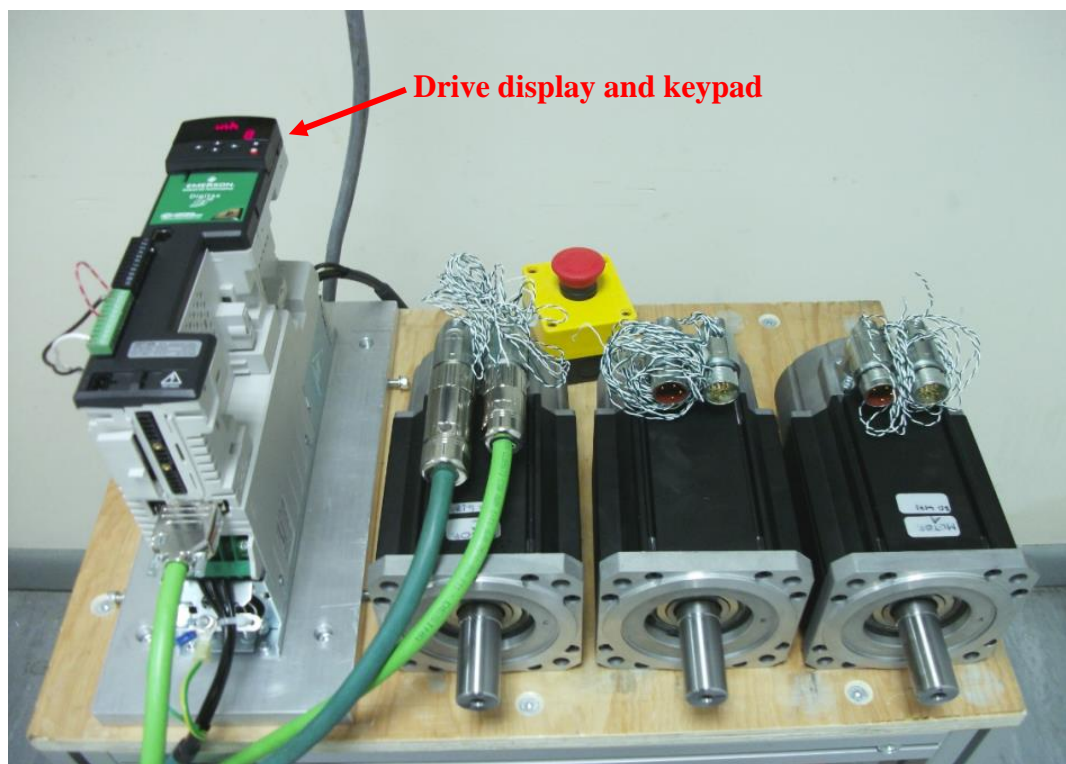


Fig. 4.6. Control Techniques Digitax drive control system and the prototypes.

The measurement of the DC bus voltage is an RMS value since, in practice, it contains a significant ripple component due to the power electronic switching. This contamination of the DC bus signal and its effects, however, are not considered to have a large impact on the current research investigation and are not considered further. Each of the three phase-to-phase PWM drive output voltage waveforms, one of which is shown in Fig. 4.7, are processed by the power analyser shown in the laboratory environment of Fig. 4.8. In Fig. 4.7 it can be observed that the output waveform of the PWM drive contains a mixture of high frequency components due to the carrier signal (PWM) and useful low frequency fundamental components shown as an alternating approximately sinusoidal signal.

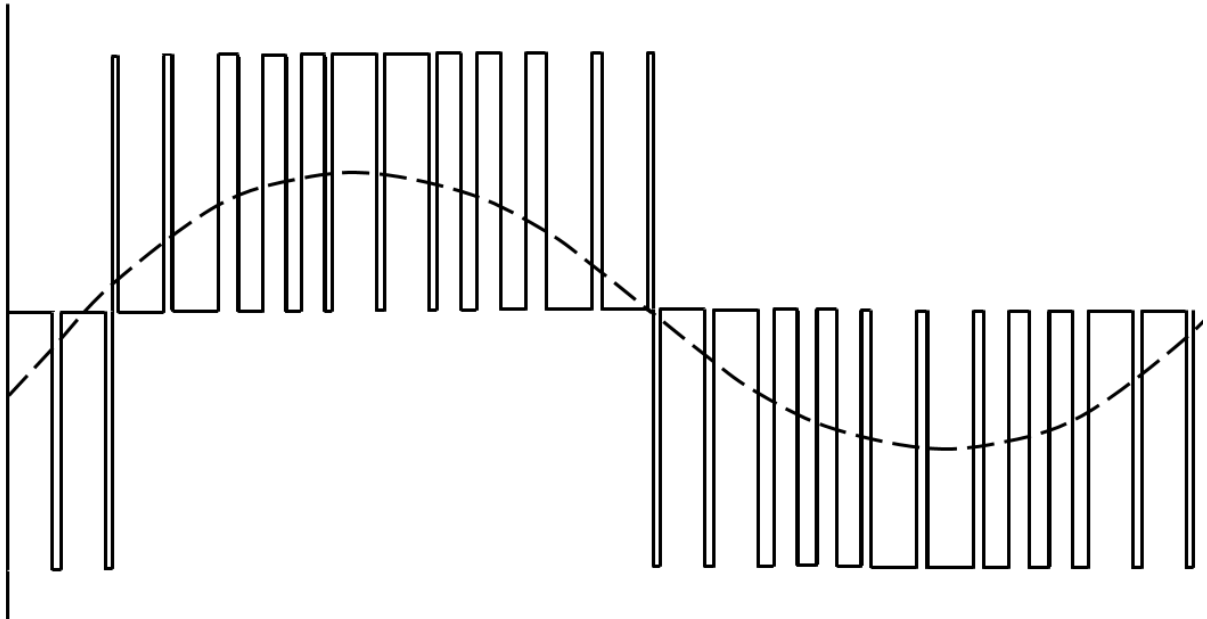


Fig. 4.7. Drive control PWM with high frequency carrier and low frequency phase-to-phase components.

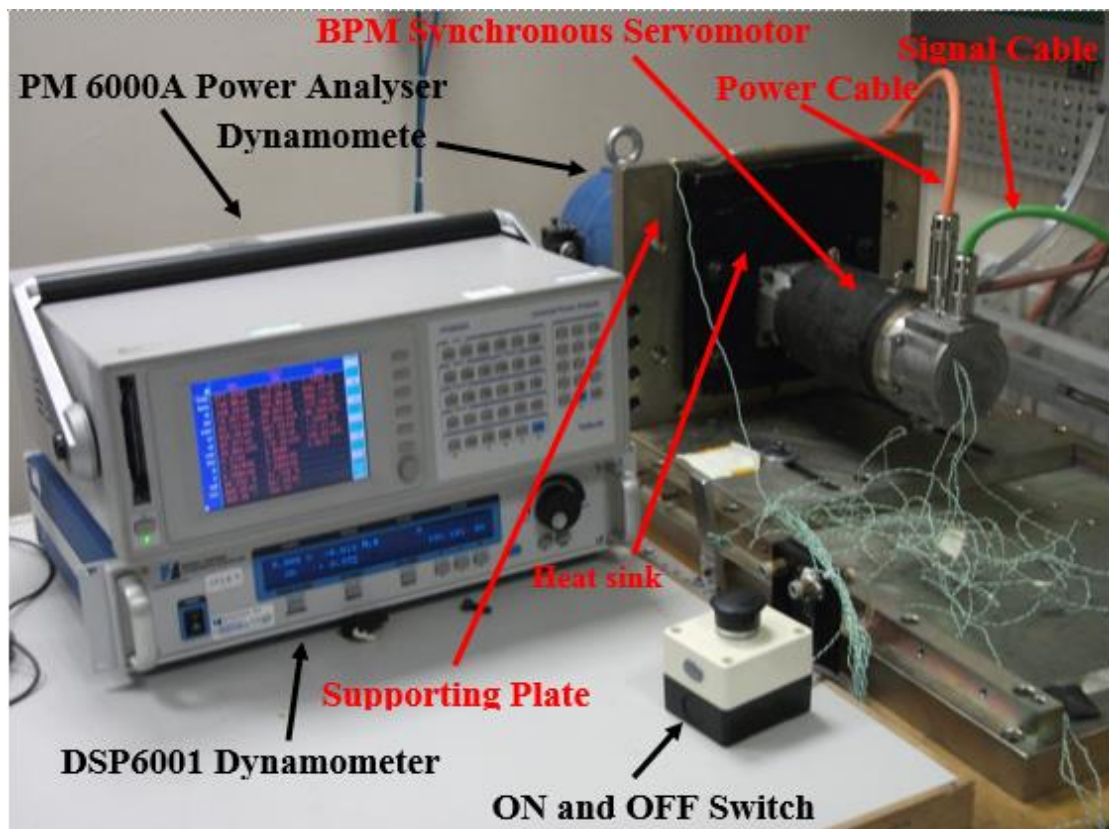


Fig. 4.8. Test setup for dynamic torque rating of brushless servomotor.

The current power analyser can either measure the high frequency components or the low frequency components but not both together. However, for this investigation, only the low frequency components are of interest. In view of the limitations of the power analyser, the low frequency waveform needs to be observed on an oscilloscope to assess the quality of the phase-to-phase voltages applied to the servomotor stator windings. The Dynamometer controller shown in Fig. 4.8 has the capability of controlling the load machine to produce a demanded load torque and display the torque level and the speed of the servomotor under test.

In preparation for this procedure, it is most important for the servomotor under test to be a) accurately aligned with the dynamometer load machine to ensure free shaft rotation and b) rigidly coupled to the dynamometer load machine to avoid torsional oscillatory modes.

Finally, the temperatures in the different sections of the servomotor under test need to be monitored.

The most important locations are the stator windings, the stator outside surface, the heat sink plate, the encoder housing and the surroundings.

It is assumed that all the power dissipation or the heat transfer from the servomotor takes place via these locations when the natural cooling process is implemented.

4.3. Experimental Procedures

The cogging torque test can be considered a zero-current, open circuit test. Assuming that the bearing friction is negligible, the torque is only due to the interaction between the magnets in the rotor and the slotted stator structure of the servomotor under test, i.e., the rate of change of the stored energy in the magnetic field with respect to the rotation angle.

For the majority of servo applications this is an unwanted effect since it impairs accuracy in position control applications and causes vibrations in speed control applications.

A simple means for the measurement of cogging torque is to rotate the servomotor shaft at a constant speed by means of the DC motor, now used as a prime mover and measure the cogging torque. It is also pertinent to monitor the flux density of the magnet poles in the rotor as this is evidence of the variation of the stored energy referred to above.

The relationship between the torque and the iron losses is very predictable due to the machine maximum power dissipation. The iron losses will be relatively low at increased torques and low to moderate speeds, but in applications requiring dynamic performance, these losses can be quite significant at higher speeds and therefore require minimisation in the servomotor design. As for the cogging torque test, the iron loss test is a zero current, open circuit test and just requires a rotating field, as explained in Chapter 3. In order to experimentally measure the iron losses, the servomotor shaft needs to be rotated at fixed speed and the flux density of the rotating field measured.

The dynamic torque rating test is arguably the most important test of this research programme, since the key aim is to produce a new servomotor with a torque speed curve lying above that of a conventional servomotor for a fixed frame size. As shown in Fig. 4.5, a considerable number of components are required to perform dynamic torque rating test. The servomotor needs to be loaded and run up to a reference temperature and then the torque speed curve measured.

4.3.1. Cogging Torque Test Procedure

The vibrometer and the sensor are used to obtain the cogging waveform on the oscilloscope as shown in Fig. 4.2.

The signal viewed on the oscilloscope can, however, contain components from sources other than the cogging torque such as mechanical vibrations due to the rotation of the shaft. To overcome this problem, frequency domain analysis is performed. So the cogging torque signal of Fig. 4.2 is sampled at a frequency known to be much higher than the highest expected frequency of its spectrum and a Fast Fourier Transform (FFT) performed.

Then the amplitude of the frequency component corresponding to the lowest common multiple of the number of stator poles and the number of rotor poles is proportional to the cogging torque amplitude. In the case of the new prototyped BPM synchronous servomotor with the 12-10 slot-pole combination, the cogging torque component is the 60th frequency component.

4.3.2. Open Circuit Iron Loss Test Procedure

The open circuit iron loss test apparatus is shown in Fig. 4.3. The procedure consists of using the drive servomotor to back-drive the servomotor under test with its stator open circuit. Then using the torque transducer for the measurement of the mean value in voltage that need to be multiply by a multiplication factor (or adjustable factor) that need to be obtained from the test assembly. The apparatus is operated at speeds of 500, 1000, 1500 and so on up to 6000 rpm. The losses are measured for both clockwise and anticlockwise rotation at these different speeds.

The iron losses are measured at the cold condition (ambient temperature) and at the hot condition (T_8 approximately 80°C), and then compared. For the hot iron losses the servomotor is run for approximately four hours at 4000 rpm monitoring the thermocouple sensor T_8 . These experimentally determined iron losses are subsequently compared with the predicted iron losses using FEA.

4.3.3. Dynamic Torque Rating Test Procedure

The simplest way to perform the dynamic torque rating test is as shown in Fig. 4.5. The load system hardware is complex and expensive but is a readily available industrial electric drive, which allows a relatively simple procedure for the dynamic torque rating, consisting of controlling the load machine to present different load torques to the servomotor and directly measuring the shaft speed.

First the servomotor under test is mounted on the rig as shown in Fig. 4.8. The next step is to set the corresponding drive parameters for the servomotor using the drive display and keypad shown in Fig. 4.6. The critical parameter settings are the number of rotor poles, the maximum speed limit (both clockwise and anticlockwise), the maximum stator current, and the drive

switching frequency, the stator voltage limit and the required speed. Then the drive is set to the auto-tune mode in which the best current angle for the servomotor is found automatically and set. Then the ON and OFF switch is used to run the servomotor. The load torque is set and applied using the dynamometer controller. The load torque is continuously adjusted until the required steady state winding temperature is reached. The speeds, temperatures, currents and torques are recorded.

4.4. Temperature Measurements

The temperature measurements are related to the dynamic torque rating test as described in subsection 4.3.3.

The open circuit iron loss test only requires a single temperature reading from the thermocouple on the servomotor stator surface temperature and any other thermometer that can be used to monitor the surface temperature.

The cogging torque test does not require any temperature reading since there is not any significant mechanical movement or current flow in the winding that would cause a temperature rise in the servomotor shown in Fig. 4.9 (a).

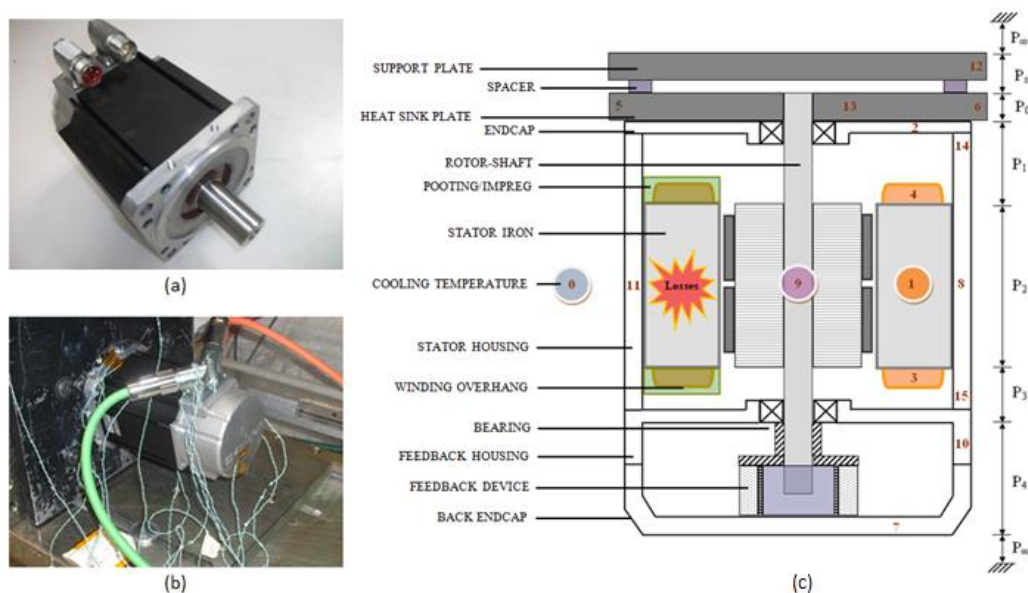


Fig. 4.9. (a) Brushless servomotor (b) mounted prototype on the test rig and (c) parts and thermocouple locations on the servomotor under test.

Sixteen J-K type thermocouples are used for temperature readings on the servomotor under test in the dynamic torque rating rig, as shown in Fig. 4.9

(b). The thermocouple locations in the servomotor are shown in Fig. 4.9 (c) which also defines the different servomotor components whose temperatures are of interest. The thermocouple reading T_0 (0) in Fig. 4.9 (c) is for the cooling temperature, i.e., the ambient surrounding temperature. The thermocouple reading T_1 (1) is located in the middle region of the stator winding.

The T_2 (2) thermocouple is located in the servomotor end-cap. The thermocouples, T_3 (3) and T_4 (4), are located on the winding overhangs. The thermocouples, T_5 (5) and T_6 (6), are located on the upper and the lower ends of the mounting flange.

Thermocouple T_7 (7) senses the feedback device housing surface temperature. The thermocouple T_8 (8) is located on the middle top surface of the servomotor stator. The thermocouple T_9 (9) is mounted on the right-hand middle surface of the stator. The thermocouple T_{10} (10) is mounted on the back end-cap. The thermocouple T_{11} (11) is located on the middle bottom surface of the servomotor stator. The thermocouple T_{12} (12) is mounted on the support plate. The thermocouple T_{13} (13) is located at the more central and hottest point of the mounting (heat sink) plate. Finally, thermocouples T_{14} (14) and T_{15} (15) are located on the front and back top locations of the housing surface.

In the dynamic torque rating test the LabView software is used for temperature data acquisition and for the load torque demands. The torque rating test system visual interface (VI) front panel of the LabView software is shown in Fig. 4.10. Successive measurements of the 16 J-K thermocouples in the torque rating testing are repeated every minute until steady state, indicated by horizontal line traces, is obtained for all the temperature measurement graphs in Fig. 4.10. Constant temperature measurements indicate either thermal saturation of the thermocouple and its associated electronics, which should be avoided, or the equilibrium (steady state) condition where the maximum temperature is reached for a constant torque. The temperatures and the demanded torque are easily monitored as shown. The data acquisition device is a National Instruments cFP-TC-120. The VI of

Fig. 4.10 is linked to the field point (FP) device and real-time acquisition temperature data are obtained for each testing point. The VI allows for a file path facilitating the recording of the data to an Excel file.

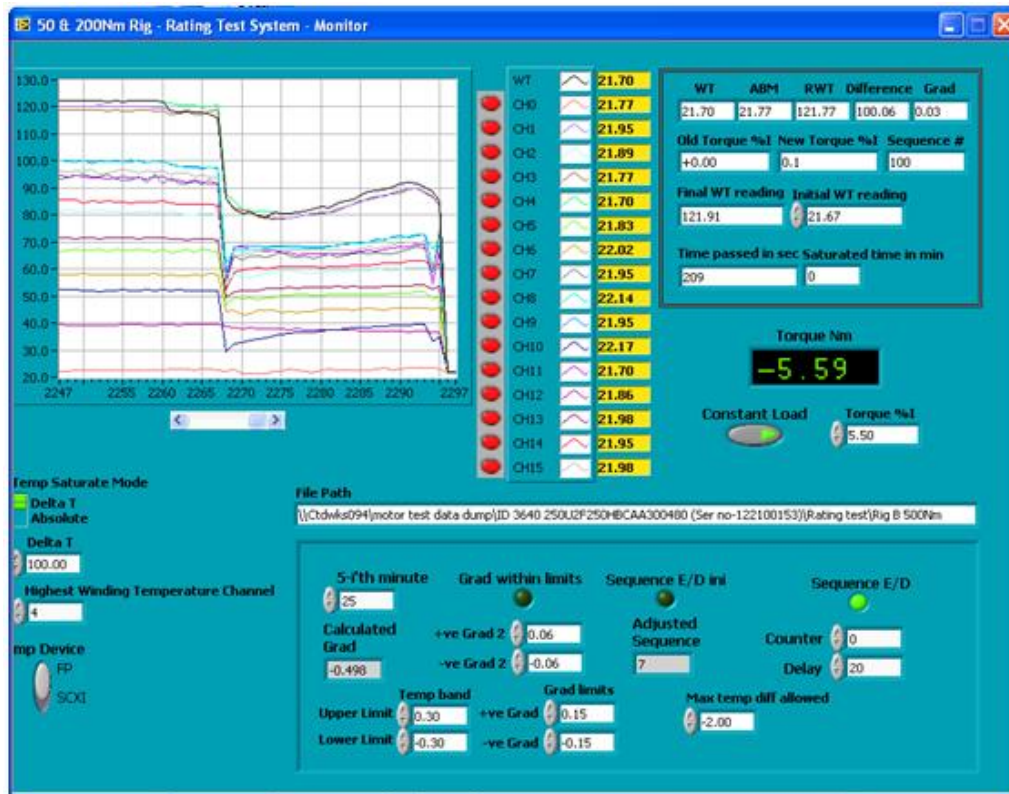


Fig. 4.10. LabView visual interface for torque rating.

4.5. Summary

The main elements of the experimental rigs have been presented for the measurements of cogging torque, open circuit iron losses and the dynamic torque rating. The experimental setup have been described for measurement. The operational principle of each test has been explained, aided by pictorial views of the apparatus. The techniques employed to measure and acquire data from the tests have been described. All the test results are presented in Chapter 5.

CHAPTER 5

RESULTS AND COMPARISON OF WINDING DESIGN TECHNOLOGIES

5.1. Introduction

The experimental results for cogging torque, open circuit iron losses and dynamic torque rating are presented in this Chapter. The results are analysed and compared with the results from simulations where possible.

The cogging torque data for the new segmented stator, concentrated winding servomotor demonstrates that neither analytical equations nor FEA can be used to accurately predict the cogging amplitude and waveform shape. This is due to the rotor lamination feature used to retain the permanent magnets on the high speed rotor not being taken into account using these methods.

This conclusion is supported by the experimental signals from the vibrometer presented in Chapter 4 showing significant frequency components in the cogging signal introduced by this lamination feature. Hence FFT analysis is performed on this experimentally obtained cogging torque waveform to check that the peak in the resulting frequency response characteristic is within the specification (below 1% stall torque).

In order to determine whether the temperature of the permanent magnets significantly affects the remanence value, the open circuit iron loss test is performed in the cold (ambient) condition and in the hot (stator surface temperature T_8 at 81°C) condition.

The iron losses were performed with clockwise and anticlockwise rotation and the difference was not found to be significant.

In the following, for brevity, the new segmented stator, concentrated winding servomotor will be referred to as the 'new servomotor' and the current conventional distributed winding servomotor will be referred to as the 'conventional servomotor'.

The dynamic torque rating test is performed in order to analyse and compare the torque-speed performance characteristics of the new and conventional servomotors. It is evident that the new servomotor has a significant advantage in terms of torque level.

The percentage torque drop from the stall point to the rated 3000 rpm point is, however, greater for the new servomotor, which is attributed to the larger number of rotor poles, but the significant increase in the stall torque reduces the impact of the torque drop on a comparative basis. It is reasonable to suppose that the overall torque performance of the new servomotor would be superior to that of the conventional servomotor for the same number of rotor poles.

5.2. Cogging Torque Test Results

Fig. 5.1 shows a cogging torque cycle for a conventional surface mounted BPM synchronous servomotor (Lu et al., 2006).

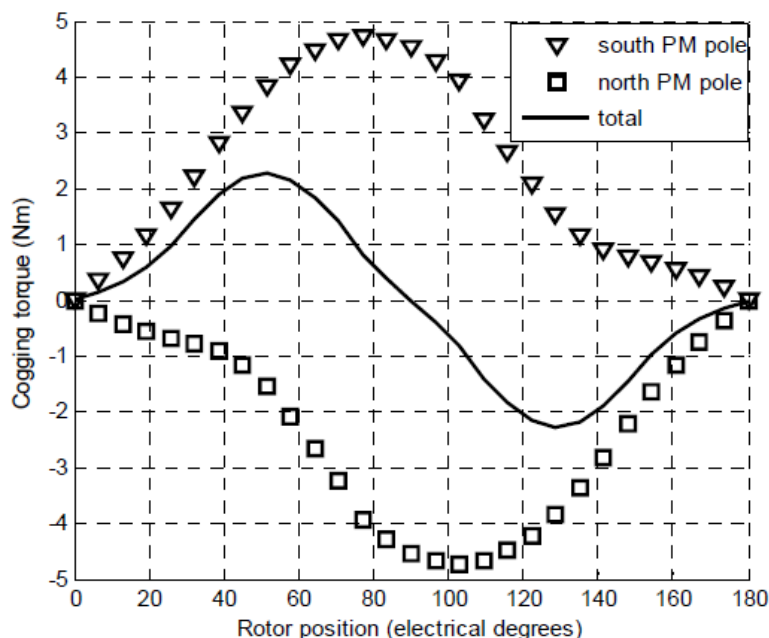


Fig. 5.1. Cogging torque produced by north, south poles and the resultant cogging torque.

The total cogging torque waveform is the resultant of the North and South pole cogging torque components due to the surface mounted magnets as shown in Fig.

5.1. It can be observed that the total cogging torque has two equal and opposite peaks less in magnitude than the single peaks of the cogging torque components due to their opposite signs (Lu et al., 2006).

The analytical and FE cogging torque predictions of (Lu et al., 2006) and (Sooriyakumar et al., 2006) (Sooriyakumar et al., 2007a) (Salon, 1995) are presented in Fig. 5.2 together with the measured cogging torque.

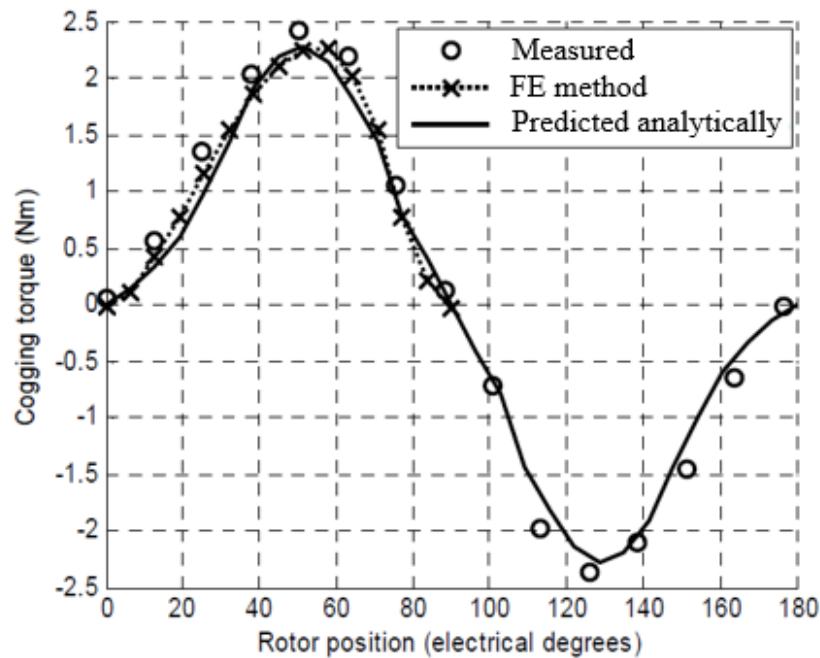


Fig. 5.2. Comparison of the measured cogging torque with the theoretical predictions using the FEA method and analytical expressions.

However, the methods presented by (Lu et al., 2006) and (Sooriyakumar, 2009) cannot predict cogging torque for the new servomotor due to the new retention technique used to hold the permanent magnets in the rotor presented in Chapter 2 . The reason for this is that the magnetic characteristics of the permanent magnet retention components make it impossible for a direct mean for the analytical or FE methods to be calculated. The experimental method used in this research programme, however, shows that it is possible to design the motor so that the cogging torque satisfies the reference level of less than 1% of the stall torque. Fig. 5.3 shows an oscilloscope screenshot of the experimentally obtained cogging torque signal and the back EMF signal. The high frequency oscillations of the cogging torque waveform, which are absent in the cogging torque waveforms of the conventional servomotor presented in Fig. 5.1 and Fig. 5.2 are attributed to the

permanent magnet holding features. The cogging torque amplitude is measured using the oscilloscope cursors shown in Fig. 5.3. It is assumed that the cogging torque magnitude is represented by the highest rise or fall of signal that is not associated with any valley shape.

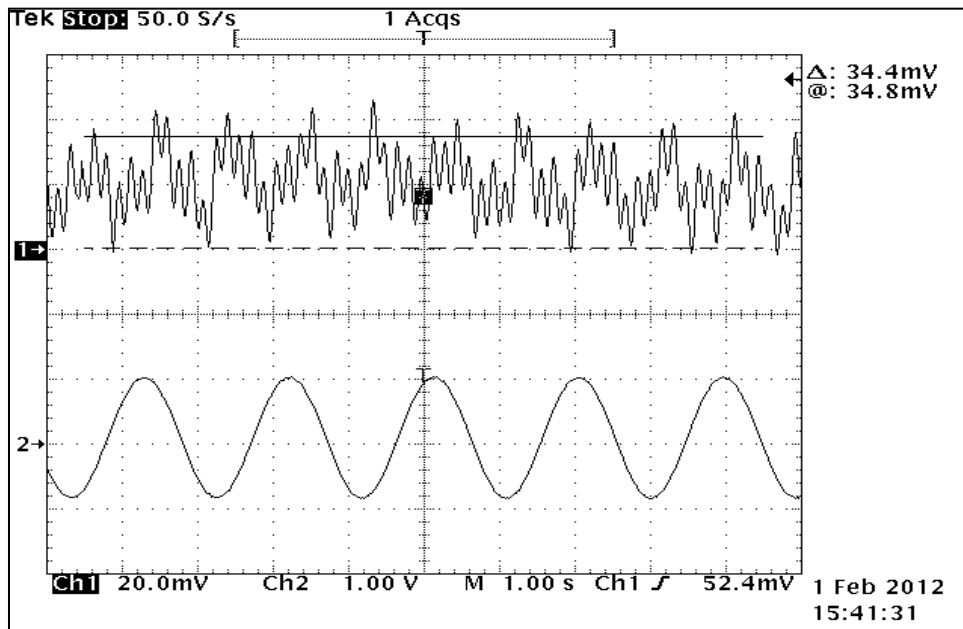


Fig. 5.3. Measured cogging torque (upper trace) and back EMF (lower trace) for the new servomotor.

This can be clarified by expanding the signal of Fig. 5.3 as shown in Fig. 5.4, also rendering the measurements easier to take.

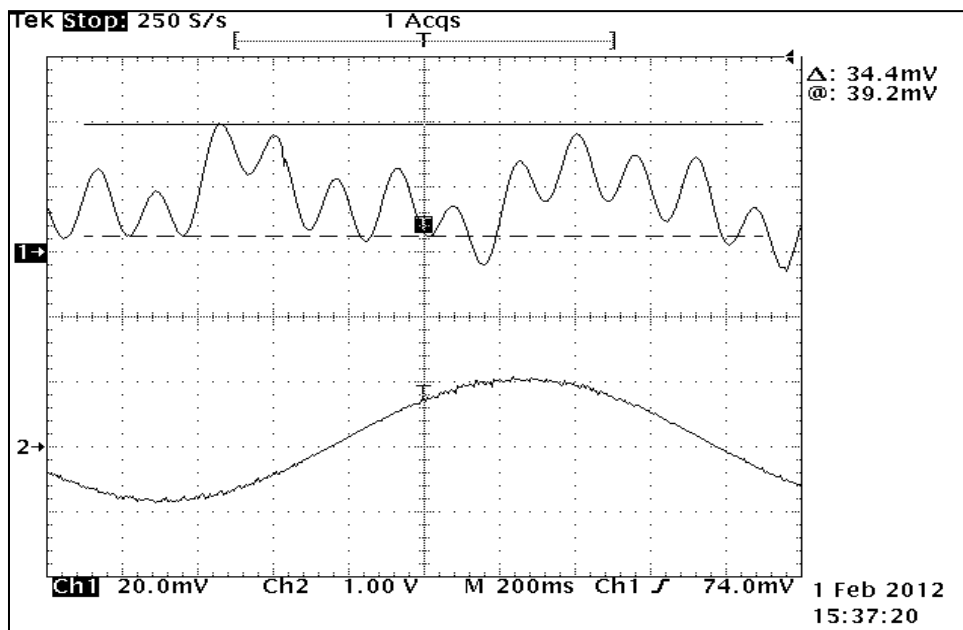


Fig. 5.4. Expanded measured cogging torque for the new servomotor.

The voltage of 39.2 mV corresponds to a torque of 0.0392 Nm which is less than the design specification that defines the cogging torque to be less than 1% of the stall torque. In order to validate the measurement taken for cogging torque measurement, the encoder feedback signal is sampled at a much higher frequency as shown in Fig. 5.5.

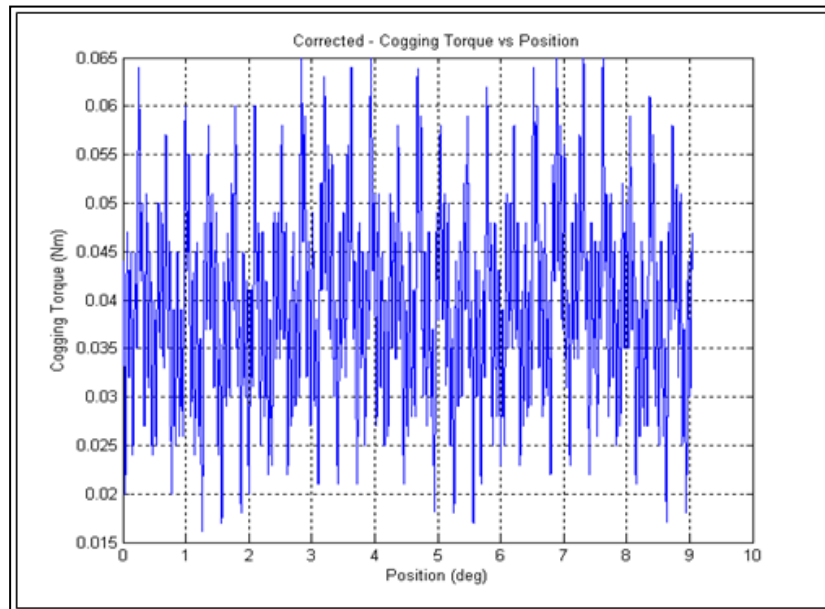


Fig. 5.5. Cogging torque signal for servomotor 1000 samples per second.

Fig. 5.6 shows a significant component at 60 [Hz] that corresponds to the cogging torque component.

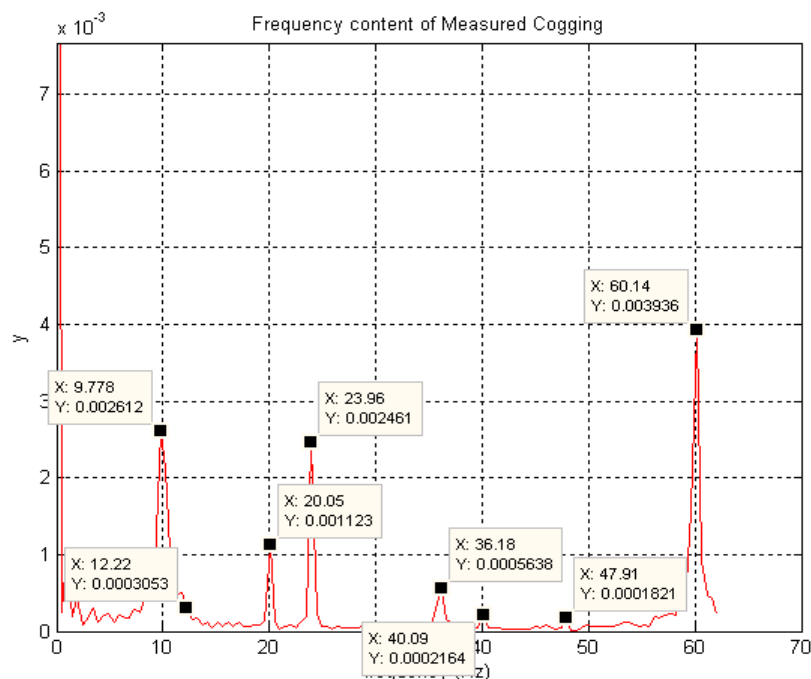


Fig. 5.6. Cogging torque spectrum produced by a FFT for new servomotor.

The result is approximately ten times smaller than the results obtained in Fig. 5.3 and Fig. 5.4.

This difference is caused by the encoder feedback signal amplitude as shown in the result of Fig. 5.5, and this is compensated by multiplying the cogging of Fig. 5.6 by ten.

This multiplication factor has been maintained for all the cogging torque measurements in order to facilitate meaningful comparisons.

5.3. Open Circuit Iron Loss Test Results

The iron loss process is explained in detail in Chapter 3. This comprises the hysteresis loss and the eddy current loss.

In this investigation the iron losses are measured and the results used to validate the analytical and numerical methods presented in Chapter 2 and Chapter 3.

Results are presented showing the variation of the iron losses with the rotor speed and the stator stack length. Then an equation for predicting the iron losses is established by means of a least-squares process.

Then the predictions using this equation are compared with the measurements for verification. The measured losses comprise the friction and windage losses as well as the iron losses and must therefore be corrected by subtracting the separately measured friction and windage losses.

The latter is found in the same fashion as the iron losses described in Chapter 4 but without the magnets mounted on the rotor surface so that the only torque needed to maintain rotation at a given speed is the combined bearing friction and windage torque.

The measured loss/speed curves for a 115 millimetres frame size and a core length of 60 millimetres measured at ambient temperature (referred to as 'cold') and for both clockwise and anticlockwise rotation is shown in Fig. 5.7, the measurements being made at 500 r/m intervals.

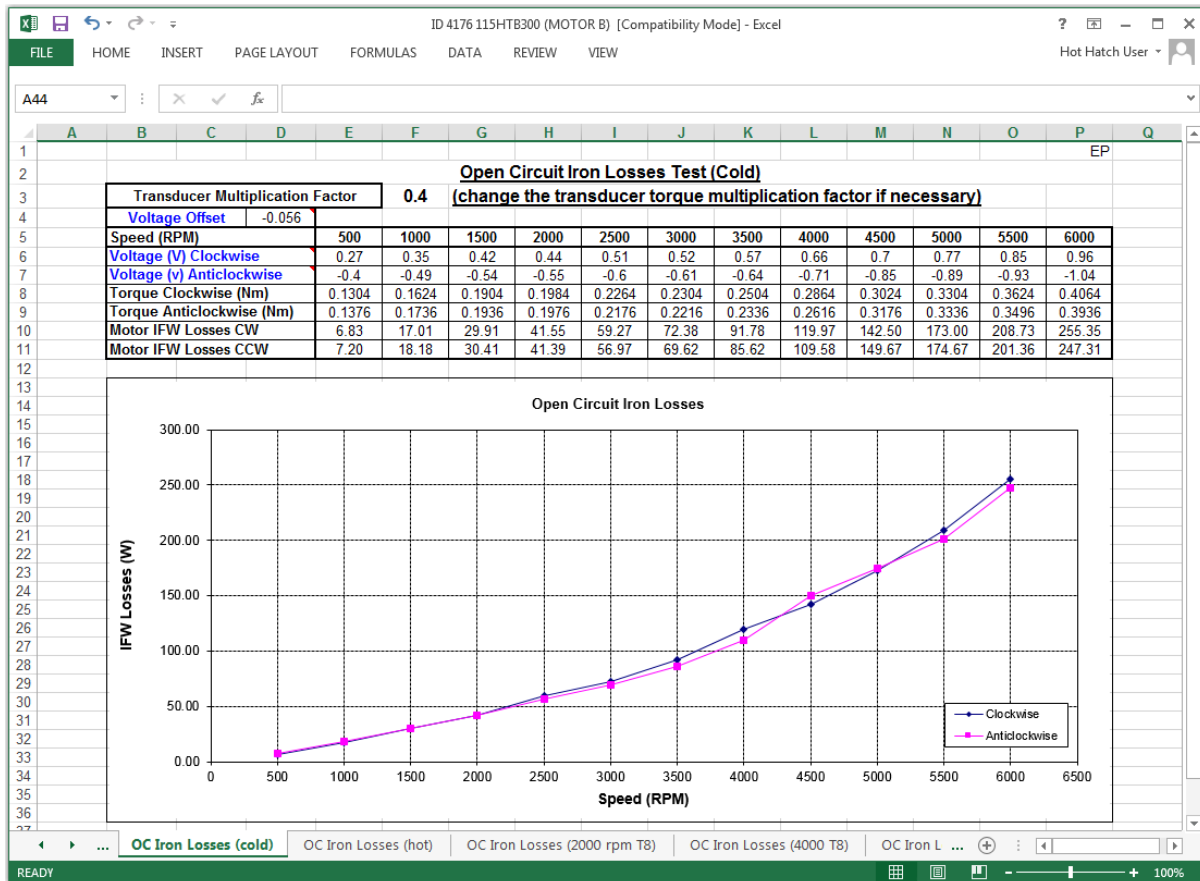


Fig. 5.7. Measured open circuit losses (cold surface) for clockwise and anticlockwise rotation.

At some speeds a significant difference between the losses in the clockwise and anticlockwise rotational directions is evident, but this effect is negligible below the rated speed of 3000 r/m.

The same test has been performed for the hot condition (obtained by running the motor under load to a steady state temperature of 80°C) and the loss/speed curves are presented in Fig. 5.8.

It may be observed that in this case the rotation direction is unimportant. Observing Fig. 5.7 and Fig. 5.8, the losses are significant, but the cold losses are higher.

It should be noted that the increase of the losses with speed is very significant above the rated speed of 3000 rpm.

The loss/speed curves are almost linear below the rated speed so that at half the rated speed, i.e., 1500 r/m, the losses drop to about half those at 3000 r/m, but when the speed is doubled to 6000 rpm the losses increase by a factor of more than three.

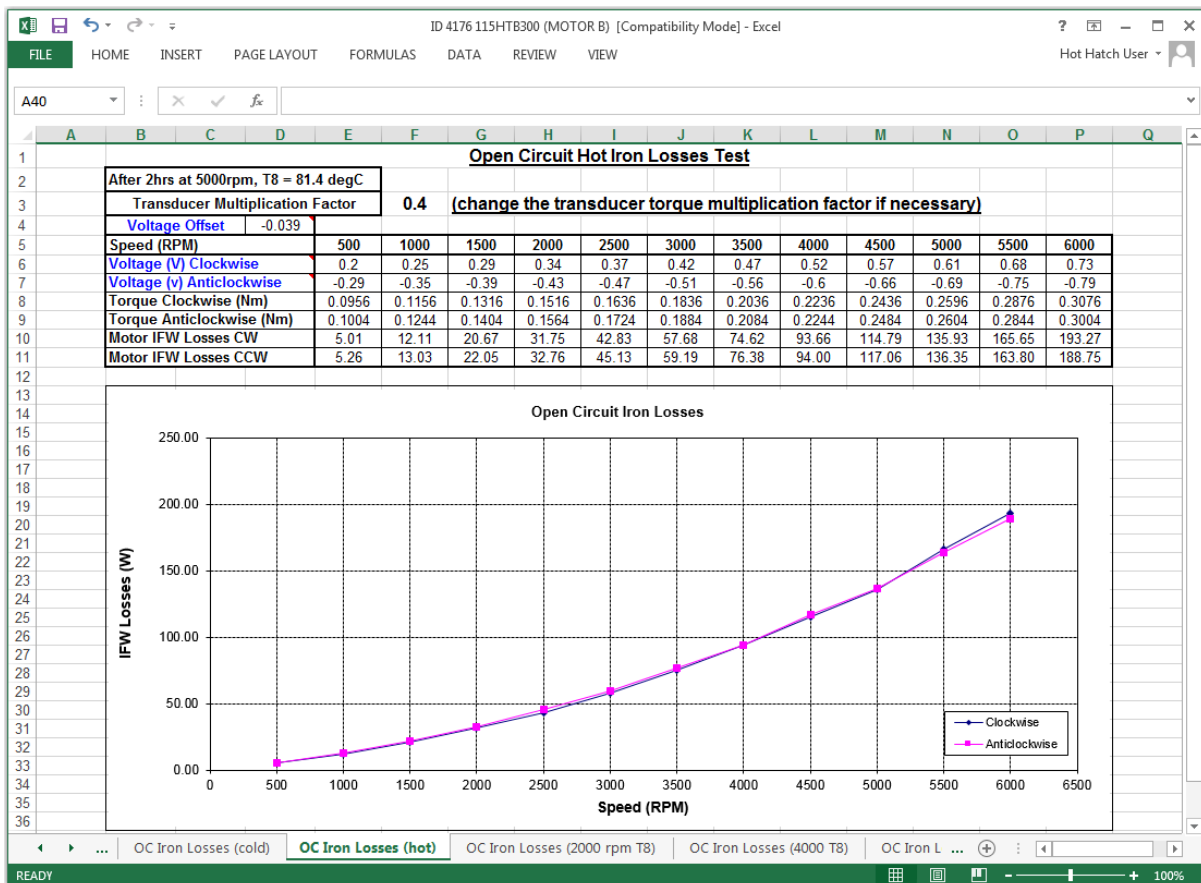


Fig. 5.8. Measured open circuit losses (hot surface) for clockwise and anticlockwise rotation.

Since the back EMF is limited by the finite power supply voltages of the power electronics, the maximum speed of a BPM synchronous servomotor is limited by the number of turns of the stator winding.

Hence halving the number of turns doubles the maximum speed. This reduces the servomotor torque constant, i.e., the maximum torque produced by the maximum permissible stator current is reduced but the increase in the maximum speed maintains the servomotor power rating.

However, in view of the loss/speed characteristics of Fig. 5.7 and Fig. 5.8, the extent to which the maximum speed may be increased is limited by the significant losses at high speeds.

Although there is a significant loss drop from the cold ambient temperature to the hot servomotor surface temperature of about 81°C, this must be exploited with extreme caution since the permanent magnet remanence also reduces with temperature,

adversely affecting the servomotor torque performance due to permanent magnet demagnetisation.

Hence the reduction of losses with temperature has been investigated for lower and therefore safer temperatures regarding the permanent magnets for the new servomotor with the 12-10 slot-pole combination.

In this case the losses are measured for a surface temperature, T_8 , of 22°C and 48°C as well as 85°C, and the results are shown in Fig. 5.9.

This shows a loss difference of about 18% at 3000 r/m between the temperature extremes and 26% at 6000 r/m as shown in Fig. 5.9.

The loss difference at 6000 r/m, however, is about five times the loss difference at 3000 r/m, which is very significant.

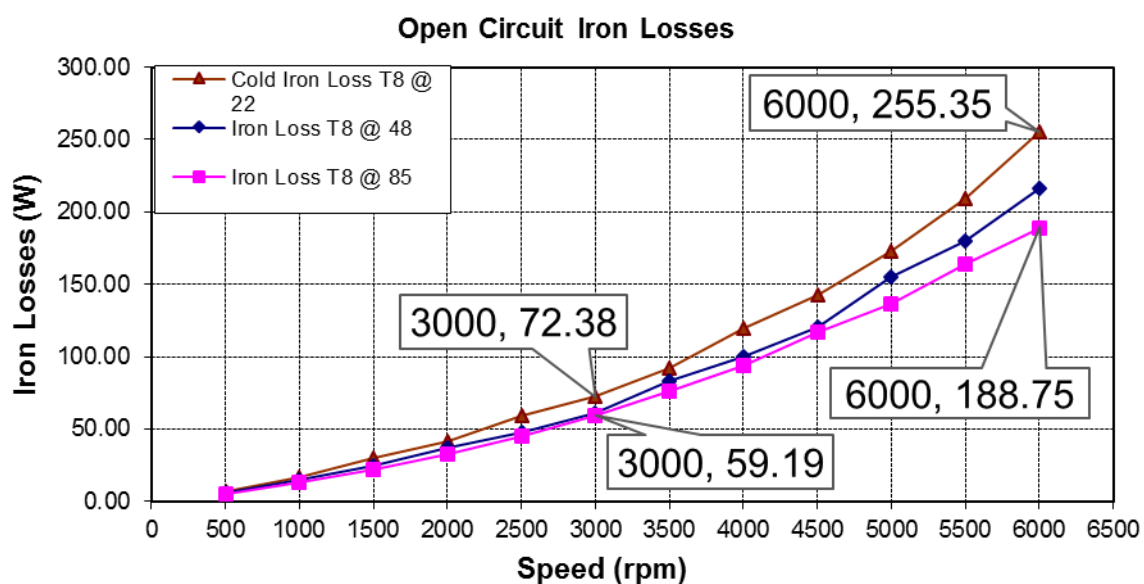


Fig. 5.9. Measured open circuit losses with surface temperature variation.

Next the variation of the losses with the stator stack length is investigated. The test results for the 115 frame size and stack lengths of 30, 90 and 120 millimetres are shown in Fig. 5.10.

Since the frame size is fixed, an increased servomotor core length means an increase in volume. As already pointed out, these test results include the rotational losses due to windage and friction. These losses are obtained experimentally using a

dummy rotor made of non-magnetic material or using the actual rotor but with the magnets removed. The test is performed in a similar way to the open circuit total loss tests.

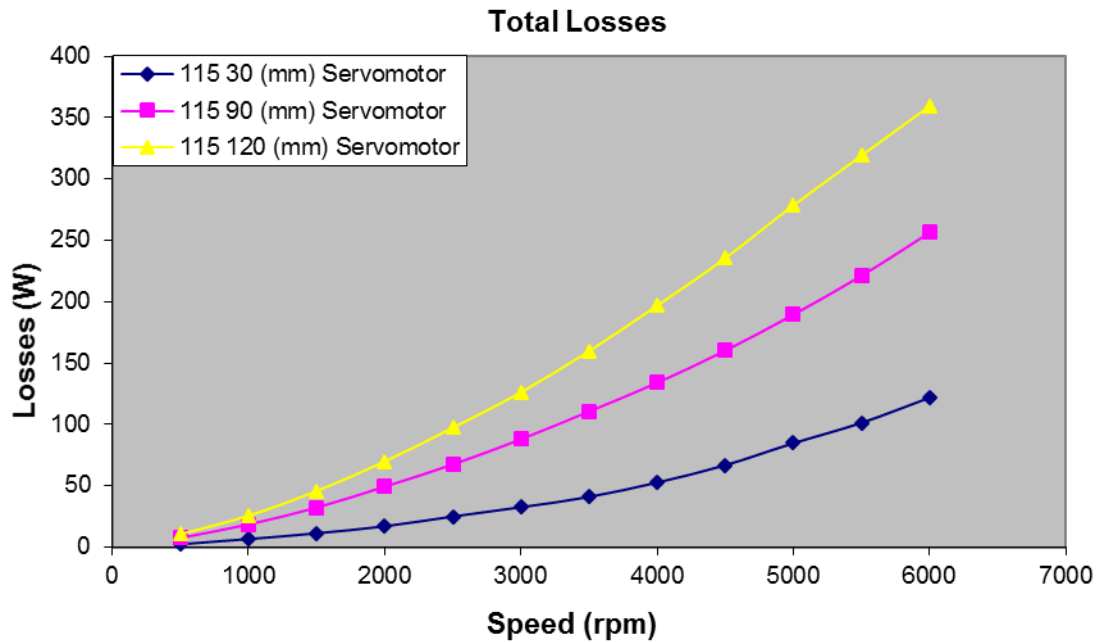


Fig. 5.10. Measured open circuit losses for different stator stack lengths.

The results for windage and friction losses up to 6000 rpm for the new servomotor are presented in Fig. 5.11.

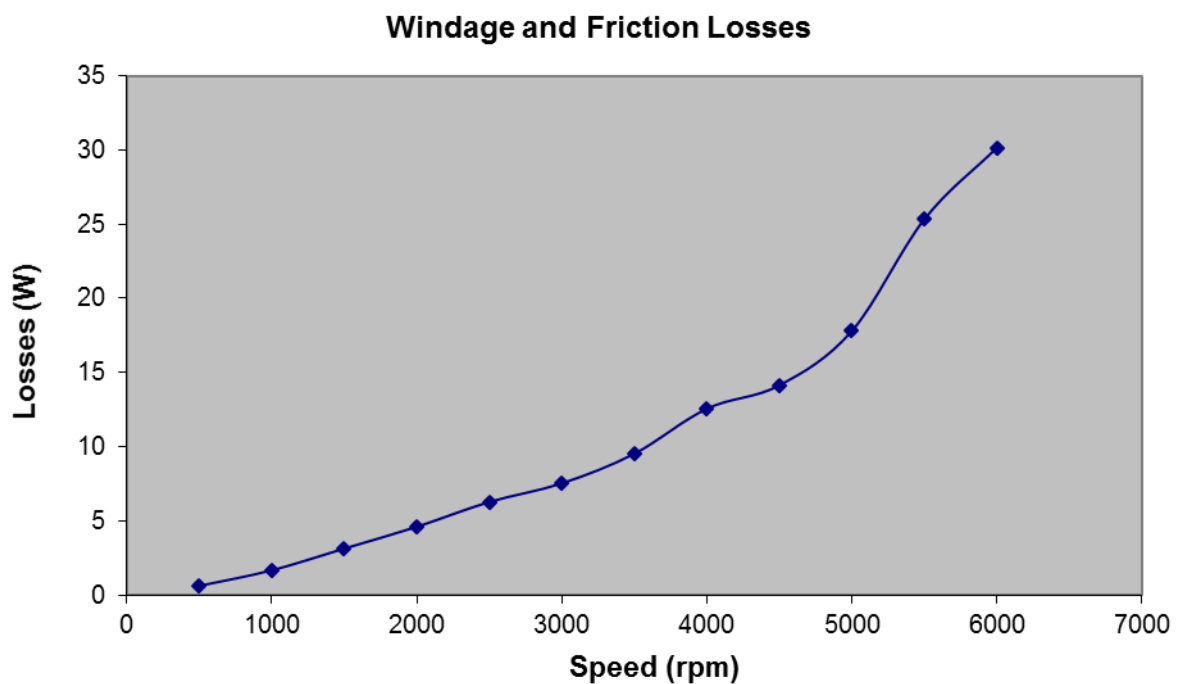


Fig. 5.11. Rotational losses due to the windage and the friction losses.

At relatively low speeds, the bearing friction, produced largely by a viscous friction torque which is directly proportional to the speed, is expected to dominate but as the speed is increased the windage losses occupy a larger proportion due to the aerodynamic drag torque being proportional to the square of the speed.

Then the loss curve of Fig. 5.11 is deducted from the curves presented in Fig. 5.10 in order to obtain the correct iron loss curves as presented in Fig. 5.12.

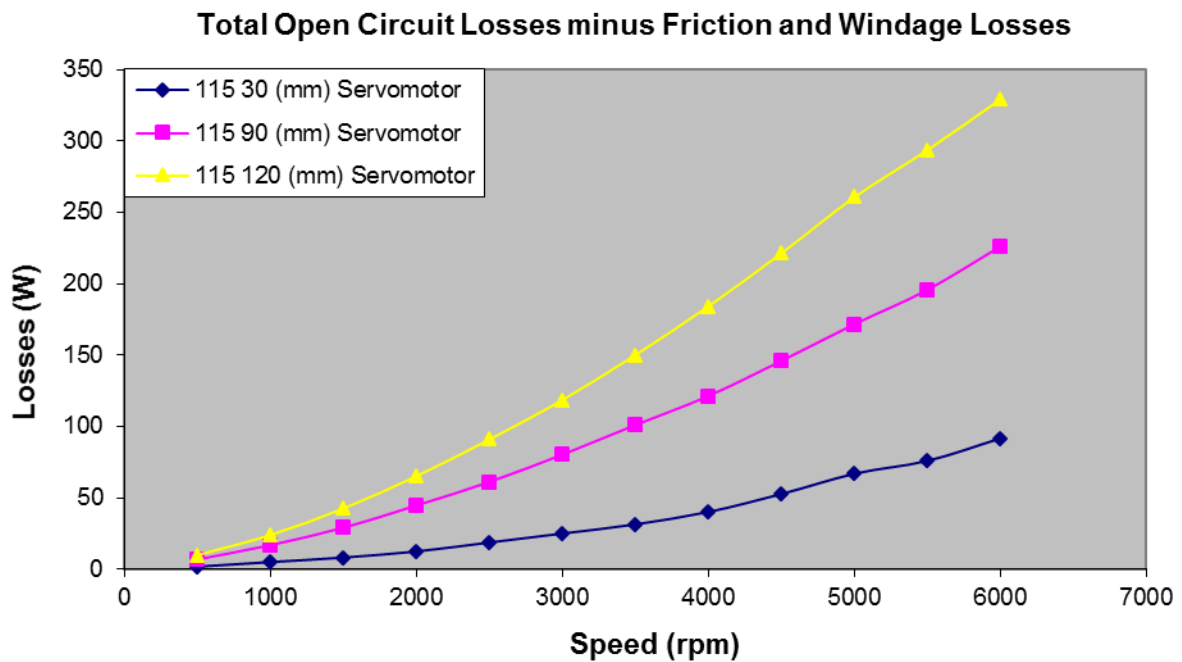


Fig. 5.12. Measured rotational iron losses for different stack lengths.

The loss curves of Fig. 5.10 and Fig. 5.12 have a similar form. FEA and Bertotti's (Staton, 2012) analytical method described in Chapter 3 can be used to predict the iron losses of a servomotor.

These methods, however, require experience with both FEA and the lamination material loss modelling. The measured and the predicted results are shown together in Fig. 5.13.

These iron loss/speed curves can be used to develop an equation to predict the iron losses. This is computationally much less demanding than the FEA or Bertotti methods. The equation is very helpful in an industrial environment since it provides an accurate iron loss prediction for any BPM synchronous servomotor of given length and frame size.

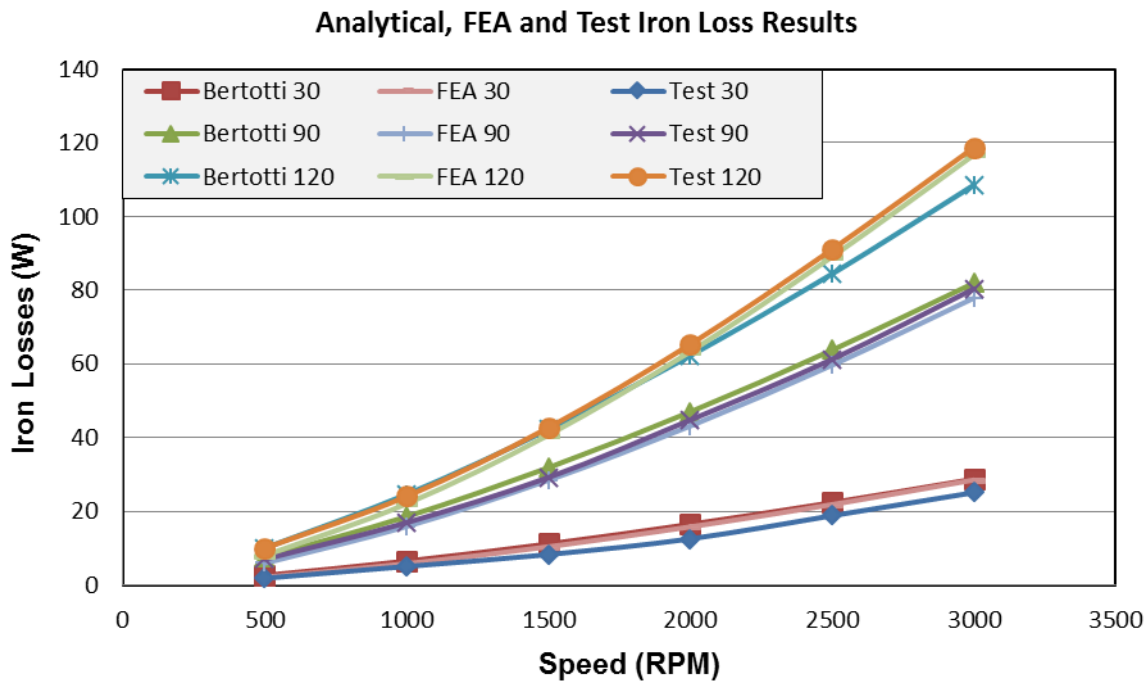


Fig. 5.13. Comparison of measured iron losses and predicted results with analytical and FEA.

Hence when a customer requests a particular servomotor length and frame size, the designer can use the equation to quantify the iron losses and the other losses to meet the customer's performance specifications.

Assuming constant magnet remanence, then the only iron loss variable is the frequency as fully discussed in Chapter 3. Then according to [Miller green book] the equation for the iron losses per unit volume of the stator core is

$$P_{fe} = k \cdot f^n \quad (5.1)$$

where f is the frequency and k and n are constant parameters.

Taking logarithms of equation (5.1) yields

$$\log(P_{fe}) = \log(k) + n \cdot \log(f) \quad (5.2)$$

This means that a straight-line fit of $\log(P_{fe})$ vs. $\log(f)$ to test data can be obtained by a least-squares regression to determine $\log(k)$ and $\log(n)$, thereby obtaining the constants k and n . Fig. 5.14 shows parameters calculation for the iron losses equation.

f (Hz)	P (W/m ³)	log f	log P
25	22654	1.40	4.36
50	56302	1.70	4.75
75	96536	1.88	4.98
100	147371	2.00	5.17
125	208367	2.10	5.32
150	274066	2.18	5.44
175	345203	2.24	5.54
200	425456	2.30	5.63
225	525776	2.35	5.72
250	634487	2.40	5.80
275	719132	2.44	5.86
300	834693	2.48	5.92

IRON LOSSES EQUATION	
$y = 1.4669x + 2.2619$	
2.2619	182.77
$P = 182.77 \cdot f^{1.4669}$	

Fig. 5.14. Frequency, loss per volume, constants and the iron losses equation.

Fig. 5.15 shows the trendline results for calculation of the constants.

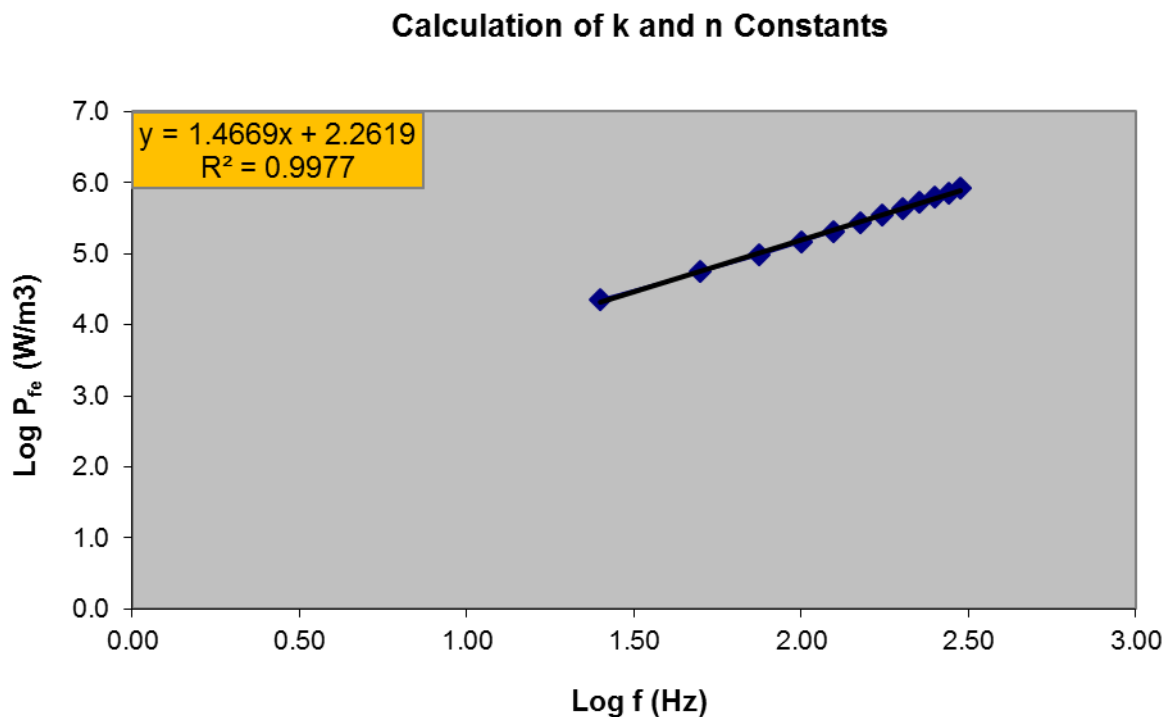


Fig. 5.15. Determination of constants k and n by linear regression.

$$y = 2.2619 + 1.4669x \quad (5.3)$$

Comparison of equations (5.2) and (5.3) yields

$$\underbrace{\log(P_{fe})}_y = \underbrace{\log(k)}_{2.2619} + n \cdot \underbrace{\log(f)}_{1.4669x} \quad (5.4)$$

Hence

$$\left. \begin{array}{l} \log(k) = 2.2619 \Rightarrow k = 182.77 \\ \text{and } n = 1.4669 \end{array} \right\} \quad (5.5)$$

Therefore equation that predicts the iron losses per unit volume for the new servomotor is

$$P_{fe} = 182.77 \cdot f^{1.4669} \quad (5.6)$$

The closeness of the predicted and measured iron loss curves in Fig. 5.16 is sufficient below the rated speed of 3000 r/m.

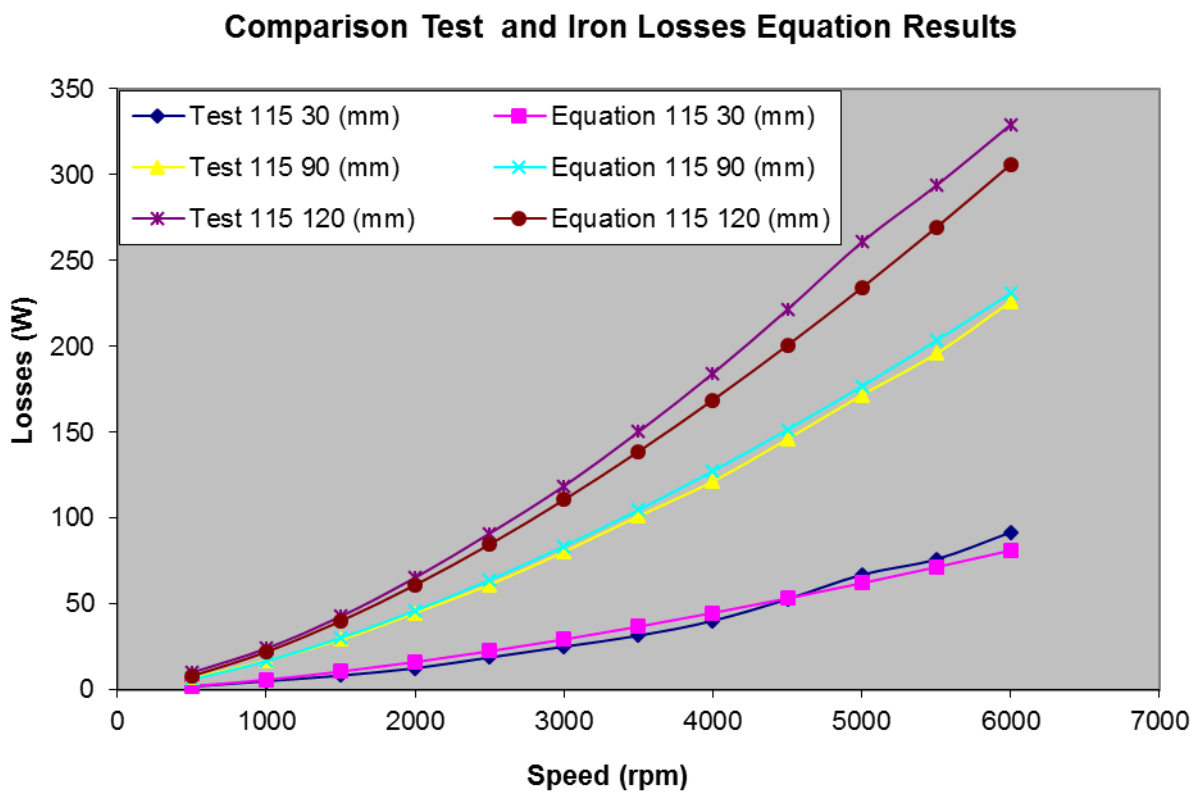


Fig. 5.16. Predicted versus measured iron losses for different stack lengths.

Above this speed, the iron losses are significantly under predicted for the 120 mm stator stack length, which is undesirable for servomotor design and slightly under predicted for the 30 mm stator stack length.

The best situation is for the 90 (mm) stator stack length, where the iron losses are slightly over predicted.

Since speeds beyond 3000 r/m will rarely occur in practice, however, the less accurate predictions for those speeds do not constitute a real issue. The results for Fig. 5.16 are presented in TABLE 5.1 numerically with the percentage prediction errors.

The positive percentage errors are desirable since they indicate over predicted losses. The negative percentage errors are undesirable since they indicate under-predicted losses upon which incorrect design decisions may be taken, resulting in severe thermal problems in service.

TABLE 5. 1.
Brushless servomotor iron losses for different lengths.

SPEED (rpm)	115 Size 30 mm Iron Losses (W)			115 Size 90 mm Iron Losses (W)			115 Size 120 mm Iron Losses (W)		
	Test	Equation	Error	Test	Equation	Error	Test	Equation	Error
500	1.89	2.12	12%	7.02	6.04	-14%	10.05	7.99	-20%
1000	5.09	5.86	15%	16.96	16.68	-2%	24.09	22.09	-8%
1500	8.30	10.63	28%	29.22	30.24	4%	42.73	40.05	-6%
2000	12.57	16.20	29%	44.85	46.12	3%	65.34	61.07	-7%
2500	18.85	22.48	19%	61.26	63.98	4%	91.11	84.73	-7%
3000	25.13	29.37	17%	80.42	83.59	4%	118.75	110.71	-7%
3500	31.52	36.82	17%	101.16	104.80	4%	150.27	138.80	-8%
4000	40.21	44.79	11%	121.47	127.48	5%	184.31	168.83	-8%
4500	52.78	53.24	1%	146.08	151.52	4%	221.48	200.67	-9%
5000	67.02	62.14	-7%	171.74	176.85	3%	260.75	234.21	-10%
5500	76.03	71.46	-6%	195.83	203.39	4%	293.74	269.35	-8%
6000	91.73	81.19	-11%	226.19	231.08	2%	329.24	306.02	-7%

5.4. Dynamic Torque Rating Test Results

The dynamic torque rating is the most important performance indicator in this research project.

The prime research objective is to achieve a higher thermal performance and superior torque per volume ratio through eliminating unnecessary non-torque producing material, consequently making substantial material and cost savings.

The servomotor prototypes having the new segmented stator core with concentrated windings and the current conventional stator core with distributed windings are shown in Fig. 5.17.

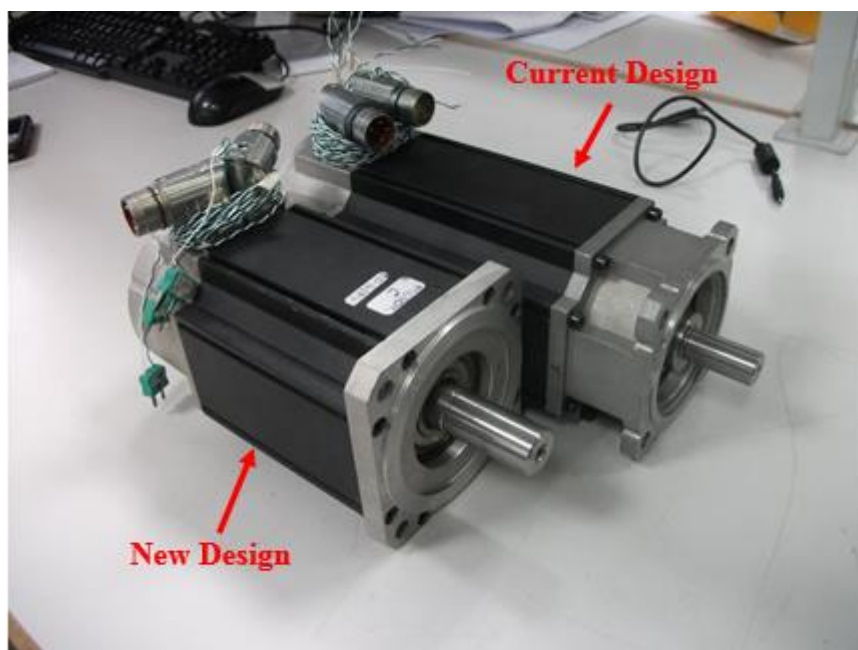


Fig. 5.17. The prototype of new concentrated and current distributed design brushless servomotors.

For a fixed frame-size of 115 mm, it can be noticed that the new servomotor has a substantially shorter housing when compared with the current design.

It should be noted, however, that the larger surface area of the current design enhances the power dissipation to the surroundings.

The dynamic rating test is performed on both prototypes for comparison. The results presented in this chapter utilize the testing procedures presented in Chapter 4.

In order to have a fair comparison between the designs, both have the same material active length and quality.

Since the frame-size is fixed, the split ratio chosen to maximise the output torque is equal for both designs.

The magnet thicknesses have a small difference between the servomotors and are both parallel magnetized.

The winding operating temperature and the ambient temperature are fixed for both designs. They are not, however, placed on an equal footing regarding their thermal efficiencies, the new design having a higher slot-fill and fewer slots are when compared with the current design.

Tests are performed and a typical results sheet tabulating important performance data for this project is shown in Fig. 5.18.

The most important results are the speed, torque, RMS current and the 16 thermocouple temperatures.

The torque-speed curves from Fig. 5.18 for both designs at a fixed maximum temperature are plotted in Fig. 5.19.

The two significant characteristics that can affect the torque capability are the current carrying capability of the copper wire and flux-carrying capability of the stator core.

It is evident from Fig. 5.19 that the segmented servomotor prototype delivers nearly 40% more torque compared with the conventional servomotor prototype near the stall condition and 35% more torque at the rated speed of 3000 rpm.

The negative gradient of the torque-speed characteristic of Fig. 5.19, however, is much greater for the segmented servomotor prototype than it is for the conventional servomotor prototype.

This is mainly attributed to the increased iron losses due to the increase in the number of rotor magnet poles used in the new design. This shows that the increase of iron losses affects the torque level of the servomotor.

Motor Dynamic Rating Test									
Transducer zero load offset									
Speed	RPM	3000	2500	2000	1500	1000	500		
Switching Frequency	kHz	12	12	12	12	12	12		
Torque (Nm)		0.87619	0.90476	0.94286	0.96857	0.98095	1		
Kt (Nm/Arms)		1.38	1.41	1.44	1.44	1.47	1.55		
Current (A _{RMS})	CH 1	6.656	6.749	6.859	7.053	7.247	7.441		
	CH 2	6.625	6.738	6.914	7.037	7.16	7.283		
	CH 3	6.691	6.776	6.897	7.084	7.271	7.458		
	SUM	6.657	6.753	6.89	7.058	7.026	6.794		
Voltage (V _{RMS})	CH 1	253.94	239.01	226.08	211.19	196.3	181.41		
	CH 2	246.58	232.05	219.35	204.54	189.73	174.92		
	CH 3	246.98	231.16	217.52	202.11	186.7	171.29		
	SUM	431.35	405.42	382.76	356.73	330.7	304.67		
Motor Input Power (W)		3477	2982	2484	1969	1454	939		
Motor Output Power (W)		275.12	236.75	197.37	152.07	152.67	122.33		
Drive Input Power (W)									
Total Loss(W)		3201.88	2745.25	2286.63	1816.93	1301.33	816.667		
Copper Loss(W)									
Iron +Mech Loss (W)									
Efficiency %		7.91	7.94	7.95	7.72	10.50	13.03		
THD Current (%)									
Fundamental Current (A _{RMS})	CH 1	6.1	6.8	8.1	6.05	6	6.8		
	CH 2		6.9	6.8	6.5	6.7	7		
	CH 3		6.86	8	6.6	6.8	7.1		
	SUM								
Fundamental Voltage (V _{RMS})	CH 1	61.2	70.84	79.4	86.4	92.4	98.4		
	CH 2	62.4	70.18	78.6	85.8	90.8	95.8		
	CH 3	60.4	68.78	77.7	85.1	91.1	97.1		
	SUM								
Thermocouple		Temp °C							
T0: Ambient		19	20	21	21	21	20		
T1: Winding Top (inside slot)		120	120	120	120	121	120		
T2: Top of Motor (front end frame)		75	76	75	76	77	76		
T3: Winding Middle		115	115	114	114	114	115		
T4: Winding Bottom (inside slot)		121	121	120	120	119	119		
T5: RHS Bottom of Mounting plate (motor side)		61	62	63	63	65	63		
T6: RHS op of Mounting Plate (motor side)		57	59	59	60	61	60		
T7: Back End Frame / Encoder Housing Cover		107	107	106	103	104	102		
T8: Top Motor Housing Middle		94	94	93	92	94	93		
T9: RHS Motor Housing Middle		92	92	91	90	91	90		
T10: Encoder Housing		88	88	87	86	87	87		
T11: Bottom Motor Housing Middle		93	93	93	92	93	92		
T12: L Plate Top		29	30	30	30	30	30		
T13: Mounting Plate (near to front end frame)		62	63	64	64	65	64		
T14: Top of Motor (front end of housing)		77	78	77	78	79	79		
T15: Top of Motor (rear end of housing)		93	93	92	91	92	91		

Fig. 5.18. Dynamic torque rating test results for the new segmented design.

Section 5.3 showed that the cold iron losses are higher when compared with the hot iron losses and this is mainly caused by the reduction of permanent magnet remanence level.

As already mentioned, however this magnetic field reduction due to the temperature increase does reduce the maximum output torque of the servomotor.

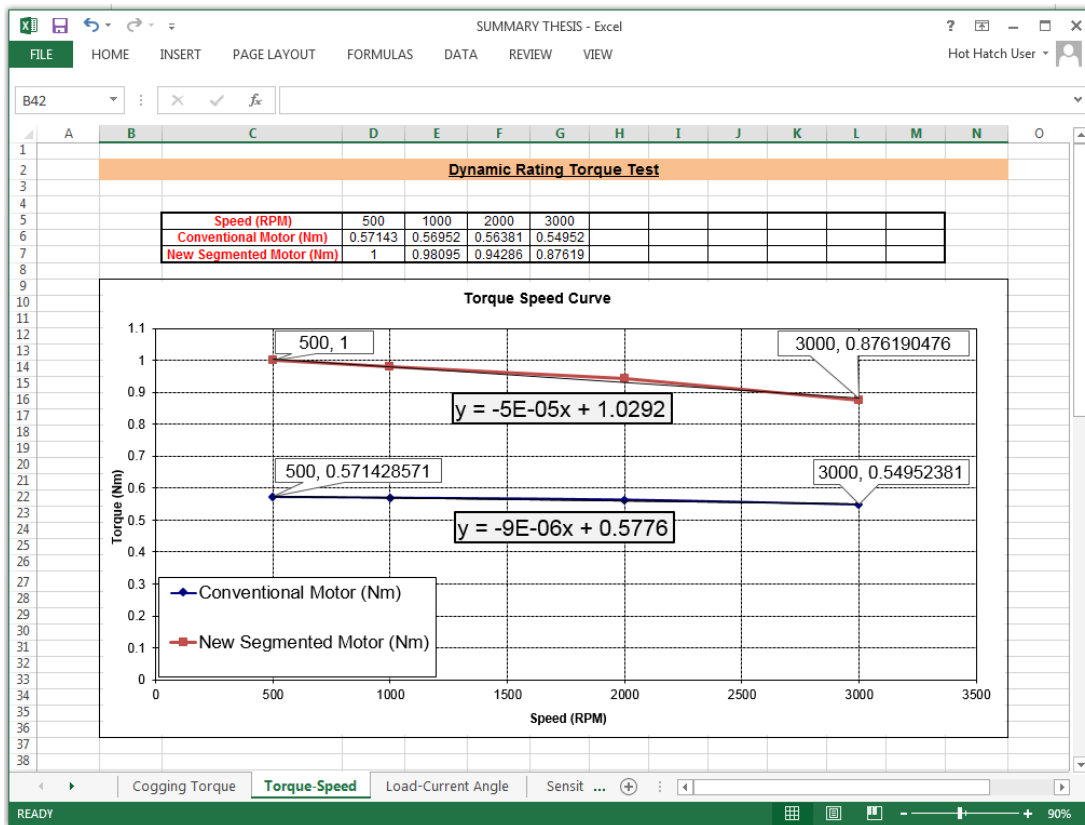


Fig. 5.19. Comparison of dynamic torque rating-speed characteristics for current solid stator core and the new segmented stator design.

Motor Dynamic Rating Test ID 4176 Motor B															
Speed	RPM	50	50	500	500	1000	1000	1500	1500	2000	2000	2500	2500	3000	3000
Transducer zero load offset															
Switching Frequency	kHz	12	12	12	12	12	12	12	12	12	12	12	12	12	12
Torque (Nm)		0.91926	1	0.89528	0.98481	0.85931	0.95364	0.78657	0.8785	0.76739	0.86731	0.7474	0.84732	0.71942	0.82814
Kt (Nm/Arms)		1.69	1.64	1.88	1.63	1.67	1.62	1.58	1.55	1.58	1.57	1.54	1.57	1.53	1.57
Current (A _{RM3})	CH 1	6.87	7.7	6.666	7.568	6.457	7.39	6.204	7.09	6.052	6.997	5.935	6.89	5.735	6.765
	CH 2	8.8	7.6	6.644	7.544	6.371	7.295	6.208	7.091	6.088	7.07	5.941	6.9	5.737	6.771
	CH 3	6.81	7.63	6.682	7.581	6.479	7.409	6.241	7.128	6.125	7.057	5.973	6.932	5.784	6.792
	SUM	6.82	7.624	6.665	7.564	6.437	7.364	6.217	7.103	6.088	7.041	5.949	6.906	5.747	6.777
Voltage (V _{RM3})	CH 1	158.24	157.3	179.88	180.89	195.22	196.91	158.25	159.13	175.9	177.8	194.53	197.22	214.8	218.1
	CH 2	156.8	155.6	174.3	175.11	188	189.53	156.22	157.07	173.7	176	192.59	195.54	212.8	216.4
	CH 3	156.42	155.3	174.61	175.58	189.32	191.08	158.24	159.24	176.9	178.6	192.59	195.48	212	221.6
	SUM	271.1	270	305.2	306.9	330.2	333.2	272.9	274.2	304.1	307	349.49	341.9	372.8	378.8
Motor Input Power (W)		237	304.9	732.6	858.2	1246	1434	1714.7	1953.6	2186	2508	2626	3017	3013	3505
Motor Output Power (W)		4.81	5.23	46.85	51.54	89.94	99.81	123.49	137.92	160.64	181.56	195.57	221.72	225.90	260.04
Drive Input Power (W)		232.189	299.667	685.747	806.661	1156.06	1334.19	1591.21	1815.68	2025.36	2328.44	2430.43	2795.28	2787.1	3244.96
Copper Loss(W)															
Iron +Mech Loss (W)															
Efficiency %		2.03	1.72	6.40	6.01	7.22	6.96	7.20	7.06	7.35	7.24	7.45	7.35	7.50	7.42
THD Current (%)															
Fundamental Current (A _{RM3})	CH 1	17	21	3.5	3.9	4.6	4.5	2.9	3	3.6	3.7	4.8	4.9	5.7	5.3
	CH 2	15	15	3.6	3.7	4.3	4.1	2.7	2.7	4	3.9	4.7	4.5	5.8	5.6
	CH 3	10	8	3.8	4.1	4.7	4.5	3.3	3.5	4.2	4.2	5	4.7	5.9	5.7
	SUM														
Fundamental Voltage (V _{RM3})	CH 1	99.75	99.64	97.44	97.2	92.9	92.46	118.2	113	87.25	83.6	66.17	63.11	51.46	48.29
	CH 2	99.7	99.62	97.3	97.04	92.46	92	115.4	110	84.86	80.6	63.92	60.93	49.38	46.2
	CH 3	99.73	99.65	97.29	97.05	92.44	92	115.9	111	84.7	81	64.2	61.3	49.78	46.7
	SUM														
Thermocouple	Temp °C														
T0: Ambient		19.9	20.65	20.44	20.37	21.45	20.72	20.388	19.517	20.388	20.242	21.036	20.313	20.683	20.538
T1: Winding Top (inside slot)		101.22	125.67	100.92	126.21	100.83	126.6	100.781	124.923	100.88	124.954	102.801	125.321	101.264	125.484
T2: Top of Motor (front end frame)		63.5	75.2	64.06	75.72	64.31	76.78	67.017	78.697	66.662	78.302	67.102	78.025	66.275	77.757
T3: Winding Middle		101.22	125.63	100.81	126.2	100.78	126.79								
T4: Winding Bottom (inside slot)		96.41	119.32	96.44	120.27	96.47	120.8								
T5: RHS Bottom of Mounting plate (motor side)		52.63	61.83	53.47	62.05	53.45	62.17	55.831	64.786	55.102	63.252	54.882	62.333	53.366	60.614
T6: RHS op of Mounting Plate (motor side)		51.21	59.84	52.06	60.09	51.91	59.62	54.292	62.318	53.094	61.088	53.464	60.102	52.088	59.922
T7: Back End Frame / Encoder Housing Cover		66.33	79.06	67.14	79.18	69.05	82.04	94.181	115.96	94.738	113.545	96.162	114.32	95.85	115.557
T8: Top Motor Housing Middle		75.27	91.43	76.68	92.88	77.4	92.61	78.527	93.574	78.741	93.837	80.503	94.451	80.366	95.059
T9: RHS Motor Housing Middle		77.7	94.41	78.4	95.45	79.27	96.41	79.809	96.75	79.912	96.377	81.686	96.193	81.243	97.053
T10: Encoder Housing		74	88.29	74.32	89.32	75.54	90.78	76.998	91.567	77.805	91.785	78.851	92.234	78.121	93.055
T11: Bottom Motor Housing Middle		78.95	95.26	79.36	96.1	80.36	97.57	80.878	97.108	81.003	96.588	81.182	96.009	79.808	94.394
T12: L Plate Top		30.27	32.49	30.7	33.8	31.12	33.38	28.671	29.717	28.398	30.337	28.649	30.118	28.667	30.637
T13: Mounting Plate (near to front end frame)		56.68	66.8	57.47	67.47	56.7	67.54	58.57	67.744	57.7	67.206	57.595	66.34	57.118	65.671
T14: Top of Motor (front end of housing)		65.81	79.35	66.88	79.37	66.62	79.95	69.877	81.814	69.505	81.769	69.83	82.361	69.955	81.6
T15: Top of Motor (rear end of housing)		78.09	92.73	77.37	92.47	77.14	93.81	79.75	95.56	80.043	95.861	82.038	96.404	81.275	97.135

Fig. 5.20. Dynamic torque rating test results for the new design at increased winding temperature.

Hence tests are performed for two different maximum winding temperature levels, one with a delta temperature of 80°C and another with a delta temperature of 100°C . The performance test data is shown in Fig. 5.20 and plotted in Fig. 5.21.

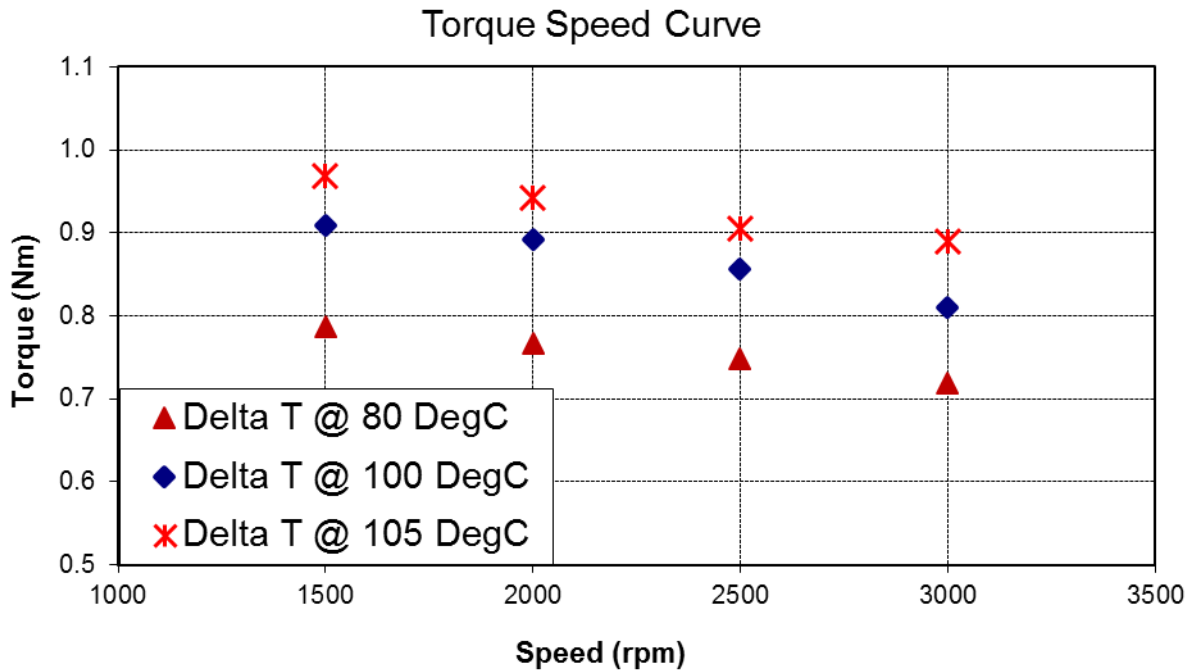


Fig. 5.21. Dynamic torque rating-speed curve characteristics for different winding temperatures.

Test results of the maximum torque as function of the maximum winding temperature are presented in Fig. 5.21. It can be observed clearly that the torque-speed curve improves with the maximum winding temperature increase.

An almost 20% torque increase with a 25°C delta temperature change for a given speed is evident. Fig. 5.22 shows the variation of maximum torque with the winding temperature at a given speed, which is almost linear.

The increasing temperatures are reached by increasing the current in the windings. It is evident that if temperature can be reduced by removing heat, then an increased torque producing current can be accommodated in the winding, thereby increasing the torque density of the servomotor.

For the servomotor presented in Chapter 2 and used in this investigation, the stator components contributing heat flow resistance are the contact between components, the electrical wall insulation material, the stator iron core and the aluminium housing.

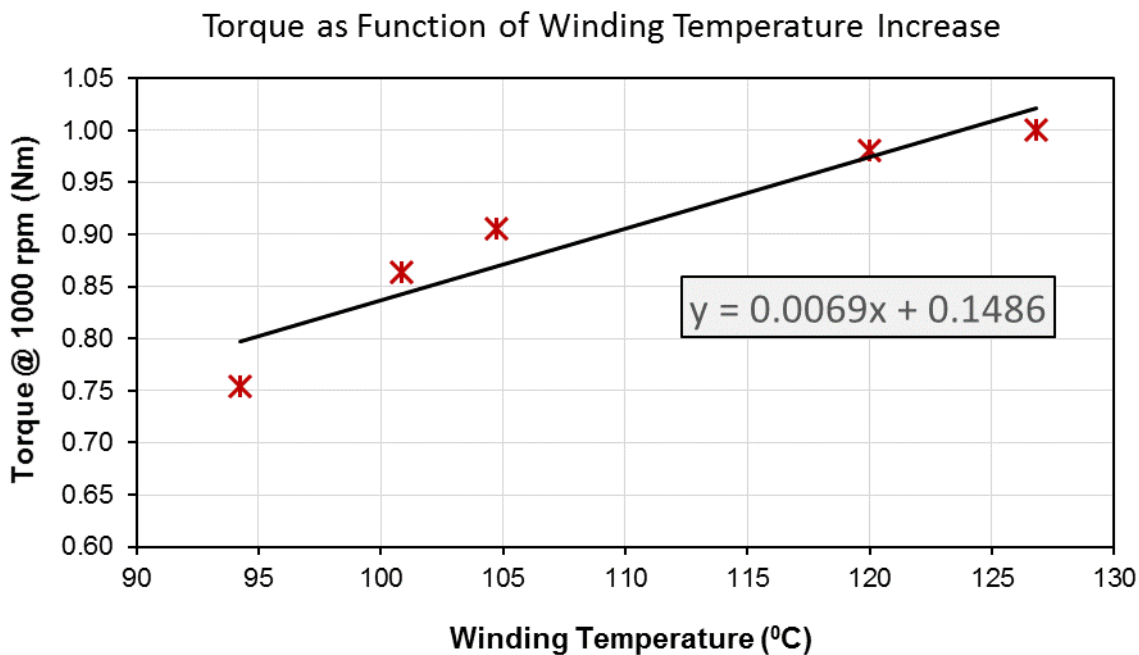


Fig. 5.22. Variation of servomotor torque level with the winding temperature

The contact resistances between the materials are dependent on the manufacturing methods. The thermal resistances of the wall insulation material, stator iron and aluminium housing are more dependent on their thermal conductivities. The wall insulation material thermal conductivity is typically around $0.14 \text{ W/m}^{\circ}\text{C}$. The thermal conductivity for the iron core material and the aluminium housing are around $55 \text{ W/m}^{\circ}\text{C}$ and $240 \text{ W/m}^{\circ}\text{C}$, respectively.

Hence the thermal resistance contribution of the iron and aluminium components can be neglected. Consequently, the wall insulation presents the most significant thermal barrier between the stator winding and the housing surface.

Hence the thermal conductivities of different paper wall insulation materials are investigated in Chapter 6.

5.5. Summary

The test results for cogging torque, open circuit iron losses and dynamic torque rating tests have been presented in this chapter.

Due to the permanent magnet retention devices in the rotor it was not possible to use an analytical method or FEA to predict the cogging torque.

However, FFT analysis is applied to the measurements from the torque sensor to obtain the 60 [Hz] frequency component correspondent to the cogging torque for the new design.

Iron losses are obtained clockwise and anticlockwise for both the cold and hot servomotor conditions. An equation based on the test results has been derived and its predictions compared with test results for different servomotor lengths.

Finally, dynamic torque rating performance test results are presented and compared for both the new and conventional servomotor prototypes. Different maximum reference winding temperatures are compared regarding torque levels. A stator system conductivity improvement is proposed in order to enhance the torque density of the new servomotor.

CHAPTER 6

INFLUENCE OF WALL INSULATION MATERIAL

6.1. Introduction

This chapter provides a study of the main stator thermal barrier of inner-rotor cylindrical brushless permanent magnet (BPM) synchronous servomotors with distributed and concentrated winding configurations. This thermal barrier is the electrical wall insulation material between the winding and the stator core. Different electrical insulation materials such as ceramic plastic can be used for this purpose.

However the best solution for the new BPM synchronous servomotor found in this research work is the paper type slot-liner used in conventional motors.

Therefore thermal impact of a selection of paper based materials is investigated for both the conventional stator and segmented stator technologies in order to identify their impact on the motor performance.

It is important to realise that the intended purpose of the material under study is electrical insulation.

The fact that it forms a thermal barrier is an undesirable side effect because heat generated within the stator windings due to copper loss should be removed as quickly as possible to minimise harmful temperature rises.

Unfortunately good electrical insulators tend also to be good thermal insulators and therefore the search is for a good compromise in which the material has a minimal electrical conductivity while having an acceptably high thermal conductivity.

6.2. Why Paper Electric Wall Insulation Material

Electric motors controlled with variable frequency drives (VFD), of which the BPM synchronous servomotors under study are examples, normally use switched power electronics with pulse width modulation (PWM) techniques that entail sudden changes of current during the switching that causes very high short term induced

voltages due to the inductance of the windings. An example of the voltage spikes caused by this process is shown in Fig. 6.1 for a simple 50% duty cycle PWM.

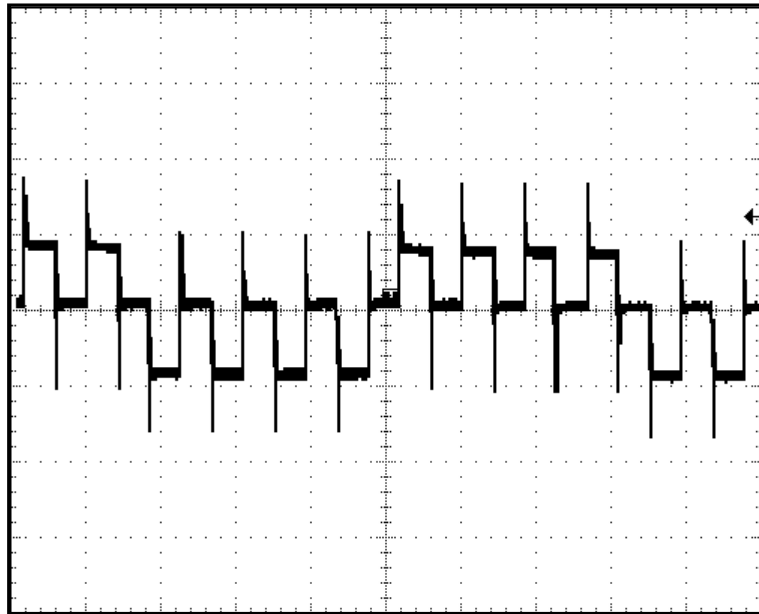


Fig. 6.1. Typical peak transition caused by PWM switching in motor with oscilloscope reading 400 Volts per division.

A primary insulation system such as the enamel coating of the copper conductors is subject to breakdown due to the associated high electric fields.

Typically secondary insulation systems such as combined wall insulation materials and resins are used to solve this problem.

However, in the situations where high performance and small size are desired such as in the servomotors under study, the thermal characteristics of the electrical insulation materials become a problem in terms of the motor performance and lifespan.

In this regard, this research work investigates the thermal impact of using different paper wall insulation materials on high-performance TENV BPM synchronous servomotors.

6.3. Thermal Properties of Paper Electric Wall Insulation Material

In this section five different commercially available electrical paper wall insulation materials are evaluated for their thermal conductivities, mechanical and electrical properties under force. These characteristics are very critical in motor manufacturing with high slot-fill, segmented or concentrated double-layer winding configurations.

Good contact and thermal distribution within the coil enhance the heat transfer from the windings to the stator core.

However considerable mechanical stress is normally applied to the wall insulation material in service. It is therefore pertinent to analyse the more popular insulation materials and find out how they behave under such stress.

The five selected paper wall insulation materials are denoted as Materials A, B, C, D and E, as shown in Fig. 6.2, and their main properties are presented in Table 6.1.

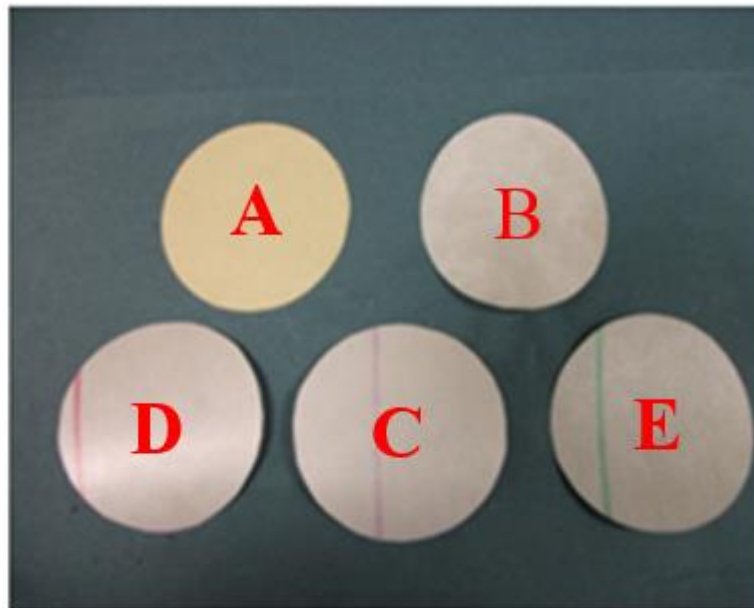


Fig. 6.2. Wall insulation materials for the thermal conductivity test.

Material A has the best dielectric strength and the best thermal conductivity values. Material C is the worse material regarding these properties.

TABLE 6.1.
Important material properties and delta temperature

Properties	Unit	A	B	C	D	E
Thickness	mm	0.25	0.25	0.25	0.25	0.25
Dielectric Strength	KV/mm	37	32	19	29	25
Shrinkage at 300 °C	%	0	0.4	-	1.5	1.6
Density	g/cm ³	1.05	0.96	0.67	0.65	0.92
Thermal Conductivity	W/mK	0.25	0.139	0.086	-	0.13
Sample ΔT @ 0 Force	°C	17.53	19.59	26.61	21.47	19.64

6.4. Two-Plate Experimental Rig

A simple approach is taken for the measurement of the mean value of the thermal conductivity of the materials, as moderate accuracy is sufficient. This is achieved using a guarded heater test stack as shown in Fig. 6.3.

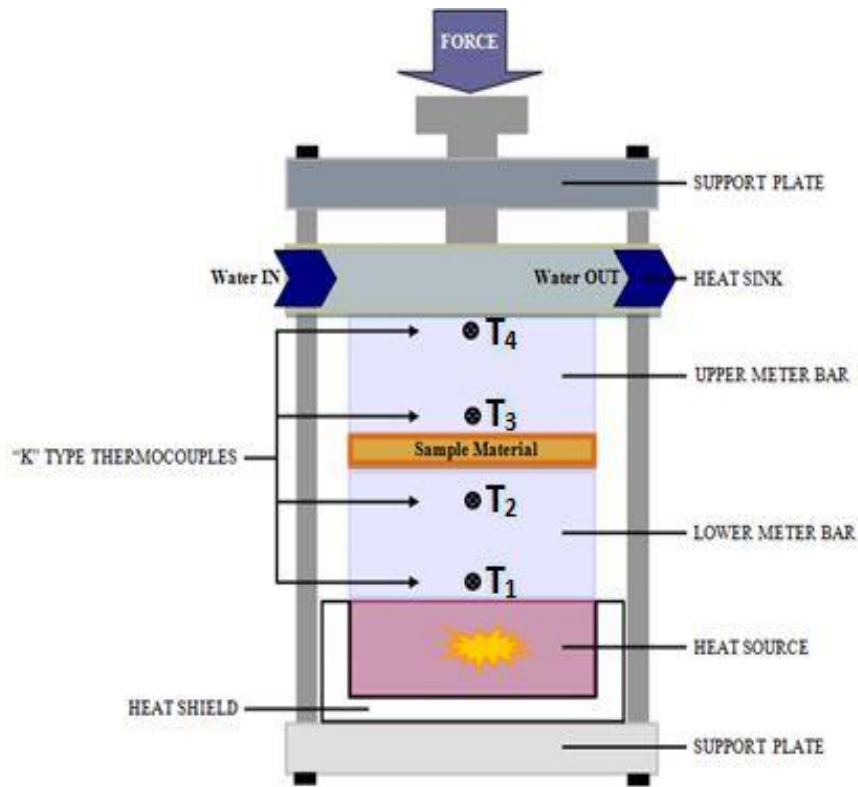


Fig. 6.3. Two-plate system test rig for wall insulation materials.

The main components of this test rig are the heat source, lower and upper meter bar, sample material and the heat-sink. These components form the main heat path to the system rig and the material is the only changeable component of the test, thereby ensuring fair comparisons. The guarded heater test stack is shown in laboratory environment in Fig. 6.4

The thermal behaviour of a TENV BPM synchronous servomotor is very complex and its analysis is a 3D problem.

In contrast, a two-plate thermal conductivity test rig as used for ASTM D5470-06 (ASTM, 2011), presents a 1D thermal problem and may be used to easily evaluate the wall insulation material thermal conductivity, electrical and the mechanical properties. It is reasonable to suppose that good results from this test on a given

insulation material imply good performance of the same insulation material in the servomotor.

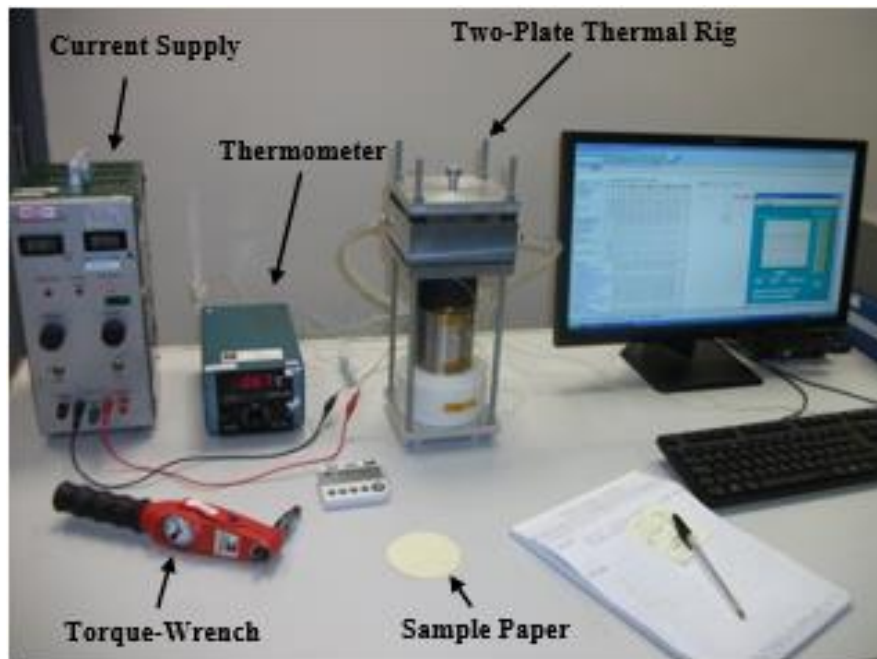


Fig. 6.4. Test setup for paper wall insulation material thermal conductivity.

Such an apparatus has therefore been used for preliminary tests and this is shown in Fig. 6.3 and Fig. 6.4. It is based on upper and lower plates, referred to as meter bars, between which the insulation sample is placed.

6.4.1. Thermal Conductivity Test

The lower meter bar is in direct contact with a heat source and the upper meter bar is in direct contact with a water cooled heat sink.

For the wall insulation material thermal conductivity test the DC current referenced power supply, shown in the laboratory environment of Fig. 6.4, is used to keep the current density in the heater constant. The five wall insulation samples have been cut and labelled material A to material E as shown in Fig. 6.2, the two most promising of which have been fitted to the prototype servomotors for the torque-speed performance tests.

In a double-layer winding, when good mechanical contact is achieved between the copper conductors, the insulating layer and the stator core, the thermal distribution within the stator improves (Magnusson, 2003), consequently enhancing the heat transfer from windings to the stator core.

This improvement, however, is only possible with considerable mechanical stress applied to the wall insulation in service.

This is therefore simulated by applying a force to compress the insulation sample between the plates, by means of a screw torque, as shown in Fig. 6.3.

The rig provides temperature measurements from which the mean value of the thermal conductivity for each wall insulation sample can be determined.

The power dissipated in the heat source of Fig. 6.3 is $P_R = VI$, where I is constant and V varies only as a function of the copper coil resistance that is a function of the resistivity, $\rho = \rho_0(1 + \alpha \times (T_c - T_0))$, where $\alpha = 0.00393 / ^\circ C$ is the temperature coefficient of resistivity for copper, T_c is the coil temperature and T_0 is the ambient temperature.

The insulation samples do not receive impregnation treatment similar to that used for the servomotors with the impregnating resin (Nategh et al., 2014). However their thicknesses are identical in order for meaningful comparisons of their intrinsic heat conduction properties to be made.

Table 6.1 shows the relevant sample properties. From Table 6.1 is evident that there is a positive correlation between the thermal conductivity of the insulation material and its density.

The last row of Table 6.1 shows the results of a preliminary experiment, i.e., the temperature difference, ΔT at 0 Nm screw torque.

These are the first points on the graphs of Fig. 6.5, which present the results of further experiments, i.e., graphs of the temperature difference, ΔT , between the thermocouples, T_2 and T_3 plotted against the applied screw torque over the range, 0 Nm to 10 Nm.

It is evident in Fig. 6.5 (a), where no material is inserted between the meter-bars, that the test rig is non-linear.

This is attributed to the surface roughness of the meter-bars. This nonlinearity, however, appears less pronounced with the paper insulation samples inserted between the upper and lower meter-bars as shown in Fig. 6.5 (b) to Fig. 6.5 (f).

This is attributed to microscopic deformation of the material improving contact with the cast iron meter-bars despite the surface undulations. In view of this, least square regression has been applied to obtain straight line fits to the data.

It can also be deduced, by comparing Fig. 6.6 (a) with Fig. 6.5 (b) to Fig. 6.5 (f), that the contribution of the rig to the overall temperature drop obtained with each sample in place is insufficient to affect the order of the samples regarding the temperature differences.

First, it can be observed in Table 6.1 that materials A and B have the lowest temperature differences of $\Delta T=17.53\text{ }^{\circ}\text{C}$ and $\Delta T=19.59\text{ }^{\circ}\text{C}$ at zero screw torque.

As would be expected, Fig. 6.5 (b) to Fig. 6.5 (f) indicated that the temperature differences reduce with the screw torque.

Comparison of Fig. 6.5 (b) to Fig. 6.5 (f) then reveals that Material A has the minimum temperature drop over the whole screw torque range and is therefore thermally selected for the motor prototypes.

Regarding the second thermal candidate, comparing Fig. 6.5 (c) to Fig. 6.5 (f), it is evident that material E has a lower temperature difference than materials B, C and D for screw torques above 2Nm.

In view of the variations in pressure at the insulation interface likely to occur in the real servomotor, however, considerable weighting should be given to the results at zero screw torque as these represent the worst case.

Hence all insulation materials are preselected for the dielectric strength test before prototyping of BPM synchronous servomotors.

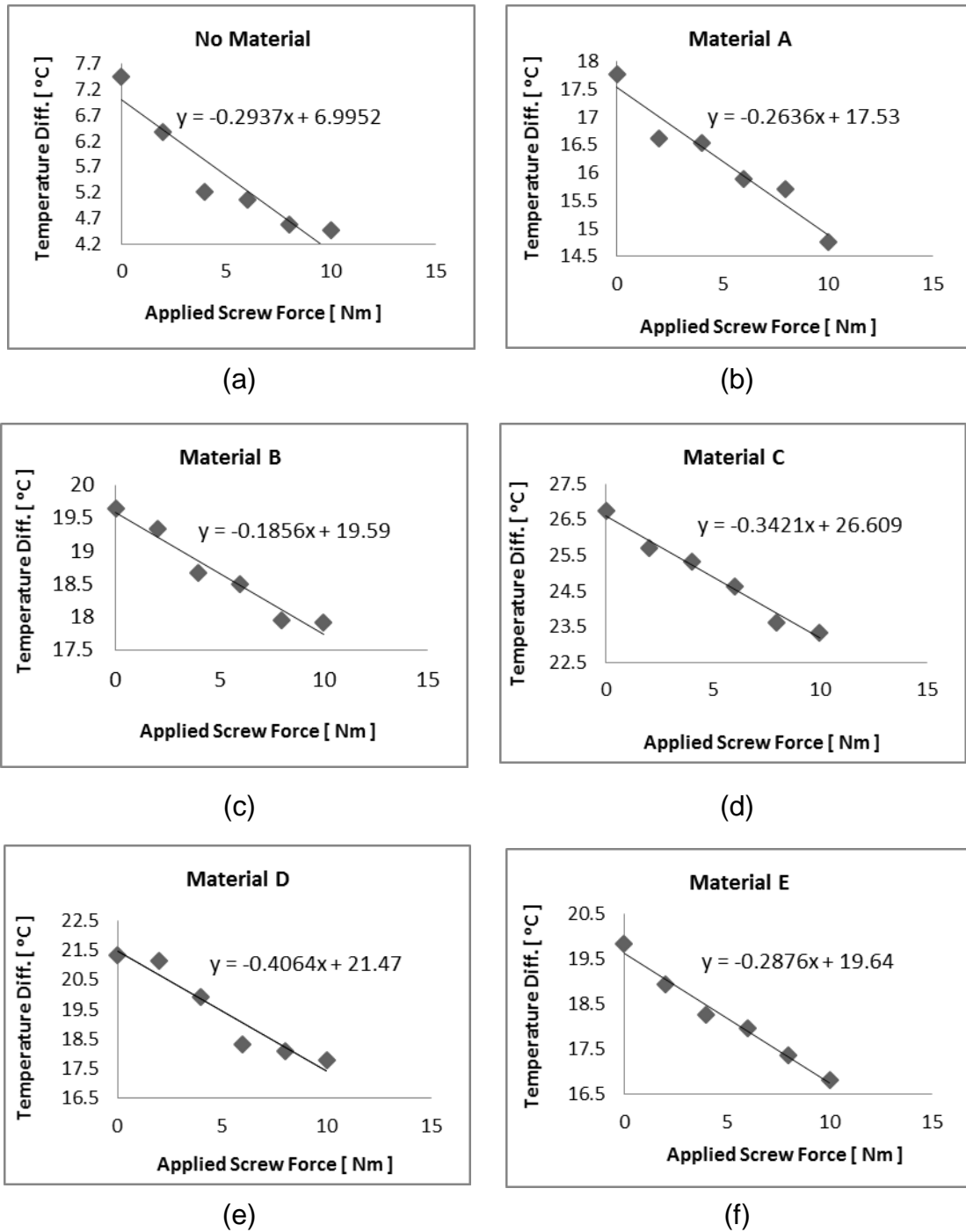


Fig. 6.5. Paper wall insulation material testing for thermal conductivity.

6.4.2. High-Voltage Insulation Material Testing for Safety

Apart from its thermal and mechanical requirements, the main function of the paper wall insulation material is to insulate the copper conductors electrically.

These slot-liners between the windings and the laminations prevent short circuits of the servomotor phases to the ground. Based on (ASTM, 2011) it is assumed that

after impregnation, the dielectric strengths are of the same order of magnitude. However, the intrinsic dielectric strength needs to be sufficient to handle the PWM peak voltages since perfect impregnation cannot be secured during the manufacturing shown in Chapter 2.

Therefore the standard dielectric strength testing is performed for all five materials. Fig. 6.6 shows all slot insulation components of a BPM synchronous servomotor.

Without any water running in the two-plate system for the wall insulation material dielectric strength test, 2000 volts peak signal is applied for a short period (125 microseconds) across the heater coil shown in the laboratory environment of Fig. 6.4.

The heat-sink is connected to earth and therefore the master and test waveforms need to be similar if there is no conduction to the ground. The results for the five wall insulation samples are shown from Fig. 6.7 to Fig. 6.11. Apart from Fig. 6.9, all master and test waveforms are similar.

In Fig. 6.9 the peak value of the waveform is significantly lower than the master waveform and therefore Material C has to be rejected and not considered further.

Material B is selected together with material A for prototyping in view of their thermal and electric performances.

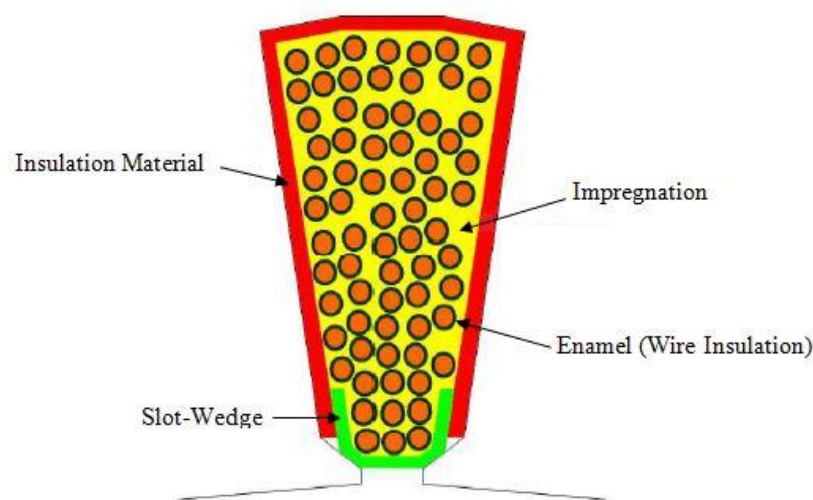


Fig. 6.6. Slot insulation system for electric motors.

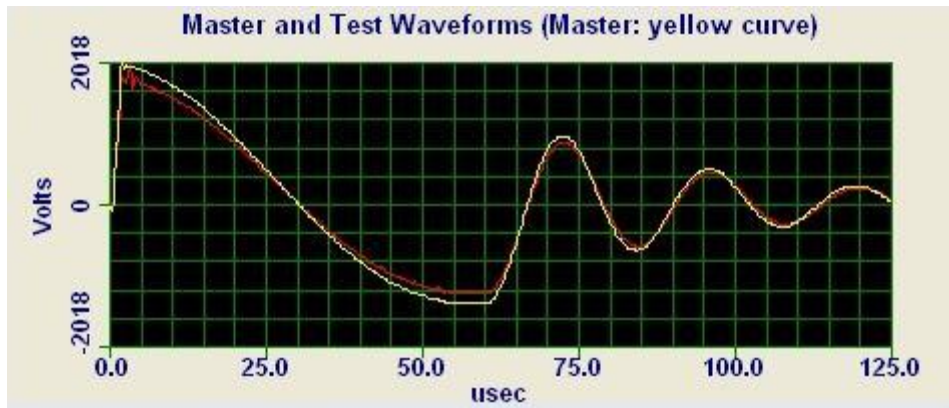


Fig. 6.7. Paper wall insulation Material A flash test.

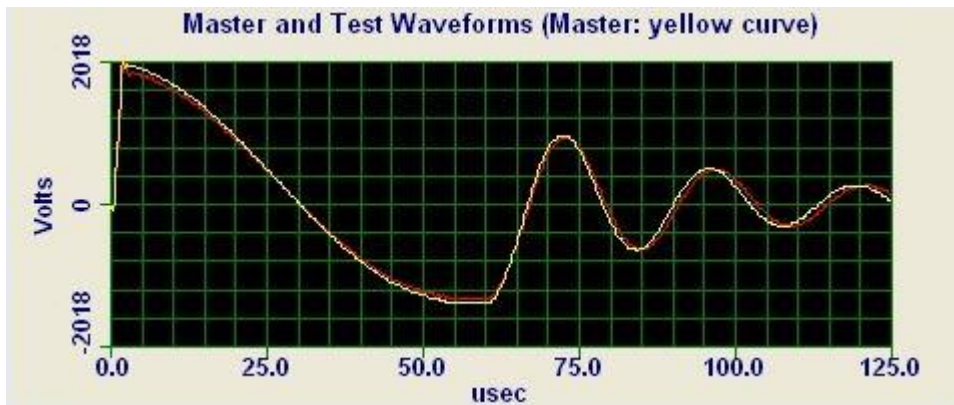


Fig. 6.8. Paper wall insulation Material B flash test.

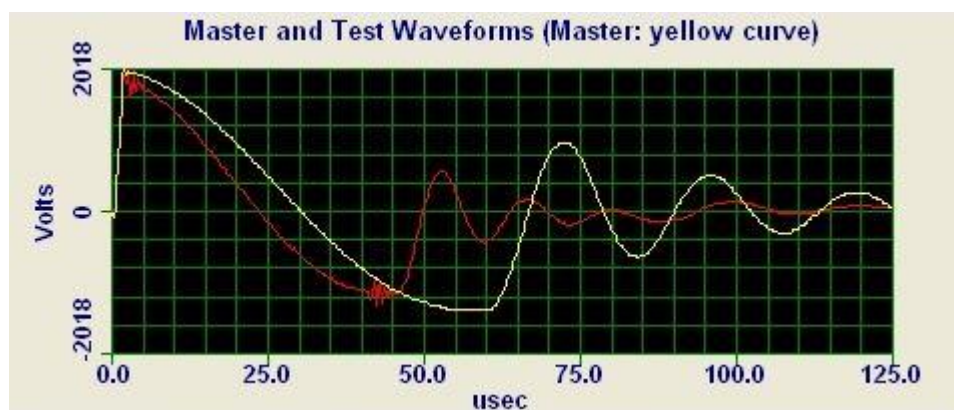


Fig. 6.9. Paper wall insulation Material C flash test.

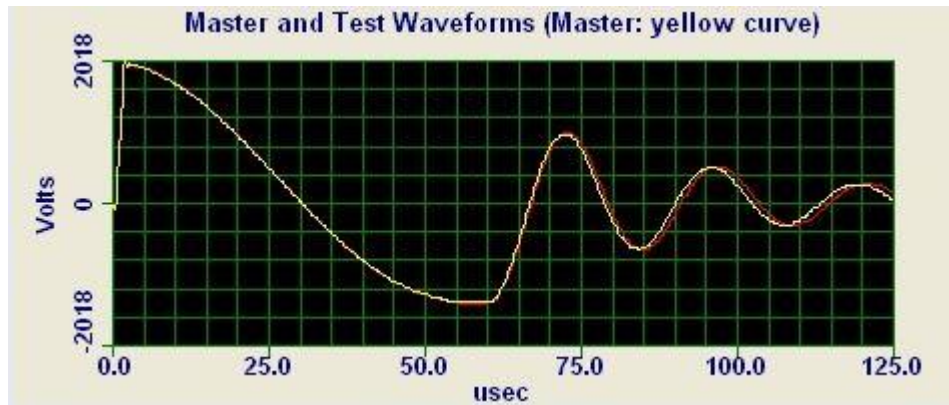


Fig. 6.10. Paper wall insulation Material D flash test.

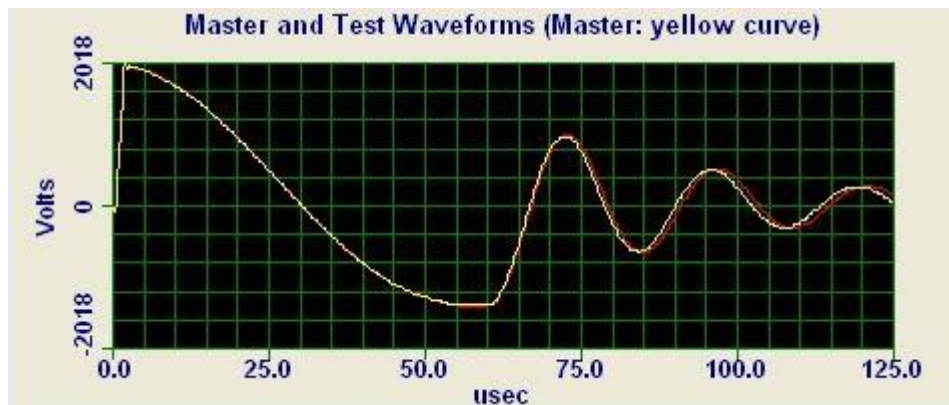


Fig. 6.11. Paper wall insulation Material E flash test.

6.5. Experiments Investigating Variation of Thermal Conductivity

The selected insulation Material A is fitted to one conventional and one segmented prototype and similarly insulation Material B is fitted to the remaining conventional and segmented prototypes.

Fig. 6.12 and Fig. 6.13 show, respectively, the structures of the conventional and segmented stators. A similar phenomena is found to take place in these stators to that observed in the two-plate test rig of Fig. 6.3.

This can be detected using readings from the J-K type thermocouple located in the winding and the thermocouple on the stator core, which are equivalent to thermocouples T_2 and T_3 in the test rig of Fig. 6.3. Since only copper loss occurs at

the stall condition, the heat transfer within the servomotor is only from the winding to its surroundings via the wall insulation and the stator stack as shown in Fig. 6.12 and Fig. 6.13.

In this case the copper wire acts similarly to the lower meter bar of the test rig, the stator iron core acts similarly to the higher meter bar of the test rig, the wall insulation material acts as the test rig sample and the surroundings acts as the heat sink of the test rig.

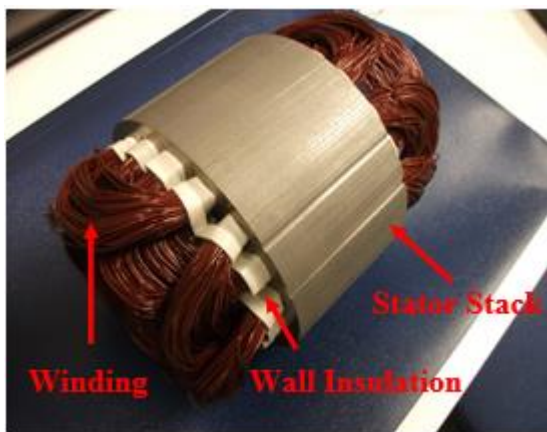


Fig. 6.12. Conventional stator with paper wall insulation and winding.

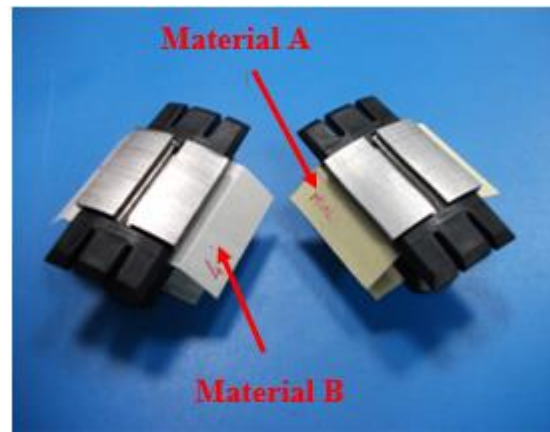


Fig. 6.13. Two stator segments with two paper wall insulation materials.

If good contact is achieved between the winding, the wall insulation and the stator stack, then the dominant thermal resistance contribution is from the wall insulation material.

This statement is supported by the thermal conductivities listed in TABLE 6.1 which are very low compared with 55 or $280 \text{ Wm}^{-1}\text{K}^{-1}$ for iron or copper, respectively, for the stator core and the stator windings.

The thermal resistance due to the copper and iron can therefore be neglected in theory. It must be realised, however, that in a real servomotor, the contact between components cannot be perfect, meaning that the gaps between the components may contribute significantly to the thermal resistance.

This effect has to be minimised in the design and manufacturing processes of the servomotors.

6.5.1. Prototype Construction

This section describes the construction of the conventional prototype motor whose stator is shown in Fig. 6.12 and the segmented prototype motor, two stator segments of which are shown in Fig. 6.13, that are fitted with the Material A and Material B insulation materials.

It is well known that the most significant problem with the segmented stator design is the high harmonic content that induces significant eddy-currents in the magnets (Popescu, 2012) (Dajaku, 2011).

This disadvantage is offset, however, by the lower copper loss and the higher torque density that can be obtained using this configuration together with improved manufacturing processes when compared with the conventional motor as described in Chapter 2.

Here a design comparison between the segmented 12-10 slot-pole prototype motor and the conventional 18-6 slot-pole prototype motor is presented. First, both servomotors are inner-rotor type machines as illustrated in Fig. 1.1 (a), Fig. 6.12 and Fig. 6.13. This construction is advantageous compared with the outer rotor configuration of Fig. 1.1 (b) due to the main motor losses taking place in the stator.

From the thermal viewpoint it is easier to cool down a stationary component compared with a rotating component, and it is easier to cool an external component than a hidden internal component within a motor structure.

Also, from a safety viewpoint it is advisable to keep the rotating components within a fixed structure rather than exposing them for easy contact with foreign objects. However in some applications such as wheel motors for electric vehicle propulsion it is required to have the outer part rotating.

In this research work, all the applications are catered for by considering only the configuration of Fig. 6.12 or Fig.13. The winding configurations for both the 18-6 and 12-10 slot-pole machines are shown in Chapter 2, Fig. 2.15 and Fig. 2.16, respectively.

Table 6.2 compares the design parameters of the two BPM synchronous servomotors for each selected materials.

For a fair comparison, both servomotors have the same split ratio (i.e., the ratio of the stator bore diameter to the stator outer diameter) and the same stack length.

TABLE 6.2.
Brushless servomotor details for the same application.

	Conventional Servomotor	Segmented Servomotor
Outer Diameter	115 mm	115 mm
Stack Length	60 mm	60 mm
Housing Length	186.8	156.8 mm
Bore Diameter	62 mm	62 mm
Magnet Length	2.95 mm	3 mm
Magnet Type	Bonded NdFeB	Bonded NdFeB
Sleeve Material	Carbon Fibre	N/A
Air Gap Length	0.75 mm	0.6 mm
Number of Teeth	18	12
Number of Poles	6	10
DC Link Voltage	350 V	350 V
Winding Type	Distributed, wound (1 – 4)	Single tooth, concentrated
Winding Connection	star	star
Number of Turns Per Coil	25	89
Number of Filers	2	1
Wire Diameter	0.644 & 0.608 mm	0.9 mm
Lamination Type	Silicon steel	Silicon steel
slot fill	38.39 %	55 %
split ratio	0.579	0.579
Back EMF Waveform	93 V	103 V

Both servomotors use bonded NdFeB permanent magnet material and low loss silicon steel laminations.

The significant differences between the two designs are their slot-pole combinations, winding configurations and stator core construction as follows:

- The current conventional motor has a through of 3 teeth that causes a relatively long winding overhang as shown in Fig. 2.15 or Fig. 6.12. In contrast, the segmented motor of Fig. 2.16 or Fig. 6.13 allows a much shorter overhang.
- The shorter winding overhang of the segmented stator design allows a shorter housing length and consequently a shorter overall length for the segmented motor. Also, thicker wire can be used allowing higher winding currents due to lower winding resistance and therefore providing an improved power/weight ratio

and torque/volume ratio. However for the same coil current, the copper loss tends to be much lower in the concentrated winding compared with the conventional overlapping winding due to improved compactness.

–Regarding manufacture, the insertion technique implemented with the conventional distributed winding does not allow a high slot-fill factor. The maximum slot-fill factor achieved was 38% compared with the 55% using the bobbin winding technique for the segmented double side stator winding. This is well described in Chapter 2.

–As shown in Fig. 6.12 and Fig. 6.13, the conventional motor has a single stator stack while the segmented stator comprises separate parts upon which the coils are wound.

The complete impregnated stator for both technologies is shown in Fig. 6.14 and Fig. 6.15, see next page.

As mentioned previously, when the wall insulation paper material is denser it enhances the heat transfer due to improved thermal conductivity.

However, when the servomotor is impregnated as shown in Fig. 6.14 or Fig. 6.15, the material with less density tends to have higher impregnability, which also may help to improve the heat transfer.

This is due to a higher proportion of air cavity volume in the lower density material being filled with resin impregnation.

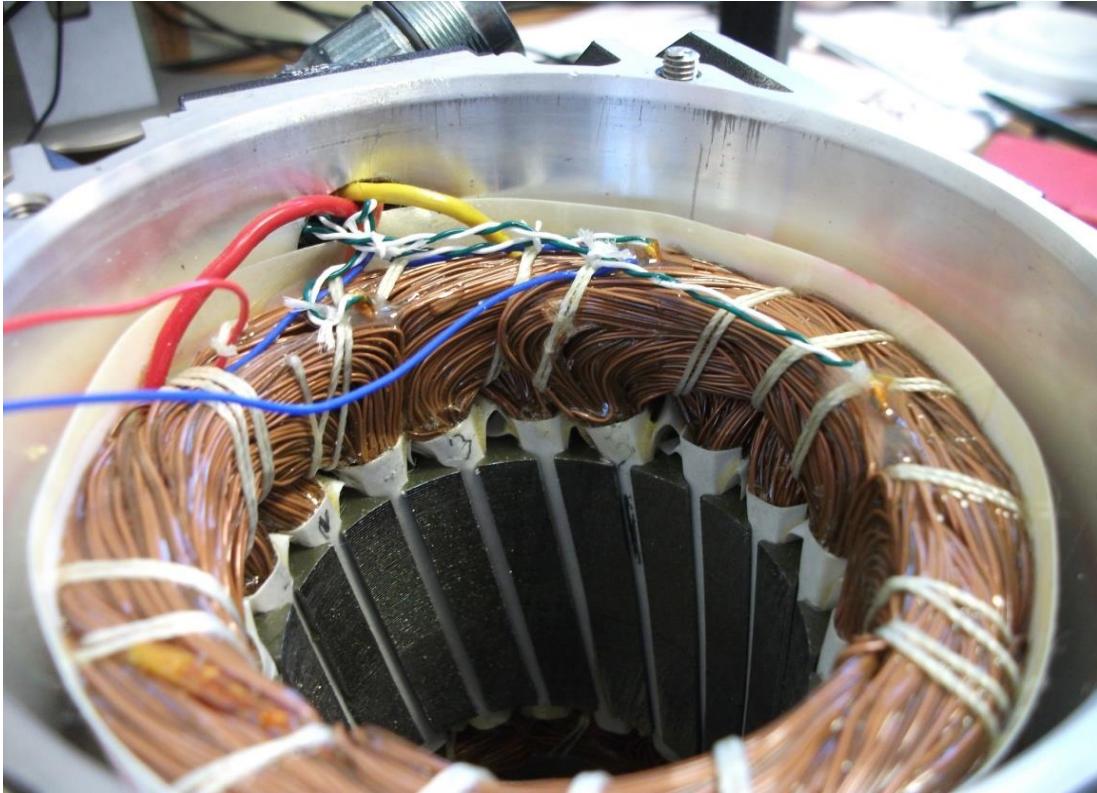


Fig. 6.14. Impregnated stator of skewed conventional motor.

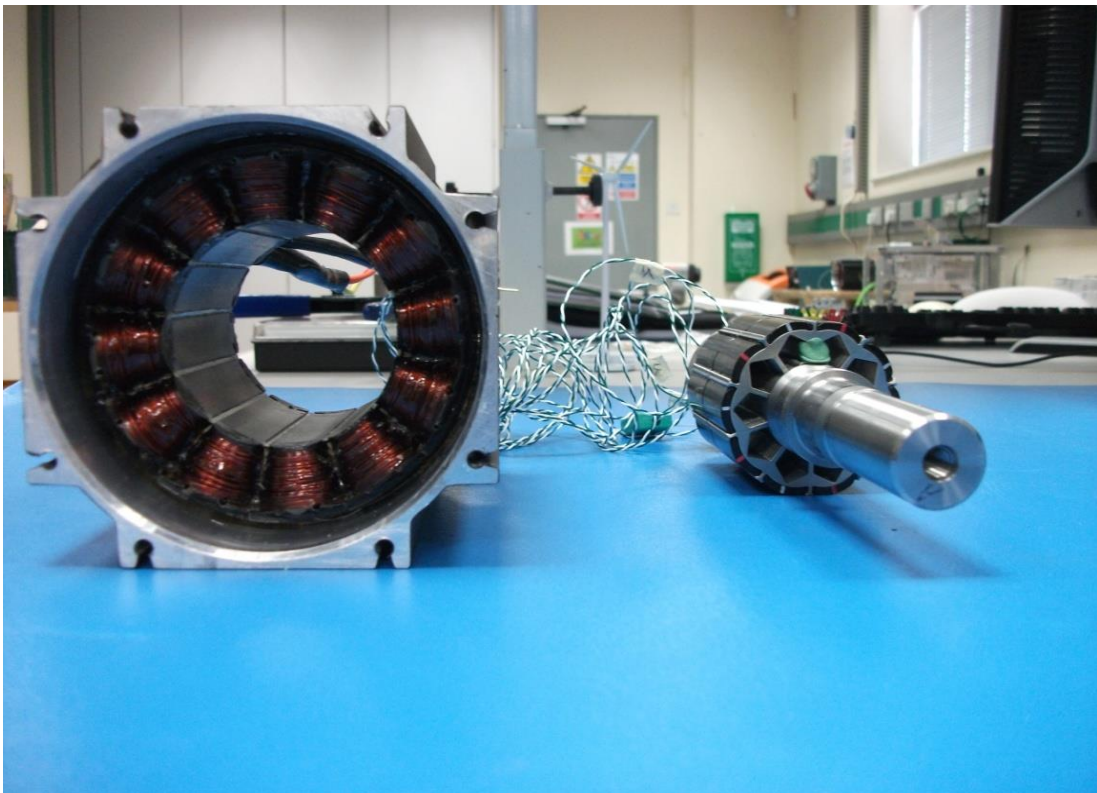


Fig. 6.15. Impregnated segmented stator and rotor of new non-skewed motor.

The microscopic views of Fig. 6.16 and Fig. 6.17 show, respectively, the material without impregnation and the material with impregnation.



Fig. 6.16. Paper wall insulation material without resin impregnation (DuPont, 2012).

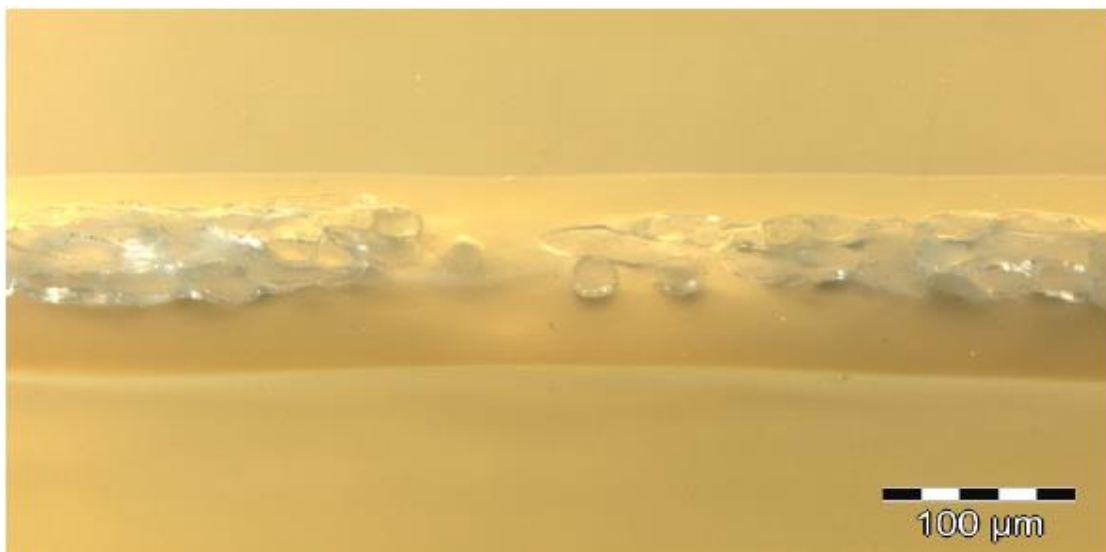


Fig. 6.17. Paper wall insulation material with resin impregnation (DuPont, 2012).

In this research programme, however, this impregnation effect is neglected in the choice of the materials intrinsic thermal conductivity and dielectric strength, since it assumed to have an insignificant effect on the thermal and electrical insulations.

Therefore the materials are selected only considering their thermal performance and the electrical insulation characteristics.

The impregnation is more important regarding the mechanical integrity of the winding structure for both structures as shown in Fig. 6.14 and Fig. 6.15.

6.5.2. BPM Synchronous Servomotor Torque Performance

A significant performance characteristic in a BPM synchronous servomotor is the torque density, which is the output torque per unit volume of the stator iron lamination stack.

In this research, the torque capability of the servomotor is quantified on the rig by means of a load torque generated from a second motor coupled rigidly to the servomotor under test, as shown in Fig. 6.18.

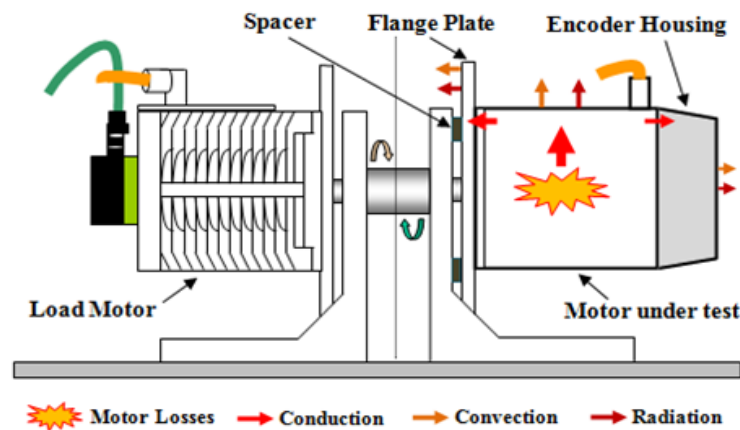


Fig. 6.18. System load testing.

The results in Fig. 6.19 include the rated speed of 3000 r/min of the prototypes.

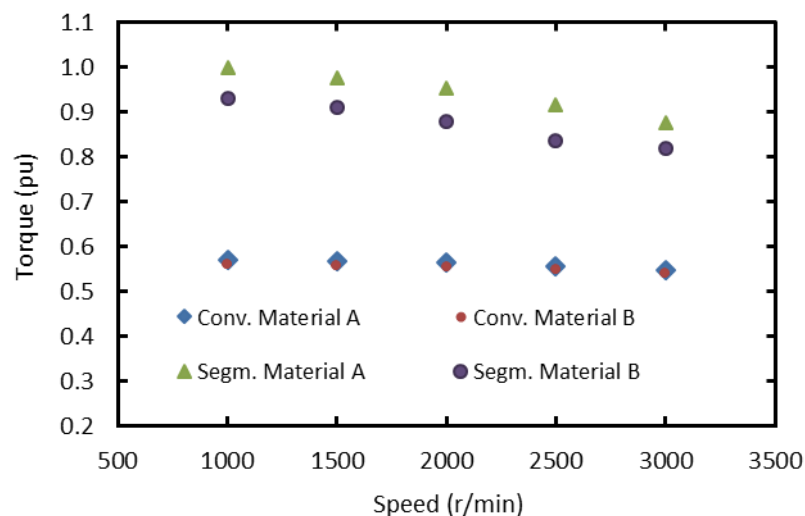


Fig. 6.19. Torque-speed curves for concentrated and distributed winding configurations using wall insulation paper materials A and B.

The maximum specified winding temperature of the prototypes is set to be around 125°C.

The two significant characteristics that can affect the torque capability are the current conduction capability of the copper wire and flux-carrying capability of the stator core. It is evident from Fig. 6.19 that the segmented prototypes deliver 40% more torque than the conventional prototypes near the stall condition and 35% more torque at the rated speed. It should be noted that the best current manufacturing process was used to maximise the torque performance for both the conventional and the segmented prototypes.

The negative gradient of the torque/speed characteristic of Fig. 6.19, however, is six times greater for the segmented prototype than it is for the conventional prototype. This is mainly attributed to the increased iron loss due to the increase in the number of rotor magnet poles in segmented motor.

The stall torque performances are compared by means of histograms in Fig. 6.20. This also compares the torque-constants (kt) and the winding currents. Hence the segmented motor offers a higher torque constant. The most notable improvement, however, is the input current capability of the segmented motor compared with the conventional one, the increase being approximately around 25%. Increase due to torque is around 40%, while the torque constant increase is about 10%.

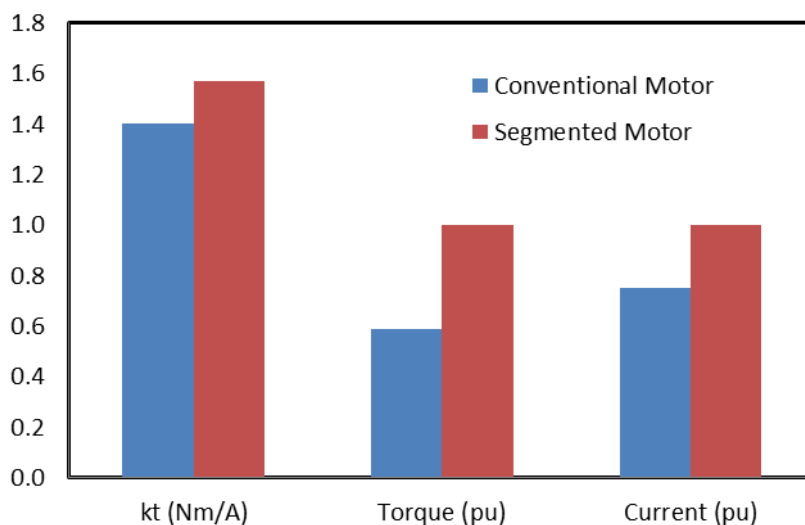


Fig. 6.20. Torque-constant, torque performance and current injected to the winding comparison between 12-10 and 18-6 slot-pole combinations.

Further test results for the selected wall insulation materials are presented in TABLE 6.3. It is evident that the only power loss component of the system is the stator winding copper loss or Joule loss, I^2R , due to the very low speed of 50 r/min.

As previously demonstrated, the phase resistances for both prototypes are equal to yield similar temperature rises due to copper resistivity increase as $\rho = \rho_0(1 + \alpha \times (T_c - T_0))$, while both brushless PM synchronous servomotors delta temperatures are $\Delta T = 80^\circ\text{C}$. Also $\Delta T = T_c - T_0$. Therefore comparing the winding temperature rises in degree C per watt will favour material A since it will tolerate a larger winding current (about 291 mA) than material B.

TABLE 6.3.
Temperature difference between winding and housing

MOTOR COMPONENT	Temperatures degree C at 50 r/min			
	Servomotor with Material A		Servomotor with Material B	
	$\Delta T = 80$	$\Delta T = 105$	$\Delta T = 80$	$\Delta T = 105$
Winding $^\circ\text{C}$	100.85	125.93	100.84	126.05
Housing $^\circ\text{C}$	69.97	85.06	68.47	81.84
Difference $^\circ\text{C}$	30.88	40.87	32.37	44.21
RMS Current A	6.514	7.32	6.223	7.072

6.6. Simulation Predicting Variations of Thermal Conductivity

Previous experimental work performed in section 6.5 showed that the use of the concentrated winding configuration with a high slot-fill benefits greatly from improvements in the conductivity of the paper wall insulation material.

Thus, if an alternative material with a higher thermal conductivity is used the maximum output torque increases and this is shown in Fig. 6.19.

Optimisation is required nowadays due to the current requirement for smaller and cheaper servomotors with higher efficiency due to material scarcity and the environmental impact.

The size of the BPM synchronous servomotor is ultimately dependent on the servomotor temperature limit and the rate of heat dissipation. Also many

components used in the BPM synchronous servomotor have different temperature limits.

Therefore it is very important to be able to estimate the temperatures in different locations in order to be able to estimate the BPM synchronous servomotor operating performance limits and life time. Advanced modelling software such as Motor-CAD is essential. The impregnation quality and gap variation temperature effects will be analysed here using Motor-CAD.

The effect of the improved thermal conductivity of the paper wall insulation material is analysed and the results compared with those obtained from the test and the analytical thermal model presented in Chapter 3.

6.6.1. Motor-CAD Thermal Modelling

The combination of the SPEED software and the Motor-CAD software is used for modelling of the prototype BPM synchronous servomotor thermal performances according to (Popescu, 2012).

The SPEED Outline model for the new fractional-slot concentrated winding tested in section 6.5 of this research work is presented in Fig. 6.21.

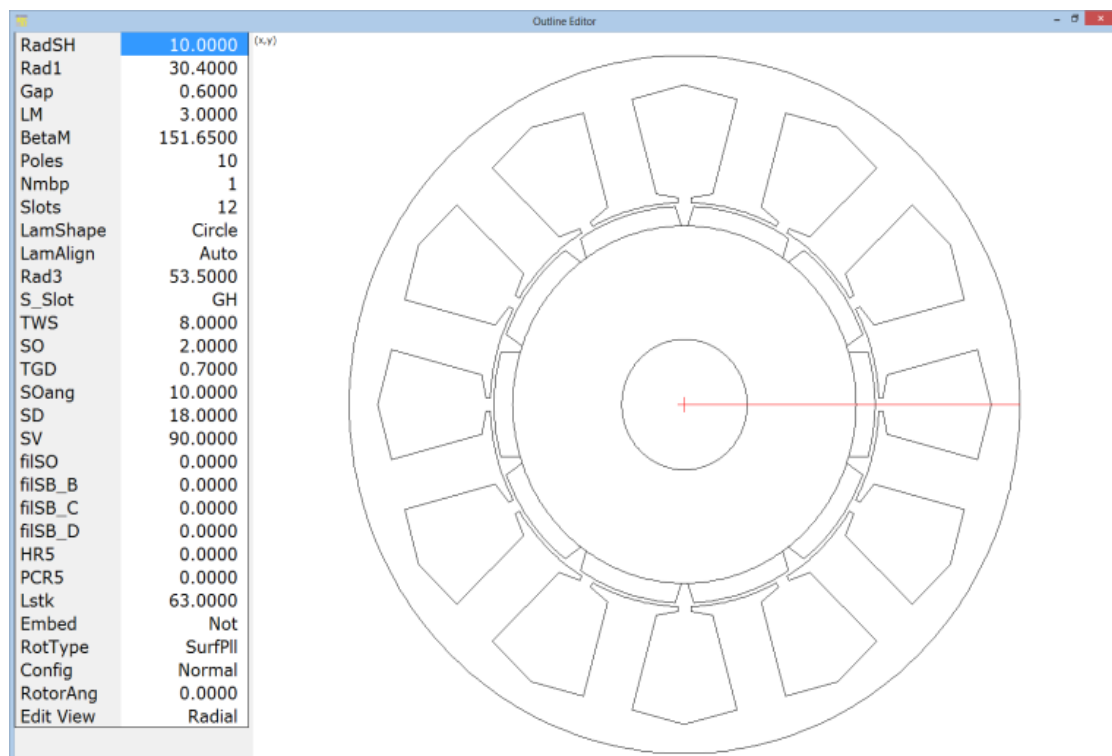


Fig. 6.21. SPEED: Outline Editor for new design brushless servomotor cross-section with 12 slots and 10 poles.

The SPEED Winding Layout for the new fractional-slot concentrated winding tested in the section 6.5 is shown in Fig. 6.22.

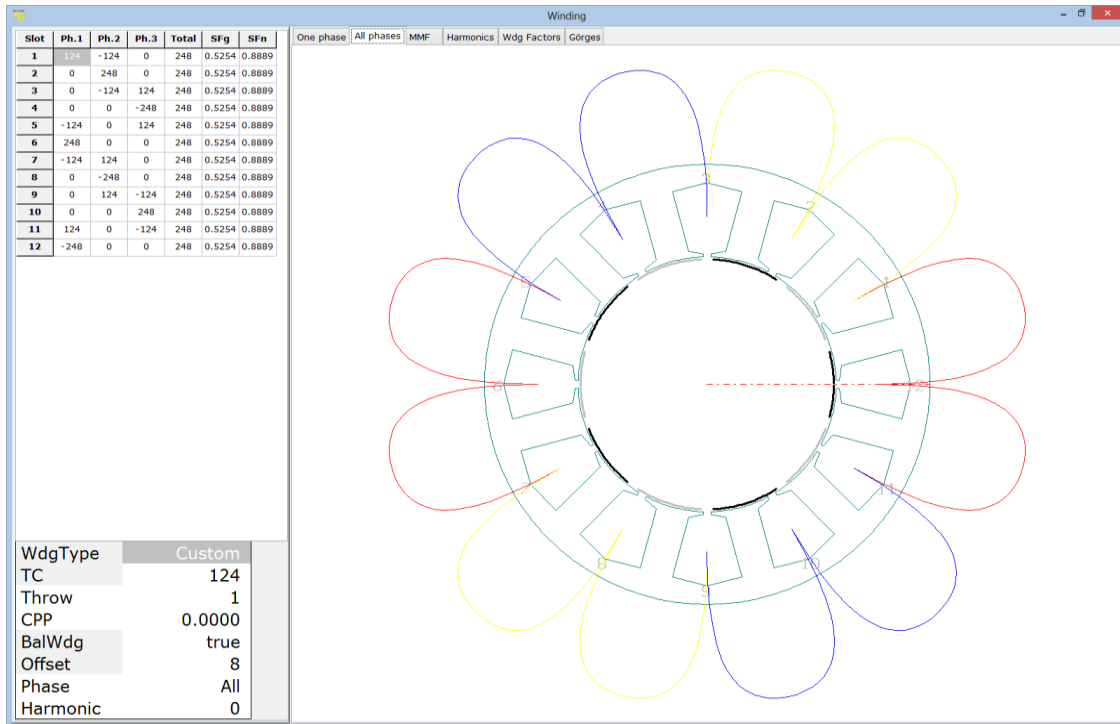


Fig. 6.22. SPEED: WINDING EDITOR for the segmented stator and concentrated windings.

The SPEED Outline model and Winding Layout for the new fractional-slot concentrated winding tested in the section 6.5 of this research work are presented in Fig. 6.21 and Fig. 6.22, respectively. When using SPEED, the prototype servomotor active material dimensions are input using the Outline Editor shown in Fig. 6.21. The next step is to define the winding details such as the number of turns, wire gauge, number of fillers, winding offset, throw, go-and-returns, etc...

Then the RMS current level from the test point is set on PC-BDC as highlighted in Fig. 6.23. The friction loss needs to be accounted for at 1000 r/min, and in this case it is set for 1.68W as shown in Fig. 6.24 based on pass results for same size BPM synchronous servomotor

Control							
RPM	1000.0000	Vs	620.0000	Drive	Sine	DCSource	Fixed DC
ISP	5.9040	DuCy	0.5000	Sw_Ctl	ISP_HB	gamma	0.0000
HBA	64.0000	HBtype	Constant	dq0	false	alpha6	0.0000
ChopType	Soft	FixfChop	No	fChop	0.0000	uCFR	600.0000
SVmode	Auto	VGcoefft	1.0000	u_MSVM	0.8000	MIX	1.0000
uVdm	0.0000	uVqm	0.0000	PGain	1.0000	IGain	0.0000
G_d	0.0000	G_q	0.0000	G_dq	0.0000	G_qd	0.0000
NumPoly	1	PolyOffs	1	SolvMG	false	MIX3	0.0000
Bifilar	false	NphUni	4	kBif	0.0000	ISPSpec	rms

Fig. 6.23. SPEED: PC-BDC | Control Set.

Windage & Friction, and Bearing Loss							
Wf0	1.6800	RPM0	1000.0000	NWFT	1.0000	Xmb	1.0000
cWmb	false	a_mb	0.0000	b_mb	0.0000	c_mb	0.0000

Fig. 6.24. SPEED: PC-BDC | Rotational Losses.

Then the ambient, winding and magnet temperatures need to be defined. In this case the ambient and winding temperatures were obtained from test as 21.1°C and 101.5°C. No information is available for the magnet temperature and therefore an initial guess is made as indicated in Fig. 6.25.

Thermal							
TempCalc	Fixed	FixTMag	IterX	Wdg2Mag	0.8000	Ambient	21.1000
T_Mag	80.0000	T_Wdg	101.5000	T_Brg	25.0000	T_Gap	25.0000
DegCW	0.0000	HTCcycl	0.0000	HTCend	0.0000	ThTol	1.0000

Fig. 6.25. SPEED: PC-BDC | Thermal Information.

Then one test point from section 6.5.2 is selected, in this particular case 1000 r/min is the selected test point from Fig. 6.19. Fig. 6.26 shows the prototype servomotor mounted on the rig, cables and 16 J-K type thermocouples at different motor locations.



Fig. 6.26. Prototype mounted in the rig system for the performance test.

The 16 J-K thermocouple locations in the servomotor test rig system are shown in Fig. 6.27. The performance results for the selected servomotor test point are presented in Fig. 6.28.

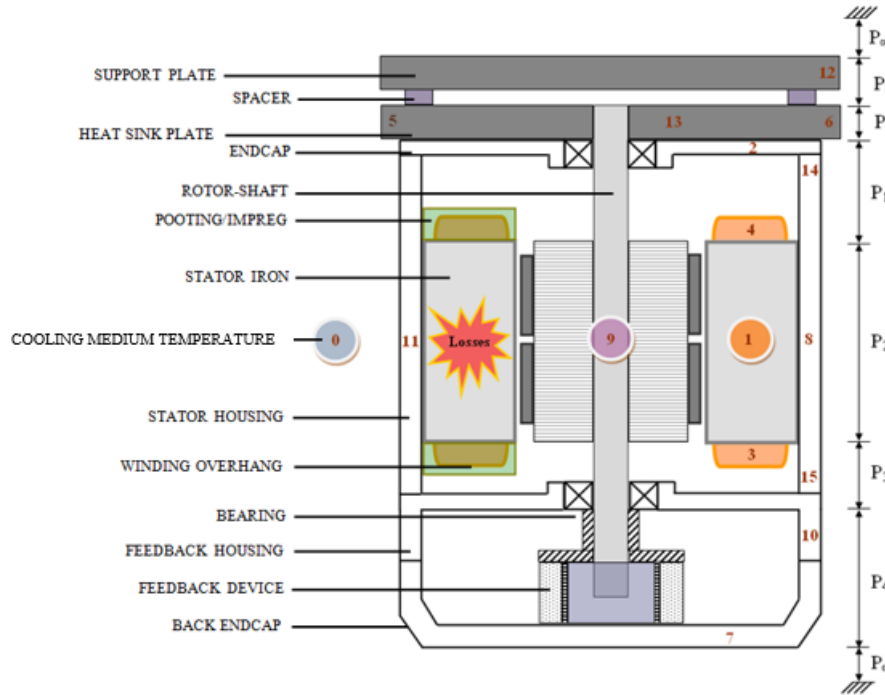


Fig. 6.27. Parts of servomotor and rig showing positions of thermocouples.

	RPM	50	50	500	500	1000	1000	1500	1500	2000	2000	2500	2500
Speed		50	50	500	500	1000	1000	1500	1500	2000	2000	2500	2500
Torque	Nm	10.1	11.19	9.81	10.95	9.43	10.65	9.05	10.3	8.84	10.2	8.5	9.95
Current (A _{avg})	SUM	6.223	7.072	6.103	6.944	5.904	6.782	5.653	6.565	5.547	6.524	5.359	6.4
Thermocouple Temperature Location													
T0: Ambient		21.04	20.55	20.82	21	21.1	20.51	19.116	20.037	19.659	19.514	20.263	19.995
T1: Winding Top (inside slot)		100.2	125.05	100.98	126.18	101.57	125.85	100.31	126.229	99.592	124.757	100.963	126.65
T2: Top of Motor (front end frame)		56.38	66.59	57.68	68.15	59.34	69.5	61.038	72.882	60.512	71.047	62.097	72.732
T3: Winding Middle		100.62	125.73	100.61	125.98	101.47	125.68	100.31	126.229	99.592	124.757	100.963	126.65
T4: Winding Bottom (inside slot)		100.84	126.05	100.89	126.27	101.35	125.67	100.31	126.229	99.592	124.757	100.963	126.65
T5: Right Hand Side Bottom of Mounting plate (motor side)		48.42	55.97	49.17	57.03	50.47	58.37	23.186	24.576	23.197	24.105	24.941	25.565
T6: Right Hand Side Up of Mounting Plate (motor side)		46.66	53.48	47.52	55.44	49.06	56.08	50.328	59.244	49.076	56.47	50.448	57.791
T7: Back End Frame / Encoder Housing Cover		60.45	71.17	60.75	73.09	63.03	74.6	81.229	100.073	77.357	93.554	84.223	99.77
T8: Top Motor Housing Middle		68.47	81.84	69.48	83.49	71.26	85.3	71.502	86.817	72.03	85.9	74.004	88.594
T9: RHS Motor Housing Middle		68.47	82.74	69.82	83.87	71.02	86.03	71.139	86.069	70.94	85.126	73.286	87.643
T10: Encoder Housing		65.51	78.01	65.94	80.08	68.32	81.35	69.371	83.995	69.888	83.272	72.361	85.768
T11: Bottom Motor Housing Middle		68.22	82.43	69.03	84.2	72.12	85.69	72.455	88.392	72.097	86.445	73.534	88.407
T12: L Plate Top		28.68	30.84	29.48	31.96	31.36	33.07	26.476	28.765	26.468	28.374	27.263	28.727
T13: Mounting Plate (near to front end frame)		51.02	59.75	52.33	60.58	53.79	62.06	54.54	64.54	53.739	62.65	54.457	63.558
T14: Top of Motor (front end of housing)		59.34	70.43	60.52	72.3	62.27	73.2	62.486	74	62.531	74.103	63.71	74.233
T15: Top of Motor (rear end of housing)		66.85	80.53	68.3	81.75	69.96	83.6	70.891	85.92	70.893	85.273	73.534	88.234
Temperature of Winding (Maximum)		100.84	126.05	100.98	126.27	101.57	125.85	100.31	126.229	99.592	124.757	100.963	126.65
Temperature of Winding (Delta T)		79.8	105.5	80.16	105.27	80.47	105.34	81.194	106.192	79.933	105.243	80.7	106.655

Fig. 6.28. Selected test point of delta winding temperature of 80.47°C for thermal modelling.

The SPEED software can be used to predict the servomotor performance at the given ambient temperature as shown in Fig. 6.29 and Fig. 6.30.

```

4 Winding Data:-----
Connex          Wye          NPhases          3
WdgType         Custom
Offset          8          CPP          0.4000
Tph            248.0000          PPATHS          2          SPP          0.4000
Layers          2.0000          CSidesPh          8          Z          2976.0000
MLT            189.0404 mm          LgthOEnd          83.0664 mm          Ext          0.0000 mm
EndFill         0.5000          LaxPack          81.8971 mm          Liner          0.4000 mm
WireSpec        BareDia          Wire          0.7500
NSH            1          WireDia          0.7500 mm          InsThick          0.0332 mm
Sfg            0.5254          SFn          0.8889          MaxSFn          0.8889
Aslot          208.5259 mm²          ASlotLL          185.9683 mm²          ACond          0.4418 mm²
GPAslot        209.9582 mm²          TopStick          false
TwjWid         3.0000 mm          TwjLeg          3.5000 mm          TwjThk          0.0000 mm
PhsWid         3.0000 mm          PhsLeg          3.5000 mm          PhsThk          0.0000 mm
ATwj           0.0000 mm²          APhs          0.0000 mm²
XET            1.4000          ETCalc          BDC 6.5          Rext          0.0000 ohm
Nse            291.2574          X_R          1.0000          Ax1          57.0000 °m
T_wdg          101.5000 °C          Rph0          1.2077 ohm          R_LL          2.4155 ohm
T_c            101.5000 °C          Rph          1.2077 ohm/ph          TFRho          1.3203
Rph20          0.9147 ohm          RLL20          1.8295 ohm

```

Fig. 6.29. SPEED: Extract of winding section from DESIGN SHEET.

```

6 Sine-wave static design [phasor diagram]:-----
OpMode          Motoring          Vs          620.0000 V          RPM          1000.0000 rpm
Tshaft          10.8717 Nm          Pshaft          1138.4781 W          Eff          89.0050 %
WCu            126.2950 W          WFe          12.6641 W          WWF          1.6800 W
WMagnet         0.0000 W          TempRise          80.4000 °C          MechLoss          14.3441 W
WTot          140.6390 W          IWav          5.3154 A          Jrms          6.6820 A/mm²
IWpk           8.3495 A          ILav          5.3154 A          IWrms          5.9040 A
ILpk           8.3495 A          WFeCalc          OC          ILrms          5.9040 A
IDC_P          2.0631 A          Vph1          78.1068 V          Pelec          1279.1172 W
Eq1            66.4832 V          Id1          0.0000 A          VLL1          135.2849 V
Iq1            5.9040 A          Vd1          -26.1092 V          gamma          0.0000 °
Vq1            73.6137 V          phi          19.5285 °          delta          19.5285 °
Vtph           78.1068 V          phiIs          19.5285 °          PF          0.9425
VtLL           135.2849 V          jXdId1          0.0000 V          SPF          0.9425
RI1            7.1305 V          Psiad1          0.0000 mVs          jXqIq1          26.1092 V
Psi_1          136.4141 mVs          Phida1          0.0000 mWb          Psiaq1          49.8650 mVs
Bqad           0.0000 T          hBq          0.0000 mm²          Phiqa1          0.0810 mWb
BqAvg          0.0000 T          Bma          0.0000 T          BglLoad          1.0681 T
BmLoad         0.9315 T          TEI_PS          11.2448 Nm          Fda1          0.0000 At/gap
Tgap_PS        11.2448 Nm          Tei          11.0086 Nm          Trel_PS          0.0000 Nm
Tgap           11.0086 Nm          Trel          7.9712E-18 Nm
Tloop          11.0084 Nm

```

Fig. 6.30. SPEED: Extract of static design output from DESIGN SHEET

The measured phase-phase resistance at ambient temperature is 1.814 ohm which compares well with the PC-BDC prediction of 1.829 Ohm (<1% error).

Without knowledge of the temperature at which the resistance was measured, no further adjustment was considered beneficial.

The Slot-fill appears acceptable at a value of $SF_g = 0.5254 = 52.54\%$ with a 0.75 mm wire diameter, which is close to the slot-fill value of the winding machine of 53% (<1% error).

All the other important winding information such as connection type, winding offset and the number of phases is given in Fig. 6.29.

The predicted servomotor torque performance using the SPEED software is given in Fig. 6.30. This predicts 10.8717 Nm, the measured value being 9.43 Nm as indicated in Fig. 6.28.

This difference could be due to the calibration of the magnetic circuit in the PC-BDC at the constant current kept for all temperatures. Since there is more interest in the losses than the torque performance in this thermal programme, there is no need to involve the magnetic circuit.

The torque performance is already predicted using the FEA tool and the thermal matrix. The iron loss $P_{fe} = 12.7 \text{ Watts}$ is well close when compared with the iron loss obtained in Chapter 3 from test results and the empirical loss equation.

The predicted performance given in Fig. 6.30 for the losses are 126.3 W of copper loss, 12.7 W of iron loss and 1.68 W of friction loss. The SPEED software gives the iron loss and the copper loss.

However the detailed information about the temperature distribution within the BPM synchronous servomotor is unknown at this stage.

The Motor-CAD software, whose interface is shown in Fig. 6.31, is needed to provide this information by estimating the thermal distribution within the servomotor as shown in Fig. 6.32.

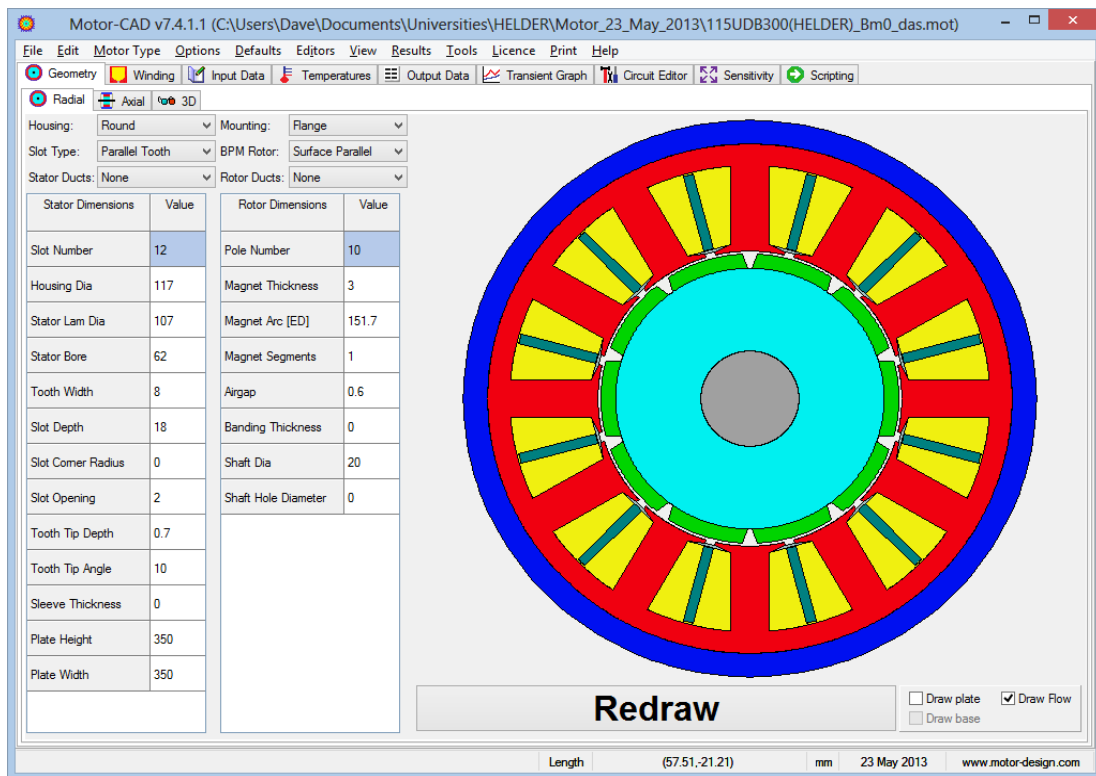


Fig. 6.31. Motor-CAD: Geometry | Cross-section with data imported from SPEED PC-BDC.

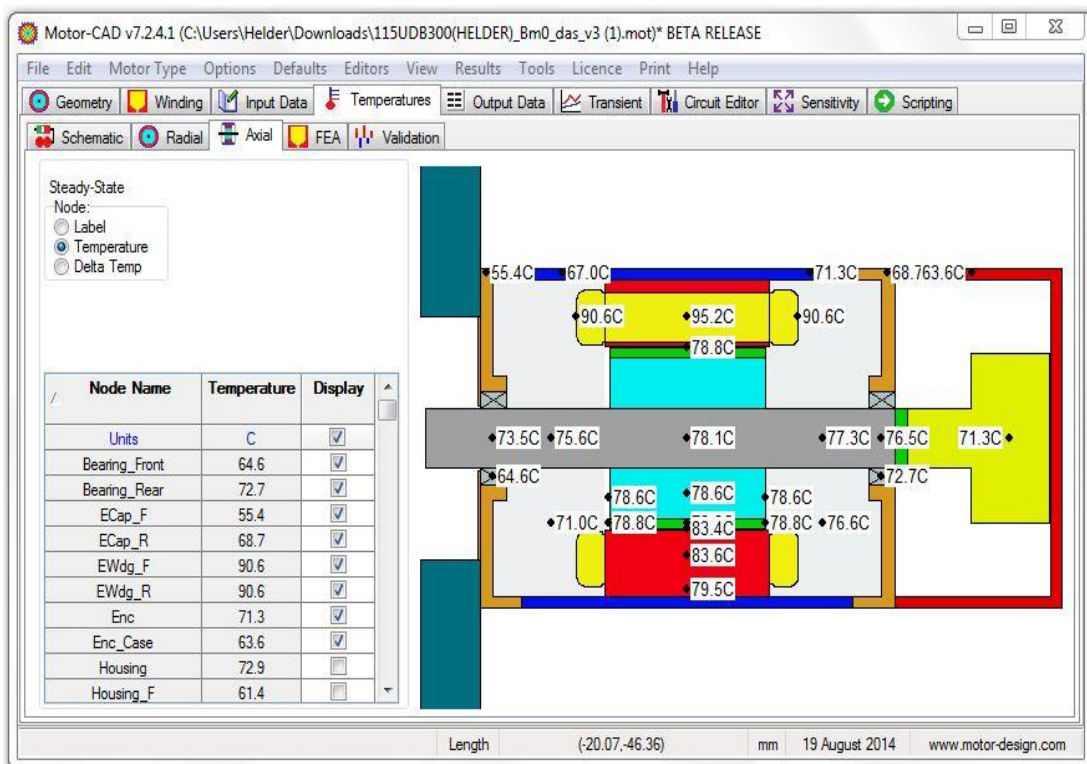


Fig. 6.32. Motor-CAD: Geometry Axial Output Data | Temperature.

The motor configuration information used for SPEED shown in Fig. 6.21 is imported to Motor-CAD as shown in Fig. 6.31. The Motor-CAD software accommodates all the thermal modelling details needed for the current servomotor configuration and its

related testing components such as the flange plate shown in Fig. 6.27 as a heat sink plate.

It is possible and it is also convenient to change the slot-liner (paper wall insulation material) thickness imported from SPEED. In the SPEED input data of Fig. 6.29 the slot liner thickness is equal to 0.4 mm but the correct value is 0.25 mm as shown in TABLE. 6.1 for all the wall insulation samples used in this investigation. Accordingly, the slot liner thickness is corrected in the winding editor of Fig. 6.33 to set *Liner Thickness* = 0.25 mm.

The properties such as conductivity are changeable in the Input Data – Material and therefore sensitivity analysis with respect to the paper wall insulation material properties can be performed. Also all the other input and output parameters such as goodness or slot-fill are set in the winding editor, as shown in Fig. 6.33.

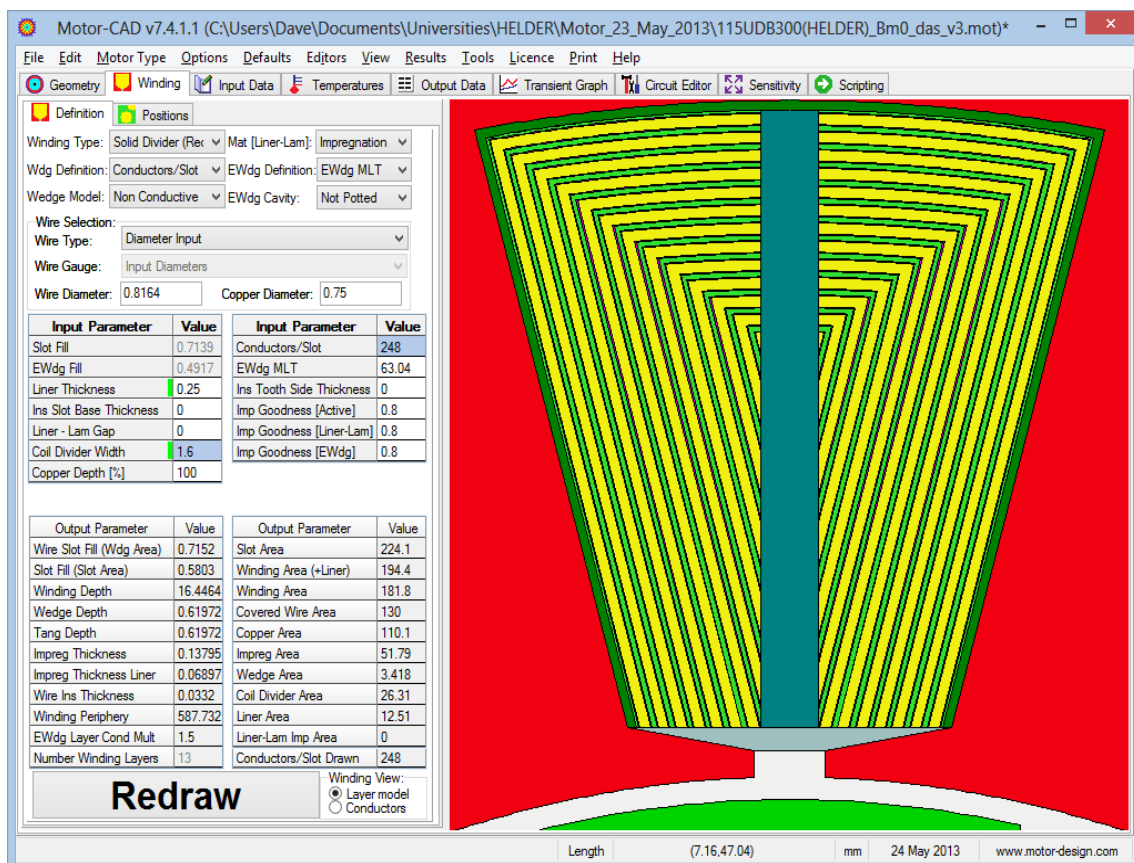


Fig. 6.33. Motor-CAD: Winding Editor - Winding View | Material layer.

The layers of different colours in the slots represent different materials as defined in TABLE 6.4.

TABLE 6.4.

Colour of layers in Fig. 6.33 representing different brushless servomotor materials in the slot.

Dark green	Slot liner or paper wall insulation
Yellow	Conductor
Purple	Enamel
Light green	Varnish/impregnation

The number of layers can be specified to calculate a set of thermal resistances from slot-centre to slot wall, by simply using a replica of the conduction heat transfer formula $R = L/(kA)$ for thermal resistance [$^{\circ}\text{C}/\text{W}$]. Where L , k and A are, respectively, the layer thickness, the material thermal conductivity and the area through which the heat passes.

The Motor-CAD software also allows the conductor distributions within the slot to be changed and therefore many different machines can be simulated. This is shown in Fig. 6.34 but the default winding distribution is maintained in this investigation.

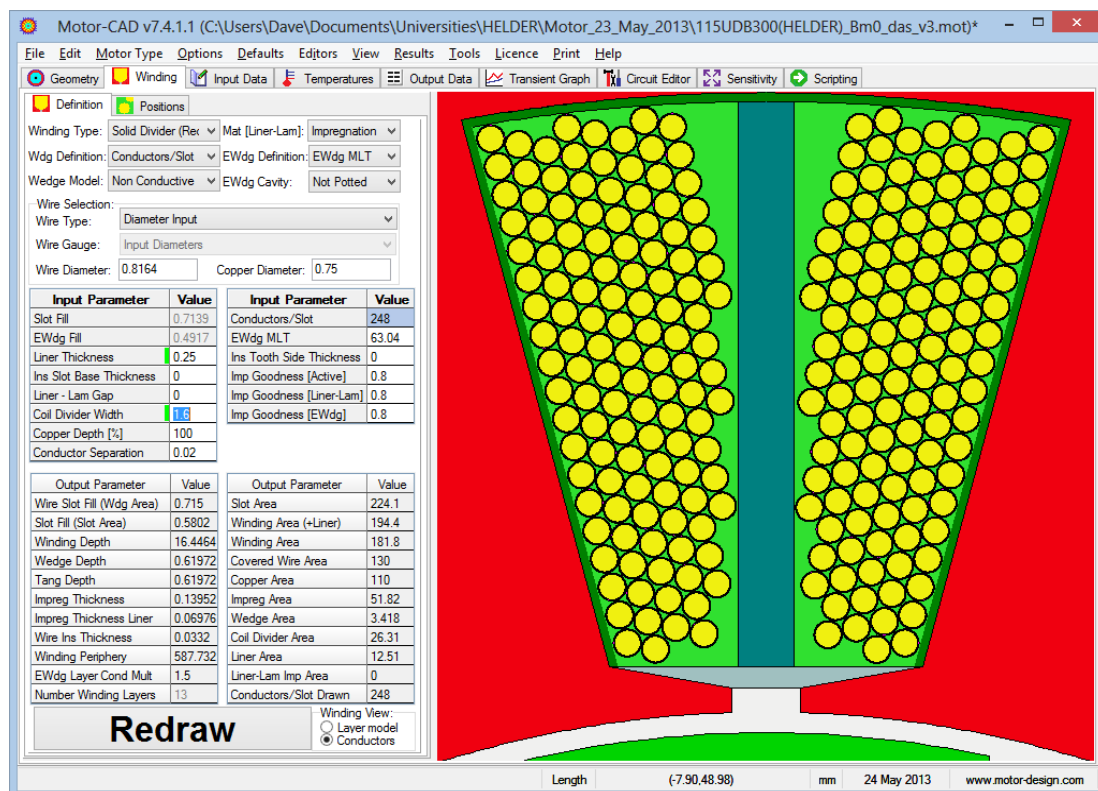


Fig. 6.34. Motor-CAD: Winding Editor - Winding View | Conductors.

The prototype servomotor is connected to a relatively large flange mounting plate (350mm x 350mm x 23mm), and this is defined in the Motor-CAD as shown in Fig. 6.35. The equations in Chapter 3 show that this can significantly influence the

cooling of the servomotor when the natural cooling method is used. The size of the plate is inversely proportional to its thermal resistance and therefore increasing the plate size simulates reduction of the thermal resistance between the motor and its surroundings.

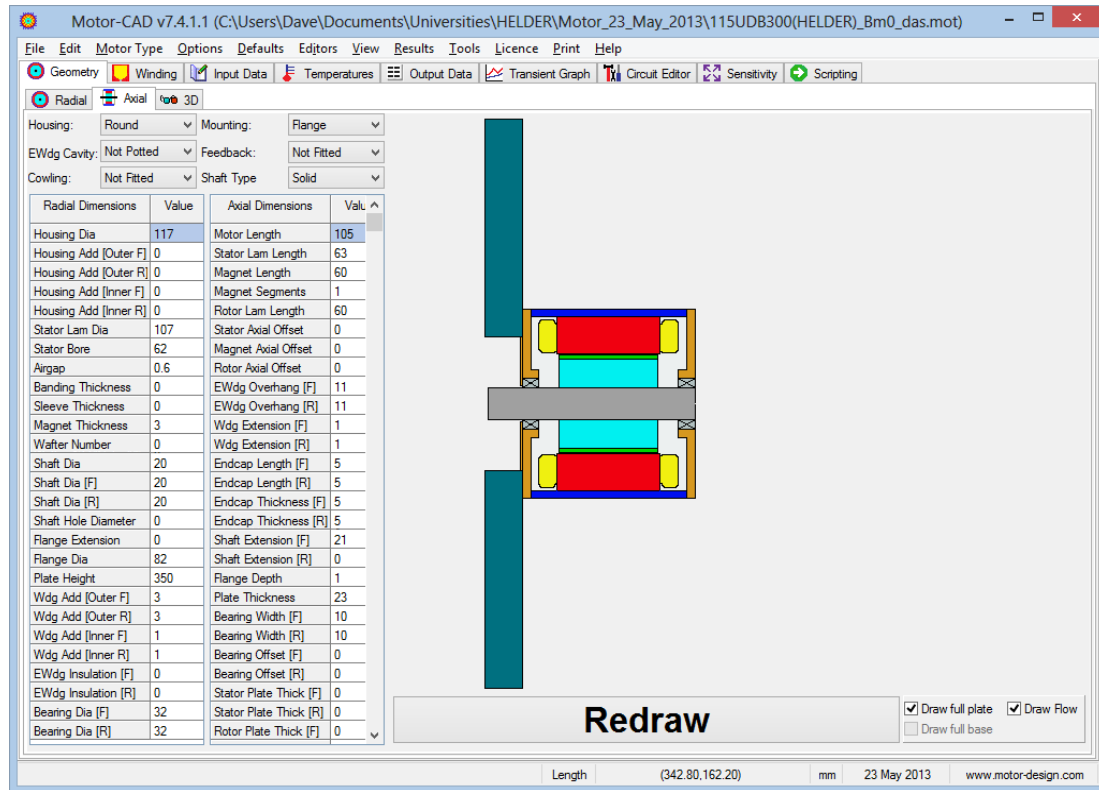


Fig. 6.35. Motor-CAD: Geometry | Axial View for mounting plate and no encoder model.

In order to obtain the correct surface area for cooling in Motor-CAD, it is important to adjust the housing, endcap and encoder housing/cover dimensions. These can be obtained from the prototype shown in Fig. 6.26. The housing material is defined as Aluminium Alloy and the required dimensions to obtain the correct surface area for cooling are as follows:

- Outer Housing = 115 mm
- Inner Housing = 107 mm
- Housing Length = 127 mm
- End Caps = 16 mm
- Encoder Housing = 64 mm
- Total servomotor length = $127 + 16 + 16 + 64 = 223$ mm

Total servomotor length (no Encoder) = $127 + 16 + 16 = 159$ mm as shown in Fig. 6.35.

The losses previously calculated in SPEED can be imported to Motor-CAD as shown in Fig. 6.36 for the steady state temperature calculation. Then the temperatures of different parts of the servomotor predicted by Motor-CAD are later compared with the corresponding experimentally obtained temperatures and the corresponding temperatures predicted by the analytical model using the matrix solver of Chapter 3.

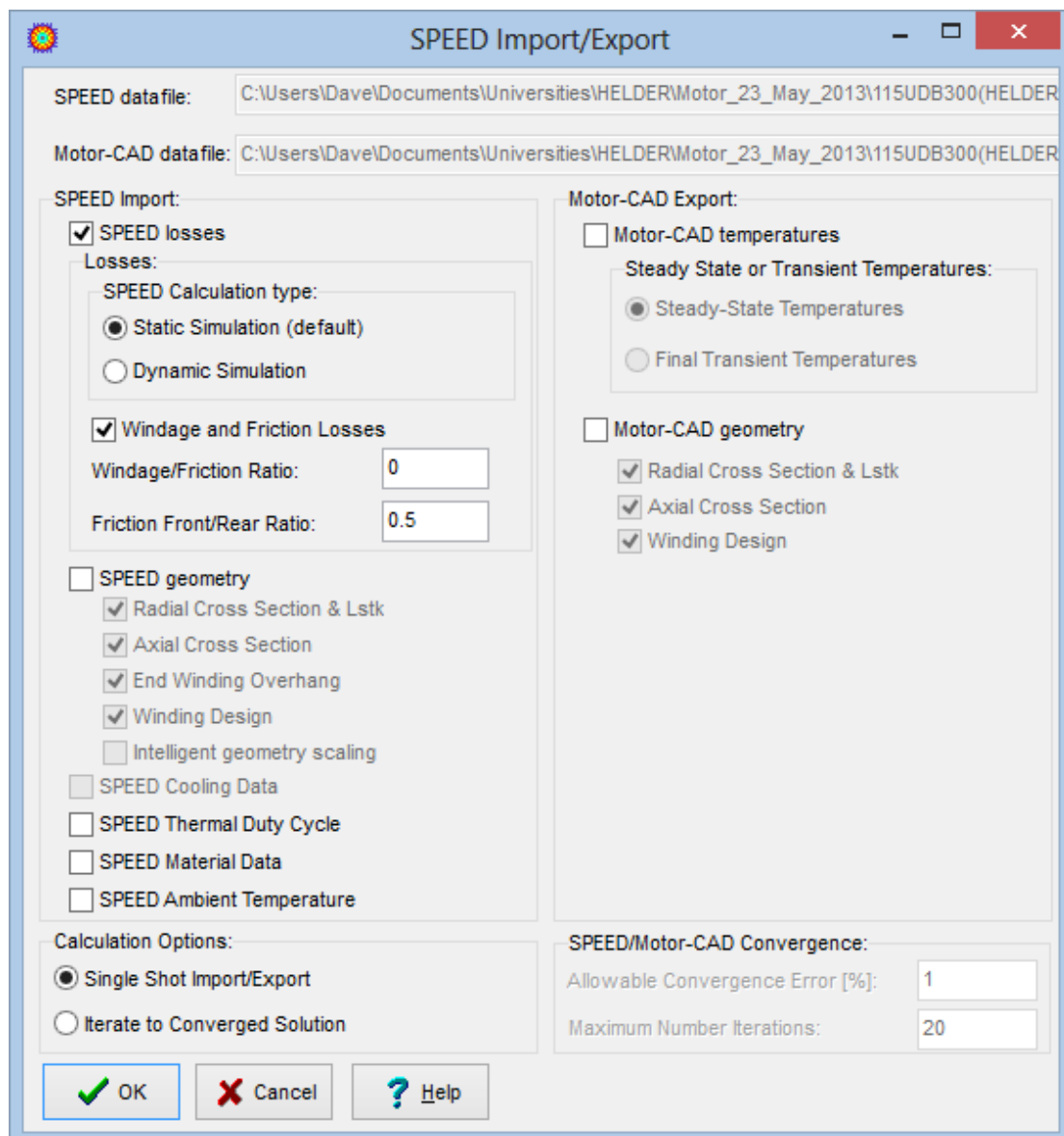


Fig. 6.36. Motor-CAD: Import/Export | Losses in SPEED & temperatures in Motor-CAD.

Since the current and the winding resistances are known, the losses are set to vary with the temperature and the load.

This is shown in Fig. 6.37 for the Motor-CAD loss model where the current is set to be constant for the selected operating point.

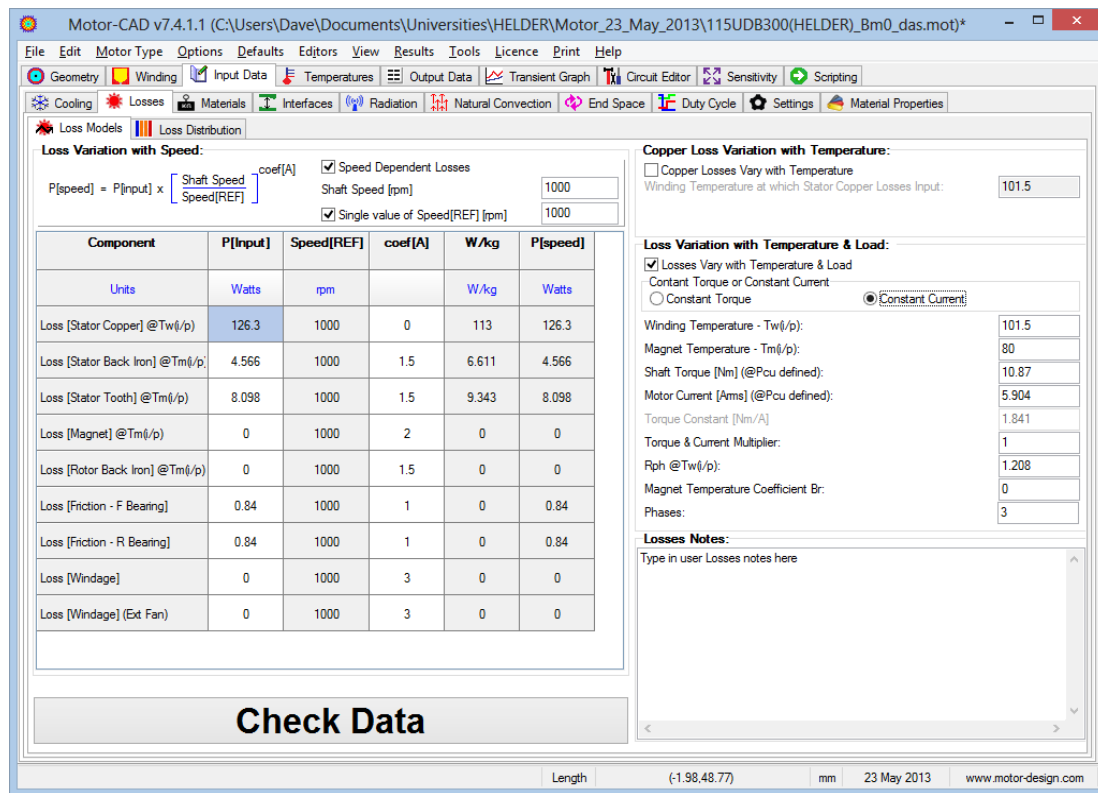


Fig. 6.37. Motor-CAD: Input Data | Losses.

Loss due to windage is set to zero because this is already included in the rotational losses obtained experimentally.

These losses are divided by two before being input as Motor-CAD frictional loss components due to the software interpreting this applying to the front and the rear bearings.

Based on the servomotor dimensions, the Motor-CAD calculates iron loss in the back iron to be equal to 4.566 W and the iron loss due the stator tooth is calculated by the software to be equal to 8.098 W.

The back iron loss is approximately 36% of the total loss and the stator tooth loss is about 64% of the total loss, as calculated using the PC-BDC SPEED software.

The ambient temperature is set to 21.1⁰C as measured in the test environment, and the **Cooling Option** is set to natural convection and the **Motor Orientation** to horizontal as shown in Fig. 6.38.

The lamination stack factor is defined to be 0.97 for both the stator and the rotor core. External and internal fluid (air) characteristics are defined as shown in Fig 6.38.

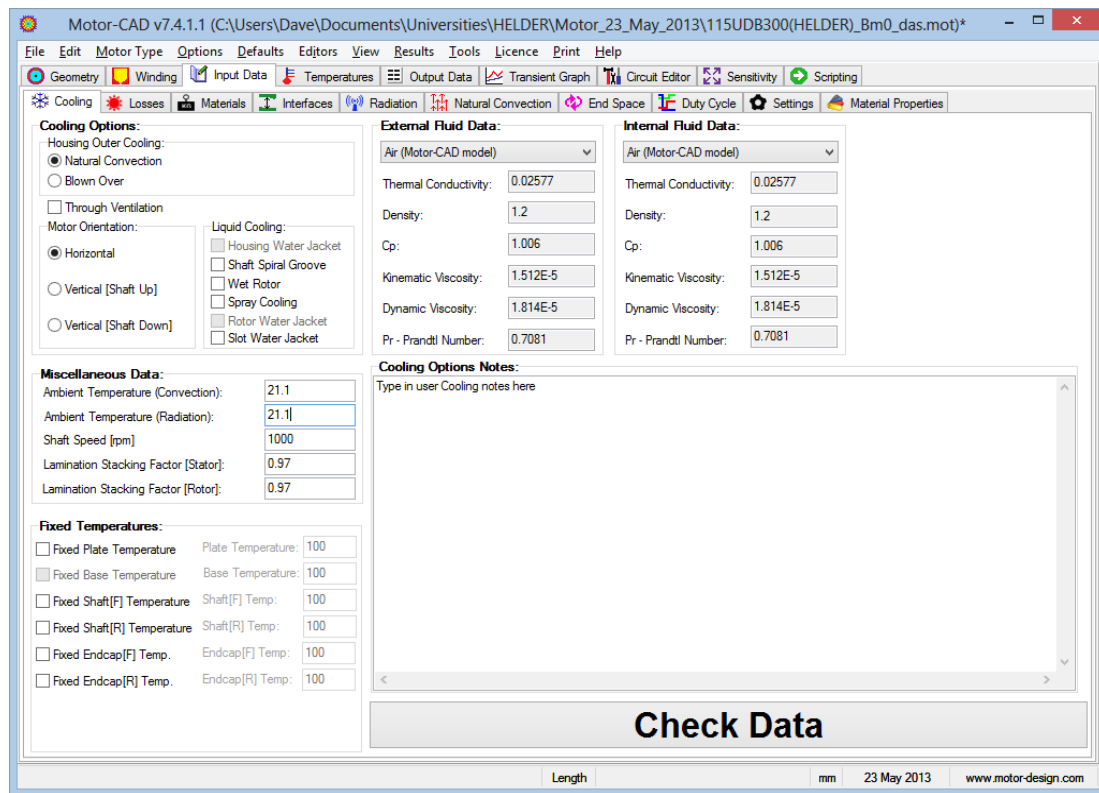


Fig. 6.38. Motor-CAD: Input Data | Cooling Options.

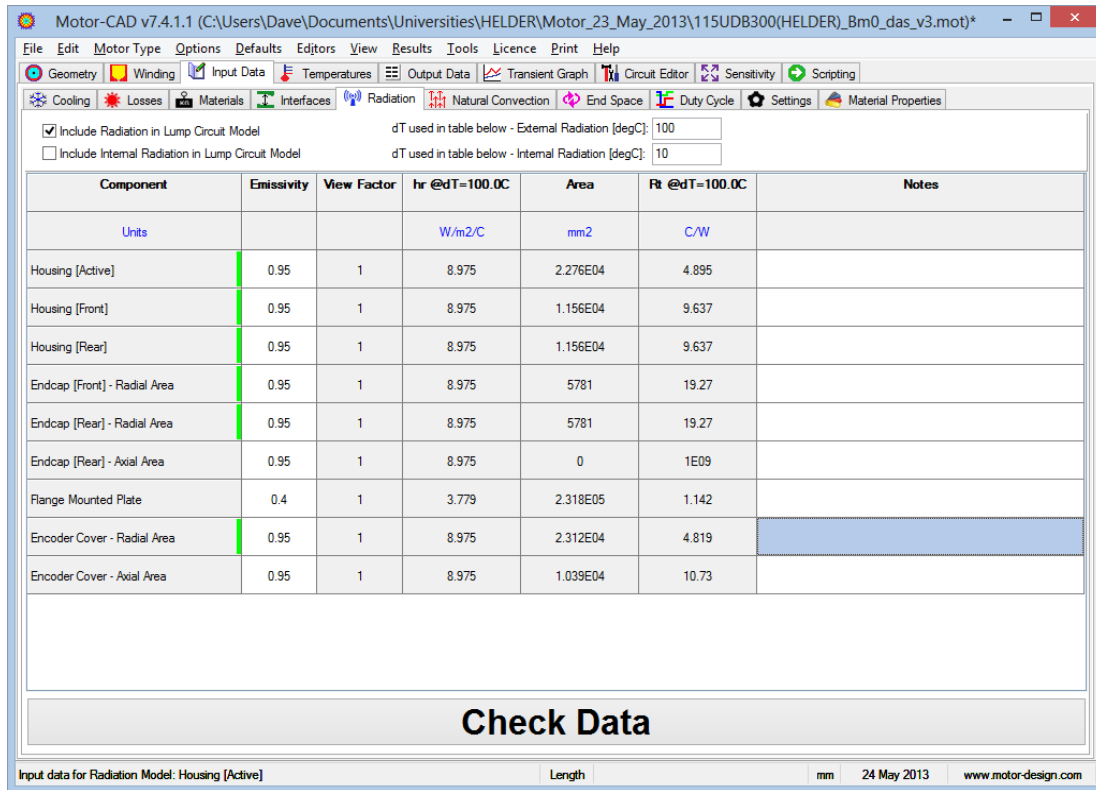
When natural cooling is applied, as required for this investigation, the radiation heat transfer mode accounts for a significant proportion of the heat dissipation from the servomotor and heat sink plate.

The emissivity varies significantly with the type and colour of paint covering, the maximum value being 1 for a black body.

The Input Data tab and Radiation allow the emissivity value for each motor system component to be defined as shown in Fig. 6.39.

Note that in order to simplify the problem, the emissivity's of all the components are first defined as 0.95 and then the emissivity's of the mounting plate and adjusted to predict the temperature distribution. Due to 'no fins' in the servomotor surface and the heat sink plate surface, as shown in Fig. 6.26, the view factor is set to 1 for all the bodies where radiation heat transfer takes place.

Based on the input data, the Motor-CAD software performs all the required calculations to predict the temperature distribution including the radiation heat transfer calculations using the radiation thermal resistances for the different components at a delta temperature of 100 °C, as shown in Fig. 6.39.



Component	Emissivity	View Factor	hr @dT=100.0C	Area	Rt @dT=100.0C	Notes
Units			W/m ² /C	mm ²	C/W	
Housing [Active]	0.95	1	8.975	2.276E04	4.895	
Housing [Front]	0.95	1	8.975	1.156E04	9.637	
Housing [Rear]	0.95	1	8.975	1.156E04	9.637	
Endcap [Front] - Radial Area	0.95	1	8.975	5781	19.27	
Endcap [Rear] - Radial Area	0.95	1	8.975	5781	19.27	
Endcap [Rear] - Axial Area	0.95	1	8.975	0	1E09	
Flange Mounted Plate	0.4	1	3.779	2.318E05	1.142	
Encoder Cover - Radial Area	0.95	1	8.975	2.312E04	4.819	
Encoder Cover - Axial Area	0.95	1	8.975	1.039E04	10.73	

Check Data

Input data for Radiation Model: Housing [Active] Length mm 24 May 2013 www.motor-design.com

Fig. 6.39. Motor-CAD: Input Data | Radiation.

Motor-CAD also contains the material information data base for all the servomotor system components and this is shown in Fig. 6.40.

In this work the Motor-CAD default materials are used for the servomotor components for the initial temperature calculations.

Examples of material components are copper conductors, aluminium housing, and so on.

Standard values are selected for the material component thermal conductivities and the specific heat values. Many options are, however, available for the component materials under the Material Database options of Fig. 6.40.

Component	Thermal Conductivity	Specific Heat	Density	Weight Internal	Weight Multiplier	Weight Addition	Weight Total	Material from Database	Notes
Units	W/m/C	kJ/kg/C	kg/m3	kg		kg	kg		
Housing [Active]	167.4	0.8708	2707	0.2379	1	0	0.2379	Aluminum Alloy 6061-T6	
Housing [Front]	167.4	0.8708	2707	0.1208	1	0	0.1208	Aluminum Alloy 6061-T6	
Housing [Rear]	167.4	0.8708	2707	0.1208	1	0	0.1208	Aluminum Alloy 6061-T6	
Housing [Total]				0.4795			0.4795		
Endcap [Front]	167.4	0.8708	2707	0.1791	1	0	0.1791	Aluminum Alloy 6061-T6	
Endcap [Rear]	167.4	0.8708	2707	0.1791	1	0	0.1791	Aluminum Alloy 6061-T6	
Stator Lam (Back Iron)	28	0.46	7800	0.6907	1	0	0.6907		
Inter Lam (Back Iron)	0.02723	1.007	1.127	3.087E-06	1	0	3.087E-06		
Stator Lam (Tooth)	28	0.46	7800	0.8668	1	0	0.8668		
Inter Lam (Tooth)	0.02723	1.007	1.127	3.873E-06	1	0	3.873E-06		
Stator Lamination				1.557			1.557		
Copper [Active]	386	0.4	8954	0.7454	1	0	0.7454		
Copper [Front End-Wdg]	386	0.4	8954	0.1865	1	0	0.1865		
Copper [Rear End-Wdg]	386	0.4	8954	0.1865	1	0	0.1865		
Copper [Total]				1.118			1.118		
End Winding Ins. [Front]	0.2	1.7	1400	0	1	0	0		
End Winding Ins. [Rear]	0.2	1.7	1400	0	1	0	0		
Wire Ins. [Active]	0.21	1	1400	0.01786	1	0	0.01786		
Wire Ins. [Front End-Wdg]	0.21	1	1400	0.00455	1	0	0.00455		
Wire Ins. [Rear End-Wdg]	0.21	1	1400	0.00455	1	0	0.00455		
Wire Ins. [Total]				0.02696			0.02696		
Impreg. [Active]	0.2	1.7	1400	0.04386	1	0	0.04386		
Impreg. [Front End-Wdg.]	0.2	1.7	1400	0.02789	1	0	0.02789		
Impreg. [Rear End-Wdg.]	0.2	1.7	1400	0.02789	1	0	0.02789		
Impreg. [Total]				0.09963			0.09963		
Coil Divider	0.2	1.2	1000	0.01989	1	0	0.01989		
Slot Wedge	0.2	1.2	1000	0.002584	1	0	0.002584		

Fig. 6.40. Motor-CAD: Input Data | Materials & Weights.

After updating the materials, Motor-CAD can set up a table to compare the computed temperatures with the validation temperatures (i.e., the temperatures of the test point of Fig. 6.26 and Fig. 6.27).

In the **Temperatures | Validation** section, temperature values can be compared on the Setup as shown in Fig. 6.41. By ticking the components to be presented in the graph, the validation temperatures are input to the Motor-CAD in the column and the percentage difference between the predicted temperatures and the test validation temperatures can be displayed as shown in Fig. 6.41.

The comparison results are shown in Fig. 6.42 with the default material settings of Motor-CAD. Fig. 6.42 indicates over prediction of all the temperatures by similar orders of magnitude.

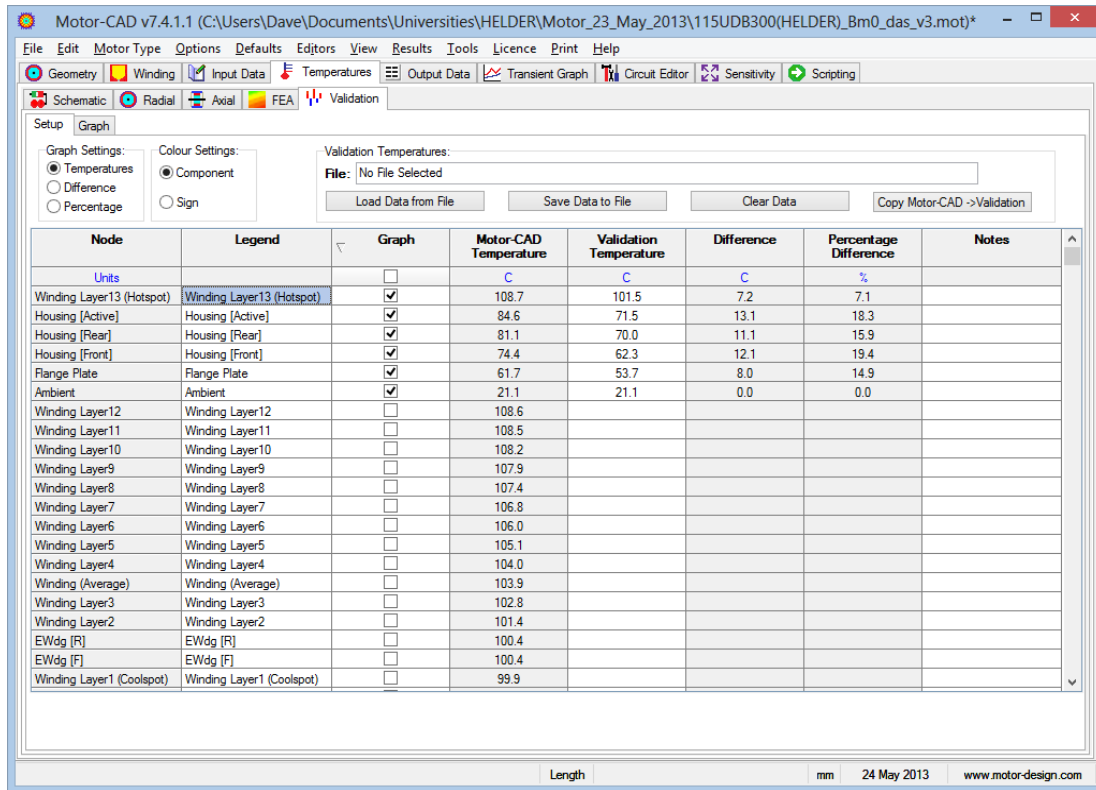


Fig. 6.41. Setup for temperature selection for validation.

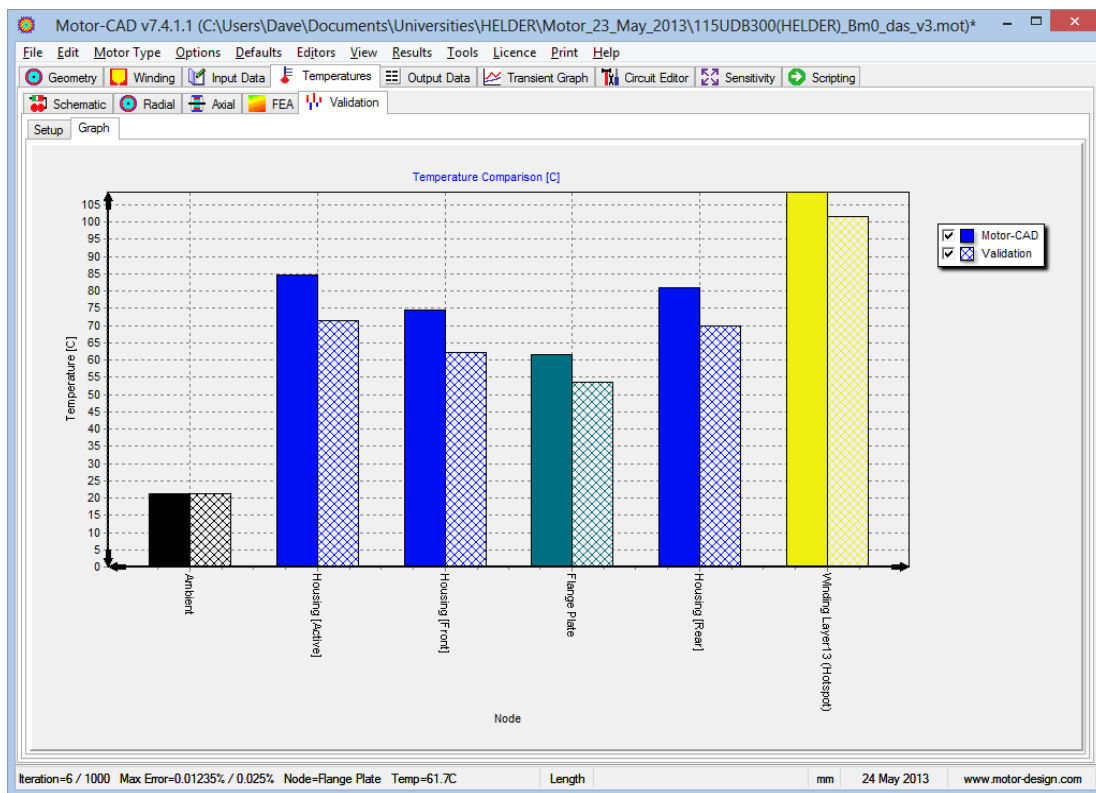


Fig. 6.42. Motor-CAD: Validation | Showing predictions vs test steady-state temperatures.

The other components causing over prediction are the housing-stator lamination interface fit or incorrect material data for the slot liner, impregnation material or impregnation quality.

Published thermal conductivity data for unsaturated polyester resin is 0.17 – 0.22 W/m⁰C. So far, Motor-CAD has been using 0.2 W/m⁰C. This value has been changed to 0.17 W/m⁰C and also the conductivity of the wall insulation material has been updated to more than 0.14 W/m⁰C for Material B to allow for the impregnation.

The problem is to obtain good thermal conductivity data for the slot liner and impregnation material. Also the process used for impregnation (dip, trickle, vacuum) determines the impregnation goodness factor (0.8 used in winding editor at present). In this case, the trickle impregnation process is used and 0.8 goodness factor appears to be a good value.

After calibration or adjustment of all these parameters in the Motor-CAD **Materials** and **Geometry**, the predicted temperatures for validation are as shown in Fig. 6.43. Now quite a good match is obtained.

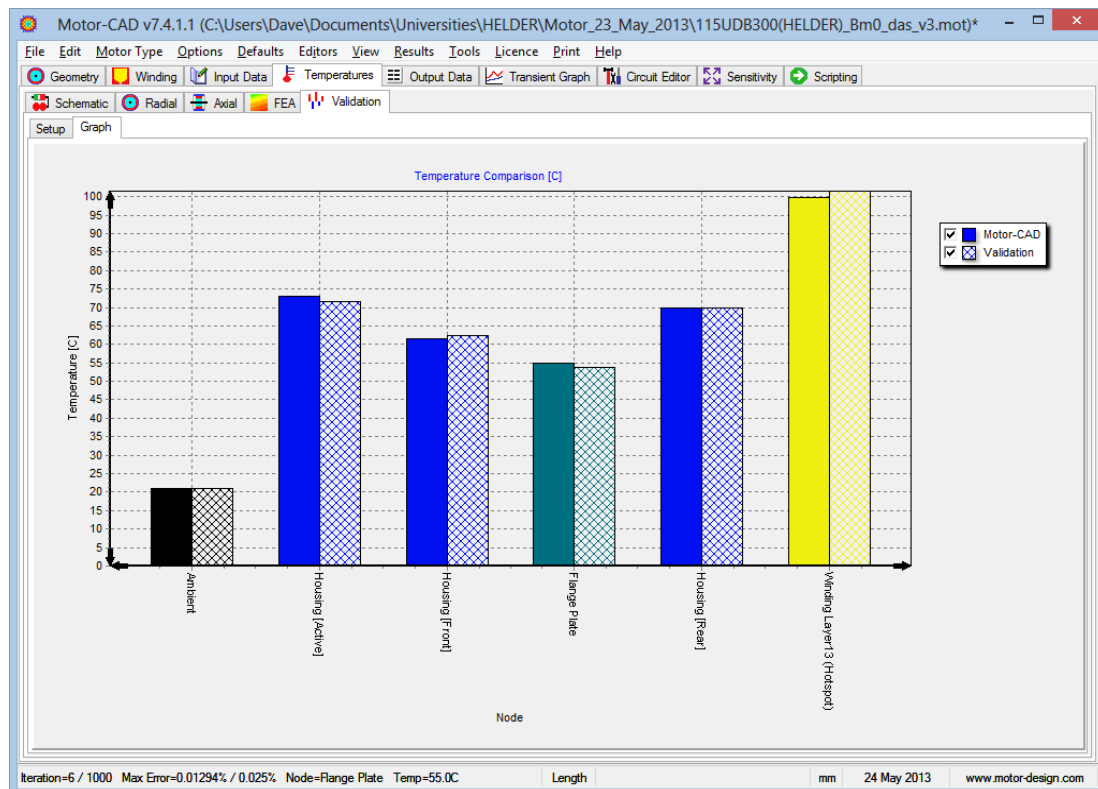


Fig. 6.43. Motor-CAD: Validation | Showing good predictions versus test steady-state temperatures

The thermal calculations using Motor-CAD can be performed in the **Temperatures | Schematic** tab shown in Fig. 6.44. This shows the thermal network and the steady-state temperatures for the servomotor components.

Fig. 6.44 shows the complete temperature and power distribution within the servomotor components. In the **Temperatures | Schematic** tab a clear view is given of the thermal resistances between the nodes, which are connected to the power sources that represent the losses in the servomotor components.

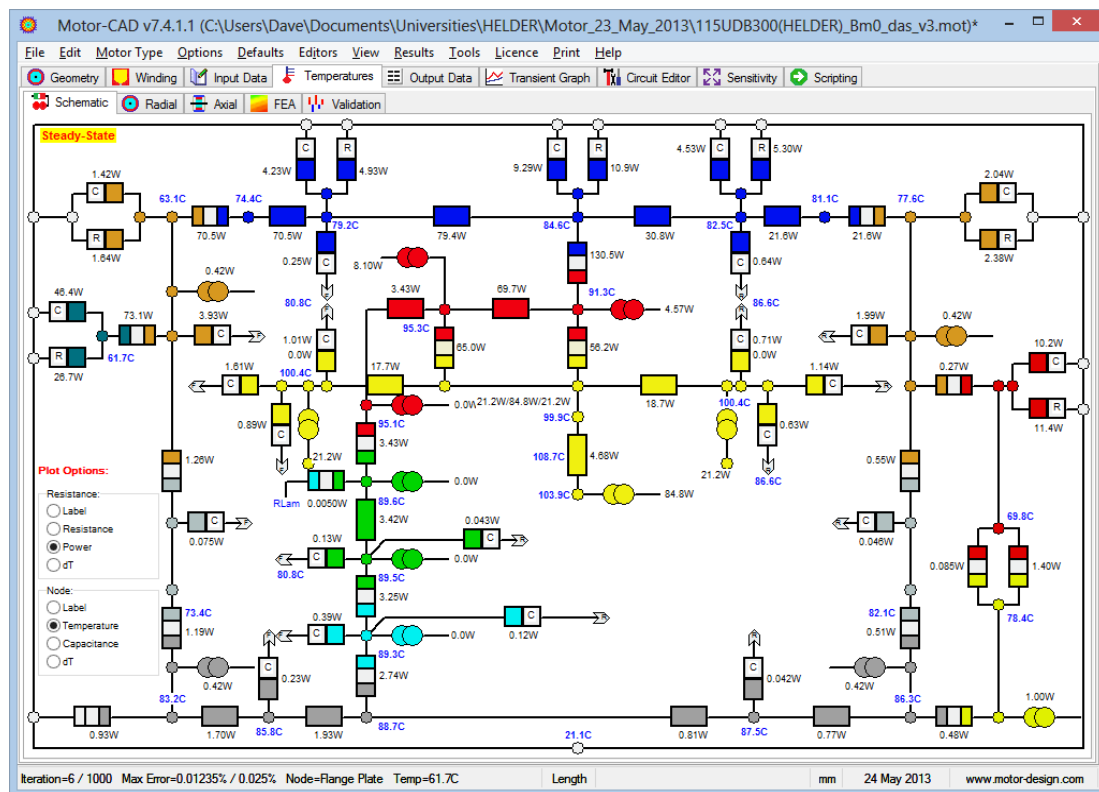


Fig. 6.44. Motor-CAD: Schematic | Showing the thermal network and the steady-state temperatures

The colours of the components are mainly the same as the colours used in Fig. 6.32 or Fig. 6.35 for the cross-section editor.

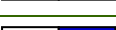
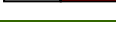
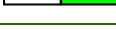
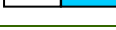
The radial and axial heat transfer paths are, respectively, represented by vertical and horizontal thermal resistances shown in the Fig. 6.44.

TABLE 6.5 defines the physical components represented by the thermal resistor colours in Fig. 6.44.

Most of the power generated in the servomotor is dissipated via the housing surface.

TABLE 6.5.

Colour coding for thermal resistors of MOTOR-CAD software

Colour	Description of Physical Component
	Housing
	Stator Lamination
	Winding
	Magnets
	Rotor Lamination or Back Iron
	Shaft
	Endcap
	Mounting Plate
	Convection/Radiation from Endcaps
	Convection/Radiation from Mounting Plate
	Convection/Radiation from Shaft
	Convection/Radiation from End Winding
	Convection/Radiation from Housing
	Convection/Radiation from Stator Lam
	Convection/Radiation from Magnets
	Convection/Radiation from Rotor Lam
	Interface Gap Housing – Endcap
	Interface Gap Endcap – Mounting Plate
	Interface Gap Liner – Lamination
	Interface Gap Magnet – Rotor

Furthermore, the steady-state temperature comparison is performed at 1000 r/min for the analytical model, Motor-CAD.

The main component thermal test results are presented in TABLE 6.6 for comparison.

The temperature distribution between the main components of the servomotor system rig (winding, housing and flange plate) shown in TABLE 6.6 indicates that the

mounting arrangement has a great influence on the cooling process of the servomotor, not only the flange plate but also where it is supported.

TABLE 6.6.
Results for naturally cooled servomotor.

SERVOMOTOR COMPONENT	Temperatures °C at 1000 r/min		
	Analytical	MOTOR-CAD	Test
Winding	101	98.8	101.08
Housing	73.9	73.2	72.47
Flange Plate	68.56	55	54

Assuming a good contact between the front endplate and the servomotor housing. Therefore contact resistance is between thermocouple 13 on the flange plate (heat sink plate) and thermocouple 2 located on the endplate in Fig. 6.27.

Then total power dissipated in the flange plate via convection and radiation defines the critical thermal contact resistance that can help enhance the effect of the wall insulation when implementing the natural cooling method.

The analytical, Motor-CAD and experimental temperatures are compared at 1000 rpm in TABLE 6.6 and the results agree to a moderate accuracy.

The flange plate temperature was over predicted because the thermocouple 12 temperature change in Fig. 6.27 was not considered, assuming that the spacer insulates the heat from the flange to the support as shown in Fig. 6.18.

This is not true because the support plate increases the power dissipation.

6.6.2. Motor-CAD Sensitivity Analysis

Motor-CAD **Sensitivity | Graph** allows for many *what if* scenarios to be investigated for the thermal analysis of electric machines.

The impregnation quality, the gap within the heat path and thermal conductivity of the paper wall insulation material are investigated in terms of their thermal impact in the servomotor when natural cooling is used. In Fig. 6.45 the winding temperature varies as a function of impregnation quality or goodness for different gaps.

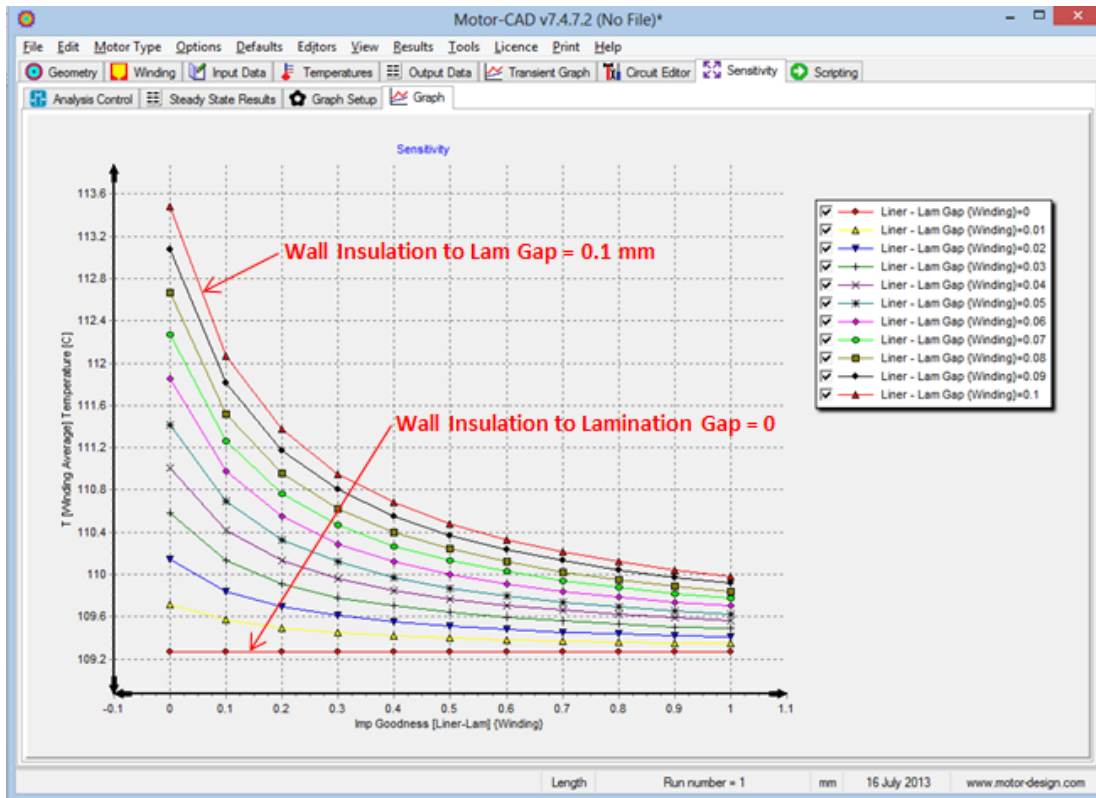


Fig. 6.45. Motor-CAD: Sensitivity analysis of winding temperature vs. air-gap.

In Fig. 6.46 the temperature varies as function of the Gap for different impregnation goodness.

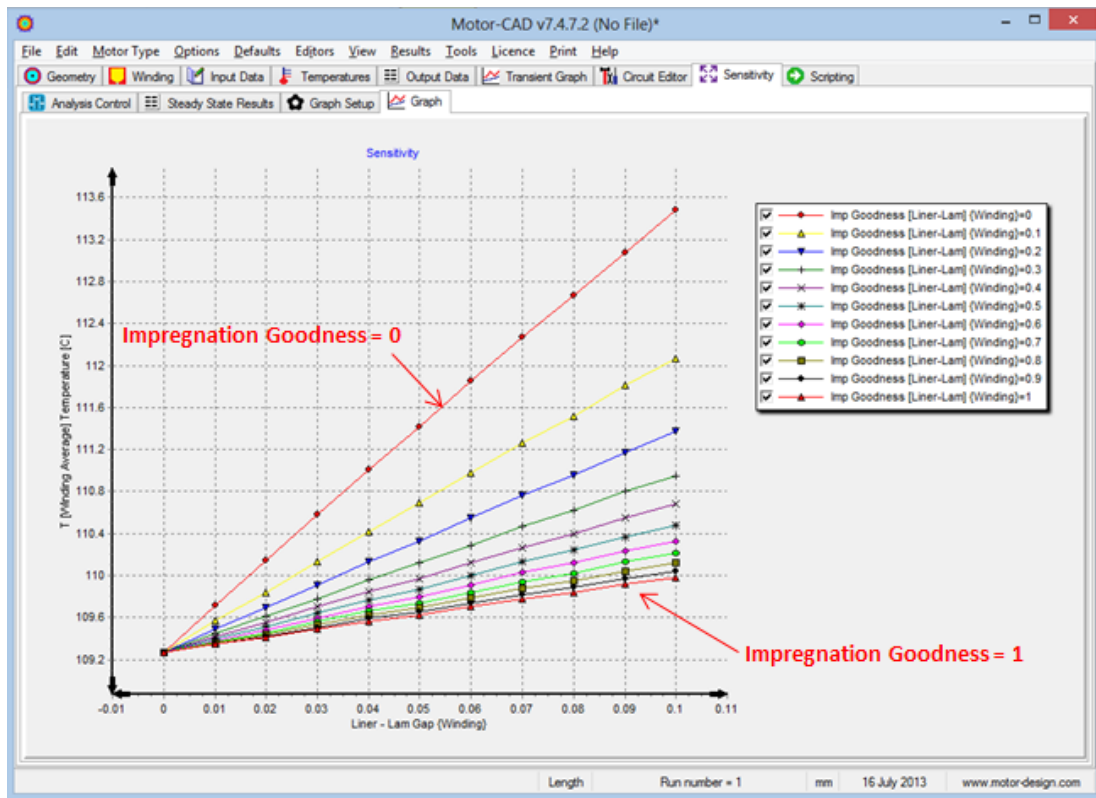


Fig. 6.46. Motor-CAD: Sensitivity analysis of winding hotspot temperature vs. impregnation.

And in Fig. 6.47 the temperature varies as function of paper wall insulation thermal conductivity.

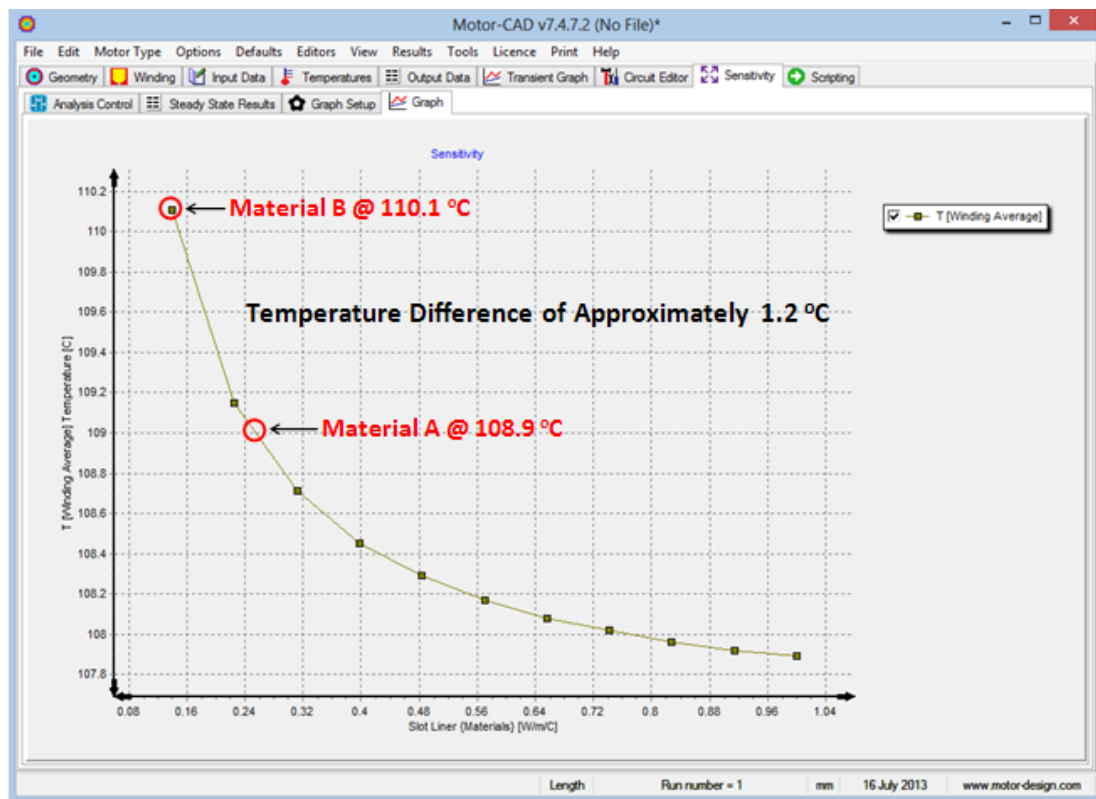


Fig. 6.47. Motor-CAD: Sensitivity analysis of winding temperature vs. thermal conductivity.

Sensitivity analysis of the contact resistance between the wall insulation to the laminations as a function of the goodness factor has been performed using the Motor-CAD. Improving impregnation Goodness clearly reduces the thermal effect of the existing gap between the wall insulation and the stator lamination.

With the ideal impregnation, the Goodness factor equals 1, the temperature difference between $Gap = 0 \text{ mm}$ and $Gap = 0.1 \text{ mm}$ is about 0.8°C .

Fig. 6.46 shows the effect of the impregnation quality, and this is simulated by changing the gap between the wall insulation paper material and the stator core to obtain the hot spot temperature value.

There is a linear relationship of proportionality between the Gap and the temperature. The Goodness factor reduces the Gap thermal effect by approximately 3°C .

The Motor-CAD software is also used to perform sensitivity analysis with respect to changes in the wall insulation components located on the stator (Staton, 2001).

The SPEED and Motor-CAD models were developed based on one test point. The ambient temperature, the RMS current and the rotational losses were set from the experimental test results for the corresponding speed.

As already noted above, an important parameter is the impregnation goodness. This was set to 0.8 because it yields the best match between the simulation results from the Motor-CAD and the prototype test results.

The test results and the simulation results using the Motor-CAD package show improvements on the torque and temperature levels, as shown in Fig. 6.19 and TABLE 6.3. However, the improvement of the wall insulation thermal conductivity will not lead to a very significant increase of the maximum permitted stator current due to the motor being totally enclosed and non-ventilated.

This case is very different to that described by (Dajaku, 2006) using simulation results for a forced cooled motor.

This corresponds to the increased dominance of the thermal resistance between servomotor surface component temperature, T_s , and the surrounding ambient temperature, T_0 .

The combination of the increasing convection and radiation thermal resistances is shown in Fig. 6.44 for the servomotor housing, mounting flange plate and encoder housing.

Fig. 6.47 shows that from Material A to Material B the reduced thermal conductivity causes a 1.2°C temperature increase. Material A has a thermal conductivity of 0.25 W/m/°C. Twice this conductivity would not be sufficient to drop the winding temperature by 1°C based on the Motor-CAD simulation result in Fig. 6.47.

Therefore when selecting the wall insulation material for a naturally cooled motor it is recommended to find a high thermal conductivity material. It is more important, however, to focus on the mechanical characteristics of the materials in view of the stress caused by the winding manufacturing system implemented in the

concentrated winding configuration, which should not damage the paper wall insulation material. When a high slot-fill is achieved as shown in Fig. 6.17 and when the segments are assembled to form the stator, considerable stress is imposed on the wall insulation material. The designer needs to focus more on these issues when designing a fractional-slot concentrated-winding machine. Damaging or weakening of the paper wall insulation electrical characteristics can cause serious problems in terms of safety and lifetime of the servomotor.

6.7. Summary and Concluding Remarks

The thermal influence of the paper wall insulation material in TENV BPM synchronous servomotors has been investigated experimentally.

The method of analysis for the mechanical properties of the selected insulation materials follows the two plate approach of ASTM D5470-06 (ASTM, 2011). Meaningful comparisons have been made by ensuring identical conditions for each material sample, the differences between the thermal conductivities being detected via the temperature differences across the samples.

The two most promising materials have been selected from five commercially available materials for further comparative experiments using four especially constructed prototype BPM synchronous servomotors.

Two servomotors are identical with a conventional distributed winding configuration but fitted with different insulation materials and the other two servomotors are identical with a concentrated winding configuration but fitted with the same two different insulation materials.

The results have been compared for the two selected materials and the two winding configurations. A significant torque performance difference was found between the two servomotor configurations and it has been demonstrated that the impact of the wall insulation paper material is more significant with the concentrated winding configuration.

The experimental work presented in this chapter shows that the segmented motor can achieve a stall torque that is 40 percent higher than that of the conventional motor for the same frame size due to its higher thermal efficiency, mainly due to a significantly lower winding overhang, higher slot-fill and lower thermal resistance. In

this chapter, the thermal influence of wall insulation paper material in TENV BPM synchronous servomotors has been investigated by means of CAD software.

The impact of the insulation material was more pronounced in the segmented motor because of its high slot-fill factor. In view of this superior thermal performance, the concentrated winding configuration was selected for thermal assessment.

The analytical lumped-network thermal model developed in Chapter 3 was implemented for the segmented motor and the results were compared with the results obtained from Motor-CAD and rating test results.

The Motor-CAD software has been used in order to perform the sensitivity analysis for gap variation, impregnation goodness and insulation material thermal conductivity. When the test results, temperature predictions within acceptable limits were obtained for the winding and the housing using both the analytical model and the Motor-CAD software.

CHAPTER 7

CONCLUSIONS AND RECOMMENDATIONS

7.1. Conclusions

7.1.1. Overview

This research programme has provided a critical appraisal of the performance (torque density and thermal cooling) and manufacturability of a new segmented stator, concentrated winding, interior rotor BPM synchronous servomotor design (referred to as the 'new servomotor') against the conventional distributed winding, interior rotor BPM synchronous servomotor design (referred to as the 'conventional servomotor') that, to the knowledge of the author, has not been carried out elsewhere and therefore constitutes a valuable contribution to the field.

The research programme has been supported by a prototype new servomotor and a prototype conventional servomotor, each with the same frame size and stator stack length, manufactured to the author's designs, enabling comparative experiments to be conducted,

It has been established that for a given frame size and stator stack length, the new servomotor has a superior overall performance both electromagnetically and thermally when compared with the conventional servomotor and has distinct advantages regarding manufacturability. If the performances of the new and conventional servomotors were to be compared for the same application, the new servomotor would operate at a much lower temperature (approximately 40%) than the conventional servomotor for the same frame size and stator stack length.

For a fixed maximum torque, the new servomotor would be physically smaller than the conventional servomotor. Regarding manufacturability of the new servomotor, it was found that the existing tooling used for the conventional servomotor could be easily adapted and that the new tooling required by a first-time manufacturer of the new servomotor would be much simpler, indicating a clear economic advantage.

An original contribution of the author is a novel magnet retention notch for the surface mounted rotor magnets that enables the centrifugal forces to be withstood while retaining a uniform and small air gap. The design achieves a smaller air gap by replacing the glass retaining tape, associated glue and a balancing plate, as used in the construction of conventional rotors, all of which reduce the maximum torque for a given stator current.

The FEA based design optimisation of the stator with this new magnet mounting method, which has led to a substantial torque increase and material saving, constitutes a significant degree of novelty in servomotor design methodology [company confidentiality].

7.1.2. Manufacturing Aspects

The significant differences between the new and conventional servomotors regarding manufacturability are as follows:

- The solid core stator of the conventional servomotor with the distributed windings requires complex machinery for the winding operation. In contrast, the segmented stator with the concentrated windings used in the new servomotor requires a very simple bobbin winding machine.
- The current solid core stator of the conventional servomotor requires skewing to reduce the cogging torque to an acceptable level, while the proposed segmented core stator of the new servomotor does not require skewing, thereby simplifying manufacture.
- The winding of individual coils on the stator segments of the new servomotor entails a relatively short coil overhang beyond the ends of the stator core in contrast with the conventional servomotor that requires a much larger overhang due to the need for each conductor to be repeatedly routed between stator slots that are not adjacent and separated by several slots. This increases the size of the motor housing of the conventional servomotor as well as the amount of copper for the stator winding, considerably beyond those of the new servomotor for a given frame size and stator stack length. Also the simple bobbin winding machine used for the new servomotor achieves a considerably larger slot fill (typically 53%) than the winding machine used for the conventional servomotor (typically 38%),

enabling a higher torque density and therefore a smaller new servomotor for a given dynamic performance. The new servomotor design therefore carries the advantage of significant material saving.

7.1.3. Thermal Modelling and Performance Prediction

The main components identified for the thermal modelling are the servomotor housing, the stator core, the winding coil and the secondary insulation components. Thermal resistances have been allocated to each of these components and equivalent circuits created with interconnections corresponding to the mechanical interfaces between the components. This modelling includes convection in the air surrounding the servomotor and radiation to the surroundings, which is nonlinear, necessitating the iterative numerical solution of nonlinear simultaneous equations for the steady state temperatures using the multidimensional Newton Raphson method.

It has been established that the secondary insulation components have the greatest thermal resistances and therefore greatly influence the heat flow within the servomotor and modifications to reduce these resistances will enhance the flow of heat from the windings and stator core, where it is generated, to the ambient surroundings, allowing a higher dynamic performance for a given mean temperature or lower temperature operation for a given dynamic performance.

Poor physical contact between the stator components has been identified as the main contributor to the thermal resistances of the secondary insulation components. The critical features in this respect are: a) gaps between the soft iron laminations of the stator stack and the electrical insulation material, b) gaps between the adjacent insulated copper conductors of the stator windings, and c) gaps between the stator windings and the paper wall insulation material. It has been established that these gaps are larger in the conventional servomotor than in the new servomotor due to the mechanical constraints of the distributed winding. Consequently, the thermal efficiency of the new servomotor has been proven to be far higher than that of the conventional servomotor.

7.1.4. Electromagnetic Modelling and Performance Prediction

Regarding the electromagnetic FEA design aspect, the new and conventional servomotor prototypes have been shown to be nearly identical in Chapter 2. Despite

significant harmonics contents from the windings, generating significant eddy-current losses to the permanent magnets, the new servomotor has a significant advantage in terms of torque density as well as thermal efficiency.

7.1.5. Test Results

The permanent magnet retention feature used in the new servomotor gives rise to a high frequency oscillation superimposed on the usual oscillation of the cogging torque. This high frequency oscillation is not considered a serious issue due to the low pass filtering action of the rotor and its inertial mechanical load attenuating the resulting vibrations in the load but it is impossible to accurately reproduce this oscillation by means of a 2D FEA model or by analytical means. Therefore the cogging torque could be only be assessed by experimental means.

The measured iron losses are higher for the new servomotor prototype due to its having a larger number of poles than the conventional prototype, but the significant torque density improvement and manufacturing advantage of the new servomotor renders it much more attractive. Also if a conventional prototype with the same number of poles as the new prototype was available for the comparison, then it is reasonable to suppose that the iron losses of both would be similar for identical frame sizes and stator stack lengths.

The dynamic torque rating results emphasise the performance advantage of the new servomotor over the conventional one for the same frame size and stator stack length in that its maximum torque is 40% greater.

7.1.6. Thermal Impact of Paper Wall Insulation Material

The investigation has revealed the wall insulation thermal conductivity as a critical parameter to maximise in improving the thermal performance of a BPM synchronous servomotor. It was observed that the material density helps to increase the thermal conductivity. Comparison of the results obtained with material samples A and B in Chapter 6 confirmed this. However this performance is not very significant for a TENV BPM synchronous servomotor with distributed winding due to low slot-fill factor.

The experimental approach using a special rig taken to quantify the thermal resistances of wall insulation materials in Chapter 6 was justifiable. The different

thermal performances of the selected wall insulation materials for both prototypes yielded a significant and plausible torque improvement of the new servomotor over the conventional servomotor for a fixed maximum winding temperature. Good agreement was found between the measured temperatures and predictions using a combination of MOTOR-CAD and SPEED indicating that this software can yield a reliable prediction of the motor performance. It was also found that to improve the accuracy of the temperature predictions it is important to model the mounting arrangement since the thermal behaviour of the servomotor depends on this.

7.2. Recommendations

In view of the results of the investigation reported in this thesis, the new segmented stator, concentrated winding BPM servomotor should be establishment in industry. Hence it is recommended to optimise the manufacturing process of this type of servomotor for establishment on new production lines and replacement of worn equipment on existing production lines.

The main concern during the experimental work was the significant increase of permanent magnet temperature in the new servomotor due to the significant harmonic content of the stator MMF brought about by the concentrated winding configuration, as this can cause irreversible demagnetization of the permanent magnets in the rotor. To reduce this undesirable effect, a particularly interesting further research project would be to replace the simple single coil per segment concentrated winding configuration with a new configuration in which more than one coil is wound on each segment, not necessarily with equal numbers of turns, and the whole set of coils connected to the three phase supply in such a way that the resulting m.m.f. distribution is a better approximation to a sinusoid than previously. In addition, the design of the permanent magnets and their mounting arrangements should be reviewed together with an investigation of different magnet coating materials, including electrically conducting and non-conducting ones, with a view to further minimizing the magnet temperature rise.

The proposed research on the permanent magnet design improvements should take into account and build upon the work of other researchers, such as (Toda et al., 2005) on segmentation of permanent magnets circumferentially. A more cost

effective solution is proposed by (Dajaku et al., 2012) where flux barriers are introduced to avoid some undesirable flux paths in the stator. Another solution for specific MMF harmonic reduction is proposed by (Dajaku et al., 2011) and this is done by properly defining the tooth width in two different sizes. However the authors predict that their method will only reduce the more significant MMF harmonic to 20% of the fundamental magnitude. Another approach that should be considered is that of (Mecrow et al., 2004) who propose carbon fibre sleeves made material that can be used to protect the permanent magnets.

Finally, it is recommended to investigate the overall efficiency of the drive in which the new servomotor is used. This will not only depend upon the motor itself, the power electronic devices and modulation frequencies/methods but also on the acceleration and velocity profiles needed for particular applications, which should be replicated in the investigation.

REFERENCES

ASTM, (2011) Standard Test Method for Thermal Transmission Properties of Thermally Conductive Electrical Insulation Materials. ASTM Paper No. D5470 – 06.

Becker, K. M. and Kaye, J. (1962) Measurements of adiabatic flow in an annulus with an inner rotating cylinder. *Journal of Heat Transfer*, no. 84, page 97-105.

Beckley, P. (2002) *Electrical steels: for rotating machines*. IEE Power and Energy Series, number 37.

Boglietti, A., Cavagnino, A., Lazzari, M. and Ferraris, L. (2001) Effects of Punch Process on the magnetic and energetic properties of soft magnetic material. *Electric Machines and Drives Conference, IEMDC'01*. IEEE International, page 396 – 399.

Boglietti, A., Cavagnino, A., Ferraris, L. and Lazzari, M. (2003a) The Annealing Influence onto the Magnetic and Energetic Properties in Soft Magnetic Material after Punching Process. *Electric Machines and Drives Conference, IEMDC'03*. IEEE International, page 503 – 508, volume 1.

Boglietti, A., Cavagnino, A., Lazzari, M. and Pastorelli, M. (2003b) A simplified thermal model for variable-speed self-cooled industrial induction motor. *IEEE Transaction on Industry Application*.

Boglietti, A., Cavagnino, A., Staton, A., Shanel, M., Mueller, M., and Mejuto, C. (2009) Evolution and modern approaches for thermal analysis of electrical machines. *IEEE Transaction on Industrial Electronic*, volume 56, no. 3.

Boglietti, A., El-Refaie, A. M., Drubel, O., Omekanda, A. M., Bianchi, N., Agamloh, E. B., Mircea, P., Di Gerlando, A., and Bartolo, J. B. (2014) 'Electrical machine topologies: Hottest topics in the electrical machine research community', *Industrial Electronic Magazine, IEEE*, volume 8, no. 2, June, page 18 – 30.

Churchill, S. W. and Chu, H. H. S. (1975a) Correlating equations for laminar and turbulent free convection from a horizontal cylinder. *Int. J. Heat & Mass Transfer* 18, page 1049-1053.

Churchill, S. W. and Chu, H. H. S. (1975b) Correlating Equations for Laminar and Turbulent Free Convection from a Vertical Plate. *Int. J. Heat & Mass Transfer* 18, page 1323-1329.

Cistelecan, M., Popescu, M. and Popescu, M., (2007) Study of the number of slots/pole combinations for low speed permanent magnet synchronous generators. In *Proc. Of IEEE Int. Electric Machines and Drives Conf., (IEMDC)*, volume 2.

Clerc, A and Muetze, A., (2012) Measurement of stator core magnetic degradation during the manufacturing process. *IEEE Transactions Industry Applications*, volume 48, no. 4, page 1344–1352.

Control Techniques, (2014) Digitax ST High dynamic performance servo drive range [accessed June 2014]. <http://www.emersonindustrial.com/en-EN/controltechniques/products/servodrives/digitaxst/Pages/digitax-st.aspx>.

Cros, J. and Viarouge, P. (2002) Synthesis of high performance PM motors with concentrated windings. *IEEE Transactions on Energy Conversion*, volume 17, no. 2.

Dajaku, G. and Gerling, D. (2006) An improved lumped parameter thermal model for electrical machines. 17th International Conference on Electrical Machines (ICEM 2006).

Dajaku, G. and Gerling, D. (2011) A novel 24-slots/10-poles winding topology for electric machines. *IEEE International Electric Machines and Drives Conference, IEMDC2011*, Niagara Falls, Canada, May 15-18.

Dajaku, G., Gerling, D. (2012) A novel 12-teeth/10-poles PM machine with flux barriers in stator yoke. 20th International Conference on Electrical Machines (ICEM), Marseille, France.

Demetriades, G. D., de la Parra, H. Z., Anderson, E. and Olsson, H. (2010) A real-time thermal model of a permanent-magnet synchronous motor. IEEE Transactions on Power Electronics, Volume 25, no 2.

Dosiek, L. and Pillay, P. (2007) Cogging torque reduction in permanent magnet machines. IEEE Transactions on Industry Applications, volume 43, no 6.

DuPont, (2012) Nomex LT type 180 presentation. Nomex LT Prelim Datasheet.

El-Refaie, A. M. (2013) Fractional-Slot Concentrated-Windings: A Paradigm Shift in Electrical Machines. IEEE Workshop on Electrical Machines Design Control and Diagnosis, WEMDCD, page 208-217.

Fan, C. Z., Huang, M. X. and Ye, Y. Y. (2009) Research and industrial application of a novel compound permanent magnet synchronous machine. J Zhejiang University, Sci A 10(4): 471-477.

Gazley, C. (1958) Heat transfer characteristics of the rotational and axial flow between concentric cylinders. Transactions of the ASME, volume 80, page 79-90.

Gerling, D. and Dajaku, G. (2005) Novel lumped-parameter thermal model for electrical systems. European Conference on Power Electronic Application.

Hanselman, D. (2003) Brushless permanent magnet motor design. 2nd Edition, USA: The Writers Collective.

Hanselman, D. C. (1994) Minimum torque ripple, maximum efficiency excitation of brushless permanent magnet motors. IEEE Transactions on Industrial Electronics, volume 41, no. 3, page 292-300.

Hargreaves, P., Mecrow, B. and Hall, R. (2012) Calculation of iron loss in electrical generators using finite-element analysis. IEEE Transactions Industry Applications, volume 48, no. 5, page 1460–1466.

Hendershot, J. R. and Miller, T. J. E. (1994) Design of brushless permanent-magnet motors. Magna Physics Publications and Oxford Science Publications.

Hendershot, J. R. and Miller, T. J. E., (2010) Design of brushless permanent-magnet machines. Motor Design Books LLC.

Holman, J. P. (1981) Heat transfer. McGraw-Hill, NY.

Ibrahim, M. and Pillay, P. (2012) Advanced testing and modelling of magnetic materials including a new method of core loss separation for electrical machines. IEEE Transaction Industry Application, volume 48, no. 5, page 1507–1515.

IEA (International Energy Agency), (2008) World energy outlook. Available online from: <http://www.worldenergyoutlook.org/S.103-107>; [accessed August 2011].

IEA (International Energy Agency), (2007) “Tracking industrial energy efficiency and CO₂ emissions”, Paris: OECD/IEA; Available online from: http://www.iea.org/publications/freepublications/publication/tracking_emissions.pdf [accessed June 2012].

Incropera, F. P. and DeWitt, D. P. (2011) Fundamental of heat and mass transfer. 7th ed., John Wiley & Sons, Inc.

Incropera, F. P., Dewitt, D. P., Bergman, T. L. and Lavine, A. S. (2007) Introduction to Heat Transfer. John Wiley & Sons.

Jack, A. G., Mecrow, B. C., Dickinson, P. G., Stephenson, D., Burdess, J. S., Fawcett, N. and Evans, J. T., (2000) Permanent-magnet machines with powdered iron cores and pre-pressed windings. Industry Applications, IEEE Transactions.

Jokinen, T. (2004) Large permanent magnet machines. International Aegean Conference on Electric Machines and Power Electronics, Istanbul, Turkey.

Keyhani, A., Stunder, C. B., Sebastian, T. and Murthy, S., K. (1999) Study of cogging torque in permanent magnet machines. Electric Machines and Power Systems, page 665 – 668.

Krovel, O., Nilssen, R. K., and Nysveen, A. (2004) A study of the research activity in the Nordic countries on large permanent magnet synchronous machines. In *NORPIE*, Trondheim, Norway.

Kylander, G. (1995) Thermal modelling of small cage induction motors. PhD Thesis, School of Electrical and Computer Engineering, Chalmers University of Technology, Goteborg, Sweden. Technical report no. 265.

Libert, F. (2004a) Design, optimization and comparison of permanent magnet motors for a low-speed direct-driven mixer. Licentiate thesis, Department of Electrical Machines and Power Electronics, Royal Institute of Technology.

Libert, F. and Soulard, J., (2004b) Investigation on slot-pole combinations for permanent magnet machines with concentrated windings. International Conference on Electrical Machines, Cracow, Poland.

Libert, F. and Soulard, J., (2006) Manufacturing methods of stator cores with concentrated windings. Proceedings of IET International Conference on Power Electronics, Machines and Drives (PEMD), page 676-680.

Lindstrom, J. (1999) Thermal Model of a Permanent-Magnet Motor for a Hybrid Electric Vehicle. Chalmers University of Technology, Internal report, Goteborg, Sweden.

Liu, Z. J., Howe, D. and Mellor, P. D. (1993) Thermal analysis of permanent magnet Machines. In Proc. Sixth International Conference on Electrical Machines and Drives, page 359-364.

Lu, K., Rasmussen, P.O. and Ritchie, E. (2006) An Analytical equation for cogging torque calculation in permanent magnet motors. Institute of Energy Technology, Aalborg University, Pontoppidanstraede 101, 9220 Aalborg east, Denmark.

Magnusson, F. and Sadarangani, C. (2003) Winding factors and joules losses of permanent magnet machines with concentrated windings. Department of Electrical Engineering, Sweden.

Magnusson, F., Thelin, P. and Sadarangani, C., (2004) "Performance evaluation of permanent magnet synchronous machines with concentrated and distributed windings including the effect of the field weakening" IET Conference Publications, volume 2, no. 498, page 679-685.

Mecrow, B. C., Jack, A. G., Haylock, J. A., Hofer, U. and Dickinson, P. G. (2004) 'Simplifying the manufacturing process for electrical machines', IET Conference Publications, volume1, no. 498, page 169 – 174.

Mellor, P. H., (1983) Improvement in the efficiency and thermal ageing of single and parallel machine drives. Ph.D. dissertation, University of Liverpool.

Mellor, P. H., Roberts, D. and Turner, D. R. (1991) Lumped Parameter Thermal Model for Electrical Machines of TEFC Design. IEE Proceedings 138, page 205-218.

Miller, T.J.E. and Staton, D.A. (2013) Electric machine design – using SPEED and Motor-CAD. Handout from Motor Design Limited.

Moravec, J. (2008) Torque ripple of permanent magnet synchronous torque motor. VCSVTT. <http://stc.fs.cvut.cz/pdf/MoravecJan-302972.pdf>.

Nategh, S., Krings, A., Wallmark, O., and Leksell, M. (2014) Evaluation of Impregnation materials for thermal management of liquid-cooled electric machines. IEEE Transactions on Industrial Electronics, volume 61, no. 11.

Overshoot, K. J., (1991) "Magnetism: it is permanent", IEE Proceedings A, Volume 138, No. 1, page 22-30

Popescu, M. and Staton, D. (2012) Design of brushless permanent magnet machines. Training Course, Ellesmere, Shropshire, UK. Tutorial Course Notes.

Popescu, M., Staton, D., Dorell, D., Marignetti, F. and Hawkins, D. (2013) Study of the thermal aspects in brushless permanent magnet machines performance. IEEE Workshop on Electrical Machines Design Control and Diagnosis, WEMDCD, page 60-69.

Powell, D. J, (2003) "Modelling of high power density electrical machines for aerospace", PhD. dissertation, Univ. Sheffield, Sheffield, U.K.

Sá, H., Hosny, W. M., Dodds, S. J., and Staton, D. A., (2013) "Influence of wall insulation material in BPM synchronous servomotor", Universities Power Engineering Conference, UPEC2013 48th International Conference.

Sá, H., Jayasoma, S., Sooriyakumar, G. (2010-2013) Control Techniques Dynamics Ltd, South Way, Walworth Industrial Estate, Andover, Hampshire SP10 5AB, United Kingdom. Unimotor HD & FM Product Data 055 to 190 Frames, Helder Da Silva (University of East London) Research Work.

Saari, J. (1998) Thermal analysis of high-speed induction machines. PhD Thesis, Laboratory of Electromechanics, Helsinki University of Technology.

Salminen, P. (2004) Fractional slot permanent magnet synchronous motors for low speed applications. PhD Thesis, Lappeenranta University of Technology.

Salon, S. J. (1995) Finite Element Analysis of Electrical Machines. Kluwer Academic Publishers.

Simpson, N., Wrobel, R. and Mellor, P. H. (2013) A general arc-segment element for three-dimensional thermal modelling. 19th International Conference on the Computation of Electromagnetic Fields, Compumag2013, Budapest, Hungary.

Sooriyakumar, G., Perryman, R. and Dodds, S. J., (2006) Improved cogging calculation methods for surface mounted permanent magnet synchronous servomotors. Universities Power Engineering Conference, UPEC2006 41st International Conference.

Sooriyakumar, G., Perryman, R. and Dodds, S. J., (2007a) Cogging torque analysis for fractional slot-pole permanent magnet synchronous motors. Universities Power Engineering Conference 2007, UPEC2007 42nd International Conference.

Sooriyakumar, G., Perryman, R. and Dodds, S. J. (2007b) Design optimisation for permanent magnet synchronous motor using genetic algorithm. School of Computing, Information Technology & Engineering (CITE), University of East London (UEL).

Sooriyakumar, G., Perryman, R. and Dodds, S. J. (2007c) Analytical thermal modelling permanent magnet synchronous motors. Universities Power Engineering Conference, UPEC 2007 42nd International Conference.

Sooriyakumar, G., (2009) Efficient design methodology for permanent magnet synchronous motors. PhD Thesis, University of East London, London, UK.

Staton, D. A. (2001) Thermal computer aided design – Advancing the revolution in compact motors. In Proc. IEEE IEMDC, Boston, MA, page 858 – 863.

Staton, D., Boglietti, A. and Cavagnino, A. (2005a) Solving the more difficult aspects of electric motor thermal analysis in small and medium size industrial induction motors. IEEE Transactions on Energy Conversion, volume 20, no. 3, page 620 – 628.

Staton, D., Pickering, S. and Lampard, D. (2005b) Recent advancement in the thermal design of electric motors. in Proc. SMMA-Fall Tech. Conf., Durham, North Carolina, USA, 3-5.

Staton, D. A. and Cavagnino, A., (2008) Convection heat transfer and flow calculation suitable for electric machines thermal models. IEEE Transactions on Industrial Electronics, volume 55, no. 10, page 3509 – 3516.

Staton, D., (2012) Thermal analysis of electric motors and generators. Training Course, Ellesmere, Shropshire, UK. Tutorial Course Notes.

Stening, A. (2006) Design and optimization of a surface-mounted permanent magnet synchronous motor for a high cycle industrial cutter. Master Thesis, Royal Institution of Technology, Department of Electrical Engineering, Stockholm.

Taylor, G. I. (1935) Distribution of velocity and temperature between concentric cylinders. In Proc Royal Soc., volume 159, page 546–578.

The Carbon Trust, (2011) Motors and Drives: Introducing Energy Saving Opportunities for Business”. URL

http://www.carbontrust.com/media/13059/ctv048_motors_and_drives.pdf. [accessed June 2012].

Toda, H., Wang, J. and Howe, D. (2005) Analysis of motor loss in permanent magnet brushless motors. JFE TECHNICAL REPORT N° 6 [accessed October 2010], <http://www.jfe-steel.co.jp/en/research/report/006/pdf/006-05.pdf>.

Wu, L. J., Zhu, Z. Q., Chen, J. T., Xia, Z. P. and Jewell, G. W. (2010) Optimal split ratio in fractional slot interior permanent-magnet machines with non-overlapping windings. *IEEE Transactions on Magnetics*, volume 46, no. 5, page 1235-1242.

Yang, Y., Huang, W. C. and Lai, C. W. (2007) Optimal design of rim motor for electric powered wheelchair. *IET Electric Power Applications*, page 825-832.

Yang, Y. P., Yang, S. C. and Liu, J. J. (2009) Optimal design and control of a torque motor for machine tools. *Journal of Electromagnetic Analysis & applications*.

Zhu, Z. Q., Howe, D., Bolte, E., and Ackermann, B. (1993) Instantaneous magnetic field distribution in brushless permanent magnet dc motors, part i: Open circuit field. *IEEE Transaction on Magnetics*, volume 29, no. 1, page 124-135.

Zhu, Q. Z. and Howe, D. (2000) Influence of design parameters on cogging torque in permanent magnet machines. *IEEE Transactions on Energy Conversion*, volume 15, page 407-412.

Zhu, Z. Q. (2009) Fractional slot permanent magnet brushless machines and drives for electric and hybrid propulsion systems. *COMPEL: The International Journal for Computation and Mathematics in Electrical and Electronic Engineering*, Volume 30 Iss: 1, page 9 – 31.

APPENDIX

Appendix A - Project Structure

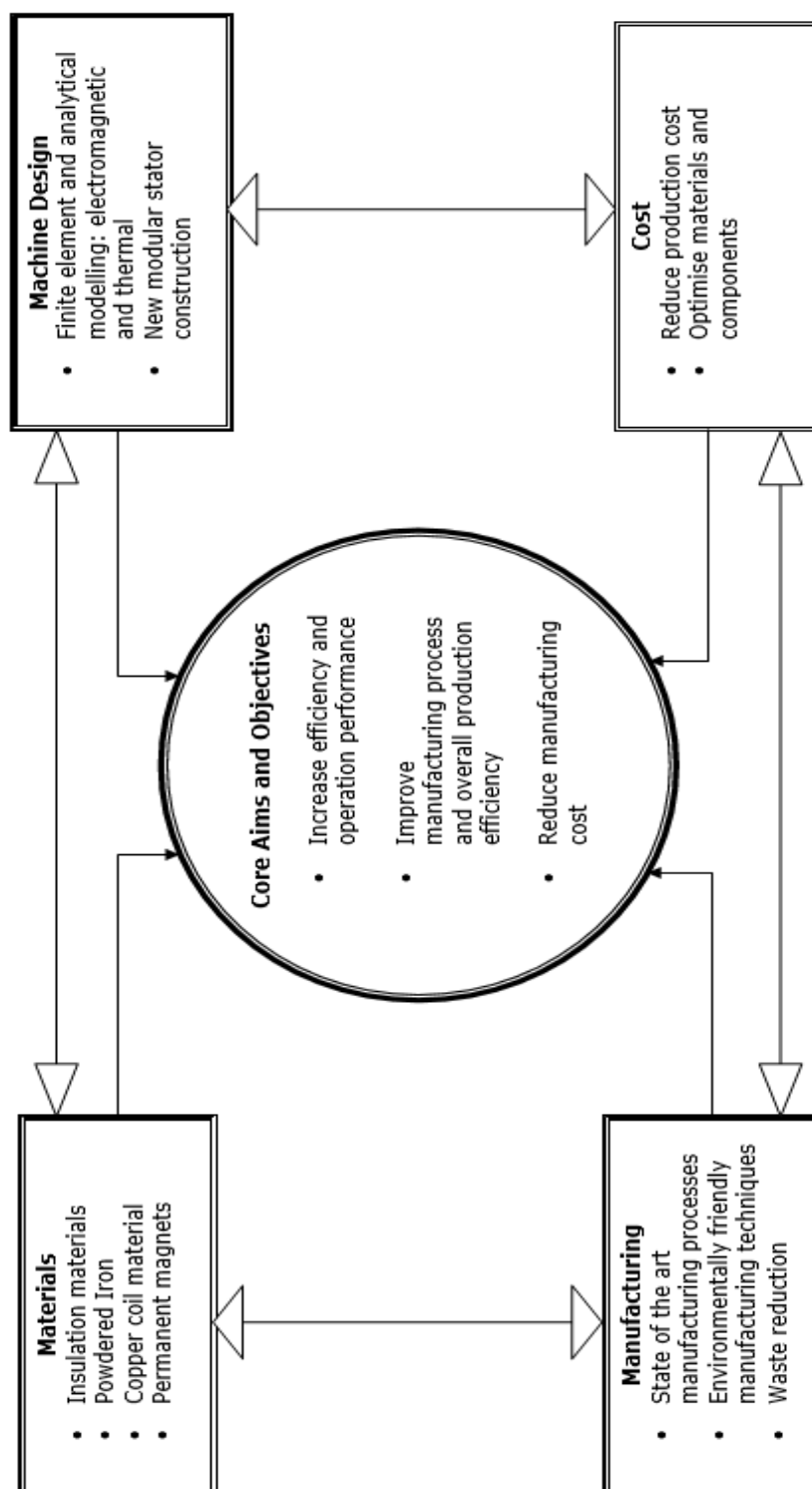


Fig. A.1. Project structure for the research program.

Appendix B Reluctance/Cogging torque

Reluctance/Cogging torque

Cogging torque is one of the main contributors to the torque ripple in the permanent magnet machines. Cogging torque is due to desire of the permanent magnets on the rotor to align at minimum opposition to magnet flux or reluctance. The Fig. B.(1, 2, 3, 4 and 5) bellow show that the mechanism of cogging torque is purely caused by the interaction between the permanent magnet on the rotor and steel stator part, and for simplicity rectangular poles and iron ring are used represent the stator, and the rotor is simple a bar of magnet.

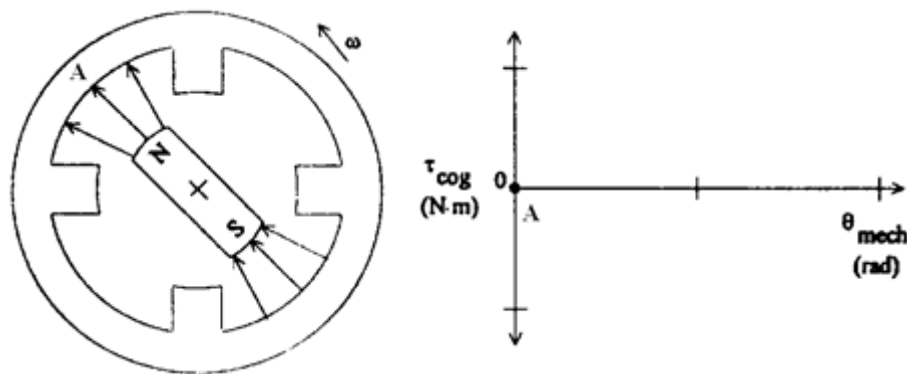


Fig. B.1. Position 'A', unstable equilibrium (Moravec, 2008).

Position 'A' is called unstable equilibrium and it is shown in the Fig. B.1, at this mechanical angle the cogging torque is assumed to be zero, because this is where any small disturbance would make the magnet bar to move away from position 'A'. It is also assumed that the bar magnet is exactly in middle of the pole pitch or in this case between the two teeth and the air gap and the flux are evenly distributed and therefore at this position there is *no torque*.

Now, if the bar magnet is slightly move anti-clockwise, in this case towards the position 'B' as shown in Fig. B.2 there will be uneven air distribution and therefore the rotor will experience an attractive force (*a force field*) to the nearest

ferromagnetic pole, and this is because the flux lines start travelling through nearest ferromagnetic path, and the rotor bar magnet will start seeking to align with ferromagnetic poles and therefore at position 'B' reluctance torque (cogging) is produced as peak cogging torque value.

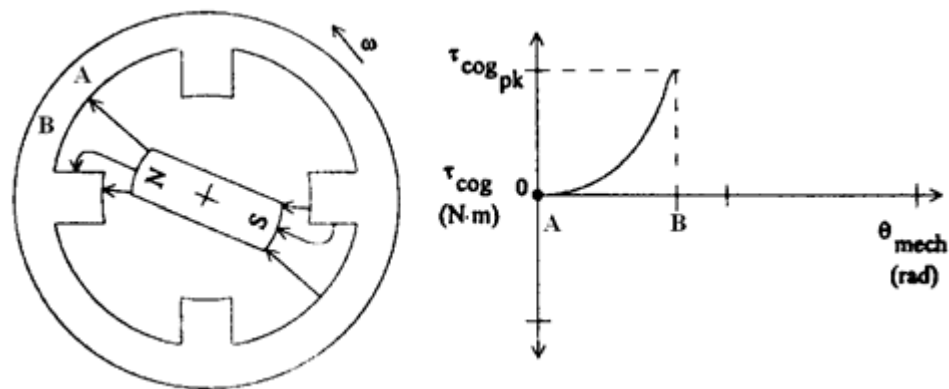


Fig. B.2. Position 'B', motor produces a torque (Moravec, 2008).

In Fig. B.3, at position 'C' the rotor bar magnet is aligned with the ferromagnetic poles and this position is called stable equilibrium position, at this point the magnet flux is symmetric or balanced around the ferromagnetic poles. The torque at this position is zero, external torque higher than its reluctance torque will need to be applied to the bar magnet in order to take it away from the stable position because when the external torque is applied the bar magnet rotor will tend to hold stable equilibrium position.

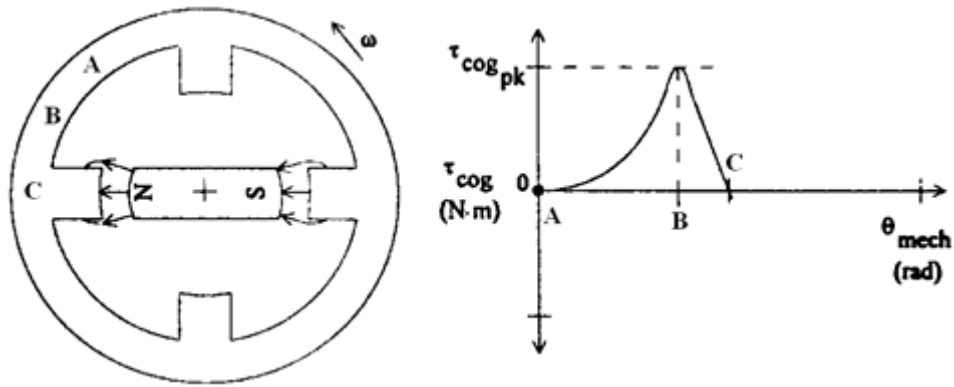


Fig. B.3. Position 'C', stable equilibrium (Moravec, 2008).

When the external torque overcomes the reluctance torque, the bar magnet rotor will move anti-clockwise and the reluctance torque will be in the opposite polarity compare to the reluctance torque of the Fig. B.1, and this can be observed in the Fig. B.4, where the bar magnet rotor has found another unstable position or in our case a new unstable equilibrium at position 'D'.

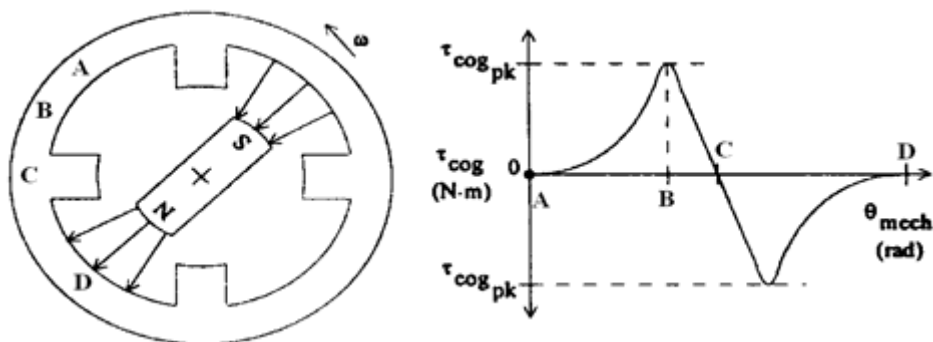


Fig. B.4. Position 'D', unstable equilibrium (Moravec, 2008).

The typical cogging torque waveform in the Fig. B.4 is the resultant or total cogging or reluctance torque between the bar magnet rotor poles (north and south). It can be observed from that Fig. B.5 that the peak torque produced solely by one pole is much higher than the resultant total cogging torque, and this that South pole is cancelling some of the cogging produced by north pole (Lu, 2006).

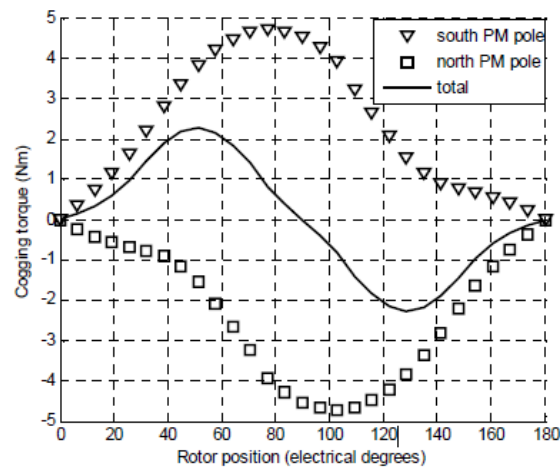


Fig. B.5. Cogging torque produce by north, south poles and resultant cogging (Lu, 2006).

The stator ferromagnetic surrounding around the air gap forms a variable magnetic resistance because of the cycled ferromagnetic poles carrying the windings that have air gaps between them. If these air gaps did not exist the cogging torque would be zero, this means that we would have a uniform air gap between the bar magnet rotor and the ferromagnetic stator (stator yoke or back iron) and any position could be taken as an *unstable equilibrium* position. This means that the cogging torque is purely the interaction between the bar magnet rotor and the ferromagnetic stator and does not need any current to the motor or system.

According to (Hanselman, 1994) exact reluctance or cogging torque can be quantify base on the rotor position and the material properties of motor parts and this is simple just one more component of the motor torque relationship

$$T_{cogg} = -\frac{1}{2} \Phi^2 \frac{dR}{d\theta} \quad (1A)$$

Where:

- τ_{cogg} [Nm] reluctance/cogging torque
- Φ [Wb] magnet flux crossing the air gap
- R [A/Wb] total reluctance through which the flux passes
- θ [rad] rotor angular position

But (Moravec, 2008) highlighted that the only reason that the equation (1A) cannot be often applied it because most of the time the knowledge of the material property is unavailable due to manufacturing secret and therefore effectively the best way is to measure the cogging torque from the motor/prototype.

The fundamental form equation (1A) shown that cogging torque is a function of air gap flux, air gap reluctance and the rotor position. And from figure 5 it can be observed that when the bar magnet rotor move from position 'A' to position 'D' a full cogging waveform is obtained and this is a rotation of 90 mechanical degrees or $\frac{1}{4}$ of the full rotation, therefore at full rotation four cogging cycles will be obtained. Here a special relation can be observed between the number of poles (N_p) and number of stator slots (N_s), their least common multiple (LCM but it is defined as N_c) will be equal to the number of cogging cycles for complete rotation or full mechanical revolution.

This reinforces the idea that cogging torque is the interaction between the magnet (the source of flux that passes through the air gap) and the stator teeth (the source of the varying air-gap reluctance), and also this interaction is periodic therefore cogging torque can be represented in general form as a Fourier series

$$T_{cogg} = \sum_{i=1,2,3,\dots}^{\infty} T_i \sin(iN_c\theta) \quad (2A)$$

Reluctance/Cogging torque is an undesirable component and theoretically it can be eliminated via machine design, from equation (1), if the air-gap flux (Φ) or rate of change of the air gap reluctance ($dR/d\theta$) is forced to zero the cogging torque will be zero. The air-gap flux cannot be zero since the gap is needed for the windings and

also without it the machine would not be able to rotate when current is applied to its windings.

According to (Dosiek et al., 2007) cogging torque can be cancel by making the air-gap reluctance to be constant with respect to the rotor position. But according to Dr Duane Hanselman, in practice the cogging torque can be greatly reduce but it cannot be eliminated, and this can be achieved mainly by two ways, *optimal pole arc* or *magnet shifting*, it is a proven fact that the magnet pole shape can affect cogging level and (Zhu, 2000) highlighted how the magnet arc can affect the peak value of cogging torque, by shifting the magnet the waveforms from Fig. B.5 (*north and south*) can be made symmetrical depending on the number of slots per pole is integer and therefore waveform will cancel out (Dosiek et al., 2007).

(Zhu, 2000) used the fundamental equation (2A) with an introduction of a skew factor and the equation became

$$T_{cogg} = \sum_{i=1,2,3,\dots}^{\infty} K_{sk} T_i \sin(iN_c \theta) \quad (3A)$$

$$K_{sk} = \frac{\sin(iN_c \pi \alpha_{sk} / Q_s)}{iN_c \pi \alpha_{sk} / Q_s} \quad (4A)$$

Where:

i an integer

K_{sk} skew factor

Q_s slot number

N_c least common multiple

α_{sk} ratio of the total circumferential skew to the slot pitch

They mentioned that generally cogging torque (T_{cogg}) amplitude is lower when the least common multiple (N_c) is large and the number of slots (Q_s) or number of poles (N_p) is small. Therefore in order to help on the selection of Q_s and N_p for certain cogging at design stage for both overlapping and non-overlapping, they introduced a new factor C_T named “goodness” of slot and pole number combination as following:

$$C_T = \frac{2pQ_s}{N_c} \quad (5A)$$

They highlighted that there is no formal basis for relating C_T to the amplitude of cogging torque but it was found that this factor is proportional to the cogging torque peak value.

Appendix C - FEA Scripting Sample using Opera_2D

MY FIRST SCRIPT

```

/+***** TO SET THE UNITS USING (UNITS COMMAND 3-231) *****
UNITS LENGTH=CM FLUX=GAUSS FIELD=OERSTED POTENTIAL=GAUSS CM CONDUCTIVITY=SIEMENS/CM

/+***** TO SET THE VIEW (RECONSTRUCT COMMAND 3-192) *****
RECONSTRUCTXMIN=-9XMAX=9YMIN=-9YMAX=9MATERIAL=ALLNOT=ANY

/+***** TO DEFINE THE SOLUTION TYPE (SET COMMAND 3-202) *****
SETELEMENT=QUADRATIC

$constant #R2 4.13
$constant #R7 7.87
$constant #Rsh 1.49
$constant #Betar 11.25*2
$constant #Betas 11.15
$constant #SDr 2.0
$constant #SDs 1.83
$constant #GAP 0.031
$constant #SPOLESN 8
$constant #RPOLESN 6

$parameter #R4 #R2+3*#GAP/4
$parameter #R1 #R2-#SDr
$parameter #OC #R1*sinD(#Betar)
$parameter #OC1 #R4*sinD(#Betas)
$parameter #A2 AsinD(#OC/#R2)
$parameter #R3 #R2+#GAP/4
$parameter #R4 #R2+3*#GAP/4
$parameter #A3 AsinD(#OC/#R3)
$parameter #SPOLES #SPOLESN*2
$parameter #RPOLES #RPOLESN*2
$parameter #R5 #R2+#GAP
$parameter #A5 AsinD(#OC1/#R5)
$parameter #Rw #R5+0.2
$parameter #R6 #R2+#GAP+#SDs
$parameter #Aw AsinD(#OC1/#Rw)
$parameter #A6 AsinD(#OC1/#R6)
$parameter #Aw2 #A6+((360/#SPOLES)-#A6)/2
$parameter #R8 #R7+1.0

/+***** ROTOR *****

DRAWSHAPE=POLYGONxcen=0 ycen=0MATERIAL=OPERM=1DENS=ON1=1ON2=2
POLA0OC=0 n=10 b=0.5f=NO
POLA#Rsh0C=0 n=10 b=0.5f=NO

```

```

POLA#Rsh360/#RPOLESC=-1/#Rshn=10 b=0.5f=NO
FINI C=0n=10 b=0.5 f=NO
QUIT
DRAWSHAPE=POLYGONxcen=0 ycen=0MATERIAL=5PERM=2500DENS=0N1=10N2=2
POLA#Rsh0C=0 n=10 b=0.5f=NO
POLA#Rsh360/#RPOLESC=-1/#Rshn=10 b=0.5f=NO
POLA#R1360/#RPOLESC=0 n=10 b=0.5f=NO
POLA#R1#BetarC=1/#R1 n=10 b=0.5f=NO
POLA#R2#A2C=0 n=10 b=0.5f=NO
POLA#R20C=1/#R2 n=10 b=0.5f=NO
FINI C=0n=10 b=0.5 f=NO
QUIT

```

```

DRAWSHAPE=POLYGONxcen=0 ycen=0MATERIAL=0PERM=1DENS=0N1=10N2=2
POLA#R2#A2C=0 n=10 b=0.5f=NO
POLA#R20C=1/#R2n=10 b=0.5f=NO
POLA#R30C=0n=10 b=0.5f=NO
POLA#R3360/#RPOLESC=-1/#R3n=10 b=0.5f=NO
POLA#R1360/#RPOLESC=0n=10 b=0.5f=NO
POLA#R1#BetarC=1/#R1n=10 b=0.5f=NO
FINI C=0n=10 b=0.5 f=NO
QUIT

```

```

COPYREG1=1REG2=3MIRROR=YESTHETA=360/#RPOLES
COPYREG1=1REG2=6MIRROR=YESTHETA=(360/#RPOLES)*2
COPYREG1=1REG2=6MIRROR=YESTHETA=(360/#RPOLES)*3
COPYREG1=1REG2=6MIRROR=YESTHETA=(360/#RPOLES)*4
COPYREG1=1REG2=6MIRROR=YESTHETA=(360/#RPOLES)*5
COPYREG1=1REG2=6MIRROR=YESTHETA=(360/#RPOLES)*6

```

```

GAPINCLUDE=YESRADIUS=#R2+(#GAP/2)SYMMETRY=1

```

```

/+***** STATOR *****

```

```

DRAWSHAPE=POLYGONxcen=0 ycen=0MATERIAL=0PERM=1DENS=0N1=10N2=2
POLA#R40C=0 n=10 b=0.5f=NO
POLA#R4360/#SPOLESC=-1/#R4n=10 b=0.5f=NO
POLA#Rw360/#SPOLESC=0 n=10 b=0.5f=NO
POLA#Rw#AwC=1/#Rwn=10 b=0.5f=NO
POLA#R5#A5C=0n=10 b=0.5f=NO
POLA#R50C=1/#R5n=10 b=0.5f=NO
FINI C=0n=10 b=0.5 f=NO
QUIT

```

```

DRAWSHAPE=POLYGONxcen=0 ycen=0MATERIAL=5PERM=2500DENS=0N1=10N2=2
POLA#R50C=0 n=10 b=0.5f=NO
POLA#R5#A5C=-1/#R5 n=10 b=0.5f=NO
POLA#Rw#AwC=0 n=10 b=0.5f=NO
POLA#R6#A6C=0 n=10 b=0.5f=NO
POLA#R6(360/#SPOLES) C=-1/#R6 n=10 b=0.5f=NO
POLA#R7(360/#SPOLES)C=0 n=10 b=0.5f=NO
POLA#R70C=1/#R7 n=10 b=0.5f=NO
FINI C=0n=10 b=0.5 f=NO
QUIT

```

```
DRAWSHAPE=POLYGONxcen=0 ycen=0MATERIAL=1PERM=1DENS=0N1=10N2=2
POLA#Rw#AwC=0 n=10 b=0.5f=NO
POLA#R6#A6C=0 n=10 b=0.5f=NO
POLA#R6(360/#SPOLES)C=-1/#R6 n=10 b=0.5f=NO
POLA#Rw(360/#SPOLES)C=0 n=10 b=0.5f=NO
FINI C=1/#Rw n=10 b=0.5 f=NO
QUIT
```

```
COPYREG1=37REG2=39MIRROR=YESTHETA=(360/#SPOLES)
```

```
COPYREG1=37REG2=39MIRROR=NOTHETA=(360/#SPOLES)*2
COPYREG1=40REG2=42MIRROR=NOTHETA=(360/#SPOLES)*2
COPYREG1=37REG2=48MIRROR=NOTHETA=90
COPYREG1=37REG2=60MIRROR=YESTHETA=180
```

```
GROUPNAME=RotorACTION=CREATE
```

```
GROUPNAME=RotorACTION=ADDREG1=1REG2=36
```

```
MOVEREG1=RotorTHETA=12
```

```
/+***** BACKGROUND *****
```

```
DRAWSHAPE=POLYGONxcen=0 ycen=0MATERIAL=0PERM=1DENS=0N1=10N2=2
POLA#R70C=0 n=10 b=0.5f=NO
POLA#R7(360/#SPOLES)C=-1/#R7n=10 b=0.5f=NO
POLA#R8(360/#SPOLES)C=0n=10 b=0.5f=NO
POLA#R80C=1/#R8n=10 b=0.5f=NO
FINI C=0n=10 b=0.5 f=NO
QUIT
```

```
COPYREG1=85REG2=*MIRROR=YESTHETA= (360/#SPOLES)
COPYREG1=85REG2=86MIRROR=NOTHETA= (360/#SPOLES)*2
COPYREG1=85REG2=88MIRROR=NOTHETA=90
COPYREG1=85REG2=92MIRROR=YESTHETA=180
```

```
/+-----+
/+                MODIFY COMMANDS                +/
/+-----+
```

```
MODIFYREG1=51DENS=(18/AREA)*10e4
MODIFYREG1=75DENS=(18/AREA)*10e4
MODIFYREG1=48DENS=-(18/AREA)*10e4
MODIFYREG1=72DENS=-(18/AREA)*10e4
```

```
/+-----+
/+                DEFINE THE BH CHARACTERISTICS        +/
```

